



HYPER-CROSS-LINKED, HYBRID
MEMBRANES VIA INTERFACIAL
POLYMERIZATION

MICHIEL RAAIJMAKERS

**HYPER-CROSS-LINKED, HYBRID
MEMBRANES VIA INTERFACIAL
POLYMERIZATION**

Promotiecommissie:

prof. dr. ir. J.W.M. Hilgenkamp (Voorzitter)	Universiteit Twente
prof. dr. ir. Nieck E. Benes (Promotor)	Universiteit Twente
prof. dr. ir. Arian Nijmeijer (Promotor)	Universiteit Twente
prof. dr. Matthias Wessling	RWTH Aachen
dr. Anne Julbe	Institut Européen des Membranes
prof. dr. ir. Theo Dingemans	Technische Universiteit Delft
prof. dr. Jorge Gascon	Technische Universiteit Delft
dr. ir. Mark Hempenius	Universiteit Twente
prof. dr. ir. Jeroen Cornelissen	Universiteit Twente

Omslagontwerp door Inge Nahuis

Hyper-cross-linked, hybrid membranes via interfacial polymerization

ISBN: 978-90-365-3967-8

DOI: 10.3990/1.9789036539678

URL: <http://dx.doi.org/10.3990/1.9789036539678>

Printed by: Ipskamp Drukkers, Enschede

© Copyright 2015 Michiel J.T. Raaijmakers

HYPER-CROSS-LINKED, HYBRID MEMBRANES VIA INTERFACIAL POLYMERIZATION

PROEFSCHRIFT

ter verkrijging van
de graad van doctor aan de Universiteit Twente,
op gezag van de rector magnificus,
prof. dr. H. Brinksma,
volgens besluit van het College voor Promoties
in het openbaar te verdedigen
op vrijdag 2 oktober 2015 om 16:45 uur

door

Michiel Jozef Thomas Raaijmakers
geboren op 11 mei 1987
te Geldrop, Nederland

Dit proefschrift is goedgekeurd door de promotoren:

prof. dr. ir. Nieck E. Benes (Promotor)

prof. dr. ir. Arian Nijmeijer (Promotor)

This work is financially supported by the University of Twente, Inorganic Membranes Chair, and the European Union's Seventh Framework Programme for research, technological development and demonstration under CARENA grant agreement no. 263007

UNIVERSITY OF TWENTE.

MESA+

INSTITUTE FOR NANOTECHNOLOGY

Table of contents

Table of contents.....	9
Summary	15
Samenvatting	18
Chapter 1 Hybrid membranes via interfacial polymerization	21
1.1. Membrane separation	22
1.2. Hybrid materials	24
1.2.1. Nanocomposites	26
1.2.2. Covalent hybrid materials	27
1.3. Hybrid material synthesis	29
1.3.1. Sol-gel	30
1.3.2. Step polymerization.....	30
1.4. Current trends in interfacial polymerization chemistry	31
1.4.1. Interfacial polymerization	31
1.4.2. Synthesis parameters	33
1.4.3. Monomer concentration, reactivity, and solubility.....	34
1.4.4. Interfaces suitable for interfacial polymerization.....	37
1.4.5. Supported and free-standing layers via interfacial polymerization	38
1.5. Chemistry of the precursors	40
1.5.1. Polyamides	40
1.5.2. Polyurethane and polyurea	51
1.5.3. Polyesters	58
1.5.4. Polyamines	64
1.5.5. Polyimides.....	67
1.5.6. Conductive polymers.....	71
1.5.7. ZIFs and MOFs	78
1.5.8. Polysiloxanes.....	82

1.6. Conclusions and future outlook.....	87
1.7. Acknowledgements	88
1.8. Thesis outline.....	88
1.9. References	90
Chapter 2 Sieving of hot gases by hyper-cross-linked nanoscale-hybrid membranes	107
2.1. Introduction	109
2.2. Experimental.....	111
2.2.1. Synthesis of poly(POSS-imide)s via interfacial polymerization .	111
2.2.2. Material characterization.	111
2.3. Results and discussion.....	112
2.4. Conclusion.....	117
2.5. Acknowledgements	118
2.6. Appendices	118
2.6.1. Poly(POSS-imide) synthesis.....	118
2.6.2. Material characterization.....	120
2.6.3. Membrane single gas permeation experiments.....	126
2.7. References	126
Chapter 3 Hybrid poly(POSS-imide)s with tailored inter-cage spacing for sieving of hot gases.....	129
3.1. Introduction	131
3.2. Experimental section	132
3.2.1. Synthesis of poly(POSS-imide)s via interfacial polymerization .	132
3.2.2. Material characterization.....	132
3.3. Results and discussion.....	132
3.4. Conclusion.....	138
3.5. Acknowledgements	138
3.6. Appendices	138
3.6.1. Poly(POSS-imide) layer preparation.....	138

3.6.2. Material characterization	139
3.7. References	150
Chapter 4 Thermal imidization kinetics of ultrathin films of hybrid poly(POSS-imide)s	153
4.1. Introduction	155
4.2. Experimental section	156
4.2.1. Synthesis of poly[POSS-(amic acid)]s by interfacial polymerization.....	156
4.2.2. Characterization of thin films.....	157
4.2.3. Kinetic analysis	158
4.2.4. Characterization of thin films by thermo-ellipsometric analysis (TEA)	158
4.2.5. TEA data analysis.....	159
4.3. Results and discussion.....	160
4.3.1. Imidization and thermal stability of the poly[POSS-(amic acid)] groups.....	160
4.3.2. Imidization of thin layers	163
4.3.3. Density change upon imidization	166
4.3.4. Kinetic analysis of the reactions by isoconversional and multivariate analyses	167
4.4. Conclusion.....	171
4.5. Acknowledgements	171
4.6. Appendices	171
4.6.1. Conversion processes during thermal imidization	171
4.6.2. Thickness and refractive indices	173
4.6.3. Kinetic analysis	176
4.7. References	178
Chapter 5 Sorption behavior of compressed CO₂ and CH₄ in ultrathin hybrid poly(POSS-imide) layers	181
5.1. Introduction	183

5.2. Experimental.....	184
5.2.1. Membrane synthesis	184
5.2.2. Spectroscopic ellipsometry	186
5.2.3. Spectroscopic ellipsometry – high pressure CO ₂ sorption.....	187
5.2.4. Magnetic suspension balance	188
5.2.5. X-ray photoelectron spectroscopy	189
5.2.6. Scanning electron microscopy	189
5.3. Results and discussion.....	189
5.3.1. CO ₂ and CH ₄ sorption isotherms – high pressure ellipsometry ...	193
5.3.2. CO ₂ and CH ₄ partial molar volume and penetrant induced dynamics	200
5.4. Conclusions	204
5.5. Acknowledgements	204
5.6. Appendices	204
5.6.1. Spectroscopic ellipsometry.....	204
5.6.2. X-ray photoelectron spectroscopy	205
5.6.3. CO ₂ sorption measurements measured by a magnetic suspension balance.....	209
5.7. References	210
Chapter 6 High pressure CO₂ permeation behavior of hybrid poly(POSS- imide)s.....	215
6.1. Introduction	217
6.2. Experimental.....	218
6.2.1. Poly(POSS-imide) membrane synthesis.....	218
6.2.2. Membrane characterization	218
6.2.3. Membrane CO ₂ permeability.....	221
6.2.4. Thickness, refractive index and CO ₂ concentrations	222
6.2.5. Apparent gas molar volumes	226
6.2.6. CO ₂ permeability and diffusivity.....	227

6.3. Conclusion.....	228
6.4. Acknowledgements	229
6.5. References	229
Chapter 7 Enzymatically-active, ultrathin pepsin membranes.....	233
7.1. Introduction	234
7.2. Experimental section	236
7.3. Results and discussion.....	236
7.3.1. Pepsin film formation.....	236
7.3.2. Pepsin layer characterization.....	238
7.3.3. Assay digestion	239
7.3.4. Pepsin layer membrane performance	241
7.4. Conclusion.....	242
7.5. Acknowledgements	243
7.6. Appendix	243
7.6.1. Pepsin film formation.....	243
7.6.2. Pepsin layer characterization.....	244
7.6.3. Assay digestion	249
7.6.4. Pepsin layer membrane performance	253
7.7. References	255
Chapter 8 Fluorescent protein thin films via interfacial polymerization	257
8.1. Introduction	259
8.2. Experimental section	259
8.2.1. Fluorescence Recovery After Photobleaching	261
8.2.2. Excitation and emission.....	261
8.2.3. Lifetime spectroscopy	262
8.3. Results and discussion.....	262
8.3.1. Fluorescence recovery after photobleaching.....	262
8.3.2. Fluorescence spectroscopy; excitation and emission	263

8.3.3. Fluorescence lifetime spectroscopy	265
8.4. Conclusions	265
8.5. References	266
Chapter 9 Reflections & Perspectives.....	269
9.1. Introduction	270
9.2. Reflections	270
9.2.1. Reflections on hyper-cross-linked, hybrid materials	270
9.2.2. Reflections on structure-property relationships.....	271
9.3. Perspectives	274
9.3.1. Membrane material design for gas separation applications.....	274
9.3.2. Structure-property-performance relationships.....	277
9.3.3. Scale-up the membrane production process	280
9.4. Conclusions	282
9.5. References	283
Dankwoord.....	285
Curriculum Vitae.....	289
List of publications	291

Summary

Hyper-cross-linked hybrid membranes consist of covalent networks of alternating organic and inorganic, or biological groups. Here, such hybrid networks have been prepared via interfacial polymerization. The structure-property relationships of the hybrid networks depend strongly on the type, size and flexibility of the constituents.

The introductory **Chapter 1** defines the characteristics of glassy membranes and hybrid materials and gives an overview of the common synthesis methods and suitable precursors that are used for synthesis of hybrid materials. In particular, the possibilities of using interfacial polymerization as a synthesis method for ultrathin hybrid films are examined. The chapter identifies a wide range of polymer chemistries that can be prepared via interfacial polymerization, and discusses the (dis)advantages of the precursors and polymer products in a review on the current trends in interfacial polymerization chemistry. The increasing number of hybrid inorganic organic, biological hybrid and nanocomposite materials that are prepared via interfacial polymerization underline the suitability of the synthesis approach for ultrathin hybrid membrane development.

In **Chapter 2**, reports for the first time a facile method for forming hybrid inorganic-organic networks of alternating polyhedral oligomeric silsesquioxane (POSS) and aromatic imide groups. The poly(POSS imide) membranes are formed by a polycondensation reaction that results in the formation of a poly[POSS-(amic acid)] layer, followed by a heat treatment to convert the amic acid groups to cyclic imides. The homogeneous distribution of POSS cages and imide bridges is demonstrated by atomic force microscopy measurements. The hybrid network characteristics are expressed by the size sieving permselectivities at temperatures up to 300 °C. In addition, the membranes show CO₂/CH₄ permselectivities of around 60 for temperatures up to 100 °C.

In **Chapter 3**, the preparation of poly(POSS-imide)s via interfacial polymerization is extended towards other precursors. The length and flexibility of the imide bridge that connects the POSS cages determines the gas separation performance at elevated temperatures. Poly(POSS-imide)s with short, rigid imide bridges show high H₂/N₂ permselectivities between 40-100 for temperatures between 50-300 °C. Long, flexible imide bridges show lower permselectivities, particularly at higher temperatures, but display larger gas

permeabilities for all gases. The tailored membrane performance allows for facile optimization of the membrane properties with respect to the requirements of the membrane process.

Chapter 4 provides new insights in the thermal imidization procedure that is required to convert the poly[POSS-(amic acid)] precursor into a poly(POSS imide). The thermal imidization occurs at temperatures between 150-350 °C. During the imidization step, the shrinkage of the material shows an inverse relation with the length of the organic bridging group. In addition to the thermal imidization, a thermally stimulated silanol condensation is detected, that originates from partially opened POSS cages. Whereas a comparable mass loss is recorded for the five different bridging groups with different lengths, a lower shrinkage is recorded for the shorter organic linkers compared to longer organic bridging because of the hampered network mobility of short linkers. The thermal imidization follows a decelerating reaction mechanism and shows a higher activation energy than the imidization of purely organic polyimides. The distinct imidization kinetics underline the strongly different characteristics of the hyper-cross-linked hybrid materials.

In **Chapter 5**, the CO₂ and CH₄ sorption behavior of ultrathin, fluoroalkane-functionalized poly(POSS imide)s is presented. The sorption capacity strongly correlates to the fluorine content in the hybrid materials, which can be tailored by using different monomer reactant concentrations in the solutions used for interfacial polymerization. The high CO₂ sorption originates from the affinity that is provided by the fluoroalkane groups. Moreover, the high gas sorption capacity is due to the high content of free spaces in the hybrid network and the flexible response of the network in a compressed gas atmosphere. At high gas concentrations in the poly(POSS-imide), the apparent molar volume of the sorbed gas molecules starts to resemble that of the fluid phase.

Chapter 6 couples the CO₂ sorption and permeability of fluoroalkane functionalized poly(POSS-imide)s. The permeability increases with increasing concentrations of sorbed gas, due to an increase in CO₂ solubility as well as diffusivity coefficient. The increased diffusivity originates from the flexible response of the network to the exposure to the compressed gas. At higher CO₂ pressures, the interaction of the CO₂ molecules with the network decreases, which is reflected by the increased apparent molar volume.

Chapter 7 presents ultrathin, cross-linked pepsin membranes that are prepared via interfacial polymerization. The presented pepsin membrane layers allow

for simultaneous enzymatic conversion and selective removal of digestion products. The pepsin activity in the layers remains after more than a day of contact with an assay solution, and demonstrates similar activity in a second digestion run. The persistent activity demonstrates that the cross-linking of pepsin into an all-protein film effectively prevent autolysis-induced deactivation. Moreover, the combination of high water fluxes and molecular retention of the pepsin layer allows for expeditious transport of solutes to the surface, where digestion can occur.

Chapter 8 illustrates that preparation of an all-protein layer via interfacial polymerization can be extended to fluorescent proteins such as EGFP and mRFP. The limited recovery of fluorescence after photobleaching illustrates the high degree of protein immobilization upon cross-linking. The emission and excitation spectra of the proteins are similar before and after cross-linking, indicating that denaturation of the protein structure is limited. A decrease in the lifetime of the fluorescence does imply that quenching occurs in the protein layers.

Chapter 9 reflects on the results that have been presented in this thesis, and provides guidelines for future development of hybrid network polymers for membrane applications. The perspectives focus on membrane material development, characterization of the structure-property-performance relationships of ultrathin membrane films and production of ultrathin membrane layers on tubular and hollow fiber supports for large-scale applications.

Samenvatting

Hyperverknoopte hybride membranen bestaan uit covalent gebonden netwerken van organische groepen alternerend met anorganische of biologische groepen. In dit proefschrift wordt een verhandeling gegeven van dergelijke hybride netwerken, die bereid zijn door middel van grensvlakpolymerisatie. De structuur-eigenschap-correlaties van de hybride netwerken zijn sterk afhankelijk van de grootte, flexibiliteit en chemische samenstelling van de subgroepen.

Hoofdstuk 1 beschouwt de eigenschappen van glasachtige membranen en hybride materialen, en geeft een overzicht van de processen en precursoren die geschikt zijn voor de synthese van hybride materialen. Met name de mogelijkheden om grensvlakpolymerisatie als synthesemethode voor ultradunne hybride films zijn onderzocht. Het hoofdstuk geeft een breed scala aan polymeertypes die bereid kunnen worden via grensvlakpolymerisatie, en bespreekt de voor- en nadelen van de precursoren en polymeer types aan de hand van huidige trends in de chemie van grensvlakpolymerisatie. De geschiktheid van deze synthesebenadering voor ultradunne hybride membraanontwikkeling wordt onderstreept door het toenemende aantal hybride anorganisch-organisch, biologisch-hybride en nanocomposiet materialen die zijn bereid via grensvlakpolymerisatie.

In **Hoofdstuk 2** wordt, voor het eerst, door middel van grensvlakpolymerisatie een ultradunne laag gemaakt, bestaande uit polyedrisch-oligomere silsesquioxaan (POSS) kooien die covalent gebrugd zijn door imidegroepen. Deze zogenaamde poly(POSS-imide) membranen worden gevormd door een polycondensatiereactie die resulteert in de vorming van een poly[POSS-(amidocarbonzuur)] laag, gevolgd door een warmtebehandeling om de amidocarbonzuurgroepen om te zetten naar cyclische imides. De homogene verdeling van POSS kooien en imidebruggen wordt aangetoond door atoomkrachtmicroscopiemetingen. De kenmerken van het hybride netwerk komen tot uiting in de selectieve scheiding van gassen bij temperaturen tot 300 °C. Daarnaast vertonen de membranen een 60 maal hogere permselectiviteit voor het transport van CO₂ in verhouding tot CH₄ voor temperaturen tot 100 °C.

In **Hoofdstuk 3** wordt de bereiding van poly(POSS-imide)s via grensvlakpolymerisatie uitgebreid naar andere bruggroepen. De lengte en flexibiliteit van imidegroepen die de POSS kooien verbinden, bepaalt de

gasscheidingseigenschappen bij verhoogde temperaturen. Poly(POSS-imide)s met korte, rigide imidebruggen vertonen een 40-100 maal hogere permselectiviteit voor het transport van H₂ in verhouding tot N₂ bij temperaturen tussen 50-300 °C. Lange, flexibele imidebruggen vertonen een lagere selectiviteit, vooral bij hogere temperaturen, maar hebben een hogere doorlaatbaarheid voor alle gassen. De mogelijkheid om te kiezen tussen de verschillende imidebruggen maakt het mogelijk de membraaneigenschappen te optimaliseren naar de eisen van het membraanproces.

Hoofdstuk 4 geeft nieuwe inzichten in de thermische imidisatie procedure die nodig is om de poly[POSS-(amidocarbonzuur)] precursor om te zetten naar een poly(POSS-imide). De thermische imidisering treedt op bij temperaturen tussen 150-350 °C. Tijdens de imidiseringstap houdt de krimp van het materiaal een invers verband met de lengte van de organische bruggroep. Parallel aan de thermische imidisering werd een thermisch-geactiveerde silanolcondensatie ten gevolge van partieel geopende POSS-kooien waargenomen. Terwijl een vergelijkbaar massaverlies werd geregistreerd voor de vijf verschillende brugvormende groepen met verschillende lengten, belemmeren kortere organische bruggroepen de netwerk mobiliteit, wat resulteert in een lagere krimp in vergelijking met langere organische bruggroepen. De thermische imidisering laat een afremmende reactiesnelheid zien en heeft een hogere activeringsenergie dan de imidisering van een puur organisch polyimide. De verschillen tussen de imidiseringkinetiek onderstreept de sterk afwijkende eigenschappen van het hyperverknootte hybride netwerk materiaal ten opzichte van haar organische tegenhanger.

Hoofdstuk 5 presenteert het CO₂- en CH₄-sorptiegedrag van ultradunne, fluoralkaan-gefunctionaliseerde poly(POSS-imide)s. De gassorptiecapaciteit correleert sterk met het fluorgehalte in de hybride materialen, dat aangepast kan worden door de concentratie van het monomeerreactant in de oplossing die wordt gebruikt voor de grensvlakpolymerisatie te variëren. De hoge CO₂ sorptie is afkomstig van de CO₂ affiniteit van de fluoralkaan groepen. Daarbovenop is de hoge gassorptiecapaciteit een gevolg van het hoge gehalte aan vrije ruimte in het hybride netwerk en de rekbaarheid van het netwerk onder hoge druk. Bij hoge gasconcentraties in het poly(POSS-imide) komt het schijnbare molair volume van de gesorbeerde gasmoleculen overeen met die van een vloeibaar gas.

Hoofdstuk 6 koppelt het CO₂-sorptie- en permeabiliteitsgedrag van fluoroalkaan-gefunctionaliseerde poly(POSS-imide)s. De permeabiliteit wordt hoger naarmate de concentratie van gesorbeerd gas stijgt, mede door een toename in de oplosbaarheid en diffusiecoëfficiënt van het gas. De toename in diffusie is een gevolg van de flexibele respons van het netwerk onder blootstelling aan hoge gasdruk. De interactie van de CO₂ moleculen met het netwerk nemen af bij een hogere CO₂ druk., wat tot uiting komt door de grotere schijnbare molair volumes van het gesorbeerde gas.

Hoofdstuk 7 presenteert ultradunne, pepsine netwerkmembranen die zijn bereid via grensvlakpolymerisatie. De pepsine membraanlagen zorgen voor een gelijktijdige enzymatische omzetting en selectieve verwijdering van producten. De pepsine-activiteit van de lagen houdt stand na langer dan een dag contact met een testoplossing, en toont vergelijkbare resultaten in de eerste en een tweede activiteitstest. De aanhoudende activiteit toont aan dat de verknoping van pepsine in een proteïne netwerk effectief de deactivatie van de laag door middel van autolyse voorkomt. De combinatie van een hoge waterdoorlaatbaarheid en hoge retentie van opgeloste stoffen zorgt ervoor dat de opgeloste stoffen zich verzamelen aan het oppervlak van de pepsine membrane, waar de enzymatische omzetting gebeurt.

Hoofdstuk 8 illustreert dat de bereiding van volledig proteïne netwerken via grensvlakpolymerisatie kan worden uitgebreid naar fluorescente proteïnen zoals EGFP en mRFP. Het beperkte herstel van fluorescentie na bleiking door licht illustreert de hoge immobilisatiegraad van de proteïne. De emissie- en excitatiespectra van de eiwitten voor en na verknoping zijn vergelijkbaar, wat aangeeft dat de proteïnes slechts beperkt denatureren. De afname in de levensduur van de fluorescentie impliceert dat uitdoving van de fluorescentie in de proteïne netwerken plaatsvindt.

Het laatste **hoofdstuk 9** reflecteert op de resultaten die zijn beschreven in dit proefschrift, en geeft richtlijnen voor de toekomstige ontwikkeling van hybride netwerkpolymeren voor membraantoepassingen. Een vooruitblik wordt gegeven op membraanmateriaalontwikkeling, karakterisering van de structuur-eigenschappen-prestatiëcorrelaties van ultradunne membraanlagen en productie van ultradunne membraanlagen op buisvormige en holle vezel dragers voor grootschalige toepassingen.

Chapter 1

Hybrid membranes via interfacial polymerization

A part of this chapter has been submitted for publication as: Raaijmakers, M.J.T., Benes, N.E. Current trends in interfacial polymerization chemistry.

1.1. Membrane separation

Membrane separation is a technology that allows for the selective separation of one or more components from a mixture. The membrane material acts as a barrier that selectively permeates one of the components over the others. Membrane performance is commonly expressed in terms of permeability and selectivity. The permeance is the rate at which a component passes through a membrane of a certain thickness. The membrane permselectivity is the ratio of the permeances of two pure components. The membrane selectivity, given by the ratio of the permeances of the components in a mixture, can differ significantly from the permselectivity and depends on the material properties and process operating conditions. A membrane with high selectivity and permeance is desirable; the separation process will require less precious membrane surface area and potentially yields higher product purities.

Membranes can be either porous or dense. Porous membranes are used on a large scale in ultrafiltration and microfiltration processes.¹ The pore size distribution and membrane surface charge governs which components are retained by the membrane. The size of the pores can be in between 1 nm - 10 μm , depending on size of the molecules or particles that need to be retained. Porous membranes are currently only used for liquid separation and purification processes,² although they have been used to separate gases decades ago.¹

Dense membranes do not have any discrete pores. Instead, transport through a dense membrane occurs via dissolution of a component into the membrane matrix, followed by diffusive transport of the component through the layer. The mechanism of separation by a dense membrane is based on differences in solubility and/or diffusivity of the permeating components. In rubbery dense membranes solubility differences dictate the membrane selectivity for low molecular weight components.³ The liquid-like properties of a rubbery membrane allow for fast diffusion of all soluble components. The solubility of components can differ significantly, and depends on the degree of component condensability and affinity towards the membrane material.³ A component with a higher condensability, such as butane, will have a higher solubility, and hence a higher permeability, compared to a poorly condensable component such as methane.^{4, 5} Rubbery membranes are particularly useful for separation of mixtures with small amounts of contaminants, such as aqueous streams with small fractions of volatile organic components⁶⁻⁸ or recovery of hydrocarbons.^{9, 10}

In glassy dense membranes, the difference in diffusivity governs the selectivity. Permeation occurs via the space between the (polymeric or inorganic) chains, that is commonly considered to be either excess free volume (EFV) or microporous elements.¹¹⁻¹⁷ The degree of permeability is determined by the size and amount of the elements that are trapped in the glassy matrix of the dense layer.^{18, 19} Small molecules such as hydrogen rapidly pass through the glassy matrix, while diffusion of larger molecules is hampered by the rigid network. Glassy membranes can differentiate between gases with small differences in molecule size, and are therefore considered promising candidate materials for gas separation applications. Nonetheless, membrane application in large-scale gas separation processes is limited by a lack of membrane materials with performance in relevant process conditions.

The performance of a membrane separation process is governed by both the process operating conditions, and the membrane material properties. From a process perspective, the driving force for permeation is related to the difference in chemical potential between the feed and permeate side of the membrane. From a material's perspective, differences in permeability originate from differences in solubility and diffusivity of the components in the membrane matrix. However, the degree of solubility and diffusivity often depends on the driving force (pressure, concentration, ...) and operating conditions (temperature, pH, ...). Therefore, the membrane material properties need to be tailored to fit the process operating requirements. This thesis deals with the design of glassy materials that have tailored membrane properties, and the study of their performance at relevant process conditions. Both gas separation and nanofiltration applications will be addressed.

Dense (glassy) membrane systems generally consist of a porous substrate with a dense polymeric separation layer.²⁰⁻²² Conventional polymeric membranes are mechanically stable, versatile, easy to process and relatively cheap. However, even in the case of state-of-the-art membranes, the molecular sieving performance subsides at high temperatures,²³⁻²⁵ in presence of penetrants at high pressures,²⁶⁻²⁹ or in harsh chemical environments.^{30, 31} The development of highly permeable polymers has brought about new classes of membranes, including polymers of intrinsic microporosity (PIMs),¹⁴⁻¹⁷ thermally rearranged (TR) polymers,³²⁻³⁵ polyethers³⁶ and substituted polyacetylenes.³⁷ Their high EFV contributes to a high permeability in combination with excellent selectivities. In terms of membrane performance (i.e., permeability and selectivity), these membranes may well approach the

ideal separation layer. However, particularly the high EFV polymeric membranes suffer from penetrant-induced changes such as plasticization and physical ageing, as a result of increased macromolecular dynamics.³⁸ Moreover, the changes of membrane performance in time are particularly pronounced for ultrathin films that suffer from nano-confinement effects and accelerated aging.³⁸⁻⁴⁷ The dilemma of every membrane scientist therefore remains: how to come up with a material that has a high permeability and selectivity, which maintains its performance at relevant operating conditions (i.e., temperature, pressure, penetrant) and reliably operates over a long period of time.

In this respect, inorganic membranes offer interesting prospects. Inorganic membranes are stable at much higher temperatures and are less prone to penetrant-induced changes. The stability of inorganic membranes is related to the rigid nature of the inorganic backbone. Although the markets are still relatively small, Mitsui⁴⁸ and the Energy Research Centre of the Netherlands⁴⁹ have successfully commercialized inorganic membranes for pervaporation applications. In addition, metal membranes (palladium) are currently in pilot plant testing phase for gas separation applications.^{50, 51} Nonetheless, widespread implementation of inorganic membranes is hampered by the lack of stable, cheap, easy-to-process, defect-free inorganic layers. Moreover, the cost price for ceramic supports remains high, while they offer a low specific surface area compared to polymer hollow fibers or spiral-wound modules. To overcome the drawbacks of both organic and inorganic materials, the best of both should be incorporated in one material; large-scale, defect-free processability in combination with stable membrane performance at the relevant process conditions. Such a synergistic combination of material properties can be attained by using hybrid materials.

1.2. Hybrid materials

Hybrid materials represent a class of materials that combine two or more chemically and physically different constituents in one material. The synergistic combination of the constituents allows for the design of materials with properties that are distinct from their individual counterparts. Hybrid materials allow for the design of materials that, for example, combine electronic, photonic, and catalytic nanoparticle properties, with molecular sensing and catalytic biomaterial properties.⁵² In addition, many hybrid materials are designed to have the flexibility of a polymer combined with the

mechanical toughness of a ceramic⁵³ or to combine the rigidity of an inorganic network with the chemical affinity of organic groups.^{54, 55}

The term hybrid is mainly used when a material combines organic and inorganic constituents. In general, the organic constituent is considered to be the more flexible, cheaper and more easily processable component. The inorganic constituent, often either a metal or metal oxide, acts as the more rigid framework element. In case a biological constituent is included in a hybrid material, it is often referred to as bio(logical) hybrid,^{56, 57} hybrid biopolymer⁵⁸ or bionanocomposite.⁵⁹ The development of methods that incorporate inorganic, organic, and even biological constituents in a single material has resulted in the synthesis of numerous novel, multifunctional materials.⁶⁰

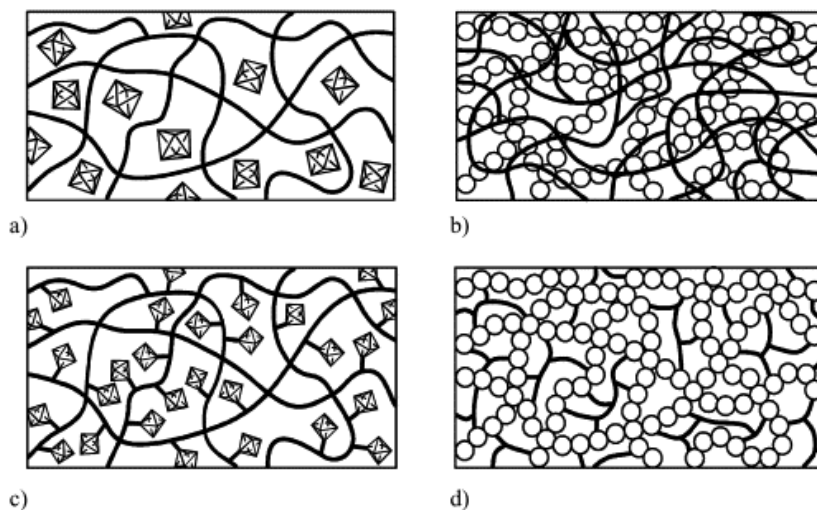


Figure 1-1. Different classes of hybrid organic-inorganic materials. (a) inorganic particles dispersed in a polymer, (b) interpenetrating networks (IPNs), (c) inorganic groups tethered to a polymer main chain. (d) covalently-bonded network of inorganic and organic groups.⁶¹ Copyright 2003. Adapted with permission from Elsevier Science Ltd..

Figure 1-1 shows the different types of (inorganic-organic) hybrid materials that are recognized as such in literature. The term hybrid is commonly used to denote materials that combine constituents with length-scales of the individual constituents ranging from Å up to several μm . The synergistic properties of a hybrid material depend to a great extent on these length-scales: materials that combine inorganic and organic groups on a nanoscale level will show

completely distinct properties from a material that is merely a physical dispersion of inorganic particles in an organic matrix.

1.2.1. Nanocomposites

Nanocomposites, shown in **Figure 1-1(a)**, are physical dispersions of inorganic particles in a polymer matrix. Particularly in membrane science and composite materials science, the combination of inorganic particles in a polymer matrix is regularly denoted as “hybrid”.⁶²⁻⁶⁶ Although such materials do combine two constituents in one material, the physical properties will in general be in between those of the two individual constituents. Examples of this class include polymer modification by dispersing polyhedral oligomeric silsesquioxanes (POSS),^{67, 68} zeolite,⁶⁹ or silica⁷⁰⁻⁷² particles in the polymeric phase during processing. Conductive properties of POSS and silica particles are used to improve the proton conductivity of proton exchange membranes for fuel cell applications.⁷³⁻⁷⁶ Improved material properties include increased degradation temperature, glass transition temperature (T_g) and polymer rigidity of POSS⁷⁷⁻⁸⁰ and silica filled materials.⁸¹⁻⁸³ In addition, better membrane separation properties are achieved by an increase in EFV and affinity separation properties.^{73, 84, 85} However, addition of particles does not necessarily result in a combination of these effects.⁸⁶ materials that show an increased EFV, often show a reduction in T_g .⁸⁷ The introduction of affinity domains and additional particle-polymer interface are considered as the main reasons for these material property changes. The main drawback of particle dispersions is the strong tendency towards agglomeration or phase demixing during processing, in particular for high surface area particles with strong interparticle interaction.⁸⁸⁻⁹⁰ Improved dispersion stability can be accomplished by particle surface modification, although this potentially renders the implementation of affinity domains ineffective.

Completely distinct properties can only be attained by integrating two or more constituents at the nano-length scale. One way to obtain higher loading homogeneous hybrid materials is by simultaneous polymerization of the inorganic and organic phase. The (semi)-interpenetrating character of the polymeric and inorganic network, as shown in **Figure 1-1(b)**, allows for synthesis of materials with excellent thermo-mechanical properties. Most (semi)-interpenetrating networks are produced by a simultaneous (radical) polymerization reaction and a sol-gel synthesis^{53, 91-93} Although some interpenetrating networks are cross-linked, most of the interactions between

the two components is based on non-covalent bonding types such as Van der Waals forces.⁹⁴⁻⁹⁶

1.2.2. Covalent hybrid materials

Covalent bonding between the inorganic and organic moieties, as shown in **Figure 1-1(c) and (d)**, on a nanoscale level results in materials that have structure-properties and physicochemical behavior that is distinct from their individual constituents. The formation of inorganic-organic hybrid, covalent networks can be accomplished by tethering inorganic constituents to a polymer main chain, cross-linking of the polymer network with inorganic groups, or incorporating the inorganic constituent in the main chain.^{67, 68, 97-99} The degree of branching, or network formation, depends on the number of reactive groups on both organic and inorganic precursors. The two types of precursors that are used in this thesis are polyhedral oligomeric silsesquioxanes (POSS) and proteins. POSS are silicon oxide nano-building blocks with the general structural formula $R_nSi_nO_{1.5n}$ ($n = 6, 8, 10, 12$).¹⁰⁰ POSS has been applied in nanocomposites, catalysis, biomaterials, optics, and coating technologies.^{67, 101-103} **Figure 1-2** shows the schematic structure formula of a POSS molecule with $n=8$, and some commonly used functional groups (R) for the synthesis of hybrid materials.

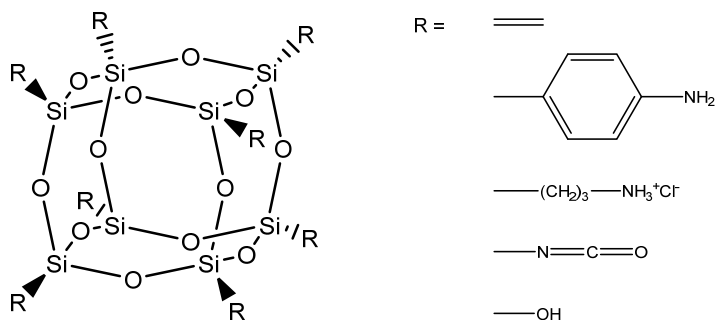


Figure 1-2. The general features of POSS with $n=8$

POSS molecules are synthesized via hydrolysis and condensation reactions of chloro- or alkoxy silanes ($RSiX_3$). The cubic, polyhedral ($n=8$) species are preferentially formed in case a single $RSiX_3$ precursor is used, although formation of ladder ($n=8$) and non-polyhedral ($n=10,12$) by-products is common.⁶⁷ Post-treatment of the non-polyhedral silsesquioxanes can be used to yield polyhedral ($n=10,12$) structures.¹⁰⁴ POSS molecules with various functional groups are available, due to the large availability of

organo-functionalized silanes.¹⁰³ The inorganic-organic functionality of POSS classifies them as hybrid materials. The large number of reactive groups on each POSS cage allows for network formation in three dimensions.¹⁰⁵⁻¹⁰⁹ POSS based hybrid layers have been prepared by step-polymerization¹⁰⁷, sol-gel processing¹¹⁰ and interfacial polymerization.¹¹¹

Proteins are a class of biomacromolecules that consist of amino acid subunits. Protein properties depend on the number and type of amino acids, as well as the structural conformation in a given environment. The unique architecture of proteins is expressed in functionalities such as enzymatic activity,¹¹² fluorescence,¹¹² transport channel properties,¹¹³ specific recognition of molecules,¹¹⁴ adhesive and other mechanical properties,¹¹⁵ and more. The amino acids groups of proteins can form non-covalent and covalent bonds with other molecules, and are therefore potentially suitable for the formation of biological hybrid materials.

Examples of different hybrid inorganic-organic and biological hybrid network materials are given in **Figure 1-3**.

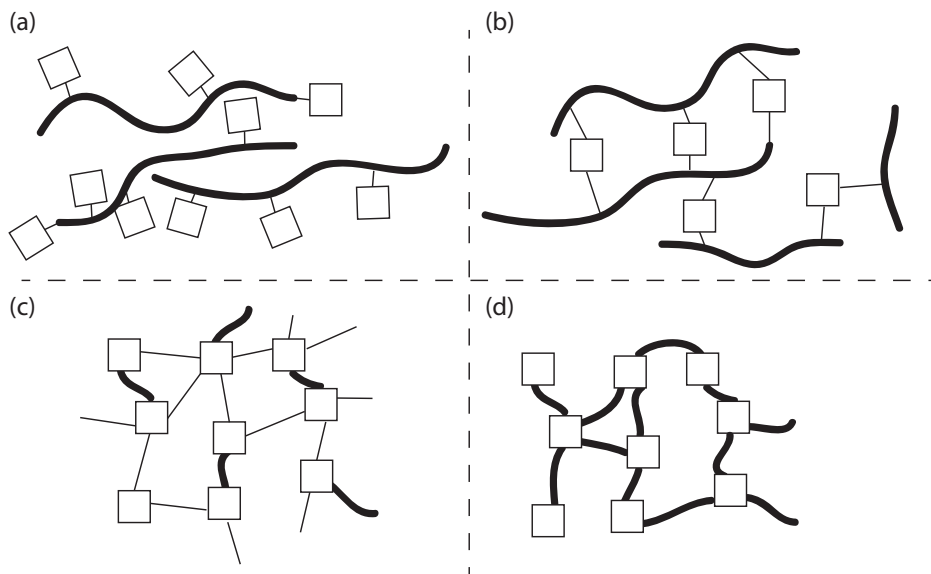


Figure 1-3. Different types of covalently-bonded hybrid organic-inorganic materials. (a) side- or end-group tethered inorganic groups on a polymer chain (b) polymer networks cross-linked by inorganic groups (c) sol-gel-based hybrid silica networks (d) alternating networks of organic and inorganic constituents.

Polymers that are tethered with inorganic groups such as POSS, as shown in **Figure 1-3(a)**, have a relatively low degree of network formation. Tethering pendant side or end-groups usually results in distortion of the polymer chain organization, and increased rigidity of the network.¹¹⁶⁻¹¹⁹ In prevalent cases, slightly increased T_g values are observed.⁸⁶ However, high loading of tethered groups may also lead to the formation of self-organized domains that result in very high EFV and lowered T_g values.¹²⁰⁻¹²² Although the tethering of side- and end-groups is an effective modification method, calculations suggest that the influence of the inorganic constituent is most pronounced if the number of covalent bonds between the organic and inorganic groups is larger.^{67, 123} Examples include hybrid cross-linked materials, as shown in **Figure 1-3(b-d)**. **Figure 1-3(b)** shows a schematic representation of a cross-linked hybrid material. Cross-linking with inorganic groups such as POSS is generally done by co-polymerization of the inorganic precursor and (pre-)polymer in solution. POSS cross-linked materials generally display improved mechanical properties and significant increases in T_g .^{124, 125}

Figure 1-3(c) shows a hybrid network prepared using sol-gel synthesis. Commonly, bi- or multifunctional siloxane precursors containing an organic functional group are used, such as 1,2-bis(triethoxysilyl)ethane (BTESE), 3-glycidoxypropyltrimethoxysilane and 3-aminopropyltrimethoxysilane.^{61, 126-129} Depending on the reaction conditions, high degrees of branching can be obtained.¹³⁰ Generally, the influence of pendant organic groups are different from organic groups as bridging constituent.¹³¹ Alkoxysilanes with built-in organic bridge are available, and have been successfully applied for synthesis of membranes for vapor¹³² and gas separation.¹³³

Figure 1-3(d) shows a network that consists of alternating organic and inorganic constituents, prepared using multi-functional precursors such as POSS, dendrimers and proteins. The large number of reactive groups on these precursors allows for covalent bond formation in three dimensions. The multifunctional character of these precursors are used as a platform for material synthesis for membrane applications. In this thesis, a number of hybrid network materials have been prepared via interfacial polymerization.

1.3. Hybrid material synthesis

Hybrid material synthesis can be accomplished via polymerization of suitable inorganic and organic precursors in one or more suitable solvent phases. The most common methods used for hybrid material synthesis include sol-gel

synthesis and step polymerization. In this thesis, interfacial polymerization has been explored as an alternative route for preparation of hybrid network materials.

1.3.1. Sol-gel

Most of the early work on inorganic-organic hybrid materials has been done using sol-gel approaches.¹³⁴⁻¹³⁸ The sol-gel method involves the preparation of a stable sol, a colloidal suspension of particles in a liquid. The class of precursors mainly used in sol-gel processing are the alkoxides of transition metals such as silicon, because they are readily hydrolyzed in the presence of water.¹³⁰ During the hydrolysis step an alkoxide bonded to a metal atom is replaced by a hydroxyl group. Subsequently, condensation between the hydroxyl groups can occur, resulting in the formation of a metal oxide network.

Hybrid materials can be obtained by using sol-gel precursors that have pendant or bridged organic groups. Example precursors often used in sol-gel chemistry for membrane applications include 1,2-bis(triethoxysilyl)ethane (BTESE) and 1,2-bis(triethoxysilyl)methane (BTESM), but a wide variety of organic bridges can be used to obtain different membrane functionalities.^{139, 140} In addition, surface modification has been done by increasing hydrophobicity with increasing fluorine content⁵⁴ and increasing CO₂ sorption with tertiary, secondary and primary amine group content.⁵⁵

1.3.2. Step polymerization

Step polymerization (n -mer + m -mer = $(n + m)$ -mer) of hybrid materials is often done in aprotic polar solvents.^{109, 141} The reaction can be achieved by living polymerization techniques, such as ring-opening polymerization and living free-radical polymerization or coupling reactions such as click chemistry and hydrosilylation.^{105, 142} Commonly, reaction times of several hours at elevated temperatures are used to obtain hybrid polymers with sufficiently high molecular weights.¹²³ Because the solubility of the hybrid network depends on the molecular weight and degree of branching, careful control of the reaction conditions is required to allow for further processing of the materials. The advantages of step-polymerization include the careful control of the molecular weight (distribution) and wide range of chemistries that can be used for polymer synthesis.¹⁰³ Drawbacks of highly cross-linked networks is their brittleness after evaporation of the solvent, and cracking can occur due to shrinkage induced stresses in the layers.¹⁴³

1.4. Current trends in interfacial polymerization chemistry

Interfacial polymerization is an enabling technique for the large-scale production of ultrathin layers, hollow nanospheres and nanofibers. The availability of a wide range of suitable monomer reactants allows for the synthesis of an impressive collection of polymers, including polyamides, polyurethanes, polyureas, polyanilines, polyimides, and polycarbonates. In addition, the technique has been used to prepare defect-free, ultrathin films of metal organic frameworks, organic-inorganic hybrids, and bio-hybrids. This review provides an overview of the chemistry that is used in interfacial polymerization, discusses the (dis)advantages of derived material types, and assesses the future prospects for synthesis of ultrathin functional materials via interfacial polymerization.

1.4.1. Interfacial polymerization

Interfacial polymerization is a technique that allows for the synthesis of ultrathin functional layers, capsules or fibers, at the interface between two phases. Commonly, the polymerization is a polycondensation reaction between two highly reactive monomers that are dissolved in two immiscible liquids.¹⁴⁴ Alternatively, one of the phases only contains a reaction initiator or a catalyst (e.g., a strong oxidizing agent¹⁴⁵), or acts as the reactive monomer by itself (e.g., water as reactant¹⁴⁶). In some studies, ultraviolet light is employed for a photopolymerization at the interface.¹⁴⁷⁻¹⁴⁹ In all cases, the separation of monomer precursors in two phases results in the localized reaction and formation of a polymer. **Figure 1-4** shows a schematic of an interfacial polymerization reaction between monomer reactants A and B.

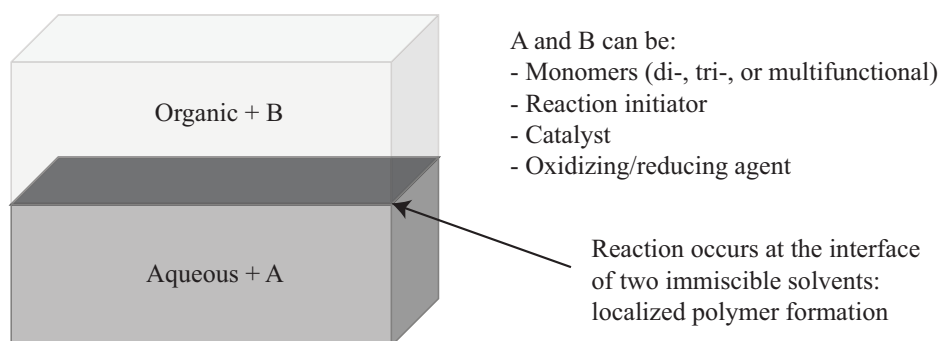


Figure 1-4. Schematic of an interfacial polymerization reaction.

Because the polymer formation is confined to the interface, reactants will more likely encounter the growing polymer chain instead of other monomers. As a result, as compared to bulk polymerization, higher molecular weights can be obtained at mild reaction conditions.¹⁵⁰ Precipitation of the polymer at the interface might occur at a given molecular weight range, resulting in polydispersities that are distinct from bulk polymerization.¹⁵¹

The properties of the formed polymer depend, to a great extent, on the reactivity and (local) concentration of the monomers, the stability of the solvent interface and the number of reactive groups on each of the monomers.¹⁵²⁻¹⁵⁶ Interfacial polymerization involves the reaction of di-, tri- or multi-functionalized monomers.^{144, 157, 158} Usually, one of the phases contains a nucleophile reactant (i.e., amines, alcohols, ...) and the other contains an electrophile reactant (i.e., acid chlorides, isocyanates, ...). Because most of the electrophilic monomers used for interfacial polymerization are susceptible to reaction with water, they are commonly dissolved in the organic phase. The reaction of two di-functional monomers results in formation of a linear polymer chain. Examples of linear polymers include the synthesis of polyamides (e.g., nylon¹⁵⁹) and polycarbonates.¹⁶⁰ Syntheses with large yields are performed by either by stirring to create more liquid-liquid interface or by continuous removal of the formed polymer from the interface. The resulting high molecular weight linear polymers can be dissolved again for further processing. Only for some polymers, such as polyaniline, the synthesized linear polymers are used as synthesized and are not redissolved.

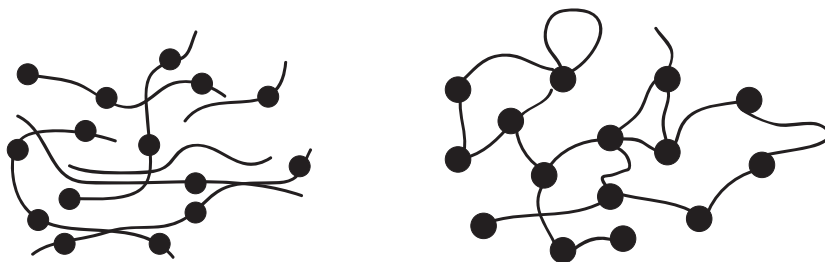


Figure 1-5. Schematic of (left) a linear polymer and (right) a polymer network prepared by interfacial polymerization. The ball and chain represent the different functional segments of the polymer main chain.

The production of branched polymers requires at least one precursor with three or more reactive functional groups. The degree of branching and cross-linked network formation depends on the number and reactivity of the functional groups. The properties of such polymer networks are completely distinct from linear polymers. **Figure 1-5** shows a schematic representation of a linear polymer (left) and a polymer network prepared by interfacial polymerization (right). Linear polymers have properties that depend, to a large extent, on their chemistry, chain-chain interactions and molecular weight distribution. Because each polymer chain has freedom of movement, polymer chain dynamics occur over a range of time-scales. Even glassy polymers, that display slow chain dynamics due to the rigid nature of their polymer chains, inherently display chain reorganizations. On the other hand, polymers prepared by interfacial polymerization potentially consist of networks of semi-infinite molecular weight that moderate such polymer reorganizations. This is reflected by the poor solubility in any type of solvent, the absence of any crystallinity, and the distinct layer morphology of branched polymers prepared via interfacial polymerization. In particular such branched and network polymers are applied in the configuration that is obtained upon interfacial polymerization. This review focusses on interfacial polymerization that is used for synthesis of structures and layers with large lateral dimensions and small thicknesses. This excludes materials that are redissolved after preparation, because they are not used in the same configuration as is achieved by interfacial polymerization.

1.4.2. Synthesis parameters

Interfacial polymerization reactions generally result in fast polymer chain growth and polymer precipitation at the liquid-liquid interface. The properties of the polymer depend on a large number of parameters. Polymer properties that can be varied using these reaction parameters include: molecular weight, polydispersity, degree of branching or cross-linking, residual group content, shape (fibrils, capsules, layers), thickness, density, layer roughness, component (membrane) transport, mechanical strength,¹⁵⁷ and stimuli responsive properties.^{161, 162} **Figure 1-6** gives an overview of the most important synthesis parameters that influence the properties of the formed polymer, and coupling between these parameters. Several of the most important parameters will be discussed in detail here in this review.

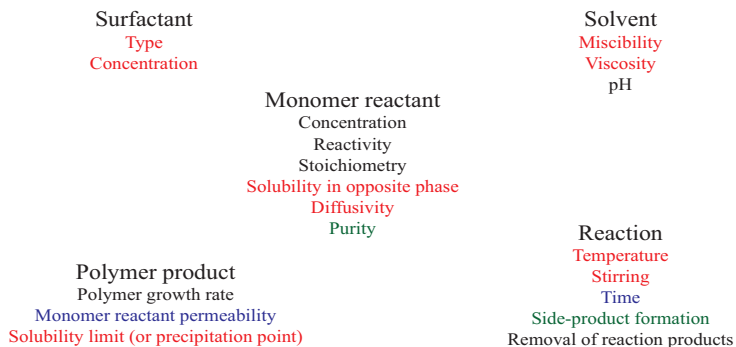


Figure 1-6. Overview of the synthesis parameters that determine the nature of the polymer formation during interfacial polymerization. The synthesis parameters are categorized by color and type of parameter. The colors indicate a strong interdependency of the parameters. For example, the solvent miscibility and viscosity will influence the monomer diffusivity and solubility in the opposite phase. Stirring, addition of a surfactant and temperature will influence the solubility as well. The concentration, reactivity, stoichiometry, solvent pH and removal of reaction products will influence the polymer growth rate. Reactant purity can result in side-product formation. The interdependency is not limited to the colors shown here: diffusivity is for example also coupled to the monomer reactant permeability.

1.4.3. Monomer concentration, reactivity, and solubility

The nature of the localized layer formation is determined mainly by the nature of the two monomer reactants that are dissolved in the aqueous and the organic phase, respectively. Monomers with a high reactivity allow for film formation in a matter of min or even seconds. Diffusion limitations of monomer reactants upon film formation decelerate the film growth, typically restricting film thicknesses to the sub- μm range. Although film growth decelerates upon film formation, the properties can still change with longer reaction times due to continued covalent bond formation and material densification.¹⁶³ Lower reactant reactivities commonly result in thicker films, with thicknesses than can go up to several μm . Layers produced by interfacial polymerization are inherently defect-free, because monomer diffusion in areas without layer formation allows for continued polymer growth. In addition, the potentially unlimited lateral dimensions of an interface of two immiscible phases enables synthesis of ultrathin layers with similarly large areas. The prospect of large surface areas of ultrathin, defect-free films are two of the key aspects that

underline the attractiveness of interfacial polymerization as a layer synthesis technique.

In contrast to polymerization in a single solvent, the reactant stoichiometry of the monomers during interfacial polymerization is not necessarily in agreement with the final composition of the polymer. Instead, the reactant stoichiometry at the interface is a function of the monomer reactivities, concentrations, diffusivities and solubilities in either phase. Hence, each individual combination of monomers requires an optimization of reactant concentrations. Empirical data of the influence of reaction conditions on molecular weight,^{159, 160, 164, 165} surface roughness,^{166, 167} layer thickness,¹⁶³ and (membrane) material performance, provides general guidelines for sensible reaction conditions. In general, a high monomer reactivity and low solubility in the opposite phase are required to obtain dense, well-defined films.

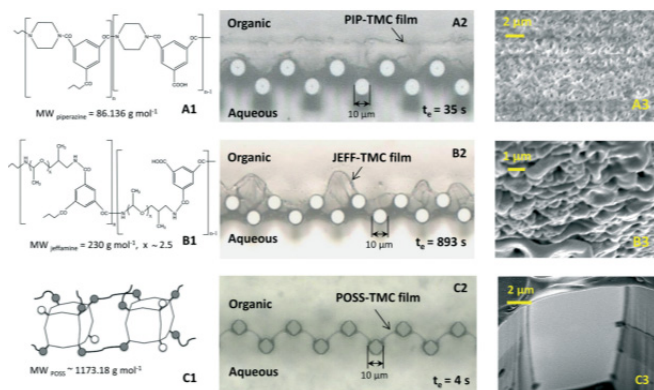


Figure 1-7. Optical microscopy images of a piperazine (top panels), Jeffamine (middle panels) and POSS (bottom panels) based interfacial polymerization layers, formed in a microchannel.¹⁶⁸ Copyright 2015. Adapted with permission from the Royal Society of Chemistry.

A high solubility of one of the reactants in the other phase may lead to the formation of more corrugated films.¹⁶⁸ Film morphology depends on the type of reactants used for interfacial polymerization. This is illustrated by optical microscopy images of films prepared with different aqueous phase precursors, in a microchannel, shown in **Figure 1-7**. The layers show distinct thicknesses and morphologies, which is due to the difference of the amine (aq. phase) reactivity and solubility in the opposite organic phase. The large differences between the layer morphologies and the thicknesses underline that the type of reactant affects both the physical and chemical properties of the material. In

case both reactants solubilize in the opposite phase, their concentration can be used to obtain diffusion controlled reaction either in the organic phase or the aqueous phase.¹⁶³ A low organic reactant concentration results in layer formation that is controlled by the diffusion in the organic layer. At high organic reactant concentrations, the monomer diffusion of the aqueous phase will predominate.

Interfacial polymerization membranes commonly have a gradient in the chemical composition, charge and number of residual groups as function of the layer thickness. The composition of the unreacted residual groups depends on which of the monomers are supplied in excess. On the aqueous side, excess of e.g. amine groups results in residual amine groups, while on the organic side excess acid chloride monomers result in formation of residual carboxylic acid groups. Depending on the size, concentration, diffusivity and solubility, one type of residual groups might be prevalent. However, in many interfacial polymerization layers, both monomer reactants can remain as partially unreacted residual groups. Post functionalization by cross-linking or end-capping reagents can be used to change the composition of the layers. Unreacted residual groups can post-functionalized by stepwise contacting with reactant solutions, as an additional treatment after the conventional interfacial polymerization procedure.¹⁶⁹ Another example employs the stepwise addition of the reactant solutions to a support fixed on a spin coater, although such an approach is not easily scalable for large surface area applications.¹⁷⁰ Usually, post-functionalization only results in a changed surface composition of the layers. The slow monomer diffusion in the layers complicates post-functionalization throughout the layer. To overcome the diffusion limitations of post-functionalization, end-capping reagents are added to one of the monomer solutions, including 3,5-diaminobenzoic acid (BA) and o-aminobenzoic acid-triethylamine (o-ABA-TEA) salt, that increase the hydrophilicity.¹⁷¹ The drawback of the latter approach is that the degree of network formation is inherently lower as compared to conventional interfacial polymerization.

A number of models have been developed to predict the growth of interfacial polymerization layers.¹⁷²⁻¹⁷⁵ Many attempts have been made to predict the reaction-diffusion behaviour of the components responsible for thin film formation. This resulted in the availability of various models that all focus on different assumptions and key parameters, and as such there is no consensus on the location, size and direction of the actual reaction zone. Three different

modelling approaches can be identified. In the first modelling approach, the reaction initially occurs at the interface and from there it grows into the organic phase. A second approach places the reaction zone in the organic phase and lets it shift further into the organic phase as the film is growing. The third approach involves determining a steady reaction zone with a finite thickness in which the reaction takes place and the polymer film is formed. An overview of the different models is given by Dhurmatal. ¹⁷⁶

1.4.4. Interfaces suitable for interfacial polymerization

The interface is key for controlling the localized polymerization reaction. Most commonly, an aqueous phase and a hexane phase are used. Hexane and water mix very poorly, and provide a very stable interface. Alternative combinations can be made with methanol, acetonitrile, nitromethane, formamide, dimethylformamide or dimethylsulfoxide instead of the aqueous phase and cyclohexane, hexane and higher alkenes, chloroform, dichloromethane, higher alcohols such as octanol, xylene and toluene as the organic phase. ¹⁷⁷ Although the solvent combinations are not miscible, small amounts of solvent can dissolve in either phase. ¹⁷⁷ The exchange of solvent at the interface potentially disturbs the reaction zone and changes the solubility of the monomer reactants in either phase. The liquid phase mixing is not necessarily a drawback; the diffuse reaction zone can promote layer growth. Moreover, in many interfacial polymerization syntheses an additional surfactant is used to improve the materials properties. ^{152, 178, 179} For example, for interfacial polymerized polyamide membranes, surfactants are beneficial for the flux. ¹⁸⁰ Commonly, the enhanced flux is ascribed to the increased roughness and hence surface area. ¹⁶⁶ In other work, the flux increase has been attributed by the combination of a higher roughness and a higher excess free volume content that allows for faster water permeation. ¹⁸¹

Interfacial polymerization is not limited to the combination of two liquid phases. Alternative approaches include vapor-liquid interfacial polymerization (VLIP) via supercritical CO₂ to supply vapor phase reactant ¹⁸² and vaporizing of the reactant with an inert gas stream to induce a polymerization reaction at a stable aqueous interface on a hydrophobic support. ¹⁸³ In addition, it is possible to perform solid-liquid interfacial polymerization by freezing interfacial polymerization. ¹⁸⁴ Here, the crystallization of the solvents is accompanied by the formation of a layer of monomer reactants on the outside of the crystal. One of the monomer reactants (pyrrole) is still liquid, and can diffuse to the oxidant and dopant on the ice surface.

1.4.5. Supported and free-standing layers via interfacial polymerization

Most interfacial polymerization layers are prepared on top of a porous support, because the mechanical strength of sub- μm thin free-standing films not sufficient for many applications. The properties of the support are important for the characteristics of the interfacial polymerization layer. The pore size and hydrophobicity have more practical implications for the reaction. When the aqueous phase is used to wet the porous substrate, the stability of the interface of the water that fills the pores depends on the pore size. Very small pores provide a stable interface, but are more difficult to pre-wet. Too large pores might suffer from loss of wetting and fast evaporation of the liquid that fills the pores. In general, pores with a size below 100 nm are considered as suitable for interfacial polymerization reactions. For larger pores defects can occur, simply because there will be no liquid-liquid interface in an empty pore.

The support hydrophobicity has a similar influence on wetting as the pore size. Hydrophobic supports often require a pre-wetting step with a surfactant solution and the wetting liquid in hydrophobic supports might be confined to the pores. Hydrophilic supports are wetted more easily, and might have a thin wetting layer (of water) on top of the support. Therefore the location of the interface might be distinct for hydrophobic and hydrophilic supports.

When preparing a supported membrane via interfacial polymerization, the following practical steps are commonly employed:

1. Pre-wetting of the support by a surfactant solution.
2. Pre-wetting of the support by the monomer reactant solution.
3. Removal of excess liquid from the surface using a roller or by evaporation under an atmosphere.
4. Interfacial reaction on the support by static contact or active flow of the organic phase.
5. Removal of the organic phase from the surface by washing with excess solvent.
6. Removal of the aqueous phase from the pores by solvent exchange and/or evaporation.
7. Drying to remove residual solvent, or storage in a suitable liquid.

The pre-wetting step is commonly done by forcing a liquid flow through the support, by means of a pressure difference. Sufficient time must be used for pre-wetting of the support, as residual surfactant can influence the stability of the interface and layer formation. The removal of the aqueous phase often

requires a solvent exchange step. When water is directly evaporated from the pore, pore collapse might occur due to the large negative Laplace pressure upon water evaporation. Therefore a low surface tension solvent is often used to replace the aqueous phase and to remove any residual, unreacted monomers. Commonly, the pores of the support are wetted with the aqueous phase. However, it is possible to use the organic phase to wet the support instead.¹⁸⁵ The main difficulty with such an approach is maintaining a stable interface at the surface of the porous support.

Free-standing films can be prepared by simply contacting two phases containing monomer reactants. Usually this is done to prepare micro- or nanocapsules. For small particle dimensions, even small layer thicknesses provide sufficient mechanical strength. When preparing capsules via interfacial polymerization, the following practical steps are commonly employed:

1. Preparation of a stable emulsion by mixing and ultrasonic treatment or the preparation of droplets via microfluidic devices. Commonly, surfactants such as sodium dodecyl sulfate are added as emulsion stabilizers.^{177, 186-188} Usually, only one of the phases contains a monomer reactant. In some cases both reactants are present, and the capsules are removed as they are formed.¹⁸⁹
2. Addition (at once or dropwise) of a solution of the other monomer reactant. This can be during stirring and/or ultrasonic treatment. In a microfluidic device the monomer solution can simply be added at a location downstream, where the droplets are stable.
3. Removal of monomer reactants by washing in excess solvent.
4. Concentration of particles by settling, solvent evaporation, solvent exchange or centrifugal separation.
5. Drying to remove residual solvent, or storage in a suitable liquid.

Preparation of capsules via interfacial polymerization requires the addition of surfactants to obtain a stable emulsion with a narrow size distribution. The size of the capsules is determined by the stirring rate at which the emulsion is prepared.¹⁹⁰ The addition of surfactants is known to change the nature of the interfacial polymerization reaction, and characteristics of the synthesized material. This is because the surfactant does not only stabilize the emulsion, but can also results in self-assembly of monomers at the interface. Examples include the interfacial polymerization of aniline by ammonium

peroxydisulfate. Addition of cetyltrimethylammonium bromide (CTAB) could be used to tune the polyaniline from one-dimensional nanoneedles or nanowires with a network structure (50–100 nm in diameter) to three-dimensional hollow microspheres (~ 400 nm outer diameter) via a combination of self-assembly and interfacial polymerization.

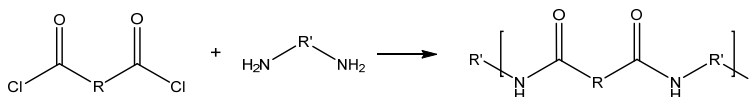
1.5. Chemistry of the precursors

Most polymers that are prepared via interfacial polymerization are polyamides. The successful commercial application of aromatic polyamides in membrane applications has surged research towards improved interfacial polymerization based layers with improved (water) permeabilities, anti-fouling properties and retention of solutes. Nonetheless, the chemistry used for interfacial polymerization is certainly not limited to polyamides. Other materials prepared by interfacial polymerization include poly(bio-amides), polyesters, polyamines, polysiloxanes, polyimides, polyanilines and other conducting polymer analogues, polyurethanes and polyureas, and hybrid inorganic-organic materials such as metal organic frameworks¹⁹¹ or POSS based network materials.¹⁹² Here, we provide an overview of new materials prepared by interfacial polymerization and their properties. This review shows that interfacial polymerization has a large unexploited potential for the design of novel, ultrathin functional films

1.5.1. Polyamides

Polyamide chemistry

Polyamide chemistry is prevalent in interfacial polymerization based materials. Preparation of composite aromatic polyamide membranes via interfacial polymerization has been the main enabling technology for membrane-based seawater desalination and water purification. In general, polyamides are formed by the reaction between acid chlorides and di-, tri-, or polyamines.



Polyamide formation can result in the release of hydrogen chloride. The formation of hydrogen chloride can locally change the reactivity of the monomer reactants in the aqueous phase. Often, a base such as sodium hydroxide or trimethylamine is added to consume the produced acid and to

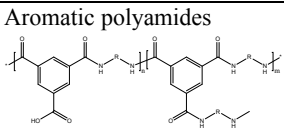
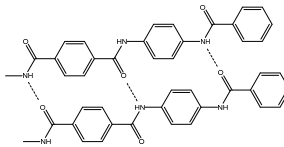
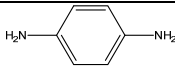
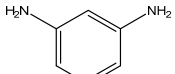
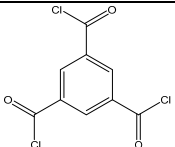
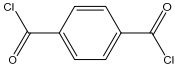
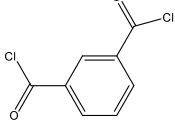
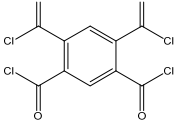
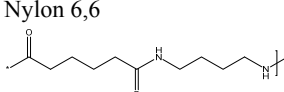
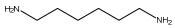
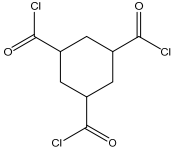
improve the reactivity of the amine reactant. In some cases, a strong base is required to make the aqueous phase monomer reactive.¹¹¹

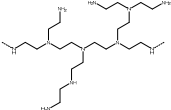
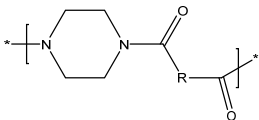
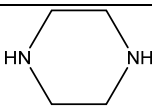
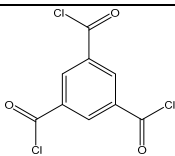
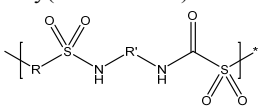

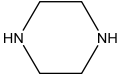
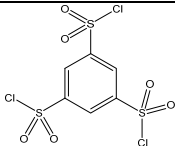
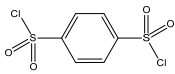
After interfacial polymerization, a large number of residual carboxylic acid and amine groups can remain in the polyamide. Post treatment to reduce the number of carboxylic acid groups on the membrane by washing with an amine solution. Both aliphatic and aromatic precursors are used for the preparation of polyamides. Commonly, aromatic polyamides are favored over aliphatic polyamides because of their higher degree of chain rigidity, more hydrophobic nature and better performance in membrane applications. Aromatic polyamides are known to be stable at pH ranging from 2-10, and are therefore used in a broad range of applications.^{193, 194} Drawbacks of polyamides include their limited stability towards chlorine treatment that is used in membrane applications to remove fouling.^{195, 196} The development of chlorine-tolerant membranes is important because it directly reduces the costs of membrane replacement, backwashing chemicals, and energy to overcome the additional osmotic pressure. Stability of polyamide membranes is improved by changing the monomer precursors used for interfacial polymerization,^{197, 198} or by chemical post-modification.¹⁹⁹ In addition, the chemical composition of the polyamide is varied to prevent fouling effects, consequently reducing the need for harsh chemical cleaning.¹⁹⁹ A number of polyamides show excellent stability and membrane performance in harsh chemical solvents such as dimethylformamide.²⁰⁰

An excellent review on the historical and current developments of reverse osmosis membranes is given by Lee et al.²⁰¹ They give an overview of the most important monomer precursors that are used for interfacial polymerization of polyamides, and a list of commercial membranes and their performance. Hermans et al. gives an overview of the membrane performance of different layers prepared by interfacial polymerization in solvent resistant nanofiltration applications.²⁰² Lau et al. and Misdan et al. have reviewed thin film composite membranes for aqueous applications, including many examples of interfacial polymerization based membranes.^{179, 203} A complete, recent overview of monomer precursors that are used for the synthesis of polyamides for membrane applications, including a variety of di- and multifunctional amines and acid chlorides, is given by Ismail et al.²⁰⁴ In the present review, the overview of polyamides prepared via interfacial polymerization will be limited to the different types of polyamides. This overview, shown in **Table 1-1**, includes common precursors for aromatic and aliphatic polyamides,

poly(piperazine-amide)s and poly(sulfon-amide)s. Almost all membranes prepared by interfacial polymerization are exclusively produced by the reaction of trimesoyl chloride (TMC) in the organic phase with either m-phenylene diamine (MPD) or piperazine (pip) in the aqueous phase. Because common polyamides are covered by several reviews, this review will instead focus on novel polyamide (inorganic-organic) composites, hybrid inorganic-organic polyamides and bio-hybrid polyamides.

Table 1-1. Polyamides types and the most commonly used precursors used for preparation via interfacial polymerization, and the most important characteristics of the polyamide. In bold: the reactant names and main polymer application.

Polyamide type	Aq. phase reactant	Org. phase reactant	Application	Ref.
<p>Aromatic polyamides</p>  	 <p>Meta-phenylene diamine</p>  <p>Para-phenylene diamine.</p>	 <p>Trimesoyl chloride</p>  <p>Terephthaloyl chloride</p>  <p>Isophthaloyl chloride</p>  <p>Tetraacyl chloride</p>	<p>Membranes mainly for reverse osmosis and nanofiltration.</p> <p>High degree of hydrogen bonding. High thermal, mechanical stability and poor solubility.</p>	153, 156, 197, 205-212
<p>Aliphatic polyamides</p> <p>Nylon 6,6</p> 	 <p>Hexamethylene diamine</p>	 <p>Cyclohexane-</p>	<p>Linear aliphatic polyamides are mainly prepared and re-dissolved for further processing.</p>	195, 213, 214

	 <p>Poly(ethyleneimine)</p>	1,3,5-tricarboyl chloride	Branched aliphatic polyamides and aliphatic-aromatic polyamides have been prepared for membrane nanofiltration and reverse osmosis applications . The chlorine resistance of aromatic polyamides is considered to be higher.	
<p>Poly(piperazine-amide)</p> 	 <p>Piperazine</p>	 <p>Trimesoyl chloride</p>	Membrane reverse osmosis and nanofiltration applications. Improved resistance against chlorine treatment with respect to other aromatic polyamides.	215-218
<p>Poly(sulfon-amide)</p> 	 <p>Meta-phenylene diamine</p>  <p>Piperazine</p>	 <p>Benzene-1,3,5-trisulphonyl chloride</p>  <p>Benzene-1,4-disulphonyl chloride.</p>	Membrane reverse osmosis and nanofiltration applications. Only stable in acid conditions. In base conditions the amide group is deprotonated. Hydrophilic character.	215, 219-221

Polyamide composites

Composites are physical dispersions of (inorganic) particles in a polymer matrix, with physical properties that are generally in between those of the two individual constituents. Composite layers can be prepared via interfacial

polymerization by addition of particles to one of the monomer phases. Particles have the tendency to assemble at the interface to minimize the surface energy, moving into the interfacial polymerization reaction zone. Different type of micro- and nanoparticles have been used to prepare composites via interfacial polymerization layers. Examples include zeolites,^{201, 222-225} ceramics (silica^{71, 146}, titania²²⁶, mostly from sol—gel), MOFs and ZIFs,²²⁷⁻²²⁹ carbon nanotubes,²³⁰⁻²³⁴ proteoliposomes containing water transport proteins,²³⁵ liquid carriers such as di-(2-ethylhexyl)dithiophosphoric acid,^{236, 237} and graphene.²³² **Figure 1-8** shows transmission electron micrographs

Most of the composites are prepared to obtain higher permeances for a selected component. Other advantageous properties include particles that act as antifoulant by reducing bacterial growth.²³⁸

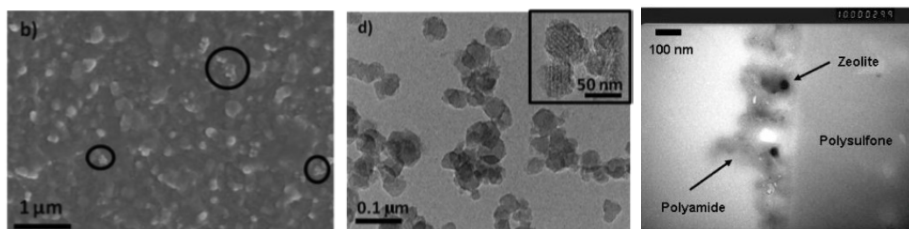
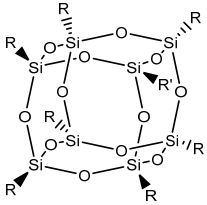
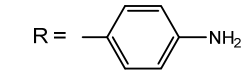
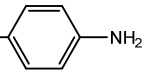
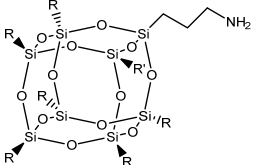
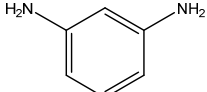
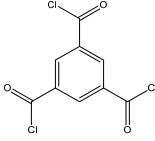


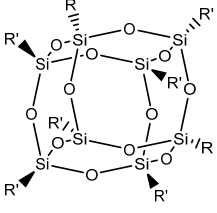
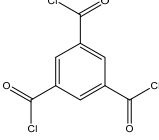
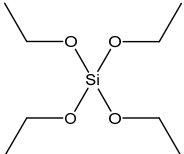
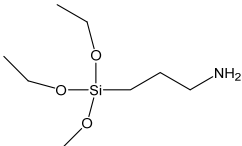
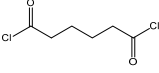
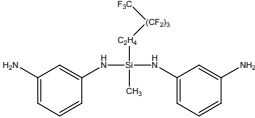
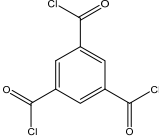
Figure 1-8. (left panel) Scanning electron micrograph of MIL-101(Cr) containing polyamide layer [0.2 wt./v.%] membrane surface after dimethylformamide dipping, (middle panel) Transmission electron micrograph of detached PA–MIL-101(Cr) thin film surface, where the inset is at a higher magnification.²²⁹ Copyright 2013. Adapted with permission from the American Chemical Society. (right panel) Transmission electron micrograph of a polyamide layer containing zeolite crystals.⁶⁹ Copyright 2007. Adapted with permission from Elsevier Science Ltd.

Hybrid inorganic-organic polyamides

Hybrid inorganic-organic polyamides have been prepared via interfacial polymerization by using amine functionalized siloxane precursors. Example precursors include amine functionalized siloxanes that are copolymerized with polyamide precursors²³⁹ and polyhedral oligomeric silsesquioxanes with amine or ammonia functional groups.^{111, 168, 240} **Table 1-2** shows an overview of the precursors used for hybrid inorganic-organic polyamides. The properties of the hybrid materials are distinct from composites due to the covalent bonds that are formed between the inorganic and organic moieties.²³⁹

Table 1-2. Precursors used for hybrid inorganic-organic polyamides prepared via interfacial polymerization, the reaction conditions, and the applications of the poly(POSS-amide)s. In bold: the reactant names, method of interfacial polymerization, reaction time and temperature and final polymer configuration.

Aq. phase reactant	Org. phase reactant	Reaction conditions	Application	Ref.
 <p>R = $-(\text{CH}_2)_3-\text{NH}_3^+\text{Cl}^-$</p> <p>Octa-ammonium POSS</p>  <p>R = </p> <p>Octa-aminophenyl POSS</p>  <p>R = $-\text{C}_4\text{H}_9$</p> <p>Aminopropylisobutyl POSS</p> <p>0.05, 0.2, 0.4 wt./v. % POSS in water, copolymerized with</p>  <p>Para-phenylene diamine (2.0 wt./v%) with trimethylamine (1, 2 and 3 wt./v.%)</p>	 <p>Trimesoyl chloride (0.15 wt./v.%) in hexane</p>	<p>Preparation of the layer on a PS20 support that is immersed in aq. solution for 20 min. Excess water is removed by rubber rollers.</p> <p>Next, the trimesoyl chloride solution in hexane is contacted with the layer for 20-60 s.</p>	<p>Membrane nanofiltration applications. NaCl salt rejection above 98% and permeances between 27-33 L m⁻² h⁻¹ bar⁻¹ (vs. 20 L m⁻² h⁻¹ bar⁻¹ for similar preparation conditions without addition of POSS).</p>	<p>240</p>

 <p>R = $-(\text{CH}_2)_3-\text{NH}_3^+\text{Cl}^-$ R' = $-(\text{CH}_2)_3-\text{NH}_2$</p> <p>Octa-ammonium POSS (0.9 wt.%) in water with pH 9.9, sodium hydroxide (NaOH) or triethyl amine (TEA) adjusted.</p>	 <p>Trimesoyl chloride (0.05 wt.%) in hexane.</p>	<p>Preparation of the layer on a polyacrylonitril (PAN) support. The aq. solution is forced through the support by means of vacuum for 30 min. Excess water is removed by drying under N_2 atmosphere, followed by contacting with the TMC in hexane phase for 1-5 min.</p>	<p>Membrane nanofiltration applications. 9.7, using NaOH as an additive, the molecular weight cut off (MWCO, for the aqueous PEG solution is 200 g mol^{-1}. For a solution of polystyrenes in toluene the MWCO is 1000 g mol^{-1}. The permeances of water and toluene are 0.3 and $0.6 \text{ L m}^{-2} \text{ h}^{-1} \text{ bar}^{-1}$, respectively.</p>	111, 168
<p>$\text{H}_2\text{N}-(\text{CH}_2)_6-\text{NH}_2$</p> <p>Hexamethylenediamine (HMDA)</p>  <p>Tetraethylorthosilicate (TEOS)</p>  <p>3-Aminopropyltriethoxy silane (APTES, 1:1 molar ratio with TEOS) in water</p>	 <p>Adipoyl chloride in toluene</p>	<p>Layer preparation was achieved by adding the adipoyl chloride in toluene solution and HMDA/TEOS/APTES solution in water within 10 s while stirring. After 90-120 s reaction time, the polymer was washed and dried under vacuum at 90°C. Finally, the polymer was washed in boiling methanol and redried in vacuum.</p>	<p>The polyamide silica hybrid consists of a network of silica particles in the range of 30-40 nm that are covalently bonded to the polyamide. The bonded silica nanocomposites exhibit superior mechanical stiffness to the pristine polyamide and unbonded, silica particle functionalized polyamide.</p>	239
 <p>Nonafluorohexylmethyl siloxane functionalized diphenylene diamine (MPDSi, 2 wt.%) in a water/ethanol 90/10 wt.%</p>	 <p>Trimesoyl chloride (0.1 wt.%) in hexane</p>	<p>Ultem hollow fibers were immersed in ethanol for 30 s, and then in water for 1 h. The fibers were then immersed in the aq. amine solution</p>	<p>Membrane pervaporation for water/ethanol separation. Separation factors between 42-108, with permeances of about $2 \text{ kg m}^{-2} \text{ h}^{-1}$.</p>	241

mixture		for 5 min. Excess liquid was removed by blotting with paper tissue. Finally, the fibers were dipped into the hexane solution for reaction times of 1,2 or 5 min.		
---------	--	---	--	--

Poly(bio-amide)s

Poly(bio-amide)s are a class of polyamides that include a biological component, such as amino acids or complete proteins.

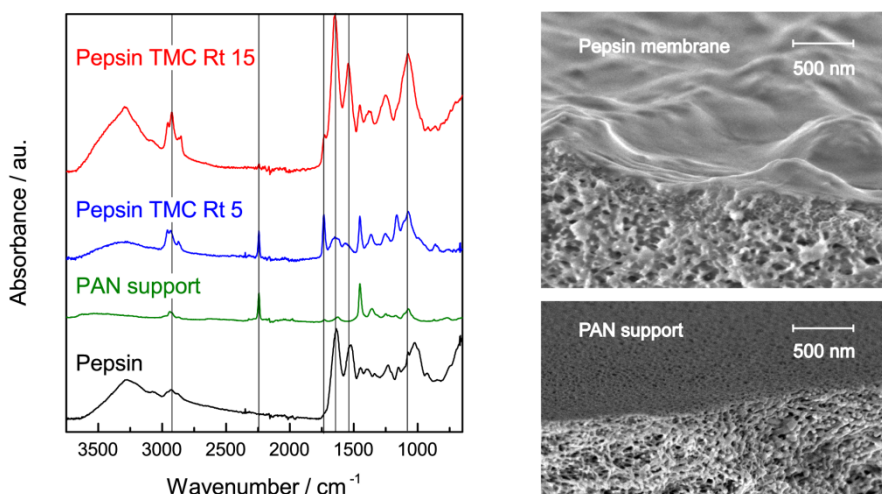
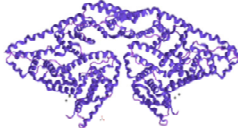
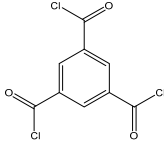
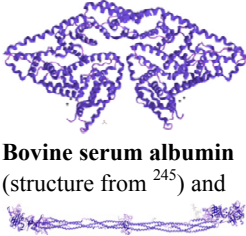
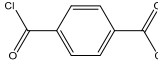
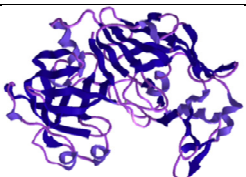
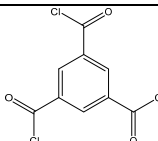
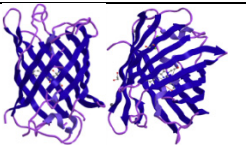
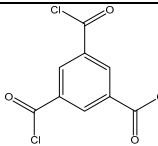
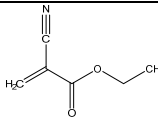


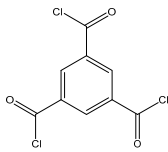
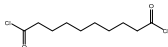
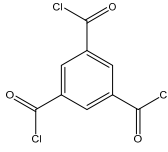
Figure 1-9. (left panel) ATR-FTIR absorbance spectrum of pepsin powder, PAN-PO supported ultrathin pepsin membranes prepared with 5 and 15 min reaction time. The absorbance peaks around $3000\text{--}3500\text{ cm}^{-1}$ represent the different C-C, C-H and O-H bonds present in the pepsin. Amino acid bonds are located at 1650 (N-H bending) and 1540 (C=O stretching) cm^{-1} . (right panel) Scanning electron micrograph of a pepsin membrane atop a PAN support (top panel) and a bare PAN support (bottom panel). The pores present on the top side of the PAN support are not visible in the pepsin membrane PAN support.²⁴³ Copyright 2015. Adapted with permission from John Wiley & Sons Inc.

Interfacial polymerization of proteins has been demonstrated by polycondensation of bovine serum albumin¹⁶² and copolymerization of aquaporin with conventional m-phenyl diamine.²³⁵ The protein immobilization allows for layer preparation with very high protein concentrations²⁴² that potentially have improved protein stability with respect to proteins in solution. Recently, the preservation of the protein function has been demonstrated by interfacially polymerized visible fluorescent proteins (VFP's) and pepsin films, as shown in **Figure 1-9**.²⁴³ **Table 1-3** shows an overview of the precursors used for the synthesis of poly(bio-amide)s. Trimesoyl chloride is the most commonly used reactant for the organic phase, although the large number of residual carboxylic acid groups in the cross-linked protein films indicates that a large fraction of the acid chloride groups does not form amide bonds.²⁴⁴ Poly(bio-amide) based membranes have relatively high molecular weight cut-off values compared to conventional polyamides. Even though the proteins are highly cross-linked, the layers display proteins functionality, biocompatibility and switchable properties.

Table 1-3. Precursors used for poly(bio-amide)s prepared by interfacial polymerization, the reaction conditions, and the applications of the poly(bio-amide) layer. In bold: the reactant names, method of interfacial polymerization, reaction time and temperature and final polymer configuration.

Aq. phase reactant	Organic phase reactant	Reaction conditions	Application	Ref.
 <p>Bovine serum albumin (structure from ²⁴⁵) (5, 10, 20, 30 g L⁻¹) in water with PBS buffer (pH 7).</p>	 <p>Trimesoyl chloride (1, 2, 3, 4, and 5 g L⁻¹) in hexane.</p>	<p>Cross-linked BSA layers were prepared by immersing PCTE substrate membrane in the aq. BSA solutions for 20 min. After removing excess solution with filter paper, the substrates were immersed into the TMC solution in hexane for 5-30 min, at 20-80 °C. Next, the cross-linked BSA layers on PCTE membranes were rinsed and stored in water.</p>	<p>Membrane nanofiltration applications. Rejection of organic GII and Congo red (20-100% retention) and pH responsive water permeability (pH 2, 110 L h⁻¹ m⁻² bar⁻¹) (pH 7, 80 L h⁻¹ m⁻² bar⁻¹) (pH 12, 160 L h⁻¹ m⁻² bar⁻¹)</p>	<p>¹⁶²</p>

 <p>Bovine serum albumin (structure from ²⁴⁵) and</p> <p>Fibrinogen (structure from ²⁴⁶, 3.8 wt.%) in PBS buffer (pH adjusted to 6.0, 7.4 and 9.0).</p>	 <p>Terephthaloyl chloride (TDC, 1.0 wt.%) in xylene</p>	<p>Protein capsules were formed by pumping BSA and fibrinogen solutions in water and TDC in xylene through an y-shaped channel to generate microdroplets. Instant layer formation occurred upon droplet formation. The droplets were allowed 24 h to react.</p>	<p>Cross-linked protein capsules for cell growth cultures. Capsules with diameters of 160-530 nm were obtained. Pore diameter increased with increasing pH of the aq. solution. At higher pH values, a smoother surface was obtained.</p>	<p>^{247, 248}</p>
 <p>Pepsin (structure from ²⁴⁹) (0.46 wt.%, PBS buffered pH 7) in water</p>	 <p>Trimesoyl chloride (0.2 and 0.5 wt.%)</p>	<p>Preparation of the layer on a polyacrylonitril (PAN) support. The aq. solution is forced through the support by means of vacuum for 30 min. Excess water is removed by drying under N₂ atmosphere, followed by contacting with the TMC in hexane phase for 5-15 min.</p>	<p>Enzymatically active pepsin membrane layer. (digestion of BSA and hemoglobin at pH 2). Clean water permeability 50 L h⁻¹ m⁻² bar⁻¹. MWCO values of 10-100 kDa.</p>	<p>²⁴⁴</p>
 <p>EGFP (left, structure from ²⁵⁰) and mRFP (right, structure from ²⁵¹) (0.087 wt.%, Tris buffered) in water.</p>	 <p>Trimesoyl chloride (0.05 wt.%) in hexane</p>	<p>EGFP and mRFP cross-linked layers were formed by contacting the aq. and hexane solutions for 15 min. After removal of the layer from the interface using a glass slide or a spatula, the film was rinsed and stored in water.</p>	<p>Fluorescent activity of EGFP and mRFP layers. high degree of immobilization of proteins (> 80%) by fluorescence recovery after photobleaching measurements.</p>	
<p>[D-Lys⁶]-LH-RH growth hormone (Sequence amino acid Glp-His-Trp-Ser-Tyr-Lys-Leu-Arg-Pro-Gly-NH₂) in water (PBS buffered, pH 7.4) with</p>	 <p>Ethylcyanoacrylate (ECA, 25 v.%) in</p>	<p>Hollow capsules were prepared from water-oil microemulsion, by stirring the aq. and ethylolate solutions at 700 rpm at 4 °C. The ECA solution in</p>	<p>Hollow capsules that allow for controlled protein delivery. The growth hormone co-polymerizes with the</p>	<p>^{252, 253}</p>

<p>surfactants sorbitan monolaurate (Crill 1) and ethoxy 20 sorbitan mono-oleate (Crillet 4).</p>	<p>chloroform. Ethyl oleate was used as oil phase for microemulsion formation.</p>	<p>chloroform was added dropwise under continued stirring. The mixture was left overnight to complete the polymerization reaction and to evaporate the chloroform.</p>	<p>polymerizing ethylcyanoacrylate.</p>	
<p>Crab protein (2.5 wt.%) and soy lecithin surfactant (2 wt.%) in water. Carboxymethyl cellulose in NaOH (1 M) was added to reduce protein agglomeration.</p>	<p>Mixtures of:</p>  <p>Trimesoyl chloride and</p>  <p>Sebacoyl chloride In cyclohexane / chloroform</p>	<p>Cross-linked protein capsules were prepared by emulsifying the aq. protein solution in cyclohexane. Capsules were prepared by adding trimesoyl chloride and sebacoyl, while stirring the emulsion. After 20 min reaction time the capsules were allowed to settle over 24 h. Finally, the capsules were removed by centrifugation.</p>	<p>Cross-linked protein capsules as a vehicle for delivery of nutrients. Higher degree of protein stability in the protein wall in case more TMC was used.</p>	242
<p>Mixture of casein, fish protein hydrolysate, octopus meal, dextrin, emulsified lipids and a vitamin mixture.</p>	 <p>Trimesoyl chloride (38 wt.%) in cyclohexane or diethyl ether</p>	<p>Cross-linked protein capsules were prepared by emulsifying the aq. protein solution in cyclohexane. Capsules were prepared by adding trimesoyl chloride in diethyl ether, while stirring at 1000 rpm. After 8 min reaction time the capsules were allowed to settle. Solvent was removed by decanting and solvent exchange.</p>	<p>Cross-linked protein capsules as a vehicle for delivery of nutrients. The capsules could substitute live food during the early stages of larval growth.</p>	254, 255

Outlook

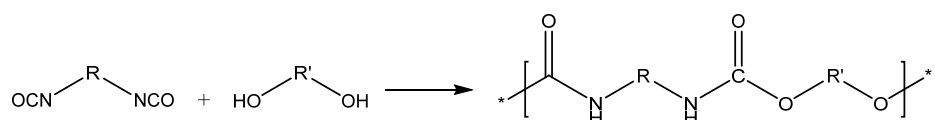
Polyamide precursors are and will remain widely used for interfacial polymerization. The relative ease by which amine functionalized precursors

can be prepared and the high reactivity of the acid chloride reactants allows for design of many polyamides. Recent work on composite, hybrid inorganic-organic and bio-hybrid materials shows that the polyamide chemistry will extend far beyond common aromatic polyamides based on the prevalent combinations of trimesoyl chloride with m-phenylene diamine and piperazine. Particularly the synergistic properties of hybrid polyamides holds much promise for the design of thin, high surface area, defect-free materials with distinct properties.

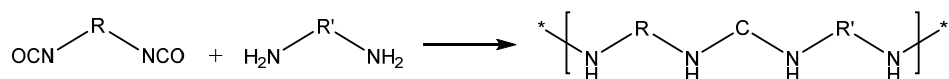
1.5.2. Polyurethane and polyurea

Polyurethane chemistry

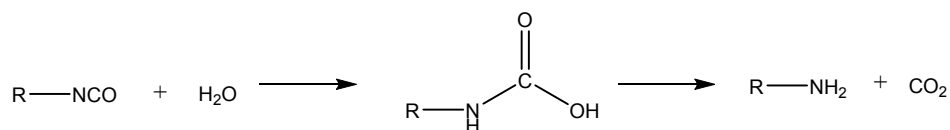
Polyurethanes and polyurea are the most common polymers that are prepared via interfacial polymerization for the synthesis (hollow) nano- and microcapsules. Polyurethanes are formed by the reaction between diisocyanate and a polyol.



Polyureas are formed by the reaction between dicyanate and diamine groups.



Urea groups are always formed during polyurethane synthesis in a water-containing system. The side-reaction of isocyanate groups with water results in the formation of an amine.²⁵⁶ The amine can subsequently react with other isocyanate groups.



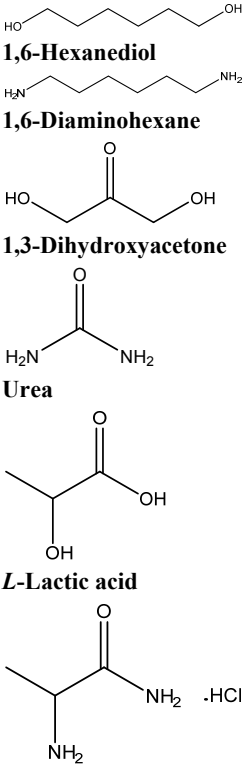
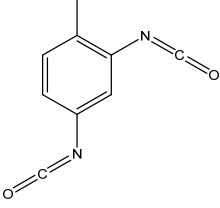
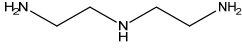
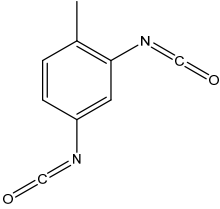
Most polyurethanes and polyureas have a low T_g , and are rubbery at room temperature. Their rubbery, dense characteristics are ideal for holding a liquid in the core of hollow capsules. The liquid core can be used as a phase change material,²⁵⁷⁻²⁶² catalyst carrier,²⁶³⁻²⁶⁶ flame retarding agent,²⁶⁷ protective agent for damaged surfaces,²⁶⁸ slow release of agrochemicals²⁶⁹⁻²⁷¹ or the delivery of

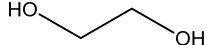
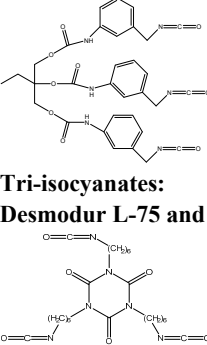
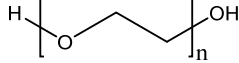
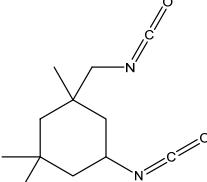
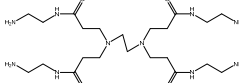
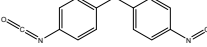
pharmaceuticals.^{272, 273} Also, residual, unreacted diisocyanate can be employed as a repair agent in self-healing materials.²⁷⁴ The release rate is controlled by the wall thickness and polymer characteristics.²⁷⁵ The main advantages of polyurethanes and polyureas are their chemical²⁷⁶ and mechanical stability (shell wall moduli of 3.7 GPa are reported, and single capsule normalized maximum strength of 1-10 MPa).^{274, 277} In addition, their biocompatibility allows for in-vitro applications.²⁷³

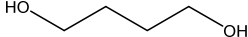
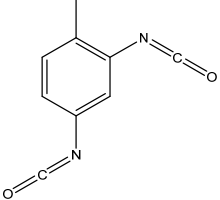
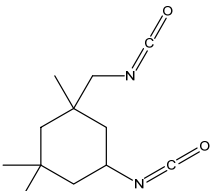
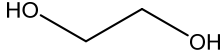
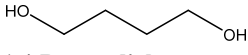
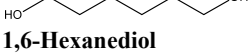
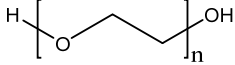
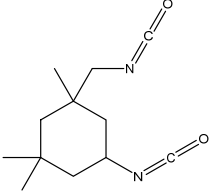
Polyurethane, polyurea and copolymers of both can be fabricated using a wide range of amine, alcohol and isocyanate precursors. **Table 1-4** shows an overview of typical precursors that are used for polyurethane synthesis, the reaction conditions employed for synthesis, and the application of the synthesized polymers. Most common used diisocyanates are diphenylmethane diisocyanate (MDI), toluene diisocyanate (TDI), hexamethylene diisocyanate (HDI) and isophorone diisocyanate (IPDI). Most of the studies on polyurethane and polyurea capsules employ aliphatic polyalcohols and polyamines that are reacted with the aromatic diisocyanates. The M_w of the polyamines and polyalcohols ranges from very small molecules such as ethane-1,2-diol to oligomers such as polyethylene glycol (PEG, with M_w 's between 200-4200 g mol⁻¹). The size of the capsules depends mainly on the method of dispersion (stirring, ultrasonic treatment, microchannel droplet formation). The size of the capsules becomes smaller with increasing stirring rate.^{257-259, 268} In addition, the capsule size depends on the type of reactant. At higher M_w 's of di- and polyols, the mean size and yield of the nanocapsules was found to increase.²⁷⁸ In addition, a higher degree of capsule agglomeration was observed when using higher M_w precursors.

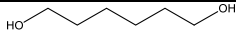
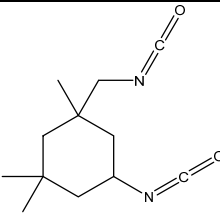
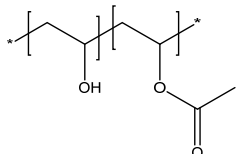
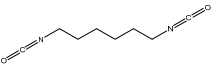
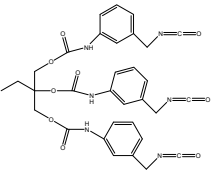
The main drawback of polyurethane synthesis via interfacial polymerization is the side-reaction of the isocyanate precursor with water, resulting in the formation of amine groups and subsequent formation of urea groups. The properties of the polymer depend on the ratio of urea and urethane groups that is determined by the hydrolysis rate of the isocyanates with respect to the layer formation rate. Urea group formation occurs in particular when the isocyanate solution is contact with water before addition of the aq. phase monomer reactant. The number of isocyanate groups that are converted to amines depends on the time that is used to prepare the emulsion, before the polymerization sets on. Addition of the isocyanate after emulsification can be used to suppress copolymer formation.

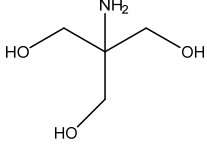
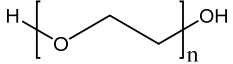
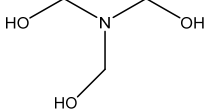
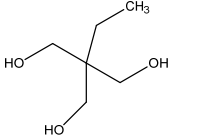
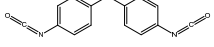
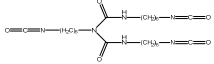
Table 1-4. Precursors used for polyurethanes and polyureas prepared via interfacial polymerization, the reaction conditions, and their applications. In bold: the reactant names, method of interfacial polymerization, reaction time and temperature and final polymer configuration.

Aq. phase reactant	Organic phase reactant	Reaction time	Application	Ref.
 <p>1,6-Hexanediol 1,6-Diaminohexane 1,3-Dihydroxyacetone Urea L-Lactic acid L-Alaninamide hydrochloride In water with sodium chloride (2.0 mM, pH 7.4)</p>	 <p>2,4-Toluene diisocyanate (TDI), 0.96 mmol) in cyclohexane. The molar ratio of monomer/TDI (1:1.5) was kept constant</p>	<p>The aq. phase was emulsified in cyclohexane with surfactant (P(E/B-b-EO) or Lubrizol U). A solution of TDI in cyclohexane was added over 5 min at 25 °C. This mixture was stirred to react for 24 h at 25 °C.</p>	<p>Poly(urethane/urea) and polyurea nanocapsules for the storage and slow release of components. pH stable in a pH range of 2.5-9. The storage capacity was tested with a sulforhodamine dye solution.</p>	276
 <p>Diethylene triamine (DETA) Nonionic surfactant, SMA (Scripset® 520, Hercules). pH adjusted to pH 10 by using 0.1</p>	 <p>2,4-Toluene diisocyanate (TDI),</p>	<p>The oil phase was emulsified by dropwise addition to the aq. phase under magnetic stirring at 1000–4000 rpm for 2 min. After 2 h reaction time, the capsules were separated by solvent</p>	<p>Polyurea microcapsules filled with a phase change material (n-octadecane) for the absorption and release of latent heat, at the</p>	257-259

<p>mol L⁻¹ NaOH. Molar ratio of DETA/TDI varied from 0.84 to 1.35</p>	<p>in n-octadecane and 20 mL of acetone as an oil phase.</p>	<p>evaporation at 40°C under reduced pressure.</p>	<p>melting point of the liquid core.</p>	
<p> Ethane-1,2-diol in water.</p>	<p> Tri-isocyanates: Desmodur L-75 and Sumidur N-3300</p>	<p>The emulsion was prepared by mixing the oil phase to the water phase for 5 min using a TK Auto Homomixer® (Primix Corporation). The interfacial polymerization reaction was initiated by heating to 75 °C and reaction for 48 h.</p>	<p>Polyurethane self-bursting microcapsules filled with pyriproxyfen, an insect growth regulator. The capsules, with diameters around, retained their shape when suspended in water, but break open after the water is removed.</p>	269
<p> Polyethylene glycol ($M_w = 200$ and 400) and L-Lysine in water</p>	<p> 5-Isocyanato-1-(isocyanatomethyl)-1,3,3-trimethyl-cyclohexane (IDPI) in saturated medium chain triglyceride (MCT) and soybean oil (SO)</p>	<p>The nano-emulsions were prepared at 25 °C by phase inversion composition emulsification. The aq. component was added dropwise under continuous mixing with a vibromixer. Polymerization was initiated by heating the emulsion to 55-80 °C. The polymerization reaction was stopped after 4 h and samples were kept at 25 °C.</p>	<p>Polyurethane and polyurea nanoparticles with a small diameter (50-90 nm) for drug delivery applications. The synthesis required low concentrations of IDPI and showed good biocompatibility.</p>	273
<p> Polyamidoamine (0th generation dendrimer) (0.005 M) in water with 1.0 wt.% of PVA.</p>	<p> 1-Isocyanato-4-[(4-isocyanatophenyl)methyl] benzene (MDI) 1.5 g of MDI and 2 g of linseed oil in xylene.</p>	<p>Dispersion of aq. solution at 3000, 5000, and 8000 rpm at 25 °C for 5 min to obtain stable emulsion. Dropwise addition of PAMAM solution at 300 rpm. The reaction was continued for 30 min at 30 °C and 1.5</p>	<p>Polyurethane microcapsules filled with anticorrosive agent. mean diameter in the range of 20–300 µm. Polyurea thermal stability up to 380 °C. PU</p>	268

		h at 45–50 °C.	coatings on steel substrate embedded with the polyurea microcapsules containing linseed oil showed corrosion protection.	
 <p>1,4-Butanediol in of water with arabic gum and surfactant 43</p>	 <p>2,4-Toluene diisocyanate (TDI) and</p>  <p>5-Isocyanato-1-(isocyanatomethyl)-1,3,3-trimethyl-cyclohexane (IDPI) in chlorobenzene.</p>	<p>Emulsification of aq. solution at 500-1500 rpm) for 3 h. The mixture was then slowly poured into the arabic gum solution. At 50 °C, the 1,4-butanediol solution was slowly added to the emulsion and reacted for 45 min. Once cooled to ambient temperature, the microcapsule suspension was rinsed with deionized water and vacuum filtered.</p>	Smooth spherical polyurethane microcapsules of 40-400 μm in diameter. The shell wall thickness to diameter ratio is constant (~0.05). High yields (~70%) of a free-flowing powder of capsules are produced with a liquid core content of 70 wt.%. The microcapsules are stable with only ~10 wt.% loss of IPDI detected after 6 months storage under ambient conditions.	274
 <p>Ethane-1,2-diol</p>  <p>1,4-Butanediol</p>  <p>1,6-Hexanediol</p>  <p>Polyethylene glycol ($M_w = 200, 300, 400,$</p>	 <p>5-Isocyanato-1-(isocyanatomethyl)-1,3,3-trimethyl-cyclohexane (IDPI) (10^{-3} mol), α-</p>	<p>Emulsification by injection of the organic phase in an aq. surfactant solution under magnetic stirring, followed by addition of the aqueous phase with monomer reactants. The magnetic stirring is maintained for 3 h at room temperature.</p>	Polyurethane and poly(ether urethane) capsules in the range of 150-500nm. Drug carriers for α -tocopherol, a strong antioxidant that is used in medical and	278

<p>425, 600) in water (80 ml), diol or polyether (10–2 mol) and hydrophilic surfactant (136 mg Tween® 20).</p>	<p>tocopherol (400 mg) and a lipophilic surfactant (86 mg Span® 85) in water-miscible solvent (40 ml acetone)</p>	<p>solvent is removed by evaporation for 45 min under reduced pressure</p>	<p>cosmetic applications. The capsules provide protection of the active component from light, heat and oxygen.</p>	
<p> 1,6-Hexanediol (0.23 M) in water.</p> <p>The emulsion is stabilized with an SDS solution (3–10 wt.% in water).</p>	<p> 5-Isocyanato-1-(isocyanatomethyl)-1,3,3-trimethylcyclohexane (IDPI, 0.43 M) in cyclohexane and hexadecane as co-stabilizer.</p>	<p>The mini-emulsion was prepared by ultrasonic treatment at various durations and amplitudes, combined with magnetic stirring at 500 rpm). Subsequently, the solution of 1,6-hexanediol) was added dropwise for 1 min under ultrasonic treatment at 20% amplitude. The temperature was then increased to 40–60 °C, under magnetic stirring at 300 rpm for 4–6 h.</p>	<p>Polyurethane capsules for drug delivery applications, with mean diameters around 200 nm. The particles were filled with an ibuprofen solution in Miglyol 812, a triglyceride oil used for drug delivery applications.</p>	<p>188, 272</p>
<p> Polyvinyl alcohol-co-vinyl acetate in water</p>	<p>Mixtures of</p> <p> 1,6-Diisocyanatohexane (HMDI) and</p> <p> Tri-isocyanate (Takenate D-110N), in ethyl acetate and dioctyl phthalate. The weight fractions of D-110N with respect to the total monomer reactants were 0, 0.25, 0.5, 0.75 and 1.</p>	<p>The organic phase was poured into a 5 wt.% protective colloid aqueous solution, and stirred vigorously at 5000 rpm for 10 min on ice with a homogenizer (HG-300D + K12S, Shuang-Tai Co., Taiwan). The suspension was stirred for another 4 h at 40 °C to complete the layer growth.</p>	<p>Poly(urethane urea) microcapsules (around 1 μm diameter) for drug delivery applications. Controlled release of a yellow oil-soluble dye was used to determine the release kinetics. A higher tri-isocyanate content resulted in slower dye release.</p>	<p>279-281</p>

 <p>2-Amino-2-(hydroxymethyl)-1,3-propanediol</p>  <p>Polyethylene glycol ($M_w = 600, 1500, 4200$)</p>  <p>Tris(2-hydroxyethyl)amine</p>  <p>2-(Hydroxymethyl)-2-ethylpropane-1,3-diol</p>	 <p>1-Isocyanato-4-[(4-isocyanatophenyl)methyl]benzene (MDI)</p>  <p>Polyhexamethylene diisocyanate (Desmodur N 100) in toluene (B 261, 1 g L⁻¹)</p>	<p>A stable inverse emulsion was formed by stirring of an aqueous di- or triols solution and toluene containing a stabilizer at 300 rpm. Once the emulsion was formed, the stirring rate was reduced to 200 rpm and an isocyanate solution in toluene was added. Finally, the reaction is continued for several hours in order to ensure the wall growth, followed by washing and recovery of the capsules.</p>	<p>Synthesis of large polyurethane capsules with diameters between 50-400 μm, for testing of mechanical properties. The number of broken capsules decreased by using a moderate amount of cross-linking agent and sufficiently long diols such as PEG. Longer diols such as PEG allow for more deformation without breakage.</p>	157
--	---	---	---	-----

Polyurethane and polyurea composites

Polyurethane and polyurea nanocomposite capsules have been prepared by combining interfacial polymerization with a Pickering emulsion. The Pickering emulsion is prepared by using particles that assemble at the liquid-liquid interface, stabilizing the emulsion without the need of additional surfactant. Upon interfacial polymerization, the particles are incorporated in the polymeric shell. Examples of particles that are used include silica (nanopowders with particle size of 5-30 nm or via sol-gel),²⁸²⁻²⁸⁶ nanoclay,²⁸⁷ magnetic nanoparticles (Fe_3O_4),²⁸⁸ and hollow capsules.²⁸⁹ The composites display improved the shelf life of the liquid core (i.e., leaching of the liquid core was slowed down) due to lowered liquid permeabilities and improved the mechanical strength.

Outlook

Polyurethanes and polyureas prepared via interfacial polymerization are currently mainly used for the synthesis of hollow capsules. However,

polyurethanes and polyureas prepared via bulk polymerization are used for membrane applications such as gas separation²⁹⁰ and the removal of volatile organic components (VOC's) from aqueous streams by pervaporation and vapor permeation.²⁹¹ Up to date, interfacial polymerization has not been used for such membrane applications. Nonetheless, the preparation of ultrathin, highly cross-linked polyurethane and polyurea rubbers might show potential for solvent nanofiltration and other affinity based separations.

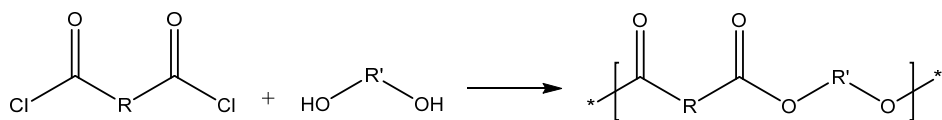
The recent developments in composite polyurethanes prepared by the combination of Pickering emulsion and interfacial polymerization show that the polymer properties can be improved by addition of nanoparticles. Much unexploited potential can be found in the wide variety of fillers used in polyurethane and polyurea nanocomposites prepared by bulk polymerization.²⁹² Moreover, in particular capsules can benefit from the addition of particles that impart stimuli-responsive properties on the capsule wall. Examples include conductive or magnetic nanoparticles, heat responsive polymers and light sensitive components that can result in the selective transport of components in and out of the capsules or that can lead to subsequent reactions in the capsule components.

Although currently no hybrid polyurethanes and polyureas are prepared via interfacial polymerization, a large number of amine, hydroxyl and isocyanate precursors are readily available. Examples of hybrid precursors include isocyanate-,²⁹³ amine-,^{111, 192, 240, 294} and alcohol-functionalized POSS molecules.^{295, 296} Bio-hybrids can be prepared by using the amino acids of biological components as reactive component, although the high reactivity of isocyanates and their poor biocompatibility might result in loss of protein function.

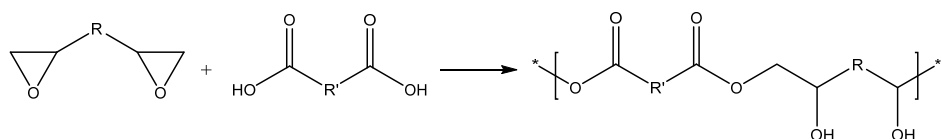
1.5.3. Polyesters

Polyester chemistry

Interfacial polymerization is not widely used for preparation of polyesters. Of the limited number of studies available in literature, most focus on polyester layer formation for membrane applications such as nanofiltration²⁹⁷⁻²⁹⁹ reverse osmosis³⁰⁰ and gas separation.³⁰¹ Polyesters can be prepared from the condensation reaction of acid halides and alcohols.

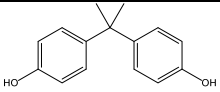
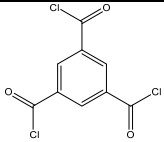


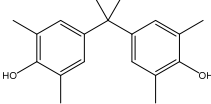
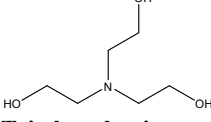
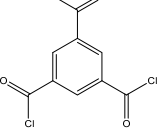
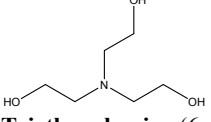
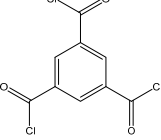
Alternatively, the interfacial polymerization of carboxylic acid and epoxy can be used to synthesize hydroxyesters.³⁰²

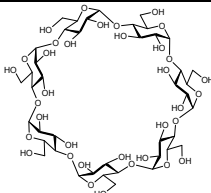
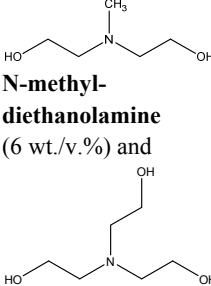
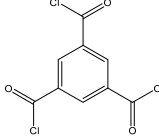
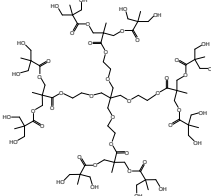
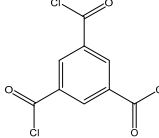


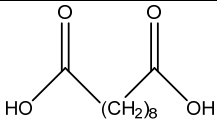
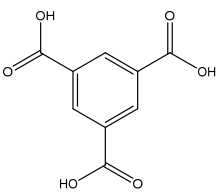
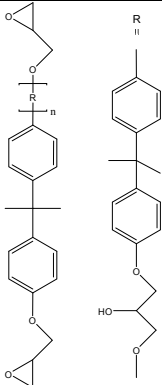
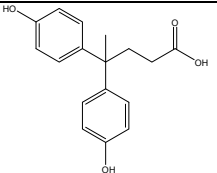
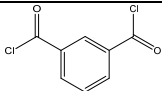
The main drawback of polyesters is their susceptibility to hydrolytic degradation under acid and base conditions, as compared to polyamides. In addition, only limited experimental data is available on polyester fouling resistance, stability against common cleaning agents, and performance at a broad range of relevant process conditions. Lastly, the membrane performance (in terms of permeance and salt rejection) is generally less than that of state-of-the-art polyamide membranes. Nonetheless, some interesting approaches have been pursued in the preparation of polyesters via interfacial polymerization. **Table 1-5** shows the precursors that are used for polyester layer formation, the synthesis conditions and their applications. Trimesoyl chloride, the most used reactant for polyamide membrane preparation, is used as the organic phase monomer. Both aliphatic and aromatic polyols are used. The molecular sizes of these polyols are larger with respect to common diamines used for polyamide preparation, namely meta-phenylene diamine and piperazine. It is almost surprising that simple benzenediols have not yet been employed in polyester synthesis, given the unsurpassed performance of polyamide membranes prepared with short amide bridges.

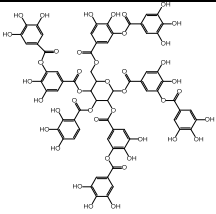
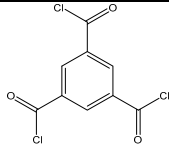
Table 1-5. Precursors used for polyesters prepared via interfacial polymerization, the reaction conditions, and their applications. In bold: the reactant names, method of interfacial polymerization, reaction time and temperature and final polymer configuration.

Aq. phase reactant	Org. phase reactant	Reaction conditions	Application	Ref.
 <p>Bisphenol A (BPA, 0.1-2 wt./v.%)</p>		NFPES10 support membrane was immersed in a TMBPA or BPA aqueous solution for 15 min.	Membranes nanofiltration applications. The layers exhibited practically no	298, 303, 304

 <p>Tetramethyl Bisphenol A (TMBPA) in water. The pH is adjusted to 11 using NaOH.</p>	<p>Trimesoyl chloride (0.15 wt./v.%) in hexane</p>	<p>The pre-soaked membrane was taken out from the aqueous solution and positioned vertically for 2 min to drain the excess monomer from the surface. Subsequently, the membrane was dipped in the TMC solution in hexane for 10, 30 or 60 s.</p>	<p>irreversible fouling by humic acid molecules at pH 7. Only at pH 3, irreversible fouling by humic acid was observed.</p>	
 <p>Triethanolamine and SDS (0.3 wt./v.%) in water. pH adjusted with of NaOH and Na₂CO₃</p>	 <p>Trimesoyl chloride in hexane</p>	<p>The polysulfone support membrane was immersed in the aq. phase for 30 min at 35 °C. A rubber roller was used to remove any bubbles from the surface. Next, the water solution was drained and the support was air-dried at room temperature. Finally, the supports are placed in the organic phase for up to 35 min. The membranes were post-treated at 60 °C for 30 min. The final membranes were washed and stored in water.</p>	<p>Membrane nanofiltration applications. Rejection of Na₂SO₄ (82.2%), MgSO₄ (76.5%), NaCl (42.2%) and MgCl₂ (23%). Water flux around 10 L m⁻² h⁻¹ bar⁻¹. Reaction time, reactant concentrations were varied to optimize membrane performance. Addition of multi-walled carbon nanotubes resulted in flux increase (max increase at 0.5 g L⁻¹ in the aq. solution used for interfacial polymerization.</p>	<p>305, 306</p>
 <p>Triethanolamine (6 wt./v.%) and</p>	 <p>Trimesoyl chloride (0.6 wt./v.%) in hexane</p>	<p>The PSf support was immersed in the organic phase for 30 min. Then, the TMC-saturated support membrane was immersed into the aqueous phase for 35 min. Afterwards, the membrane was put into</p>	<p>Membranes nanofiltration applications. The addition of β-CD increased the number of negatively charged groups, increased the flux (up to 2 times with respect</p>	<p>307</p>

 <p>β-cyclodextrin (β-CD) and sulfonated β-CD in water with SDS (0.3 wt./v.%). pH adjusted with of NaOH and Na₂CO₃</p>		<p>the organic phase again for 35 min. Finally, the membrane was subjected to a heat treatment at 60 °C for 30 min, followed by soaking the membrane in an aqueous solution of SDS (0.1%, w/v) with pH 11 for 24 h. The final membranes were washed and stored in deionized water.</p>	<p>to the bare polyester)</p>	
 <p>N-methyl-diethanolamine (6 wt./v.%) and Triethanolamine in water with SDS (0.3 wt./v.%) and LiBr salt (0-7 wt./v.%). The pH adjusted to 12 by a mixture of NaOH and Na₂CO₃</p>	 <p>Trimesoyl chloride (0.2 wt./v. %) in hexane</p>	<p>The PSf support membrane was immersed in the aqueous phase for 30 min at 35 °C. After removing excess liquids on the membrane surface, the membrane was soaked in the organic phase for 35 min. Finally, the membrane was post-treated in an oven at 60 °C for about 30 min. The membranes were thoroughly washed with deionized water.</p>	<p>Membrane nanofiltration applications. LiBr salt influenced the Na₂SO₄ and MgSO₄ rejection and permeation, by influencing the layer formation during interfacial polymerization. 3 wt.% LiBr gave highest water flux improvement. 1 wt.% LiBr dramatically decreased retention.</p>	<p>308</p>
 <p>Hyperbranched polyester (HPE, 2.7 wt.%) in water with 0.3 wt.% of SDS. 2nd, 3rd, and 4th pseudo-generation (16, 32 and 64 terminated OH-groups,</p>	 <p>Trimesoyl chloride (0.5 wt.%) in hexane.</p>	<p>PAN support membrane was pre-wetted by ethanol. The pre-wetted supports were then immersed in the HPE in ethanol solution for 40 min After draining the excess solution, the membranes were submersed in the TMC solution in hexane for 30 min. Finally, the membranes were heat treated at 80 °C for 20</p>	<p>Membrane nanofiltration applications. The membrane surface displayed a negative surface and had a MWCO of 4-6 kDa. Rejection properties of the membranes depended on the dye charge, dye concentrations and salt concentrations.</p>	<p>297, 299, 309</p>

<p>respectively).</p>		<p>min. The membrane was preserved in water for further use.</p>		
<p>  Potassium decanedioate (12.5 g) in 150 mL water </p> <p>  Potassium 1,3,5-benzene tricarboxylate (1.62 g) in 150 mL water </p>	<p>  Epoxy resin (5.465 g) in 50 mL toluene </p>	<p>The epoxy in toluene solution was emulsified by dropwise addition to tetrabutylammonium hydrogen sulfate (TBAH, 3.055 g in 150 mL water, phase transfer catalyst) in water under stirring at 700 rpm at temperatures up to 60 °C. Next, the aqueous phase with carboxylic acid monomers was added dropwise. The reaction was carried out for 5 days under reflux, with stirring (700 rpm) at 60 °C. The organic phase was evaporated under reduced pressure and further purified in tetrahydrofuran (THF), N-methylpyrrolidone (NMP) and water.</p>	<p>At lower stirring rates, microcapsules in the range of 100–400 μm were obtained. At higher stirring rates, microcapsules in the range of 10–50 μm were obtained. Intermolecular transesterification was observed as side reaction. Capsule morphology was influenced by the cross-linker content.</p>	<p>302</p>
<p>  Diphenolic acid (DPA, 0.01 mol), NaOH (0.03 mol), and tetrabutylammonium hydrogen sulfate (TBAC, 0.117 g) in 90 mL water. </p>	<p>  Isophthaloyl chloride (IPC, 0.01 mol) in 50 mL dichloromethane </p>	<p>IPC in dichloromethane was emulsified in the aq. DPA solution under stirring at 400 rpm. The reaction was performed at 25°C for 1 h, while adjusting the pH to around 3 using sulfuric acid. The acidified polyester product, poly(DPA-IPC), was washed with deionized water and acetone. Finally, it was filtered, and dried at</p>	<p>Microcapsule synthesis. Shell growth occurred towards the core, gradually increasing shell thickness. The viscosity of the reaction zone and diffusion rate of monomers and oligomers depended on the miscibility between the solvent and the polymer. Shell growth depended on solvent</p>	<p>310</p>

		100 °C in a vacuum oven.	type used for synthesis.	
 <p>Tannic acid (0.1-0.5 g L⁻¹) in water. The pH was kept at 7.0 with 0.1 M phosphate buffer solution.</p>	 <p>Trimesoyl chloride (TMC, 0.1-0.5 g L⁻¹) in hexane.</p>	<p>Polyethersulfone support membranes were first soaked into the aqueous tannic acid solution for about 10 min. The residual water on the surface was drained off using filter papers. Subsequently, the membranes were immersed into TMC solution for 1-15 min. Excess organic solution was drained and the coated surfaces were air-dried in an oven at 20-80 °C. Finally, the membranes were washed and stored in water.</p>	<p>Membrane nanofiltration applications. The permeances were in between 13-50 L m⁻² h⁻¹ bar⁻¹. Orange GII rejection was above 98% for all membranes with a reaction time above 5 min. Rejection of monovalent and divalent salts increased with increasing tannic acid concentration and decreasing TMC concentration.</p>	311

Polyester composites

Only few examples of polyester composites are available in literature. There has been some work on incorporating multi-walled carbon nanotubes to improve the membrane permeance while maintaining high selectivity.^{306, 312} Also, (sulfonated) β -cyclodextrin has been incorporated in the polymer to change the surface charge for better salt rejection performance.³⁰⁷

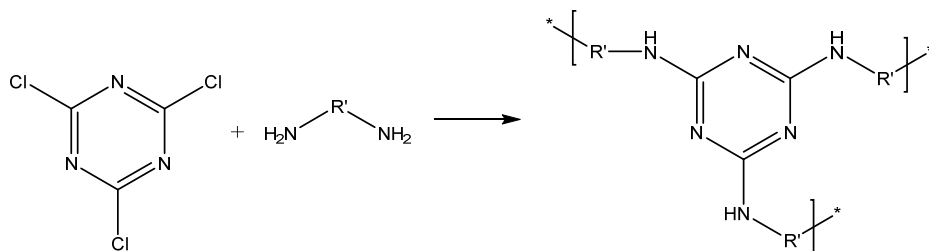
Outlook

Polyesters might provide an interesting analogue to polyamides. Differences in layer formation can be expected from the differences in reactivity and solubility of alcohol and amide groups. Further optimization of the choice in polyester precursors might yield membranes with membrane performance that is similar as for aromatic polyamides. Moreover, the distinct surface charge properties, layer morphology and affinity might provide an interesting platform for specific separation applications.

1.5.4. Polyamines

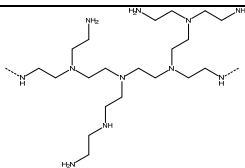
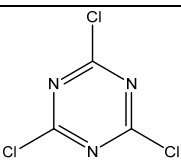
Polyamine chemistry

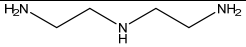
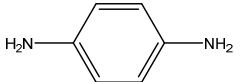

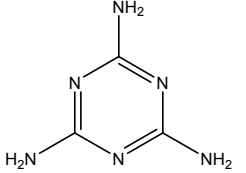
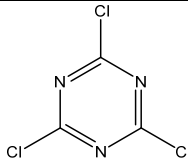
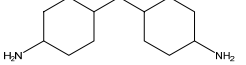

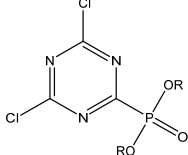
The resonance structure of s-triazines provides polymer rigidity, thermal and chemical stability. This is reflected by the pH stability of nanofiltration membranes based in cyanuric chloride prepared via interfacial polymerization.³¹³ Polyamines are prepared by a condensation reaction between a diamine and a di- or trichloride functionalized triazine.

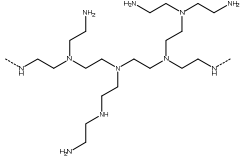

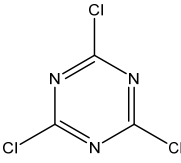
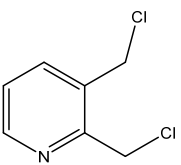
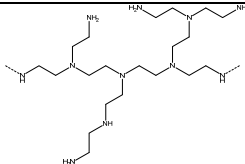
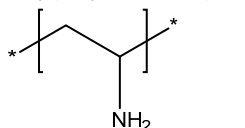
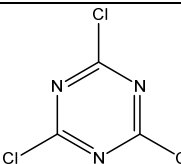


One drawback of di- or trichloride triazines is their decreasing reactivity with the number of chloride group substitutions.³¹⁴ The first chloride group will be substituted easily at room temperature. For the second and third chloride groups, temperatures of 40-60 °C may be employed to improve the reactivity. **Table 1-6** shows an overview of the monomer reactants that have been used to prepare polyamines via interfacial polymerization. Both small monomer reactants such as m-phenylene diamine and large oligomers such as poly(ethylene imine)s have been employed for layer preparation. The concentrations of the polyamines and di- and trichloride triazines are relatively high as compared to polyamide synthesis, which might be due to the lower reactivity of the chloride groups with respect to acid chlorides.

Table 1-6. Precursors used for polyamines prepared via interfacial polymerization, the reaction conditions, and their applications. In bold: the reactant names, method of interfacial polymerization, reaction time and temperature and final polymer configuration.

Aq. phase reactant	Org. phase reactant	Reaction conditions	Application	Ref
 <p>Poly(ethylene imine)</p>	 <p>Cyanuric</p>	Hydrophilised polyethersulfone (PESf) support membrane was pre-wetted by 0.05 wt% SDS solution by means	Membrane nanofiltration applications. Stable performance in a pH range of 1-13.	313

<p>(1-10 g L⁻¹) in water</p>	<p>chloride (CC, 0.5 or 2.5 g) in hexane</p>	<p>of vacuum for 10 min. Next, the PEI aqueous solution was sucked through the membrane for 10 min and the excess was drained. The membrane was clamped vertically and dried in an air atmosphere for 20 min. In the final step, CC in hexane was poured into the cell and reacted for 30 s.</p>		
<p> Diethylenetriamine (1 wt. %)</p> <p> Meta-phenylene diamine (2 wt. %)</p> <p> Piperazine (1 wt. %)</p> <p> Melamine (1 wt. %)</p>	<p> Cyanuric chloride (1-2 wt. %) in toluene</p>	<p>Polyacrylonitrile (PAN) support was first immersed in an aqueous monomer solution of 1-2 wt.% and then moved into a toluene monomer solution of 1-2 wt.%. The reaction time was varied between 1, 2, 3, 5, and 30 min. Finally, the membranes were washed using toluene, ethanol and distilled water.</p>	<p>Membrane gas separation applications. Permeability of O₂ around 1.40 GPU. O₂/N₂ selectivities ranging from 3-7.</p>	315
<p> bis(4-amino cyclohexyl)methane</p> <p> hexamethylenediamine</p>	<p> 2-Dialkoxy phosphinyl-4, 6-dichloro-s-triazine</p>			316

 <p>Poly(ethylene imine)</p>  <p>Meta-phenylene diamine</p>	 <p>Cyanuric chloride</p>  <p>Bischloromethyl pyridine Hydrocarbon solvent such as hexane</p>	(Patent)	Nanofiltration and reverse osmosis membrane applications.	317
 <p>Poly(ethylene imine)</p>  <p>Polyvinylamine</p>	 <p>Cyanuric chloride</p>	(Patent)	Nanofiltration and reverse osmosis membrane applications in solvent and acid stable media.	318

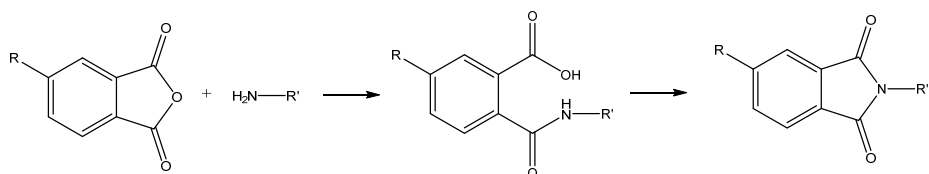
Outlook

Polyamines prepared from triazines provide a good resistance to harsh chemicals and acid or base media. Demand of clean water will only increase the need for advanced water purification techniques, in particular using membrane nanofiltration and reverse osmosis. The further optimization of the separation performance of polyamine membranes will therefore be an important development for broadening the application range of membrane based water separation. The broad range of polyethylene imine precursors leaves a wide range of possibilities for further material synthesis and membrane performance testing.

1.5.5. Polyimides

Polyimide chemistry

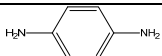
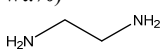
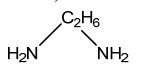
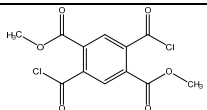

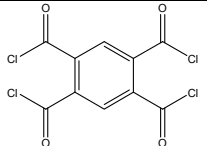
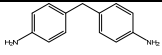
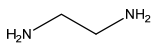
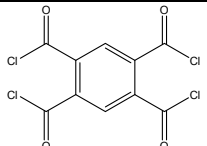
Polyimides and poly(etherimide)s represent a class of engineering polymers that are characterized by their stability at elevated temperatures, high chemical stability.²⁰⁵ Polyimides are widely used as low- κ dielectrics, high-temperature plastics, adhesives, photoresists, nonlinear optical materials and membranes. Polyimides are produced by a polymerization reaction that results in a polyamic acid intermediate, followed by thermal or chemical dehydration of the amic acid that results in the formation of imide groups.

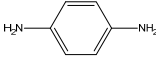
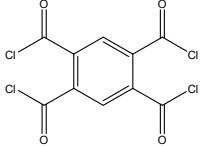


Because the amic acid groups are hydrolytically unstable, the polymer molecular weight might decrease after the reaction is terminated. This effect is particularly pronounced in aprotic polar solvents that are commonly used for bulk polymerization in a single solvent such as N-methyl pyrrolidone.³¹⁹ For poly(amic acid)s prepared via interfacial polymerization, no data on the amic acid group stability is available. Membrane performance data for gas and vapor separation suggest that high performance polyimides can be prepared via interfacial polymerization.^{192, 294, 320}

Other drawbacks include the limited solubility of dianhydride precursors in most apolar solvents. To overcome the solubility issues, alternative precursors such as tetrafunctional acid chlorides^{205, 321, 322} or acid chloride derivatives of dianhydrides have been used.³²⁰ In addition, sufficient solubility for interfacial polymerization was observed in toluene.^{192, 294} Table 1-7 shows an overview of precursors that are used for polyimide synthesis via interfacial polymerization.

Table 1-7. Precursors used for polyimides prepared via interfacial polymerization, the reaction conditions, and their applications. In bold: the reactant names, method of interfacial polymerization, reaction time and temperature and final polymer configuration.

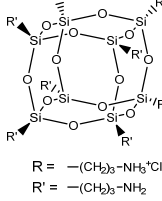
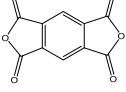
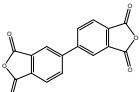
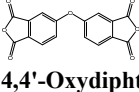
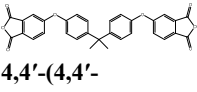
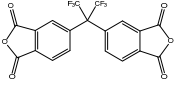
Aq. phase reactant	Org. phase reactant	Reaction conditions	Application	Ref
 <p>Meta-phenylene diamine (2 wt.%)</p>  <p>Ethylene diamine (2 wt.%)</p>  <p>Hexa methylene diamine (2 wt.%) in water</p>	 <p>2,5-Bis(methoxy carbonyl) terephthaloyl chloride (BMTC, 0.5 wt.%) in toluene</p>	<p>Polysulfone support membrane was fixed onto glass plate and immersed in an aq. diamine solution for 10 min. Next, excess diamine solution was removed from the surface using a rubber roller and immersed into the BMTC in toluene solution for 5 min. The membrane was rinsed with 50/50 (w/w) ethanol/water solution and vacuum-dried at 30°C for 24 h. Finally, it was cured in a vacuum oven at various temperatures (70, 100, 150, 180, 210 °C) for 3 h.</p>	<p>Membrane vapor separation of ethanol/water mixtures (90/10 wt./wt.) with a water permeance of 1.7 kg m⁻² h⁻¹ and water/ethanol selectivity of 240.</p>	320
 <p>Meta-phenylene diamine (2 wt.%) in water</p>	 <p>1,2,4,5'-Benzene tetraacyl chloride (0.1 and 0.05 wt.%)</p>	<p>Polysulfone support membrane immersed in aq. MPD solution. Excess liquid was removed from the surface using a rubber roller. The membrane was then immersed in an organic solution of BTC or BTC with TMC for a predetermined time. The membranes were thoroughly rinsed with deionized water for 12 h and then immersed in a TEA or TMHD solution. Finally, thermal treatment was applied to convert the poly(amic acid) to polyimide.</p>	<p>Membrane nanofiltration applications. NaCl 13.9 gfd 96.7 % rejection (with 0.1 wt.% BTC) and 18.8 gfd 96.7 % rejection (with 0.05 wt.% BTC). Improved chlorine resistance with respect to a polyamide membrane at 500 ppm Cl₂ exposure.</p>	205
 <p>4,4'-methylene dianiline</p>  <p>Ethylene</p>	 <p>1,2,4,5'-Benzene</p>		<p>Membrane gas separation applications. CO₂/CH₄ permselectivities of 20.5 CO₂ and</p>	321, 322

<p>diamine</p>	<p>tetraacyl chloride</p>		<p>permeability coefficient of 44 barrer. Film thicknesses below 20 μm.</p>	
 <p>Meta-phenylene diamine (8 g L^{-1}) in water</p>	 <p>1,2,4,5'-Benzene tetra acyl chloride (2 g L^{-1})</p>		<p>Membrane nanofiltration applications. Rejection of Na_2SO_4 (93.8%) and acid brilliant blue 6B (96.9%) at 0.5 MPa feed pressure. Negatively charged surface.</p>	<p>323</p>

Hybrid inorganic-organic polyimides

Hybrid inorganic-organic polyimides represent a class of materials that allow for combination of rigidity, thermal stability and membrane performance properties. Table 1-8 shows the precursors that are used for the preparation of hybrid polyimides. Dianhydrides and octa-ammonium functionalized POSS have been used as monomers in the interfacial polymerization reaction, resulting in the formation of a range of networks of alternating POSS and imide moieties. The large number of functional groups on the POSS cage are used to obtain a large number of covalent bonds in the hyper-cross-linked network. The length and flexibility of the dianhydride determine the changes during conversion of the amic acid to imide groups via a heat treatment. In addition, the type of dianhydride precursor determines the gas separation properties of the membrane layers.

Table 1-8. Precursors used for polyimides prepared via interfacial polymerization, the reaction conditions, and their applications. In bold: the reactant names, method of interfacial polymerization, reaction time and temperature and final polymer configuration.

Aq. phase reactant	Org. phase reactant	Reaction conditions	Application	Ref.
 <p>R = $-(CH_2)_3-NH_3^+Cl^-$ R' = $-(CH_2)_3-NH_2$</p> <p>Octa-aminonium POSS (0.9 wt.%) in water with pH 9.9 (NaOH adjusted).</p>	 <p>Pyromellitic dianhydride (PMDA)</p>  <p>3,3',4,4'-Biphenyl tetracarboxylic dianhydride (BPDA)</p>  <p>4,4'-Oxydiphthalic anhydride (ODPA)</p>  <p>4,4'-(4,4'-Isopropylidene diphenoxy)bis(phthalic anhydride) (BPADA)</p>  <p>4,4-(Hexafluoro isopropylidene) dipthalic anhydride (6FDA) (0.075 wt.%) in toluene</p>	<p>Ceramic membranes (α-alumina discs with a 3-μm-thick γ-alumina layer was pre-wetted under 0.5 bar vacuum in the aq. POSS solution for 15 min. After drying in an air atmosphere for 15 min, the dianhydride solution in toluene for contacted for 5 min.</p>	<p>Membrane gas separation applications at 50-300 °C. H_2 permeances of $0.2-5 \cdot 10^{-7} \text{ mol m}^{-2} \text{ s}^{-1} \text{ Pa}^{-1}$ (60-1500 GPU) and H_2/N_2 selectivities of 7-100. The H_2/N_2 selectivity was persistently high at temperatures up to 300 °C for poly(POSS-imide)s prepared using PMDA and BPDA</p>	<p>192, 294</p>

Outlook

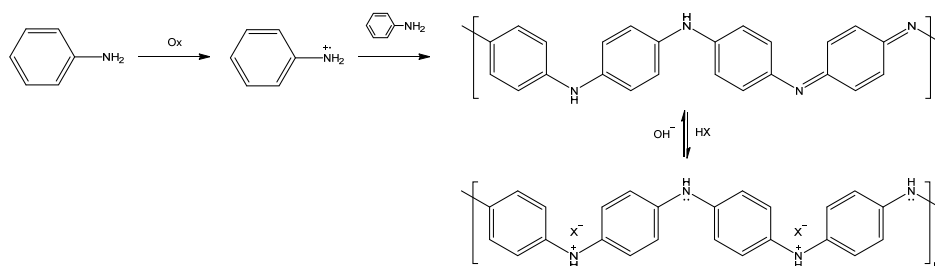
Polyimides prepared via interfacial polymerization are potentially interesting for membrane applications, due to their superior thermomechanical properties and performance in gas separation applications. Although the molecular

weight of linear polyimides might be limited due to the instability of amic acid bonds in the vicinity of water, highly branched polyimides or hybrid polyimides provide an interesting pathway for novel material development. Further study on the amic acid group stability during interfacial polymerization is required to assess material properties and optimize the synthesis conditions.

1.5.6. Conductive polymers

Polyaniline

Polyaniline layers³²⁴⁻³²⁶ nanofibers^{145, 327-332} and nanoparticles^{333, 334} have been prepared via interfacial polymerization. The interfacial synthesis is based on the oxidation of aniline at the interface by a strong oxidizing agent such as ammonium peroxydisulfate, followed by a reaction of the oxidized aniline with another aniline molecule, forming polyaniline.



A strong acid is commonly added to the aqueous phase to obtain a doped, conductive emeraldine salt form of polyaniline. The oxidation state of polyaniline is very sensitive to the level of doping, and can therefore be used as a sensor for detection of acids, bases or oxidizing and reducing compounds. Polyaniline nanofibers give larger and faster sensor response than polyaniline films due to the enhanced surface area.³³⁵ **Figure 1-10** shows the typical morphology of polyaniline nanofibers prepared via interfacial polymerization.

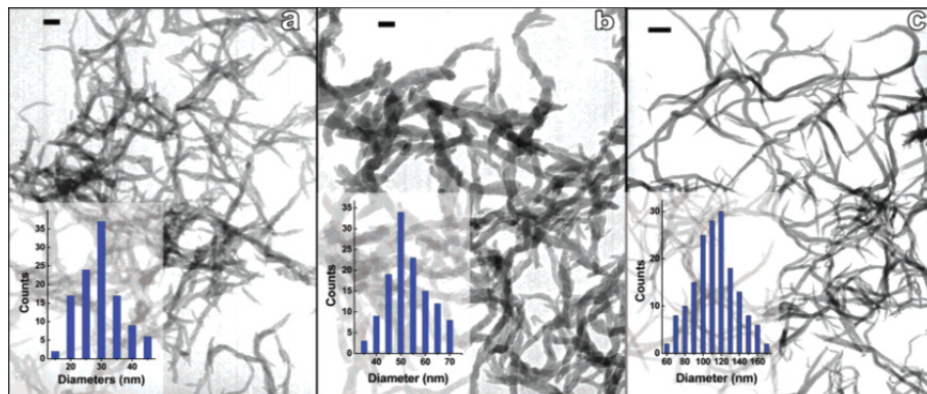
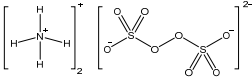
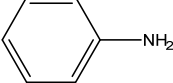
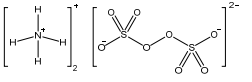
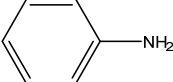
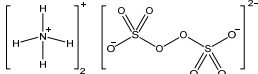
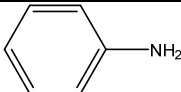


Figure 1-10. Transmission electron microscopy images of polyaniline nanofibers made by using (a) HCl (scale bar 100 nm), (b) camphorsulfonic acid (scale bar 100 nm), and (c) HClO₄ (scale bar 1 μm). The insets show the diameter distributions (nm) of the doped nanofibers (scale bars 500 nm)¹⁴⁵ Copyright 2004. Adapted with permission from the American Chemical Society.

Table 1-9 shows the precursors, synthesis conditions and applications of polyaniline prepared via interfacial polymerization. Most research on polyaniline synthesis is focused on the synthesis of nanofibers and other nanostructures. The nanofibers are preferred over solid thin film because of the increased surface area that allows for larger electrochemical response of the polymer. The nanofibers can either be coated from solution, or be grown directly on a solid interface that is placed at the interface.³²⁸ The reaction conditions influence the morphology of the polyaniline nanostructures.³³⁶ The type of structure that is obtained depends on the organic solvents, acid dopants, concentration of dopants, the reaction time, and the concentration of aniline monomer and oxidant. For example, the length of polyaniline nanofibers was found to increase with acid strength).³³⁷ A great variety of dopant acids can be used, including hydrochloric, sulfuric, nitric, phosphoric, perchloric, acetic, formic, tartaric, camphorsulfonic, methylsulfonic, ethylsulfonic, or 4-toluenesulfonic acid.

Table 1-9. Precursors used for polyanilines prepared via interfacial polymerization, the reaction conditions, and their applications. In bold: the reactant names, method of interfacial polymerization, reaction time and temperature and final polymer configuration.

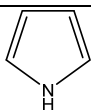
Aq. phase reactant	Org. phase reactant	Reaction conditions	Application	Ref
 <p>Ammonium peroxydisulfate in dopant acid solution (0.001 to 2.0 M). Aniline: Ammonium peroxydisulfate was kept at 4:1</p>	 <p>Aniline (0.032 to 0.32 M) in an organic phase such as hexane, benzene, toluene, xylene, diethyl ether, carbon disulfide, carbon tetrachloride, chloroform, o-dichlorobenzene, or methylene chloride.</p>	<p>Polyaniline was formed at the interface of ammonium peroxydisulfate solution in water and aniline solution in an organic phase. Excess acid and byproducts were removed by either dialysis or filtration. Doped nanofibers were obtained by dialyzing or washing with water; dedoped nanofibers were obtained by dialyzing or washing with 1 M NH₃·H₂O.</p>	<p>Polyaniline nanofibers with lengths in the range of 500 nm to several micrometers. Fiber diameters around 30-120 nm. Sensor applications, for detection of acid, base or redox active chemicals. Emeraldine salt-base switchable conductivity. BET surface area (around 50 m² g⁻¹).</p>	<p>145, 327, 331, 338</p>
 <p>Ammonium peroxydisulfate (0.009 mol L⁻¹) in 1 M HCl. H₂O₂ can be used as alternative oxidizer, but requires longer reaction times (days)</p>	 <p>Aniline (0.2 M) in chloroform with 0.01 M sodium dodecyl sulfate (SDS).</p>	<p>Interfacial chemical oxidation was performed using three immiscible liquids. The lowest section contained an aniline in chloroform solution, the middle layer the ammonium peroxydisulfate solution in HCl solution and the upper layer contained 5 ml of toluene which</p>	<p>Electro-active polyaniline membrane that exhibits redox behavior similar to conventional electro-deposited polyaniline.</p>	<p>325</p>

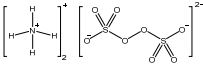
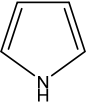
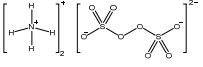
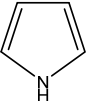
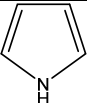
		slowly solubilizes both the ammonium peroxydisulfate and the HCl and quenches the reaction.		
 <p>Ammonium peroxydisulfate (0.01-0.4 M) in 0.5-2 M H₂SO₄, HCl, H₃PO₄, HClO₄,</p>	 <p>Aniline (0.1 M) in toluene, benzene, n-hexane, n-hexanol, carbon tetrachloride, or chloroform</p>	<p>Polyaniline was formed at the interface of ammonium peroxydisulfate solution in water and aniline solution in an organic phase. Polyaniline was removed from the interface by filtration. The reaction time varied from 1-12 h.</p>	<p>Polyaniline nanofibers for immobilization and direct electrochemistry of glucose oxidase (GOx).</p>	336

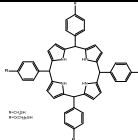
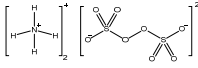
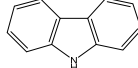
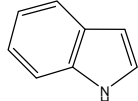
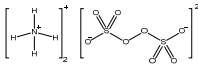
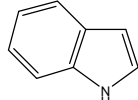
Other conducting polymers

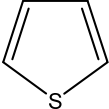
Polyaniline analogues have been prepared via interfacial polymerization in a comparable manner. Table 1-10 shows the precursors used for the synthesis of polyaniline analogues such as polypyrroles, polyindoles, polyphyrins, and polycarbazoles. The oxidant that is used in the aq. phase is commonly either ferric chloride or ammonium peroxydisulfate.

Table 1-10. Precursors used for other conducting polymers such as polypyrrole, polyindole, polyphyrin and polycarbazole prepared via interfacial polymerization, the reaction conditions, and their applications. In bold: the reactant names, method of interfacial polymerization, reaction time and temperature and final polymer configuration.

Aq. phase reactant	Org. phase reactant	Reaction conditions	Application	Ref
<p>Ferrous chloride (FeCl₂, 0.4 M) and ferric chloride (FeCl₃, 0.5M) in water.</p>	 <p>Pyrrole in hexane</p>	<p>Pyrrole in hexane was slowly added to the aq. solution of ferrous and ferric chloride. After removal of the layer by a glass slide, the polypyrrole film was washed with methanol to remove excess reagents. A</p>	<p>Polypyrrole-PDMS membranes for gas separation applications. (polypyrrole layer thickness of around 200 nm) Low</p>	339

		solution of PDMS in hexane was poured over the surface and left to evaporate for 24 h and treated at 80 °C for 15 min.	polymerization rates resulted in denser membranes. O ₂ /N ₂ selectivity of 17 and O ₂ permeability of 40 barrer.	
<p>Ferric chloride (FeCl₃, 3 mM) or</p>  <p>Ammonium peroxydisulphate (3 mM) in water with Tween80 or Span80 (0 or 2 g L⁻¹) surfactants</p>	 <p>Pyrrole (2mM) in chloroform</p>	Free-standing polypyrrole was prepared by quickly adding the pyrrole solution in chloroform to the aq. solution of ferric chloride or ammonium peroxydisulphate at 25 or 0 °C. After 8 h reaction time, the polypyrrole was collected by filtration and washing with water and ethanol. Finally, the free-standing films were dried at 60 °C for 12 h under vacuum.	Free-standing polypyrrole films for electrochemical capacitors. Polypyrrole prepared using Tween80 was highly porous. Polypyrrole prepared using Span80 are vesicular.	340
 <p>Ammonium peroxydisulphate (200 g L⁻¹) in water with sodium dodecyl benzene sulfonate (SDBS, 0-100 g L⁻¹) as surfactant.</p>	 <p>Pyrrole (0.1-0.4 v.%) in toluene</p>	Pyrrole nanocapsules were prepared by adding the pyrrole in toluene to an aq. SDBS solution, while stirring at 0 °C. Next, the aq. solution of ammonium peroxydisulphate was added and the mixture was stirred at 400 rpm for 24 h . Finally, the pyrrole nanocapsules were filtered and washed by water and ethanol.	Polypyrrole nanocapsule synthesis. Capsule diameter in the range of 100-200 nm.	341
<p>Ferric nitrate (Fe(NO₃)₃, 2.0 M) in water.</p>	 <p>Pyrrole, thiophene, N-methylpyrrole, aniline. (vapor phase)</p>	Polypyrrole is formed at the surface of an hydrophobized, anodisc support membrane. The aq. solution is contacted with the membrane surface. The monomer vapor is supplied on the other side, resulting in layer formation.	Membrane gas separation applications combined with switchable polymer conductivity. Doping with HNO ₃ results in porous films with Knudsen selectivity. Undoped films have a permeability of 6.9 barrer and a CO ₂ /CH ₄ selectivity of 32.	324

<p>Copper acetate, silver nitrate or mercury acetate as oxidant in water.</p>	 <p>5,10,15,20-tetrakis (r-mercapto p-tolyl) porphyrin (0.3 mM) in chloroform</p>	<p>The aq. copper acetate solution was added to the mercaptopyrin solution in chloroform. The solution was covered to prevent any solvent evaporation. Film formation at room temperature occurred within several hours. Silver nitrate or mercury acetate resulted in the formation of a slurry at the interface. Thiol-free porphyrins did not show any film formation.</p>	<p>Robust, free-standing polyphyrin films with thicknesses in the range 10 nm to 10 μm The highly-absorbing, shiny, purple polymer layers are amorphous and retain their ability to be metalated. Catalytic activity by photosensitized oxidation of a cyclic thioether.</p>	<p>342</p>
 <p>Ammonium peroxydisulphate (1.2 M) in HCl (0.5 M)</p>	 <p>Carbazole (60 mM) in dichloromet hane (DCM).</p>	<p>Polycarbazole was prepared by adding an aq. ammonium peroxydisulphate solution to the carbazole solution in DCM at room temperature. The optimum yield was 50% in 12 h time period.</p>	<p>Polycarbazole hollow microspheres with diameters around 3–5.5 μm and wall thickness of about 0.82 μm.</p>	<p>343</p>
<p>Chloroauric acid (HAuCl₄, 15.7 g L⁻¹) in water with HCl (0.5 M).</p>	 <p>Indole (10 g L⁻¹) in dichloromet hane (DCM)</p>	<p>Polyindole was prepared by slowly adding an aq. HAuCl₄ solution to the indole solution in DCM. The polyindole was collected by centrifugation</p>	<p>Rod-like, semi-crystalline polyindole-Au nanocomposites for application in electronic devices. The gold nanoparticles are uniformly distributed in the polymer. The polymer displayed switchable photoluminescence.</p>	<p>344, 345</p>
 <p>Ammonium peroxydisulphate in water with 10 mM CTAB</p>	 <p>Indole in chloroform</p>	<p>Polyindole nanocapsules were prepared by adding 0.35 g indole monomer to 30 mL of CTAB in water and stirring for 30 min. Then 0.68 g Ammonium peroxydisulphate in 30 mL water was added dropwise. After 24 h reaction time at room temperature, the</p>	<p>Polyindole nanocapsules with capsule diameters in the range of 1-3 μm for electrochemical applications. The morphology and the electrochemical activity changed upon</p>	<p>346</p>

		polyindole was filtered and washed with ethyl alcohol and water. Finally, it was dried under vacuum at 40 °C for 48 h. Alternatively, Ammonium peroxydisulphate in water was added dropwise to an indole solution in chloroform.	addition of a surfactant.	
Ferric chloride (FeCl ₃ , 0.525 M) in nitromethane or acetonitrile.	 <p>Thiophene (0.5 M) in hexane</p>	Polthiophene microparticles were prepared by dropwise addition of a ferric chloride solution in nitromethane or acetonitrile to thiophene in hexane, while stirring at 20 °C for 24 h . The polythiophene particles were separated from the liquid by centrifugation and washing in ethanol. Finally, the powder was dried at 50 °C for 24 h.	Polythiophene microparticles with diameters between 2.67-3.95 μm. Electrical conductivity of the polythiophene microparticles increases with reducing oxidant/monomer ratio, polymerization temperature, and the monomer concentration.	³⁴⁷

Composites

The conductive properties of conductive polymers such as polyaniline can be significantly improved by addition of nanoparticles. Examples include carbon nanotubes,^{345, 348-350} C60,^{351, 352} gold nanoparticles,^{344, 353} manganese oxide,³⁴⁶ and graphene.^{349, 354, 355} The dimensions of the polymer and metal domains of are controlled by the reaction conditions, with polymer dimensions of 50-180 nm and particle dimensions of 10-140 nm. In addition, polyelectrolytes such as poly(acrylic acid),³⁵⁶ poly(vinylsulfonate),³⁵⁷ and poly(sodium 4-styrene sulfonate)³⁵⁸ have been added to the conductive polymer matrix.

Outlook

Conductive polymers such as polyaniline have promising properties for electrochemical applications in for example electrochemical conversion and sensors. Interfacial polymerization allows for synthesis of high surface areas of conductive polymer nanostructures or membrane layers with electrochemical properties. Relevant reaction conditions for polymer formation have been studied in detail. Future research on conductive polymers prepared via

interfacial polymerization might focus on composites and covalent attachment of the polymers to a substrate or layer.

1.5.7. ZIFs and MOFs

ZIF and MOF chemistry

metal organic frameworks (MOFs) and Zeolite imidazolate frameworks (ZIFs) consist of coordination metals that are covalently bound with organic ligands. The large variety of organic ligands that can be used for the synthesis allows for tailoring of the MOF and ZIF properties.³⁵⁹ Layers of MOFs and ZIFs are commonly prepared by seeding of pre-synthesized crystals on top of a porous support, followed by a secondary growth step in a precursor solution.^{360, 361} The seeding step is required to create the interface on which crystal growth predominantly occurs. In this way, crystal growth can be directed to obtain suitable materials performance. The synthesis route allows for uniform film formation with layer thicknesses in the range of several μm , suitable for membrane applications such as gas and vapor separation.³⁶² Crystal defect formation inherently occurs, due to diffusion limitations of the crystal precursors molecules in inter-crystalline gaps that have a smaller size than the precursor. Membrane application of seeded MOF layers is limited by large penalty in selectivity due to inter-crystalline defects and by low permeance due to the relatively large thicknesses. Alternative synthesis routes that employ exfoliated MOF nanosheets have successfully been applied to decrease layer thicknesses to the nanometer range.³⁶³ However, the complex fabrication route of the exfoliated nanosheets and the limited yield of nanosheets of sufficient quality hamper large-scale implementation of these synthesis routes.

More recently, metal organic frameworks have been prepared in a single step via interfacial polymerization. By confining the crystal growth to a liquid-liquid interface, pre-seeding is no longer required. In addition, film formation limits the reactant diffusion, allowing for uniform film growth of layers with thicknesses around $\sim 2 \mu\text{m}$. The relatively large film thickness is required to obtain sufficiently large crystal sizes for a defect layer formation. **Figure 1-11** shows scanning electron micrographs of the MOF and ZIF layers prepared via interfacial polymerization. Although the common precursors used for MOF and ZIF synthesis are more soluble in polar solvents, a number of reagents can be dissolved in apolar solvents. Currently, either a solvent with some degree of polarity (i.e., octanol) or the addition of a co-solvent is employed to obtain

sufficiently high precursor solubilities, while preserving the stable liquid interface.

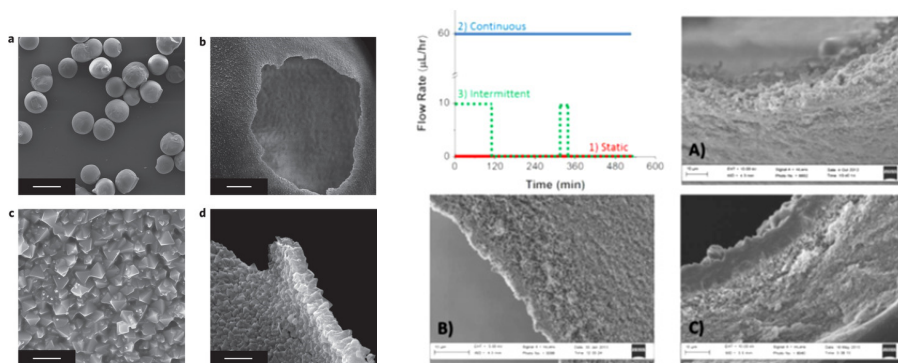
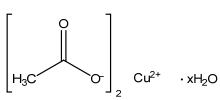
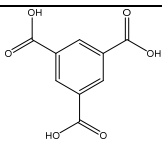
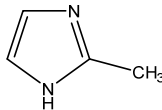
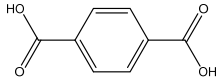
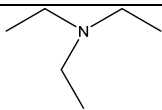


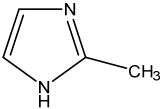
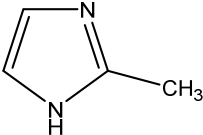
Figure 1-11. Left panels: (a) Overview of several MOF capsules illustrating their monodispersity. The capsules retain their spherical shape upon drying. Scale bar, 500 μm . (b) MOF capsule crushed with a needle tip showing its hollow interior. Scale bar, 25 μm . (c) Detail of the defect-free capsule wall. Gaps between larger crystals are sealed by intergrown smaller crystals. Scale bar, 2 μm . (d) Cross-sectional view of the capsule wall, showing its thin and uniform thickness. Scale bar, 2 μm .¹⁹¹ Copyright 2011. Adapted with permission from the Nature Publishing Group. Right panels: Bore flow rate profiles used to synthesize ZIF-8 membranes on the inner surface of Torlon hollow fibers. (A) Static growth, with a $\text{Zn}^{2+}/\text{H}_2\text{O}$ bore solution and 2-methylimidazole/octanol shell solution, produced discontinuous coatings of particles at the fiber surface on the bore side. (B) A thin, continuous ZIF-8 membrane of $\sim 2 \mu\text{m}$ thickness was obtained via growth under continuous bore flow of $60 \mu\text{L h}^{-1}$. (C) A flow profile consisting of an initial continuous flow process followed by a static growth interrupted by a reactant replenishment step, led to a ZIF-8 membrane of $\sim 9 \mu\text{m}$ thickness.³⁶⁴ Copyright 2014. Adapted with permission from the American Association for the Advancement of Science.

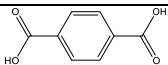
The film growth direction is predominantly towards the aqueous side, because most organic phase precursors solubilize well in the aqueous phase. Table 1-11 shows an overview of the reactants that are used for ZIF and MOF synthesis via interfacial polymerization. Both hollow capsules and supported layers have been prepared. The reaction times are usually in the range of several hours, because the precursor reactivity is not as high as in conventional interfacial polymerization syntheses. Catalysts such as tertiary amines are employed to improve the reactivity.¹⁹¹ To obtain sufficient film formation that limits the

reactant diffusion to the opposite phase, much higher monomer concentrations are used as compared to for example polyamide synthesis.

Table 1-11. Precursors used for ZIFs and MOFs prepared via interfacial polymerization, the reaction conditions, and their applications. In bold: the reactant names, method of interfacial polymerization, reaction time and temperature and final polymer configuration.

Aq. phase reactant	Org. phase reactant	Reaction conditions	Application	Reference
 <p>Copper acetate (7.2 g) in 100 g water with 1-4 wt.% polyvinyl alcohol (PVA, 98% hydrolysed; M_w, 13,000–23,000). Up to 20 % ethanol was added for the preparation of hollow capsules.</p> <p>Zinc nitrate ($ZnNO_3 \cdot H_2O$, g L⁻¹) in water.</p>	 <p>1,3,5-Benzene tricarboxylic acid (1.765 wt.%) in 1-octanol.</p>  <p>2-Methyl imidazole in 1-octanol.</p>	<p>$Cu_3(BTC)_2$ was prepared from a copper acetate in aq. PVA solution and 1,3,5-benzenetricarboxylic acid in 1-octanol. Cupric oxide particles were removed by centrifugation prior to reaction. ZIF-8 was prepared from a solution of 2-methylimidazole in 1-octanol and zinc nitrate in water. Film growth was obtained by leaving the interface to stand. Capsules were prepared from an emulsion prepared in a microchannel.</p>	<p>Membrane nanofiltration applications. $Cu_3(BTC)_2$ MOF membrane showed dye retention (Rose Bengal). Capsules were used as carriers for the dye, and showed no leaching over time. Upon capsule breakage, the dye could be released.</p>	191
<p>Zinc nitrate ($ZnNO_3 \cdot H_2O$, 0.05-0.4 M) in dimethyl formamide</p>  <p>1,4-Benzene dicarboxylic acid (TPA,) in hexane. The molar ratio of $Zn(NO_3)_2 \cdot 6H_2O$ to TPA was kept</p>	 <p>Trimethyl amine (TEA) in hexane.</p>	<p>MOF layers were prepared by adding TEA in hexane to zinc nitrate and TPA in DMF. Reaction times of 5 min to 10 h were used. Membranes were collected by a circle-shaped copper wire. Particles were filtered and washed with DMF membranes, because it caused curving in DMF. Both membrane and particle products were dried in vacuum at 70 °C for 12 h.</p>	<p>Depending on the precursor and catalyst concentrations, microparticles or membranes were obtained. Estimated Langmuir surface areas were 709 m² g⁻¹ for the membrane and 2115 m² g⁻¹ for the particles, measured with liquid N₂. No sorption hysteresis</p>	365

constant at 2.			was observed.	
<p>Zinc nitrate ($\text{ZnNO}_3 \cdot \text{H}_2\text{O}$, 15 g L^{-1}) in water.</p>	 <p>2-Methylimidazole (16.24 g L^{-1}) in hexane + ethanol as co-solvent.</p>	<p>PES membrane support was impregnated with an aq. zinc nitrate overnight. Excess liquid was removed from the support surface using a rubber wiper. Next, 2-methylimidazole in hexane was gently poured on the surface. The solution was drained off after a 1 h reaction time. The membranes were finally post-treated overnight at $100 \text{ }^\circ\text{C}$.</p>	<p>Membrane nanofiltration applications. Retention of dye (rose bengal) in water ($> 92.5\%$), ethanol ($> 50\%$) and isopropyl alcohol ($>80\%$) was observed. Permeances of water ($1.3\text{-}5.0 \text{ kg m}^{-2} \text{ h}^{-1} \text{ bar}^{-1}$), ethanol ($1.1\text{-}6.6 \text{ kg m}^{-2} \text{ h}^{-1} \text{ bar}^{-1}$) and isopropyl alcohol ($0.3\text{-}1.9 \text{ kg m}^{-2} \text{ h}^{-1} \text{ bar}^{-1}$).</p>	3 6 6
 <p>2-Methylimidazole (mIm, 0.018 M) in water</p>	<p>Zinc nitrate ($\text{ZnNO}_3 \cdot \text{H}_2\text{O}$ 1.37 M) in 1-octanol</p>	<p>A Torlon hollow fiber, with flow of the zinc nitrate in octanol solution through the bore, was immersed in the aq. mM solution. The aqueous shell solution was stirred at 60 rpm and reacted for 120 min with 30 min with continuous bore solution flow. Another 3.5 h static growth was applied, followed by another 20 min flow through the bore and a final 3.5 h growth step. Reactants were removed with neat octanol on the bore side and water at the shell side. Methanol (shell side), heptane and hexane (bore side) were used to exchange solvents before evaporation. Shell and bore side liquids and flow rates were exchanged in alternative synthesis cases. PDMS sealing was used to repair defects in the</p>	<p>Membrane gas separation applications. H_2 permeances of around 800 GPU and $\text{H}_2/\text{C}_3\text{H}_6$ separation factors above 200 and $\text{C}_3\text{H}_6/\text{C}_3\text{H}_8$ separation factors above 8 at temperatures from $25\text{-}125 \text{ }^\circ\text{C}$.</p>	3 6 4

		crystals.		
Copper nitrate (Cu(NO ₃) ₂) in N,N-dimethyl formamide (DMF)	 1,4-Benzenedicarboxylic acid in N,N-dimethyl formamide (DMF)	The solution of Cu(NO ₃) ₂ (top) and of 1,4-benzenedicarboxylic acid (bottom) are separated by an intermediate solvent layer. Diffusion of Cu ²⁺ cations and 1,4-benzenedicarboxylic acid precursors into the middle phase causes slow growth of the MOF crystals. No immiscible liquid phases are involved, and it is therefore technically no interfacial polymerization. Nonetheless, the reactants are separated by means of a multiphase system.	Membrane gas separation applications. The separation of CO ₂ from CO ₂ /CH ₄ mixtures by addition of the MOF nanosheets to a polyimide. The composites showed improved selectivity towards CO ₂ .	3 6 7

Outlook

ZIFs and MOFs represent a class of materials with great potential for sorption and membrane separation processes. The development of facile interfacial polymerization procedures for the synthesis of layers and hollow capsules can potentially bring the large-scale application of MOFs a step closer. Further development of growth protocols, variation of the monomer reactants and catalysts that improve the reaction rate might open up possibilities to obtain sub- μm layer thicknesses and synthesis time. For example, pre-seeded crystals that assemble at the liquid-liquid interface can potentially be used to aid defect-free film formation. In addition, excellent work on the controlled growth of MOF nanosheets by separating the reactants by a third interface has been presented.³⁶⁷ Although the reaction occurs in a diffuse reaction zone instead of at the interface, and therefore it is technically no interfacial polymerization, the diffusion limitations of the multiphase system aid in control over the MOF crystal growth.

1.5.8. Polysiloxanes

Polysiloxane chemistry

Polysiloxanes are a class of materials that consist of a Si-O-Si backbone and are characterized by a good thermal and chemical stability. Polysiloxanes are conventionally prepared by sol-gel synthesis. The sol-gel route employs

silanol precursors, which are commonly alkoxy silanes. The alkoxy groups hydrolyse in the presence of water to form silanol groups. Subsequent condensation of the silanol groups leads to the formation of siloxane bonds. The sol—gel route owes its success to the relatively mild reaction conditions and the good control over the colloid size and degree of branching. By controlling the temperature, pH and water concentration during sol preparation, both very dense and very porous polysiloxanes can be obtained.³⁶⁸

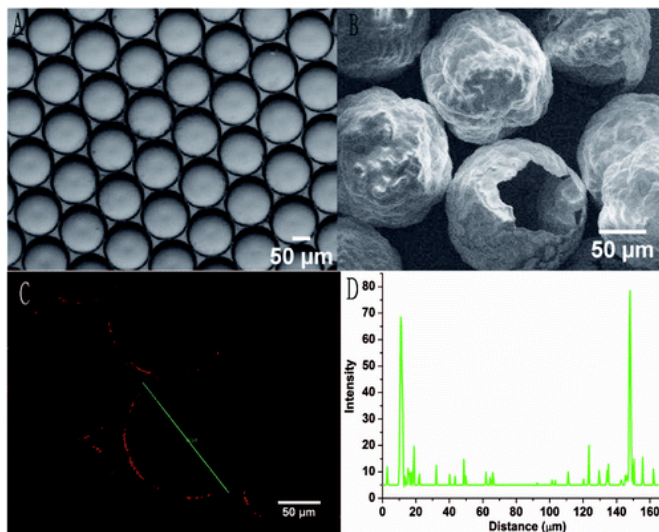
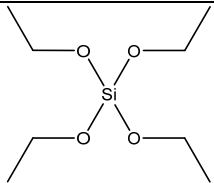
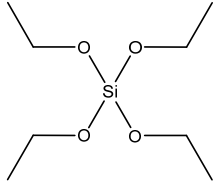


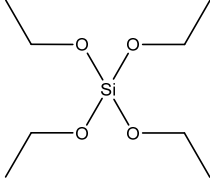
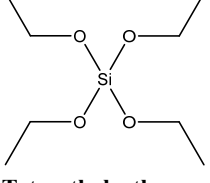
Figure 1-12. (A) Uniform droplets generated by microfluidic device. (B) Scanning electron micrograph of the as-synthesized hollow microspheres. (C) Confocal microscopy image of silica shells embedded with carboxytetramethylrhodamine. (D) Profile of luminescence intensity in a single microsphere.³⁷¹ Copyright 2010. Adapted with permission from the American Chemical Society

Sol—gel can be combined with interfacial polymerization by dissolving the alkoxy silane in an organic phase. The aqueous phase provides the interface at which hydrolysis and condensation occurs, and acts as reagent for the polymerization. This approach is mainly employed to synthesize hollow silica nano- or microspheres, although planar layers have been prepared in the past.^{369, 370} **Figure 1-12** shows an example of silica microspheres that are synthesized from uniform droplets generated by a microfluidic device. The fluorescent marker embedded in the shell could be used to carefully determine the shell diameter.

Table 1-12 shows an overview of the precursors that are used for the preparation of polysiloxanes. The alkoxy silane precursor, often tetraethoxysilane (TEOS), is dissolved in an organic phase such as hexane. Alkoxy silane hydrolysis occurs at the interface, in contact with a base or acid solution in water. The subsequent condensation does not require water as reactant, but is still more likely to occur at the interface due to the higher condensation rate in acid or base conditions.

Table 1-12. Precursors used for polysiloxanes prepared via interfacial polymerization, the reaction conditions, and their applications. In bold: the reactant names, method of interfacial polymerization, reaction time and temperature and final polymer configuration.

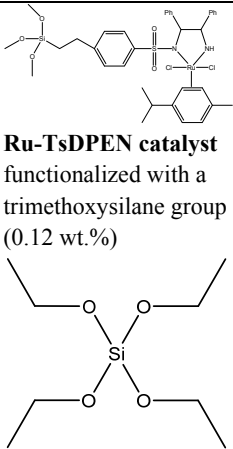
Aq. phase reactant	Org. phase reactant	Reaction Conditions	Application	Ref.
<p>Water (13.9 g) with pH adjusted to 4. A surfactant was added for emulsification : Tween 80, Triton X-100, Brij 78, SDS, Pluronic P123, Reax 88B, or Reax 88A.</p>	 <p>Tetraethylortho silicate (TEOS, 3.25–5.25 g) in 1.5–3.75 g 1-butyl-3-methylimidazolium hexafluorophosphate (ionic liquid, BMIm-PF6)</p>	<p>Silica capsules filled with ionic liquid were prepared by emulsification of BMIm-PF6 in water using a surfactant. Next, TEOS was added dropwise and the mixture was stirred for 12 h. Finally, the silica microcapsules were isolated and washed by centrifugation.</p>	<p>Entrapment of ionic liquid in hollow silica capsules. In addition, palladium catalysts is coated onto the ionic liquid filled capsules for the hydrogenation of alkynes. Reax 88A was the only surfactant that resulted in capsule formation.</p>	372
<p>Water, adjusted to the correct pH using ammonium hydroxide or sodium hydroxide</p>	 <p>Tetraethylortho silicate (TEOS, 0.5–2.5 ml) With Tegopren 7008 (1.0 v.%) as surfactant.</p>	<p>Water was added to Tegopren 7008 solution in hexadecane and emulsified at 3000 rpm stirring for 30 min at 20 °C). Next, TEOS (0.5–2.5 ml) was added and mixed for 5 min. Particles were left to form for 1-24 h reaction time.</p>	<p>Hollow silica capsules for holding a liquid core. More robust shells were found at higher TEOS concentrations. Continued inward growth of the shell was observed at high TEOS</p>	146

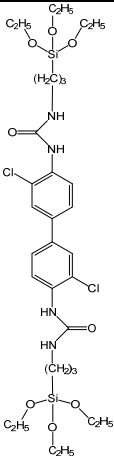
<p>Water, with 2.0 M HCl . Added to water with 0.5 wt.% PEO27-PPO61-PEO27 surfactant</p>	 <p>Tetraethylorthosilicate (TEOS, 30 g) in 30 g n-octadecane.</p>	<p>An oil-in-water emulsion was formed by dropping the TEOS solution into 300 ml aq. surfactant solution at 3000 rpm stirring for 30 min. Next, the aq. HCl solution was added dropwise at 500 rpm stirring. The reaction was continued at continued stirring at 35 °C for 48 h to. The capsules were filtered, washed by ethanol in water (30 wt.%) and dried in an oven at 50 °C for 24 h.</p>	<p>concentrations.</p> <p>Hollow silica capsules for holding phase change materials (n-octadecane). At pH 2.89, compact silica capsules with fairly smooth surface and mean particle size of 17.0 μm were obtained.</p>	<p>373</p>
<p>Water, adjusted to pH 11 with ammonia (28%) and HCl. Added to water with cetyltrimethyl ammonium bromide (CTAB, in 2 mL water and 2 mL ethanol) surfactant.</p>	 <p>Tetraethylorthosilicate. (TEOS, 160 μL and 108 μL of 100 μM ([5-(and-6)-Carboxytetramethyl rhodamine] in 2 mL carrier oil (DC 5225C, 40 wt.%) Formulation Aid (DC 749 Fluid, 30 wt.%) Ar20 Silicone Oil (30 wt.%)</p>	<p>The two phases were supplied to microchannels using syringe pumps. The droplets collected were kept at 35°C for 24 h to form hollow silica microspheres. The final products were washed with isopropanol and acetone.</p>	<p>Hollow silica capsules filled with ethylbutyrate for the extraction of iodine. Shell thickness 500 nm and 130 μm diameter. The microsphere morphology could be varied from totally hollow to partly solid by either increasing the TEOS or decreasing the CTAB concentrations.</p>	<p>371</p>
<p>Water with pH ranging from 1-13 Acid: HCl, HNO₃, acetic acid, formic acid, citric acid Base: NaOH and ammonia</p>	<p>Ethyl Silicate 40, (E-40, 0.27 M) in hexane</p>	<p>Acid and base catalyzed sol—gel at the liquid-liquid interface. The reaction was performed at 24 h reaction time, followed by 24 h drying at 30 °C and 24 h at 60 °C. Finally, the layers were calcined for 2 h at 400 °C.</p>	<p>Silica layers for optical devices such as multiplexers. The film growth rate and density depends on the type of catalyst. Crack-free 1-20 μm thick films could be formed.</p>	<p>369, 370, 374</p>

Hybrid inorganic-organic

Although hybrid inorganic-organic materials are fairly common in sol–gel science, only a few examples of silica-based hybrid materials have been prepared by sol–gel combined with interfacial polymerization. **Table 1-13** shows the precursors that are used for hybrid inorganic-organic polysiloxanes, the reaction conditions and their applications. Covalent attachment of a catalyst in the porous surface of microcapsules allowed for large-surface areas of catalytically active hollow capsules. By tuning the properties of such materials, selective transport and catalysis could be combined in a single system.

Table 1-13. Precursors used for hybrid inorganic-organic polysiloxanes prepared via interfacial polymerization, the reaction conditions, and their applications. In bold: the reactant names, method of interfacial polymerization, reaction time and temperature and final polymer configuration.

Aq. phase reactant	Org. phase reactant	Reaction Conditions	Application	Ref.
<p>Water with cetyltrimethyl ammonium chloride (CTAC, 8.7 wt.%)</p>	 <p>Ru-TsDPEN catalyst functionalized with a trimethoxysilane group (0.12 wt.%)</p> <p>Tetraethylortho silicate (TEOS, 30 wt.%) in chloroform</p>	<p>The microcapsules were prepared by emulsification of an aq. CTAC solution to a solution of TEOS and the silyl functionalized Ru-TsDPEN catalyst in chloroform that contains hydrophobic magnetic nanoparticles. The mixture was stirred at 10,000 rpm for 4 min and left to react for 24 h while stirring mechanically. The microcapsules were separated by using an external magnetic field and washed with water.</p>	<p>Silica microcapsules with catalytic activity for the asymmetric transfer hydrogenation of ketones. The ruthenium catalyst loading was 12 $\mu\text{mol g}^{-1}$.</p>	375

<p>Water with sodium hydroxide (NaOH, 0.1 M) or hydrochloric acid (HCl, 0.01 mol/L) solution in water.</p>	 <p>3,30-Dichloro-biphenylene-bridged precursor (DPBS, 0.09 mmol) in toluene.</p>	<p>DPBS in toluene was slowly added to an aq. acidic or alkaline solution. The formed solid was washed with water and ethanol, and then dried in vacuum. Dichloro-biphenylene-bridged silsesquioxanes was also prepared under an acid condition with a similar procedure, using a dilute sodium hydroxide solution.</p>	<p>Synthesis of a layered structure of biphenylene-bridged silsesquioxanes. The material shows some well-ordered features with lamellar spacing in the range of 0.25-0.30 nm.</p>	<p>³⁷⁶</p>
---	---	---	---	-----------------------

Outlook

Polysiloxanes can be readily prepared by performing sol—gel synthesis at the interface of two liquids. Although most research focused on hollow capsule synthesis,^{371, 373} formation of free-standing or supported polysiloxane layers is well possible.^{369, 370, 374} Although the number of hybrid inorganic-organic polysiloxanes prepared via interfacial polymerization is minor, there are countless options for hybrid precursors available from the well-developed field of sol—gel chemistry.

1.6. Conclusions and future outlook

In conclusion, the library of monomer precursors that are used for interfacial polymerization is expanding rapidly. The technique has proven to be useful for polymer synthesis with high surface areas of ultrathin layers on top of porous supports or nanosized structures such as fibers and capsules. The monomer reactants are generally highly reactive, but recent developments in polysiloxane and MOF layer synthesis show that smooth layer formation is even possible at lower reaction rates. Moreover, monomer reactivity does not necessarily limit the choice in reactants; reactions mediated by (homogeneous) catalysts, strong oxidizing agents and radicals can be combined readily with interfacial polymerization. The main limitation of the technique lies in the use of two immiscible solvents. The incompatibility of the solvent implicates that each of the reactants should be compatible with at least one of the phases. In

addition, the large quantities of solvents that are required for synthesis involves purification and re-usage. Therefore, libraries of suitable precursors and fundamental knowledge on the role of synthesis parameters on material properties are crucial to future developments of interfacial polymerization based synthesis.

There are still many unexplored directions for the synthesis of low dimensional, large surface area structures via interfacial polymerization. More and more novel hybrid bio-organic and hybrid inorganic-organic layers are being presented in recent literature. In addition, composite materials can be obtained by assembly of nano- or micro-sized particles at the interface during interfacial polymerization, or by co-polymerization of a second component (e.g., the combined interfacial synthesis of a polyamide by polycondensation and silica synthesis via sol—gel). Such hybrid and composite materials allow for design of materials that display unique, synergistic properties. In membranes, hybrid materials are already used to build in additional rigidity and affinity groups. The performance of conducting polymers can be greatly improved by adding for example graphene nanosheets. Polyurethane capsules can be made stimuli-responsive by incorporating magnetic nanoparticles or light sensitive components. Interfacial polymerization allows us to focus all these material property combinations to the confined lateral dimensions of an interface.

1.7. Acknowledgements

This project has received funding from the European Union's Seventh Framework Programme for research, technological development and demonstration under CARENA grant agreement no. 263007. This is, in part, a project of the Dutch Institute for Sustainable Process Technology (ISPT).

1.8. Thesis outline

In this thesis, novel hybrid membranes prepared by interfacial polymerization are described. The outline of this thesis is schematically represented by the flowchart in **Figure 1-13**.

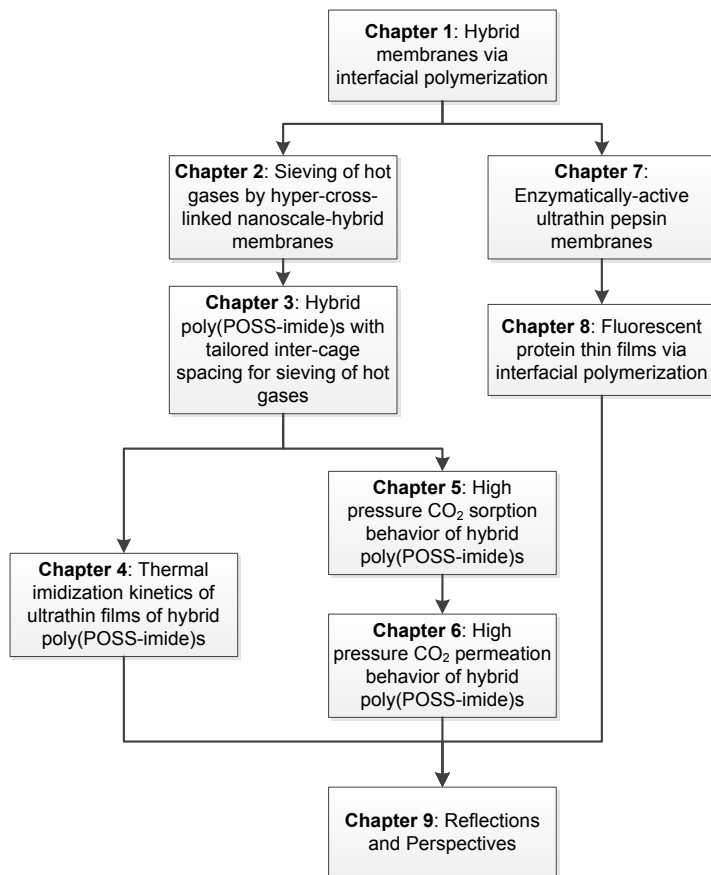


Figure 1-13. Schematic overview of the thesis outline.

Chapter 1 introduces the concept of hyper-cross-linked, hybrid membranes and gives an overview of the current trends in interfacial polymerization. The chapter demonstrates that interfacial polymerization can be used for the synthesis of ultrathin films that consist of a wide range of polymeric, inorganic and biological components. Chapter 1 provides the background for the two main directions of this thesis: hybrid inorganic-organic membranes for gas separation applications (chapters 2-6) and ultrathin biological hybrid films (chapters 7-8)

Chapter 2 reports on the synthesis of ultrathin films of novel hybrid polyhedral oligomeric silsesquioxanes-imides via interfacial polymerization. The nanoscale distribution of POSS and imide moieties is studied by atomic force microscopy. The hyper-cross-linked network characteristics of the hybrid material is used for sieving of hot gases.

Chapter 3 extends the synthesis of poly(POSS-imide)s via interfacial polymerization that is presented in chapter 2 towards other imide bridges. The length and flexibility of the imide groups can be used to tailor the intercage spacing in the hyper-cross-linked network. The gas separation performance at elevated temperatures is studied in relation with the type of imide bridge.

In **Chapter 4**, the heat treatment required for the preparation of the poly(POSS-imides) presented in chapters 2 and 3 are studied. The influence of the length and flexibility of the organic group that connect the POSS-cages on the thermal imidization is determined. Changes in chemical and physical properties are monitored by a combination of thermal analysis techniques.

In **Chapter 5** the sorption behavior of compressed CO₂ and CH₄ in hybrid poly(POSS-imides) is studied. Spectroscopic ellipsometry is used to determine the changes in thickness and refractive index in ultrathin polymer and hybrid network films. The sorbed gas concentrations and apparent molar volumes are estimated from the ellipsometry data.

In **Chapter 6** the high pressure CO₂ sorption and permeation of the hybrid poly(POSS-imide) membranes that are presented in Chapter 5 is studied.

Chapter 7 presents enzymatically-active ultrathin pepsin membranes that are prepared via interfacial polymerization. The ultrathin pepsin films are characterized with respect to enzymatic activity and membrane separation performance.

Chapter 8 continues with the cross-linked protein layer concept that is presented in Chapter 7. Here, fluorescent protein thin films are prepared via interfacial polymerization. The fluorescence recovery after photobleaching and fluorescent activity of the all-protein layers are studied.

Chapter 9 Reflects on all the chapters in this thesis and provides direction for future research on novel membrane materials, analysis of ultrathin membrane films and approaches for preparation of high surface-to-volume ratio membranes configurations for large-scale applications.

1.9. References

1. Baker, R. W., Membrane Technology and Applications. 2012.
2. Khayet, M.; Matsuura, T., Membrane distillation: principles and applications. Elsevier: 2011.
3. Wijmans, J. G.; Baker, R. W. Journal of Membrane Science **1995**, 107, (1-2), 1-21
4. Raharjo, R. D.; Freeman, B. D.; Paul, D. R.; Sarti, G. C.; Sanders, E. S. Journal of Membrane Science **2007**, 306, (1-2), 75-92

5. Raharjo, R. D.; Freeman, B. D.; Sanders, E. S. *Journal of Membrane Science* **2007**, 292, (1-2), 45-61
6. Gales, L.; Mendes, A.; Costa, C. *Journal of Membrane Science* **2002**, 197, (1-2), 211-222
7. Kim, H. J.; Nah, S. S.; Min, B. R. *Advances in Environmental Research* **2002**, 6, (3), 255-264
8. Rebollar-Perez, G.; Carretier, E.; Lesage, N.; Moulin, P. *Membranes* **2011**, 1, (1), 80-90
9. Jiang, X.; Kumar, A. *Journal of Membrane Science* **2006**, 286, (1-2), 285-292
10. Yeom, C. K.; Lee, S. H.; Song, H. Y.; Lee, J. M. *Journal of Membrane Science* **2002**, 205, (1-2), 155-174
11. Ogieglo, W.; Wormeester, H.; Wessling, M.; Benes, N. E. *Polymer (United Kingdom)* **2014**, 55, (7), 1737-1744
12. Ganesh, K.; Nagarajan, R.; Duda, J. L. *Industrial and Engineering Chemistry Research* **1992**, 31, (3), 746-755
13. Jordan, S. S.; Koros, W. J. *Macromolecules* **1995**, 28, (7), 2228-2235
14. Budd, P. M.; Elabas, E. S.; Ghanem, B. S.; Makhseed, S.; McKeown, N. B.; Msayib, K. J.; Tattershall, C. E.; Wang, D. *Advanced Materials* **2004**, 16, (5), 456-459
15. Hashem, M.; Bezzu, C. G.; Kariuki, B. M.; McKeown, N. B. *Polymer Chemistry* **2011**, 2, (10), 2190-2192
16. Budd, P. M.; McKeown, N. B.; Fritsch, D. *Journal of Materials Chemistry* **2005**, 15, (20), 1977-1986
17. Bezzu, C. G.; Carta, M.; Tonkins, A.; Jansen, J. C.; Bernardo, P.; Bazzarelli, F.; McKeown, N. B. *Advanced Materials* **2012**, 24, (44), 5930-5933
18. Nagel, C.; Günther-Schade, K.; Fritsch, D.; Strunskus, T.; Faupel, F. *Macromolecules* **2002**, 35, (6), 2071-2077
19. Park, J. Y.; Paul, D. R. *Journal of Membrane Science* **1997**, 125, (1), 23-39
20. Ree, M.; Kim, K.; Woo, S. H.; Chang, H. *Journal of Applied Physics* **1997**, 81, (2), 698-708
21. Vanherck, K.; Koeckelberghs, G.; Vankelecom, I. F. J. *Progress in Polymer Science* **2013**, 38, (6), 874-896
22. David, O. C.; Gorri, D.; Nijmeijer, K.; Ortiz, I.; Urriaga, A. *Journal of Membrane Science* **2012**, 419-420, 49-56
23. Berchtold, K. A.; Singh, R. P.; Young, J. S.; Dudeck, K. W. *Journal of Membrane Science* **2012**, 415-416, (0), 265-270
24. Rezac, M. E.; Koros, W. J.; Miller, S. J. *Journal of Membrane Science* **1994**, 93, (2), 193-201
25. Rezac, M. E.; Koros, W. J.; Miller, S. J. *Industrial and Engineering Chemistry Research* **1995**, 34, (3), 862-868
26. Duthie, X.; Kentish, S.; Powell, C.; Nagai, K.; Qiao, G.; Stevens, G. *Journal of Membrane Science* **2007**, 294, (1-2), 40-49
27. Wind, J. D.; Sirard, S. M.; Paul, D. R.; Green, P. F.; Johnston, K. P.; Koros, W. J. *Macromolecules* **2003**, 36, (17), 6433-6441
28. Wessling, M.; Schoeman, S.; van der Boomgaard, T.; Smolders, C. A. *Gas Sep. Purif.* **1991**, 5, (4), 222-228

29. Scholes, C. A.; Chen, G. Q.; Stevens, G. W.; Kentish, S. E. *Journal of Membrane Science* **2010**, *346*, (1), 208-214
30. Ogieglo, W.; Wessling, M.; Benes, N. E. *Macromolecules* **2014**, *47*, (11), 3654-3660
31. Vandezande, P.; Gevers, L. E. M.; Vankelecom, I. F. J. *Chem. Soc. Rev.* **2008**, *37*, (2), 365-405
32. Han, S. H.; Misdan, N.; Kim, S.; Doherty, C. M.; Hill, A. J.; Lee, Y. M. *Macromolecules* **2010**, *43*, (18), 7657-7667
33. Han, S. H.; Kwon, H. J.; Kim, K. Y.; Seong, J. G.; Park, C. H.; Kim, S.; Doherty, C. M.; Thornton, A. W.; Hill, A. J.; Lozano, Á. E.; Berchtold, K. A.; Lee, Y. M. *Physical Chemistry Chemical Physics* **2012**, *14*, (13), 4365-4373
34. Sanders, D. F.; Smith, Z. P.; Ribeiro, C. P.; Guo, R.; McGrath, J. E.; Paul, D. R.; Freeman, B. D. *Journal of Membrane Science* **2012**, *409-410*, 232-241
35. Calle, M.; Doherty, C. M.; Hill, A. J.; Lee, Y. M. *Macromolecules* **2013**, *46*, (20), 8179-8189
36. Sarbu, T. T. E. *J. Nature* **2000**, *405*, (6783), 165
37. Consolati, G.; Genco, I.; Pegoraro, M.; Zanderighi, L. *Journal of Polymer Science, Part B: Polymer Physics* **1996**, *34*, (2), 357-367
38. Dorkenoo, K. D.; Pfromm, P. H. *Macromolecules* **2000**, *33*, (10), 3747-3751
39. Punsalan, D.; Koros, W. J. *Journal of Applied Polymer Science* **2005**, *96*, (4), 1115-1121
40. Punsalan, D.; Koros, W. J. *Polymer* **2005**, *46*, (23), 10214-10220
41. Huang, Y.; Paul, D. R. *Journal of Membrane Science* **2004**, *244*, (1-2), 167-178
42. Huang, Y.; Paul, D. R. *Polymer* **2004**, *45*, (25), 8377-8393
43. Huang, Y.; Paul, D. R. *Macromolecules* **2005**, *38*, (24), 10148-10154
44. Huang, Y.; Paul, D. R. *Macromolecules* **2006**, *39*, (4), 1554-1559
45. Cui, L.; Qiu, W.; Paul, D. R.; Koros, W. J. *Polymer* **2011**, *52*, (15), 3374-3380
46. Horn, N. R.; Paul, D. R. *Polymer* **2011**, *52*, (7), 1619-1627
47. Horn, N. R.; Paul, D. R. *Macromolecules* **2012**, *45*, (6), 2820-2834
48. Van Hoof, V.; Dotremont, C.; Buekenhoudt, A. *Sep. Purif. Technol.* **2006**, *48*, (3), 304-309
49. Agirre, I.; Arias, P. L.; Castricum, H. L.; Creatore, M.; ten Elshof, J. E.; Paradis, G. G.; Ngamou, P. H. T.; van Veen, H. M.; Vente, J. F. *Separation and Purification Technology* **2014**, *121*, (0), 2-12
50. Boeltken, T.; Belimov, M.; Pfeifer, P.; Peters, T. A.; Bredesen, R.; Dittmeyer, R. *Chemical Engineering and Processing: Process Intensification* **2013**, *67*, 136-147
51. Peters, T. A.; Stange, M.; Sunding, M. F.; Bredesen, R. *Int. J. Hydrogen Energy* **2015**, *40*, (8), 3497-3505
52. Katz, E.; Willner, I. *Angewandte Chemie International Edition* **2004**, *43*, (45), 6042-6108
53. Vendamme, R.; Onoue, S. Y.; Nakao, A.; Kunitake, T. *Nature Materials* **2006**, *5*, (6), 494-501
54. Zhang, Q.; Yang, W.; Ma, H.; Ma, P.; Xu, Q. *Guangxue Xuebao/Acta Optica Sinica* **2009**, *29*, (6), 1719-1723
55. Ko, Y. G.; Shin, S. S.; Choi, U. S. *Journal of Colloid and Interface Science* **2011**, *361*, (2), 594-602

56. Witte, F.; Bartsch, I.; Willbold, E. *Advances in biochemical engineering/biotechnology* **2012**, 126, 285-296
57. Klok, H. A. *Journal of Polymer Science, Part A: Polymer Chemistry* **2005**, 43, (1), 1-17
58. Dušek, K.; Dušková, M.; Ilavský, M.; Stewart, R.; Kopeček, J. *Biomacromolecules* **2003**, 4, (6), 1818-1826
59. Alcântara, A. C. S.; Aranda, P.; Darder, M.; Ruiz-Hitzky, E. *Journal of Materials Chemistry* **2010**, 20, (42), 9495-9504
60. Descalzo, A. B.; Martínez-Máñez, R.; Sancenón, F.; Hoffmann, K.; Rurack, K. *Angewandte Chemie - International Edition* **2006**, 45, (36), 5924-5948
61. KICKELBICK, G. *Progress in Polymer Science (Oxford)* **2003**, 28, (1), 83-114
62. Moore, T. T.; Koros, W. J. *Journal of Molecular Structure* **2005**, 739, (1-3), 87-98
63. Goh, P. S.; Ismail, A. F.; Sanip, S. M.; Ng, B. C.; Aziz, M. *Separation and Purification Technology* **2011**, 81, (3), 243-264
64. Le, N. L.; Wang, Y.; Chung, T. S. *Journal of Membrane Science* **2011**, 379, (1-2), 174-183
65. Dai, Y.; Johnson, J. R.; Karvan, O.; Sholl, D. S.; Koros, W. J. *Journal of Membrane Science* **2012**, 401-402, 76-82
66. Campbell, J.; Székely, G.; Davies, R. P.; Braddock, D. C.; Livingston, A. G. *Journal of Materials Chemistry A* **2014**, 2, (24), 9260-9271
67. Cordes, D. B.; Lickiss, P. D.; Rataboul, F. *Chemical Reviews* **2010**, 110, (4), 2081-2173
68. Hartmann-Thompson, C., *Applications of Polyhedral Oligomeric Silsesquioxanes*. 2011; Vol. 3.
69. Jeong, B. H.; Hoek, E. M. V.; Yan, Y.; Subramani, A.; Huang, X.; Hurwitz, G.; Ghosh, A. K.; Jawor, A. J. *Membr. Sci.* **2007**, 294, (1-2), 1-7
70. Zou, H.; Wu, S.; Shen, J. *Chemical Reviews* **2008**, 108, (9), 3893-3957
71. Jadav, G. L.; Singh, P. S. J. *Membr. Sci.* **2009**, 328, (1-2), 257-267
72. Kong, C.; Kouchima, A.; Kamada, T.; Shintani, T.; Kanezashi, M.; Yoshioka, T.; Tsuru, T. *Journal of Membrane Science* **2011**, 366, (1-2), 382-388
73. Chhabra, P.; Choudhary, V. *Journal of Applied Polymer Science* **2010**, 118, (5), 3013-3023
74. Choi, J.; Lee, K. M.; Wycisk, R.; Pintauro, P. N.; Mather, P. T. *Journal of the Electrochemical Society* **2010**, 157, (6), B914-B919
75. Kayser, M. J.; Reinholdt, M. X.; Kaliaguine, S. *Journal of Physical Chemistry B* **2010**, 114, (25), 8387-8395
76. Kumar, G. G.; kim, P.; kim, A. r.; Nahm, K. s.; Elizabeth, R. N. *Materials Chemistry and Physics* **2009**, 115, (1), 40-46
77. Joshi, M.; Butola, B. S. *Journal of Macromolecular Science - Polymer Reviews* **2004**, 44, (4), 389-410
78. Kopesky, E. T.; Haddad, T. S.; Cohen, R. E.; McKinley, G. H. *Macromolecules* **2004**, 37, (24), 8992-9004
79. Kopesky, E. T.; McKinley, G. H.; Cohen, R. E. *Polymer* **2006**, 47, (1), 299-309
80. Zhang, Y.; Lee, S.; Yoonessi, M.; Liang, K.; Pittman, C. U. *Polymer* **2006**, 47, (9), 2984-2996

81. Kang, S.; Hong, S. I.; Choe, C. R.; Park, M.; Rim, S.; Kim, J. *Polymer* **2001**, 42, (3), 879-887
82. Tsagaropoulos, G.; Eisenberg, A. *Macromolecules* **1995**, 28, (18), 6067-6077
83. Wu, C. L.; Zhang, M. Q.; Rong, M. Z.; Friedrich, K. *Composites Science and Technology* **2002**, 62, (10-11), 1327-1340
84. Li, F.; Li, Y.; Chung, T. S.; Kawi, S. *Journal of Membrane Science* **2010**, 356, (1-2), 14-21
85. Dasgupta, B.; Sen, S. K.; Banerjee, S. *Materials Science and Engineering B: Solid-State Materials for Advanced Technology* **2010**, 168, (1), 30-35
86. Raftopoulos, K. N.; Pielichowski, K. *Progress in Polymer Science*, (0),
87. Feng, Y.; Jia, Y.; Guang, S.; Xu, H. *Journal of Applied Polymer Science* **2010**, 115, (4), 2212-2220
88. Hao, N.; Böhning, M.; Goering, H.; Schönhals, A. *Macromolecules* **2007**, 40, (8), 2955-2964
89. Hao, N.; Böhning, M.; Wohlrab, S.; Schönhals, A. *Macromolecular Symposia* **2008**, 267, (1), 69-73
90. Iyer, P.; Iyer, G.; Coleman, M. *Journal of Membrane Science* **2010**, 358, (1-2), 26-32
91. Jackson, C. L.; Bauer, B. J.; Nakatani, A. I.; Barnes, J. D. *Chemistry of Materials* **1996**, 8, (3), 727-733
92. Corriu, R. J. P. *Angewandte Chemie - International Edition* **2000**, 39, (8), 1376-1398
93. Jones, J. R. *Acta Biomaterialia* **2013**, 9, (1), 4457-4486
94. Watanabe, H.; Vendamme, R.; Kunitake, T. *Bulletin of the Chemical Society of Japan* **2007**, 80, (3), 433-440
95. Wu, Y.; Wu, C.; Li, Y.; Xu, T.; Fu, Y. *Journal of Membrane Science* **2010**, 350, (1-2), 322-332
96. Xie, Z.; Hoang, M.; Duong, T.; Ng, D.; Dao, B.; Gray, S. *Journal of Membrane Science* **2011**, 383, (1-2), 96-103
97. Dell'Erba, I. E.; Williams, R. J. J. *Journal of Thermal Analysis and Calorimetry* **2008**, 93, (1), 95-100
98. Strachota, A.; Whelan, P.; Kříž, J.; Brus, J.; Urbanová, M.; Šlouf, M.; Matějka, L. *Polymer* **2007**, 48, (11), 3041-3058
99. Pellice, S. A.; Fasce, D. P.; Williams, R. J. J. *Journal of Polymer Science, Part B: Polymer Physics* **2003**, 41, (13), 1451-1461
100. Tanaka, K.; Chujo, Y. *Journal of Materials Chemistry* **2012**, 22, (5), 1733-1746
101. Pielichowski, K.; Njuguna, J.; Janowski, B.; Pielichowski, J., Polyhedral Oligomeric Silsesquioxanes (POSS)-Containing Nanohybrid Polymers. In *Supramolecular Polymers Polymeric Betains Oligomers*, Springer Berlin Heidelberg: 2006; Vol. 201, pp 225-296.
102. Abe, Y.; Gunji, T. *Progress in Polymer Science (Oxford)* **2004**, 29, (3), 149-182
103. Hartmann-Thompson, C., *Applications of Polyhedral Oligomeric Silsesquioxanes*. Springer: 2011; Vol. 3.
104. Asuncion, M. Z.; Laine, R. M. *Journal of the American Chemical Society* **2010**, 132, (11), 3723-3736
105. Laine, R. M.; Roll, M. F. *Macromolecules* **2011**, 44, (5), 1073-1109
106. Nischang, I.; Brüggemann, O.; Teasdale, I. *Angewandte Chemie - International Edition* **2011**, 50, (20), 4593-4596

107. Oaten, M.; Choudhury, N. R. *Macromolecules* **2005**, *38*, (15), 6392-6401
108. Wu, G.; Su, Z. *Chemistry of Materials* **2006**, *18*, (16), 3726-3732
109. Zhang, C.; Babonneau, F.; Bonhomme, C.; Laine, R. M.; Soles, C. L.; Hristov, H. A.; Yee, A. F. *Journal of the American Chemical Society* **1998**, *120*, (33), 8380-8391
110. Kanezashi, M.; Shioda, T.; Gunji, T.; Tsuru, T. *AIChE J.* **2012**, *58*, (6), 1733-1743
111. Dalwani, M.; Zheng, J.; Hempenius, M.; Raaijmakers, M. J. T.; Doherty, C. M.; Hill, A. J.; Wessling, M.; Benes, N. E. *Journal of Materials Chemistry* **2012**, *22*, (30), 14835-14838
112. Sharma, K. P.; Collins, A. M.; Perriman, A. W.; Mann, S. *Advanced Materials* **2013**, *25*, (14), 2005-2010
113. Wang, H.; Chung, T. S.; Tong, Y. W.; Jeyaseelan, K.; Armugam, A.; Chen, Z.; Hong, M.; Meier, W. *Small* **2012**, *8*, (8), 1185-1190
114. Akira, S.; Takeda, K. *Nature Reviews Immunology* **2004**, *4*, (7), 499-511
115. Xu, L. C.; Siedlecki, C. A. *Biomaterials* **2007**, *28*, (22), 3273-3283
116. Chandramohan, A.; Nagendiran, S.; Alagar, M. *Journal of Composite Materials* **2012**, *46*, (7), 773-781
117. Huang, J.; He, C.; Liu, X.; Xu, J.; Tay, C. S. S.; Chow, S. Y. *Polymer* **2005**, *46*, (18), 7018-7027
118. Huang, J.; Xiao, Y.; Mya, K. Y.; Liu, X.; He, C.; Dai, J.; Siow, Y. P. *Journal of Materials Chemistry* **2004**, *14*, (19), 2858-2863
119. Sulaiman, S.; Brick, C. M.; De Sana, C. M.; Katzenstein, J. M.; Laine, R. M.; Basheer, R. A. *Macromolecules* **2006**, *39*, (16), 5167-5169
120. Leu, C. M.; Chang, Y. T.; Wei, K. H. *Macromolecules* **2003**, *36*, (24), 9122-9127
121. Leu, C. M.; Chang, Y. T.; Wei, K. H. *Chemistry of Materials* **2003**, *15*, (19), 3721-3727
122. Leu, C. M.; Reddy, G. M.; Wei, K. H.; Shu, C. F. *Chemistry of Materials* **2003**, *15*, (11), 2261-2265
123. Choi, J.; Tamaki, R.; Kim, S. G.; Laine, R. M. *Chemistry of Materials* **2003**, *15*, (17), 3365-3375
124. Huang, J. C.; He, C. B.; Xiao, Y.; Mya, K. Y.; Dai, J.; Siow, Y. P. *Polymer* **2003**, *44*, (16), 4491-4499
125. Devaraju, S.; Vengatesan, M. R.; Alagar, M. *High Performance Polymers* **2011**, *23*, (2), 99-111
126. Alonso, B.; Massiot, D.; Valentini, M.; Kidchob, T.; Innocenzi, P. *Journal of Non-Crystalline Solids* **2008**, *354*, (15-16), 1615-1626
127. Chattopadhyay, D. K.; Zakula, A. D.; Webster, D. C. *Progress in Organic Coatings* **2009**, *64*, (2-3), 128-137
128. Vreugdenhil, A. J.; Gelling, V. J.; Woods, M. E.; Schmelz, J. R.; Enderson, B. P. *Thin Solid Films* **2008**, *517*, (2), 538-543
129. Brusatin, G.; Innocenzi, P.; Guglielmi, M.; Babonneau, F. *Journal of Sol-gel Science and Technology* **2003**, *26*, (1-3), 303-306
130. Brinker, C. J.; Scherer, G. W., *Sol-gel science: the physics and chemistry of sol-gel processing*. Academic press, inc.: 1990.
131. Li, G.; Kanezashi, M.; Tsuru, T. *Journal of Membrane Science* **2011**, *379*, (1-2), 287-295

132. Castricum, H. L.; Paradis, G. G.; Mittelmeijer-Hazeleger, M. C.; Kreiter, R.; Vente, J. F.; ten Elshof, J. E. *Advanced Functional Materials* **2011**, 21, (12), 2319-2329
133. ten Hove, M.; Nijmeijer, A.; Winnubst, L. *Separation and Purification Technology* **2015**,
134. Mascia, L. *Trends in Polymer Science* **1995**, 3, (2), 61-66
135. Schubert, U.; Hüsing, N.; Lorenz, A. *Chemistry of Materials* **1995**, 7, (11), 2010-2027
136. Wen, J.; Wilkes, G. L. *Chemistry of Materials* **1996**, 8, (8), 1667-1681
137. Haas, K. H. *Advanced Engineering Materials* **2000**, 2, (9), 571-582
138. Schottner, G. *Chemistry of Materials* **2001**, 13, (10), 3422-3435
139. Kreiter, R.; Rietkerk, M. D. A.; Castricum, H. L.; Van Veen, H. M.; Ten Elshof, J. E.; Vente, J. F. *Journal of Sol-gel Science and Technology* 57, (3), 245-252
140. Paradis, G. G.; Kreiter, R.; van Tuel, M. M. A.; Nijmeijer, A.; Vente, J. F. *Journal of Materials Chemistry* **2012**, 22, (15), 7258-7264
141. Tomczak, S. J.; Marchant, D.; Svejda, S.; Minton, T. K.; Brunsvold, A. L.; Gouzman, I.; Grossman, E.; Schatz, G. C.; Troya, D.; Sun, L.; Gonzalez, R. I. In *Properties and improved space survivability of POSS (polyhedral oligomeric silsesquioxane) polyimides*, 2005; 2005; pp 395-406.
142. Zhang, W.; Müller, A. H. E. *Progress in Polymer Science* **2013**, 38, (8), 1121-1162
143. Choi, J.; Yee, A. F.; Laine, R. M. *Macromolecules* **2003**, 36, (15), 5666-5682
144. Morgan, P. W., *Interfacial Polymerization*. In *Encyclopedia of Polymer Science and Technology*, John Wiley & Sons, Inc.: 2002.
145. Huang, J.; Kaner, R. B. *Journal of the American Chemical Society* **2004**, 126, (3), 851-855
146. Bean, K.; Black, C. F.; Govan, N.; Reynolds, P.; Sambrook, M. R. *Journal of Colloid and Interface Science* **2012**, 366, (1), 16-22
147. Liu, D.; Yu, B.; Jiang, X.; Yin, J. *Langmuir* **2013**, 29, (17), 5307-5314
148. Sawhney, A. S.; Pathak, C. P.; Hubbell, J. A. *Biomaterials* **1993**, 14, (13), 1008-1016
149. Scott, C.; Wu, D.; Ho, C. C.; Co, C. C. *Journal of the American Chemical Society* **2005**, 127, (12), 4160-4161
150. Odian, G. G., *Principles of polymerization*. 2004; Vol. 3.
151. Morgan, P. W., *Condensation Polymers: By interfacial and Solution Methods*. 1965; p 190.
152. Ghosh, A. K.; Jeong, B. H.; Huang, X.; Hoek, E. M. V. *J. Membr. Sci.* **2008**, 311, (1-2), 34-45
153. Jin, Y.; Su, Z. *J. Membr. Sci.* **2009**, 330, (1-2), 175-179
154. Zhang, R. X.; Vanneste, J.; Poelmans, L.; Sotto, A.; Wang, X. L.; Van Der Bruggen, B. *Journal of Applied Polymer Science* **2012**, 125, (5), 3755-3769
155. Huang, J.; Kaner, R. B. *Chemical Communications* **2006**, (4), 367-376
156. Jegal, J.; Min, S. G.; Lee, K. H. *J Appl Polym Sci* **2002**, 86, (11), 2781-2787
157. Frère, Y.; Danicher, L.; Gramain, P. *European Polymer Journal* **1998**, 34, (2), 193-199
158. Chiang, Y. C.; Hsub, Y. Z.; Ruaan, R. C.; Chuang, C. J.; Tung, K. L. *J. Membr. Sci.* **2009**, 326, (1), 19-26
159. Arai, Y.; Watanabe, M.; Sanui, K.; Ogata, N. *Journal of polymer science. Part A-1, Polymer chemistry* **1985**, 23, (12), 3081-3093

160. Marks, M. J.; Munjal, S.; Namhata, S.; Scott, D. C.; Bosscher, F.; De Letter, J. A.; Klumperman, B. *Journal of Polymer Science, Part A: Polymer Chemistry* **2000**, 38, (3), 560-570
161. Chu, L. Y.; Park, S. H.; Yamaguchi, T.; Nakao, S. I. *J. Membr. Sci.* **2001**, 192, (1-2), 27-39
162. Zhao, J.; Zhang, Y.; Su, Y.; Liu, J.; Zhao, X.; Peng, J.; Jiang, Z. *Journal of Membrane Science* **2013**, 445, 1-7
163. Chai, G. Y.; Krantz, W. B. *J. Membr. Sci.* **1994**, 93, (2), 175-192
164. Karode, S. K.; Kulkarni, S. S.; Suresh, A. K.; Mashelkar, R. A. *Chemical Engineering Science* **1997**, 52, (19), 3243-3255
165. Munjal, S. *Polymer Engineering and Science* **1994**, 34, (2), 93-101
166. Freger, V. *Langmuir* **2003**, 19, (11), 4791-4797
167. Ghosh, A. K.; Hoek, E. M. V. *J. Membr. Sci.* **2009**, 336, (1-2), 140-148
168. Zhang, Y.; Benes, N. E.; Lammertink, R. G. H. *Lab on a Chip* **2015**, 15, (2), 575-580
169. Wu, D.; Huang, Y.; Yu, S.; Lawless, D.; Feng, X. *Journal of Membrane Science* **2014**, 472, 141-153
170. Hung, W. S.; Lai, C. L.; An, Q.; De Guzman, M.; Shen, T. J.; Huang, Y. H.; Chang, K. C.; Tsou, C. H.; Hu, C. C.; Lee, K. R. *J. Membr. Sci.* **2014**, 470, 513-523
171. Ahmad, A. L.; Ooi, B. S.; Choudhury, J. P. *Separation Science and Technology* **2004**, 39, (8), 1815-1831
172. Karode, S. K.; Kulkarni, S. S.; Suresh, A. K.; Mashelkar, R. A. *Chemical Engineering Science* **1998**, 53, (15), 2649-2663
173. Yashin, V. V.; Balazs, A. C. *Journal of Chemical Physics* **2004**, 121, (22), 11440-11454
174. Bouchemal, K.; Couenne, F.; Briançon, S.; Fessi, H.; Tayakout, M. *AIChE Journal* **2006**, 52, (6), 2161-2171
175. Freger, V. *Langmuir* **2005**, 21, (5), 1884-1894
176. Dhumal, S. S.; Wagh, S. J.; Suresh, A. K. *Journal of Membrane Science* **2008**, 325, (2), 758-771
177. Kobašljija, M.; McQuade, D. T. *Macromolecules* **2006**, 39, (19), 6371-6375
178. Hermans, S.; Bernstein, R.; Volodin, A.; Vankelecom, I. F. J. *Reactive and Functional Polymers* **2014**, 86, 199-208
179. Lau, W. J.; Ismail, A. F.; Misdan, N.; Kassim, M. A. *Desalination* **2012**, 287, 190-199
180. Mansourpanah, Y.; Madaeni, S. S.; Rahimpour, A. J. *J. Membr. Sci.* **2009**, 343, (1-2), 219-228
181. Kim, S. H.; Kwak, S. Y.; Suzuki, T. *Environmental Science and Technology* **2005**, 39, (6), 1764-1770
182. Du, J.; Zhang, J.; Han, B.; Liu, Z.; Wan, M. *Synthetic Metals* **2005**, 155, (3), 523-526
183. Lei, J.; Liang, W.; Brumlik, C. J.; Martin, C. R. *Synthetic Metals* **1992**, 47, (3), 351-359
184. Qi, G.; Huang, L.; Wang, H. *Chemical Communications* **2012**, 48, (66), 8246-8248
185. Wang, X.; Yeh, T. M.; Wang, Z.; Yang, R.; Wang, R.; Ma, H.; Hsiao, B. S.; Chu, B. *Polymer (United Kingdom)* **2014**, 55, (6), 1358-1366
186. Sun, Q.; Deng, Y. *Journal of the American Chemical Society* **2005**, 127, (23), 8274-8275

187. McIlroy, D. A.; Blaiszik, B. J.; Caruso, M. M.; White, S. R.; Moore, J. S.; Sottos, N. R. *Macromolecules* **2010**, *43*, (4), 1855-1859
188. Gaudin, F.; Sintez-Zydowicz, N. *Colloids and Surfaces A: Physicochemical and Engineering Aspects* **2011**, *384*, (1-3), 698-712
189. Quevedo, E.; Steinbacher, J.; McQuade, D. T. *Journal of the American Chemical Society* **2005**, *127*, (30), 10498-10499
190. Yadav, S. K.; Suresh, A. K.; Khilar, K. C. *AIChE Journal* **1990**, *36*, (3), 431-438
191. Ameloot, R.; Vermoortele, F.; Vanhove, W.; Roeffaers, M. B. J.; Sels, B. F.; De Vos, D. E. *Nature Chemistry* **2011**, *3*, (5), 382-387
192. Raaijmakers, M. J. T.; Wessling, M.; Nijmeijer, A.; Benes, N. E. *Chemistry of Materials* **2014**, *26*, (12), 3660-3664
193. Dalwani, M.; Benes, N. E.; Bargeman, G.; Stamatialis, D.; Wessling, M. *Journal of Membrane Science* **2010**, *363*, (1-2), 188-194
194. Dalwani, M.; Benes, N. E.; Bargeman, G.; Stamatialis, D.; Wessling, M. J. *Membr. Sci.* **2011**, *372*, (1-2), 228-238
195. Buch, P. R.; Jagan Mohan, D.; Reddy, A. V. R. *J. Membr. Sci.* **2008**, *309*, (1-2), 36-44
196. Kawaguchi, T.; Tamura, H. *J Appl Polym Sci* **1984**, *29*, (11), 3359-3367
197. Shintani, T.; Matsuyama, H.; Kurata, N. *Desalination* **2007**, *207*, (1-3), 340-348
198. Han, R. *Journal of Membrane Science* **2013**, *425-426*, 176-181
199. Shin, D. H.; Kim, N.; Lee, Y. T. *Journal of Membrane Science* **2011**, *376*, (1-2), 302-311
200. Jimenez Solomon, M. F.; Bhole, Y.; Livingston, A. G. J. *Membr. Sci.* **2012**, *423-424*, 371-382
201. Lee, K. P.; Arnot, T. C.; Mattia, D. J. *Membr. Sci.* **2011**, *370*, (1-2), 1-22
202. Hermans, S.; Mariën, H.; Van Goethem, C.; Vankelecom, I. F. J. *Current Opinion in Chemical Engineering* **2015**, *8*, (0), 45-54
203. Misdan, N.; Lau, W. J.; Ismail, A. F. *Desalination* **2012**, *287*, 228-237
204. Ismail, A. F.; Padaki, M.; Hilal, N.; Matsuura, T.; Lau, W. J. *Desalination* **2015**, *356*, 140-148
205. Hong, S.; Kim, I. C.; Tak, T.; Kwon, Y. N. *Desalination* **2013**, *309*, 18-26
206. Kim, C. K.; Kim, J. H.; Roh, I. J.; Kim, J. J. *Journal of Membrane Science* **2000**, *165*, (2), 189-199
207. Li, L.; Zhang, S.; Zhang, X.; Zheng, G. J. *Membr. Sci.* **2007**, *289*, (1-2), 258-267
208. Li, L.; Zhang, S.; Zhang, X.; Zheng, G. J. *Membr. Sci.* **2008**, *315*, (1-2), 20-27
209. Liu, M.; Wu, D.; Yu, S.; Gao, C. J. *Membr. Sci.* **2009**, *326*, (1), 205-214
210. Roh, I. J.; Greenberg, A. R.; Khare, V. P. *Desalination* **2006**, *191*, (1-3), 279-290
211. Xie, W.; Geise, G. M.; Freeman, B. D.; Lee, H. S.; Byun, G.; McGrath, J. E. J. *Membr. Sci.* **2012**, *403-404*, 152-161
212. Zuo, J.; Wang, Y.; Sun, S. P.; Chung, T. S. J. *Membr. Sci.* **2012**, *405-406*, 123-133
213. Arthur, S. D. J. *Membr. Sci.* **1989**, *46*, (2-3), 243-260
214. Yu, S.; Liu, M.; Lü, Z.; Zhou, Y.; Gao, C. J. *Membr. Sci.* **2009**, *344*, (1-2), 155-164
215. Liu, M.; Yao, G.; Cheng, Q.; Ma, M.; Yu, S.; Gao, C. J. *Membr. Sci.* **2012**, *415-416*, (0), 122-131
216. Oh, N. W.; Jegal, J.; Lee, K. H. *Journal of Applied Polymer Science* **2001**, *80*, (14), 2729-2736
217. Yoon, K.; Hsiao, B. S.; Chu, B. J. *Membr. Sci.* **2009**, *326*, (2), 484-492

218. Mo, Y.; Tiraferri, A.; Yip, N. Y.; Adout, A.; Huang, X.; Elimelech, M. *Environmental Science and Technology* **2012**, *46*, (24), 13253-13261
219. Sundet, S. A.; Murphey, W. A.; Speck, S. B. *Journal of Polymer Science* **1959**, *40*, (137), 389-397
220. Trushinski, B. J.; Dickson, J. M.; Smyth, T.; Childs, R. F.; McCarry, B. E. *J. Membr. Sci.* **1998**, *143*, (1-2), 181-188
221. Kurth, C. J.; Kloos, S. D. *Modified Sulfonamide Polymers*. 2008.
222. Lind, M. L.; Jeong, B. H.; Subramani, A.; Huang, X.; Hoek, E. M. V. *Journal of Materials Research* **2009**, *24*, (5), 1624-1631
223. Lind, M. L.; Suk, D. E.; Nguyen, T. V.; Hoek, E. M. V. *Environmental Science and Technology* **2010**, *44*, (21), 8230-8235
224. Fathizadeh, M.; Aroujalian, A.; Raisi, A. *J. Membr. Sci.* **2011**, *375*, (1-2), 88-95
225. Huang, H.; Qu, X.; Ji, X.; Gao, X.; Zhang, L.; Chen, H.; Hou, L. *Journal of Materials Chemistry A* **2013**, *1*, (37), 11343-11349
226. Wang, Q.; Zhang, G. S.; Li, Z. S.; Deng, S.; Chen, H.; Wang, P. *Desalination* **2014**, *352*, 38-44
227. Duan, J.; Pan, Y.; Pacheco, F.; Litwiller, E.; Lai, Z.; Pinnau, I. *J. Membr. Sci.* **2015**, *476*, 303-310
228. Huo, J.; Marcello, M.; Garai, A.; Bradshaw, D. *Advanced Materials* **2013**, *25*, (19), 2717-2722
229. Sorribas, S.; Gorgojo, P.; Téllez, C.; Coronas, J.; Livingston, A. G. *Journal of the American Chemical Society* **2013**, *135*, (40), 15201-15208
230. Hagenmueller, R.; Du, F.; Fischer, J. E.; Winey, K. I. *Polymer* **2006**, *47*, (7), 2381-2388
231. Jeong, J. Y.; Lee, H. J.; Kang, S. W.; Tan, L. S.; Baek, J. B. *Journal of Polymer Science, Part A: Polymer Chemistry* **2008**, *46*, (18), 6041-6050
232. Kim, H. J.; Lim, M. Y.; Jung, K. H.; Kim, D. G.; Lee, J. C. *Journal of Materials Chemistry A* **2015**, *3*, (13), 6798-6809
233. Kim, H. S.; Park, B. H.; Yoon, J. S.; Jin, H. J. *Materials Letters* **2007**, *61*, (11-12), 2251-2254
234. Zhao, H.; Qiu, S.; Wu, L.; Zhang, L.; Chen, H.; Gao, C. *J. Membr. Sci.* **2014**, *450*, 249-256
235. Zhao, Y.; Qiu, C.; Li, X.; Vararattanavech, A.; Shen, W.; Torres, J.; Hélix-Nielsen, C.; Wang, R.; Hu, X.; Fane, A. G.; Tang, C. Y. *Journal of Membrane Science* **2012**, *423-424*, 422-428
236. Arslan, G.; Tor, A.; Cengelöglu, Y.; Ersoz, M. *Journal of Hazardous Materials* **2009**, *165*, (1-3), 729-735
237. Oleinikova, M.; González, C.; Valiente, M.; Muñoz, M. *Polyhedron* **1999**, *18*, (25), 3353-3359
238. Lee, S. Y.; Kim, H. J.; Patel, R.; Im, S. J.; Kim, J. H.; Min, B. R. *Polymers for Advanced Technologies* **2007**, *18*, (7), 562-568
239. Kalkan-Sevinc, Z. S.; Goettler, L. A. *Polymer Engineering and Science* **2012**, *52*, (11), 2410-2416
240. Duan, J.; Litwiller, E.; Pinnau, I. *J. Membr. Sci.* **2015**, *473*, 157-164
241. Zuo, J.; Chung, T. S. *Journal of Materials Chemistry A* **2013**, *1*, (34), 9814-9826
242. Langdon, C. J. *Marine Biology* **1989**, *102*, (2), 217-224

243. Raaijmakers, M. J. T.; Schmidt, T.; Barth, M.; Tutus, M.; Benes, N. E.; Wessling, M. *Angewandte Chemie International Edition* **2015**, n/a-n/a
244. Raaijmakers, M. J. T.; Schmidt, T.; Barth, M.; Tutus, M.; Benes, N. E.; Wessling, M. *Angewandte Chemie International Edition* **2015**, *54*, (20), 5910-5914
245. Majorek, K. A.; Porebski, P. J.; Dayal, A.; Zimmerman, M. D.; Jablonska, K.; Stewart, A. J.; Chruszcz, M.; Minor, W. *Molecular Immunology* **2012**, *52*, (3-4), 174-182
246. Kollman, J. M.; Pandi, L.; Sawaya, M. R.; Riley, M.; Doolittle, R. F. *Biochemistry* **2009**, *48*, (18), 3877-86
247. Chang, H.; Khan, R.; Rong, Z.; Sapelkin, A.; Vadgama, P. *Biofabrication* **2010**, *2*, (3), 035002
248. Nair, G.; Gargiuli, J. F.; Shiju, N. R.; Rong, Z.; Shapiro, E.; Drikakis, D.; Vadgama, P. *ChemBiochem : a European journal of chemical biology* **2006**, *7*, (11), 1683-9
249. Abad-Zapatero, C.; Rydel, T. J.; Erickson, J. *Proteins* **1990**, *8*, (1), 62-81
250. Royant, A.; Noirclerc-Savoye, M. *Journal of structural biology* **2011**, *174*, (2), 385-90
251. Strongin, D. E.; Bevis, B.; Khuong, N.; Downing, M. E.; Strack, R. L.; Sundaram, K.; Glick, B. S.; Keenan, R. J. *Protein engineering, design & selection : PEDS* **2007**, *20*, (11), 525-34
252. Kafka, A. P.; Kleffmann, T.; Rades, T.; McDowell, A. *Molecular Pharmaceutics* **2009**, *6*, (5), 1483-1491
253. Kafka, A. P.; McLeod, B. J.; Rades, T.; McDowell, A. *Journal of Controlled Release* **2011**, *149*, (3), 307-313
254. Yúfera, M.; Pascual, E.; Fernández-Díaz, C. *Aquaculture* **1999**, *177*, (1-4), 249-256
255. Nordgreen, A.; Yúfera, M.; Hamre, K. *Aquaculture* **2008**, *285*, (1-4), 159-166
256. Zhang, Q.; Shi, Y.; Zhan, X.; Chen, F. *Colloids and Surfaces A: Physicochemical and Engineering Aspects* **2012**, *393*, 17-26
257. Su, J. F.; Wang, L. X.; Ren, L.; Huang, Z.; Meng, X. W. *J Appl Polym Sci* **2006**, *102*, (5), 4996-5006
258. Su, J.; Wang, S.; Huang, Z.; Liang, J., Polyurethane MicroPCMs containing N-octadecane applied in building materials synthesized by interfacial polycondensation: Thermal stability and heat absorption simulation. In *Advanced Materials Research*, 2010; Vol. 96, pp 121-127.
259. Su, J. F.; Wang, L. X.; Ren, L. *Colloids and Surfaces A: Physicochemical and Engineering Aspects* **2007**, *299*, (1-3), 268-275
260. Siddhan, F.; Jassal, M.; Agrawal, A. K. *J Appl Polym Sci* **2007**, *106*, (2), 786-792
261. Lu, S.; Xing, J.; Zhang, Z.; Jia, G. *J Appl Polym Sci* **2011**, *121*, (6), 3377-3383
262. Liang, C.; Lingling, X.; Hongbo, S.; Zhibin, Z. *Energy Conversion and Management* **2009**, *50*, (3), 723-729
263. Ley, S. V.; Ramarao, C.; Lee, A. L.; Østergaard, N.; Smith, S. C.; Shirley, I. M. *Organic Letters* **2003**, *5*, (2), 185-187
264. Crespy, D.; Stark, M.; Hoffmann-Richter, C.; Ziener, U.; Landfester, K. *Macromolecules* **2007**, *40*, (9), 3122-3135
265. Poe, S. L.; Kobašlija, M.; McQuade, D. T. *Journal of the American Chemical Society* **2007**, *129*, (29), 9216-9221
266. Ramarao, C.; Ley, S. V.; Smith, S. C.; Shirley, I. M.; DeAlmeida, N. *Chemical Communications* **2002**, (10), 1132-1133

267. Saihi, D.; Vroman, I.; Giraud, S.; Bourbigot, S. *Reactive and Functional Polymers* **2006**, *66*, (10), 1118-1125
268. Tatiya, P. D.; Hedao, R. K.; Mahulikar, P. P.; Gite, V. V. *Industrial and Engineering Chemistry Research* **2013**, *52*, (4), 1562-1570
269. Tsuda, N.; Ohtsubo, T.; Fuji, M. *Advanced Powder Technology* **2012**, *23*, (6), 724-730
270. Takahashi, T.; Taguchi, Y.; Tanaka, M. *Journal of Chemical Engineering of Japan* **2005**, *38*, (11), 929-936
271. Hirech, K.; Payan, S.; Carnelle, G.; Brujes, L.; Legrand, J. *Powder Technology* **2003**, *130*, (1-3), 324-330
272. Gaudin, F.; Sintes-Zydowicz, N. *Colloids and Surfaces A: Physicochemical and Engineering Aspects* **2008**, *331*, (1-2), 133-142
273. Morral-Ruiz, G.; Melgar-Lesmes, P.; García, M. L.; Solans, C.; García-Celma, M. J. *Polymer (United Kingdom)* **2012**, *53*, (26), 6072-6080
274. Jinglei, Y.; Keller, M. W.; Moore, J. S.; White, S. R.; Sottos, N. R. *Macromolecules* **2008**, *41*, (24), 9650-9655
275. Yadav, S. K.; Khilar, K. C.; Suresh, A. K. J. *Membr. Sci.* **1997**, *125*, (2), 213-218
276. Baier, G.; Friedemann, K.; Leuschner, E. M.; Musyanovych, A.; Landfester, K. *Macromolecular Symposia* **2013**, *331-332*, (1), 71-80
277. Brochu, A. B. W.; Chyan, W. J.; Reichert, W. M. *Journal of Biomedical Materials Research - Part B Applied Biomaterials* **2012**, *100 B*, (7), 1764-1772
278. Bouchemal, K.; Briançon, S.; Perrier, E.; Fessi, H.; Bonnet, I.; Zydowicz, N. *International Journal of Pharmaceutics* **2004**, *269*, (1), 89-100
279. Chang, C. P.; Chang, J. C.; Ichikawa, K.; Dobashi, T. *Colloids and Surfaces B: Biointerfaces* **2005**, *44*, (4), 187-190
280. Dobashi, T.; Furukawa, T.; Ichikawa, K.; Narita, T. *Langmuir* **2002**, *18*, (16), 6031-6033
281. Dobashi, T.; Furukawa, T.; Narita, T.; Shimofure, S.; Ichikawa, K.; Chu, B. *Langmuir* **2001**, *17*, (15), 4525-4528
282. Patchan, M. W.; Fuller, B. W.; Baird, L. M.; Gong, P. K.; Walter, E. C.; Vidmar, B. J.; Kyei, I.; Xia, Z.; Benkoski, J. J. *ACS Applied Materials and Interfaces* **2015**, *7*, (13), 7315-7323
283. Fielding, L. A.; Armes, S. P. *Journal of Materials Chemistry* **2012**, *22*, (22), 11235-11244
284. Wu, G.; An, J.; Sun, D.; Tang, X.; Xiang, Y.; Yang, J. *Journal of Materials Chemistry A* **2014**, *2*, (30), 11614-11620
285. Yang, Y.; Ning, Y.; Wang, C.; Tong, Z. *Polymer Chemistry* **2013**, *4*, (21), 5407-5415
286. Zhang, Q.; Yang, Y.; Wang, C. Y. *Acta Polymerica Sinica* **2014**, (7), 997-1001
287. Li, J.; Hughes, A. D.; Kalantar, T. H.; Drake, I. J.; Tucker, C. J.; Moore, J. S. *ACS Macro Letters* **2014**, *3*, (10), 976-980
288. Yang, Y.; Wei, Z.; Wang, C.; Tong, Z. *ACS Applied Materials & Interfaces* **2013**, *5*, (7), 2495-2502
289. Mookhoek, S. D.; Blaiszik, B. J.; Fischer, H. R.; Sottos, N. R.; White, S. R.; Van Der Zwaag, S. *Journal of Materials Chemistry* **2008**, *18*, (44), 5390-5394
290. Wolińska-Grabczyk, A.; Jankowski, A. *Separation and Purification Technology* **2007**, *57*, (3), 413-417

291. Khosravi, A.; Sadeghi, M. *Journal of Membrane Science* **2013**, 434, 171-183
292. Chattopadhyay, D. K.; Raju, K. V. S. N. *Progress in Polymer Science (Oxford)* **2007**, 32, (3), 352-418
293. Neumann, D.; Fisher, M.; Tran, L.; Matison, J. G. *Journal of the American Chemical Society* **2002**, 124, (47), 13998-13999
294. Raaijmakers, M. J. T.; Hempenius, M. A.; Schön, P. M.; Vancso, G. J.; Nijmeijer, A.; Wessling, M.; Benes, N. E. *Journal of the American Chemical Society* **2014**, 136, (1), 330-335
295. Fu, B. X.; Zhang, W.; Hsiao, B. S.; Rafailovich, M.; Sokolov, J.; Johansson, G.; Sauer, B. B.; Phillips, S.; Balnski, R. *High Performance Polymers* **2000**, 12, (4), 565-571
296. Wahab, M. A.; Mya, K. Y.; He, C. *Journal of Polymer Science, Part A: Polymer Chemistry* **2008**, 46, (17), 5887-5896
297. Wei, X.; Kong, X.; Yang, J.; Zhang, G.; Chen, J.; Wang, J. J. *Membr. Sci.* **2013**, 440, 67-76
298. Seman, M. N. A.; Khayet, M.; Hilal, N. J. *Membr. Sci.* **2010**, 348, (1-2), 109-116
299. Wei, X. Z.; Zhu, L. P.; Deng, H. Y.; Xu, Y. Y.; Zhu, B. K.; Huang, Z. M. *J. Membr. Sci.* **2008**, 323, (2), 278-287
300. Kwak, S. Y.; Yeom, M. O.; Roh, I. J.; Kim, D. Y.; Kim, J. J. *J. Membr. Sci.* **1997**, 132, (2), 183-191
301. Loria-Bastarrachea, M. I.; Aguilar-Vega, M. *Industrial and Engineering Chemistry Research* **2010**, 49, (23), 12060-12066
302. Pascu, O.; Garcia-Valls, R.; Giamberini, M. *Polymer International* **2008**, 57, (8), 995-1006
303. Arribas, P.; Khayet, M.; Garcia-Payo, M. C.; Gil, L. *Separation and Purification Technology* **2014**, 138, 118-129
304. Abu Seman, M. N.; Khayet, M.; Hilal, N. *Desalination* **2011**, 273, (1), 36-47
305. Tang, B.; Huo, Z.; Wu, P. J. *Membr. Sci.* **2008**, 320, (1-2), 198-205
306. Wu, H.; Tang, B.; Wu, P. J. *Membr. Sci.* **2013**, 428, 425-433
307. Wu, H.; Tang, B.; Wu, P. J. *Membr. Sci.* **2013**, 428, 301-308
308. Tang, B.; Zou, C.; Wu, P. J. *Membr. Sci.* **2010**, 365, (1-2), 276-285
309. Wei, X. Z.; Yang, J.; Zhang, G. L. *Polymers and Polymer Composites* **2012**, 20, (3), 261-270
310. Zhang, P.; Wu, L.; Bu, Z.; Li, B. G. *J Appl Polym Sci* **2008**, 108, (6), 3586-3592
311. Zhang, Y.; Su, Y.; Peng, J.; Zhao, X.; Liu, J.; Zhao, J.; Jiang, Z. J. *Membr. Sci.* **2013**, 429, 235-242
312. Wu, H.; Tang, B.; Wu, P. *Journal of Physical Chemistry C* **2010**, 114, (39), 16395-16400
313. Lee, K. P.; Zheng, J.; Bargeman, G.; Kemperman, A. J. B.; Benes, N. E. *J. Membr. Sci.* **2015**, 478, (0), 75-84
314. Thurston, J. T.; Dudley, J. R.; Kaiser, D. W.; Hechenbleikner, I.; Schaefer, F. C.; Holm-Hansen, D. *Journal of the American Chemical Society* **1951**, 73, (7), 2981-2983
315. Tsai, C. W.; Tsai, C.; Ruaan, R. C.; Hu, C. C.; Lee, K. R. *ACS Applied Materials and Interfaces* **2013**, 5, (12), 5563-5568
316. Mikroyannidis, J. A. *Journal of Polymer Science, Part A: Polymer Chemistry* **1988**, 26, (2), 583-593

317. Rice, W. C.; Puglia, J. P. High performance composite membrane. 2001.
318. Perry, M.; Ginzburg, V.; Ginzburg, B.; Lapido, P. **2010**,
319. Anon. *Journal of Polymer Science, Part A: Polymer Chemistry* **1990**, 28, (13), 3787-3793
320. Kim, J. H.; Lee, K. H.; Kim, S. Y. *Journal of Membrane Science* **2000**, 169, (1), 81-93
321. Chern, Y.-T.; Chen, L.-W. *J Appl Polym Sci* **1991**, 42, (9), 2535-2541
322. Chern, Y.-T.; Chen, L.-W. *J Appl Polym Sci* **1992**, 44, (6), 1087-1093
323. Yang, Z.; Zhang, L.; Zhang, G.; Li, C. *Huagong Xuebao* **2012**, 63, (8), 2635-2641
324. Martin, C. R.; Liang, W.; Menon, V.; Parthasarathy, R.; Parthasarathy, A. *Synthetic Metals* **1993**, 57, (1), 3766-3773
325. Michaelson, J. C.; McEvoy, A. J. *Journal of the Chemical Society, Chemical Communications* **1994**, (1), 79-80
326. Parthasarathy, A.; Brumlik, C. J.; Martin, C. R.; Collins, G. E. *Journal of Membrane Science* **1994**, 94, 249-254
327. Huang, J.; Virji, S.; Weiller, B. H.; Kaner, R. B. *Journal of the American Chemical Society* **2003**, 125, (2), 314-315
328. Sawall, D. D.; Villahermosa, R. M.; Lipeles, R. A.; Hopkins, A. R. *Chemistry of Materials* **2004**, 16, (9), 1606-1608
329. He, Y. *Materials Science and Engineering B: Solid-State Materials for Advanced Technology* **2005**, 122, (1), 76-79
330. Wang, Y.; Jing, X. *Journal of Physical Chemistry B* **2008**, 112, (4), 1157-1162
331. Li, R.; Chen, Z.; Li, J.; Zhang, C.; Guo, Q. *Synthetic Metals* **2013**, 171, 39-44
332. Nuraje, N.; Su, K.; Yang, N. I.; Matsui, H. *ACS Nano* **2008**, 2, (3), 502-506
333. Jia, Q. M.; Li, J. B.; Wang, L. F.; Zhu, J. W.; Zheng, M. *Materials Science and Engineering A* **2007**, 448, (1-2), 356-360
334. Kuo, C. W.; Wen, T. C. *European Polymer Journal* **2008**, 44, (11), 3393-3401
335. Virji, S.; Huang, J.; Kaner, R. B.; Weiller, B. H. *Nano Letters* **2004**, 4, (3), 491-496
336. Zhao, M.; Wu, X.; Cai, C. *Journal of Physical Chemistry C* **2009**, 113, (12), 4987-4996
337. Su, B.; Tong, Y.; Bai, J.; Lei, Z.; Wang, K.; Mu, H.; Dong, N. *Indian Journal of Chemistry - Section A Inorganic, Physical, Theoretical and Analytical Chemistry* **2007**, 46, (4), 595-599
338. Huang, J.; Virji, S.; Weiller, B. H.; Kaner, R. B. *Chemistry - A European Journal* **2004**, 10, (6), 1314-1319
339. Son, W. I.; Hong, J. M.; Kim, B. S. *Korean Journal of Chemical Engineering* **2005**, 22, (2), 285-290
340. Yang, Q.; Hou, Z.; Huang, T. *J Appl Polym Sci* **2015**, 132, (11),
341. Zhang, L.; Liu, P.; Ju, L.; Wang, L.; Zhao, S. *Macromolecular Research* **2010**, 18, (7), 648-652
342. Wen, L.; Li, M.; Schlenoff, J. B. *Journal of the American Chemical Society* **1997**, 119, (33), 7726-7733
343. Gupta, B.; Prakash, R. *Synthetic Metals* **2010**, 160, (5-6), 523-528
344. Joshi, L.; Prakash, R. *Materials Letters* **2012**, 66, (1), 250-253
345. Joshi, L.; Singh, A. K.; Prakash, R. *Materials Chemistry and Physics* **2012**, 135, (1), 80-87

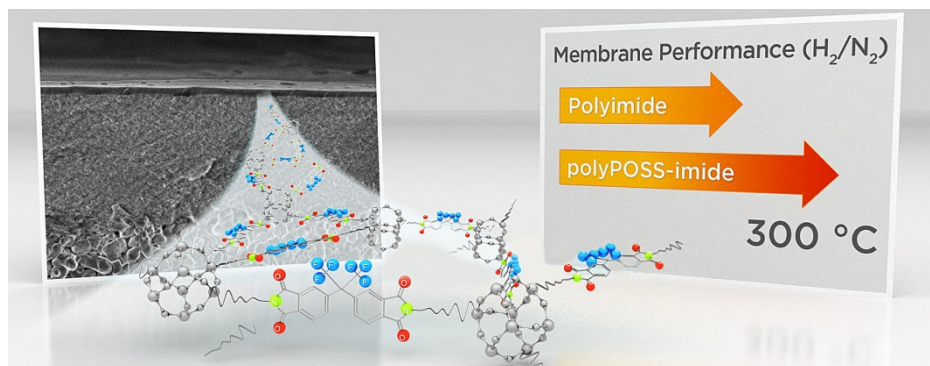
346. Wang, Y. G.; Wu, W.; Cheng, L.; He, P.; Wang, C. X.; Xia, Y. Y. *Advanced Materials* **2008**, *20*, (11), 2166-2170
347. Li, X. G.; Li, J.; Meng, Q. K.; Huang, M. R. *Journal of Physical Chemistry B* **2009**, *113*, (29), 9718-9727
348. Liu, P.; Wang, X.; Li, H. *Synthetic Metals* **2013**, *181*, 72-78
349. Shen, J.; Yang, C.; Li, X.; Wang, G. *ACS Applied Materials and Interfaces* **2013**, *5*, (17), 8467-8476
350. Salvatierra, R. V.; Oliveira, M. M.; Zarbin, A. J. G. *Chemistry of Materials* **2010**, *22*, (18), 5222-5234
351. Wang, Q.; Wang, S.; Li, J.; Moriyama, H., Synthesis of C60-doped polyaniline nanoshuttles. In *Advanced Materials Research*, 2011; Vol. 284-286, pp 1010-1013.
352. Wang, Q.; Wang, S.; Li, J.; Moriyama, H. *Journal of Polymer Science, Part B: Polymer Physics* **2012**, *50*, (20), 1426-1432
353. He, J.; Perez, M. T.; Zhang, P.; Liu, Y.; Babu, T.; Gong, J.; Nie, Z. *Journal of the American Chemical Society* **2012**, *134*, (8), 3639-3642
354. Bora, C.; Dolui, S. K. *Polymer International* **2014**, *63*, (8), 1439-1446
355. Domingues, S. H.; Salvatierra, R. V.; Oliveira, M. M.; Zarbin, A. J. G. *Chemical Communications* **2011**, *47*, (9), 2592-2594
356. Ho, C.-H.; Liu, C.-D.; Hsieh, C.-H.; Hsieh, K.-H.; Lee, S.-N. *Synthetic Metals* **2008**, *158*, (15), 630-637
357. Mafé, S.; Manzanares, J. A.; Reiss, H. *The Journal of Chemical Physics* **1993**, *98*, (3), 2408-2410
358. Kuo, C.-W.; Wen, T.-C. *European Polymer Journal* **2008**, *44*, (11), 3393-3401
359. Li, Y. S.; Bux, H.; Feldhoff, A.; Li, G. N.; Yang, W. S.; Caro, J. *Advanced Materials* **2010**, *22*, (30), 3322-3326
360. Hedlund, J.; Noack, M.; Kölsch, P.; Creaser, D.; Caro, J.; Sterte, J. *Journal of Membrane Science* **1999**, *159*, (1-2), 263-273
361. Li, Y. S.; Liang, F. Y.; Bux, H.; Feldhoff, A.; Yang, W. S.; Caro, J. *Angewandte Chemie - International Edition* **2010**, *49*, (3), 548-551
362. Li, J. R.; Sculley, J.; Zhou, H. C. *Chemical Reviews* **2012**, *112*, (2), 869-932
363. Peng, Y.; Li, Y.; Ban, Y.; Jin, H.; Jiao, W.; Liu, X.; Yang, W. *Science* **2014**, *346*, (6215), 1356-1359
364. Brown, A. J.; Brunelli, N. A.; Eum, K.; Rashidi, F.; Johnson, J. R.; Koros, W. J.; Jones, C. W.; Nair, S. *Science* **2014**, *345*, (6192), 72-75
365. Lu, H.; Zhu, S. *European Journal of Inorganic Chemistry* **2013**, (8), 1294-1300
366. Li, Y.; Wee, L. H.; Volodin, A.; Martens, J. A.; Vankelecom, I. F. J. *Chemical Communications* **2015**, *51*, (5), 918-920
367. Rodenas, T.; Luz, I.; Prieto, G.; Seoane, B.; Miro, H.; Corma, A.; Kapteijn, F.; Llabrés i Xamena, F. X.; Gascon, J. *Nat Mater* **2015**, *14*, (1), 48-55
368. Brinker, C. J.; Scherer, G. W., *Sol-gel science: the physics and chemistry of sol-gel processing*. Academic press: 2013.
369. Schulze-Bergkamen, H.; Yamane, M. *Journal of Sol-gel Science and Technology* **1995**, *5*, (3), 185-191
370. Yamane, M. *Journal of Sol-gel Science and Technology* **1997**, *8*, (1-3), 483-487
371. Li, D.; Guan, Z.; Zhang, W.; Zhou, X.; Zhang, W. Y.; Zhuang, Z.; Wang, X.; Yang, C. J. *ACS Applied Materials and Interfaces* **2010**, *2*, (10), 2711-2714

372. Weiss, E.; Dutta, B.; Kirschning, A.; Abu-Reziq, R. *Chemistry of Materials* **2014**, 26, (16), 4781-4787
373. Zhang, H.; Sun, S.; Wang, X.; Wu, D. *Colloids and Surfaces A: Physicochemical and Engineering Aspects* **2011**, 389, (1-3), 104-117
374. Yamane, M.; Shibata, S.; Yasumori, A.; Yano, T.; Uchihiro, S. *Journal of Sol-gel Science and Technology* **1994**, 2, (1-3), 457-460
375. Zoabi, A.; Omar, S.; Abu-Reziq, R. *European Journal of Inorganic Chemistry* **2015**,
376. Hu, R.; Zhu, Q.; Chen, W.; Liu, H.; Yao, B.; Zhan, J.; Hao, J.; Han, C. C. *Polymer* **2012**, 53, (2), 267-271

Chapter 2

Sieving of hot gases by hyper-cross-linked nanoscale-hybrid membranes

*This chapter has been adapted from: Raaijmakers, M.J.T., Hempenius, M.A., Schön, P.M., Vancso, G.J., Nijmeijer, A., Wessling, M., Benes, N.E., Sieving of hot gases by hyper-cross-linked nanoscale-hybrid membranes. *J. Am. Chem. Soc.*, **2014**, 136 (1), pp. 330–335. (DOI:10.1021/ja410047u)*



Abstract

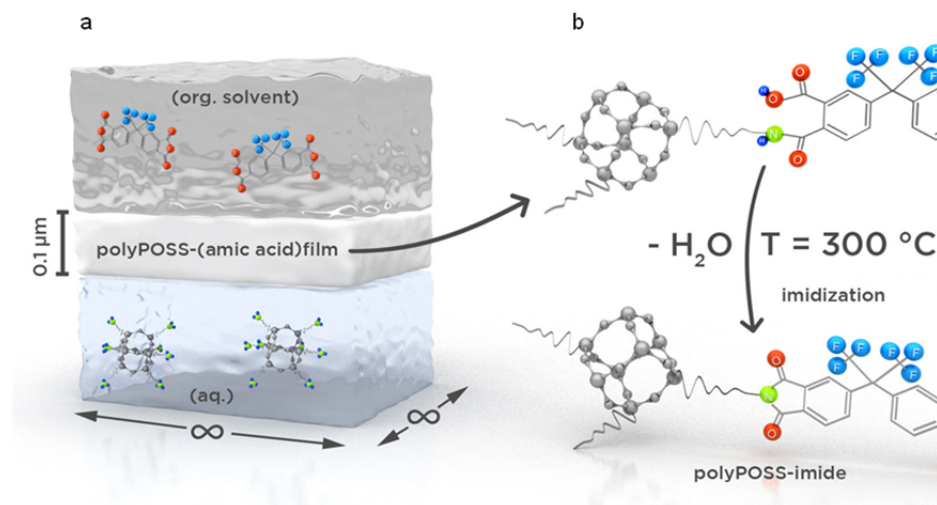
Macromolecular networks consisting of homogeneously distributed covalently bonded inorganic and organic precursors are anticipated to show remarkable characteristics, distinct from those of the individual constituents. A novel hyper-cross-linked ultrathin membrane is presented, consisting of a giant molecular network of alternating polyhedral oligomeric silsesquioxanes and aromatic imide bridges. The hybrid characteristics of the membrane are manifested in excellent gas separation performance at elevated temperatures, providing a new and key enabling technology for many important industrial scale applications.

2.1. Introduction

Membrane separation of hot gases is a key enabling technique for many large-scale chemical processes and advanced energy production technologies.¹⁻³ Today, no membranes exist that allow selective separation of hot small gas molecules on a large scale. At elevated temperatures, state-of-the-art organic polymer membranes exhibit increased macromolecular dynamics,^{4,5} whereas a high polymer chain rigidity is a prerequisite for effective molecular sieving.⁶⁻⁹ The separation performance of even very rigid polymers, such as polyimides, subsides above 200 °C.^{5,10} Development of novel high temperature polymers such as polybenzimidazoles, and thermally rearranged poly(benzoxazole)s and poly(benzoxazole-co-imides) have the potential to overcome the temperature limitations of polymers, but until now relatively few data is available for high temperature applications.¹¹⁻¹⁴ Also, recent advances in nanoengineering of materials have resulted in radically different synthesis approaches for nanostructured membranes and thin films.¹⁵⁻¹⁹ These systems may well approach the ultimate gas separation performance, yet tremendous efforts are required to allow defect-free processing at the scale of industrially relevant applications. Here, we present a method for the facile production of ultrathin films of inorganic-organic hybrid materials that provide gas separation selectivity up to 300 °C, in combination with chemical versatility and large-scale defect-free processability. The unprecedented characteristics of these membranes originate from the hyper-cross-linked periodic network of covalently bound organic and POSS moieties.

The poly(POSS-imide) material presented consists of polyhedral oligomeric silsesquioxane (POSS) molecules, covalently linked by aromatic imide bridges. Cross-linked aromatic polyimides are considered high potential membrane materials.²⁰ The POSS are silicon oxide cages with the basic formula $R_nSi_nO_{1.5n}$ ($n = 6, 8, 12$) and are decorated with various organo-functional groups. Their cubic symmetry and the availability of a large variety of functional groups allows for nanoscale assembly in three dimensions.²¹⁻²⁵ The rigidity and bulky character of POSS cages is manifested by the free volume increase observed in systems where POSS is dispersed in the polymer matrix or covalently attached to the polymer main chain.^{26,27} However, such systems are still governed by the macromolecular dynamics of the polymer main chain. Instead, we propose to use the POSS cage as a main building block for the polymer network. We suggest the synthesis of hybrid poly(POSS-imide)s films using a two-step procedure: the interfacial

polycondensation of an ammonium chloride salt-functionalized POSS and hexafluoroisopropylidene diphthalic anhydride (6FDA) based on a concept proposed by Dalwani et al.,²⁸ followed by thermal imidization. In the first step, a thin-film poly[POSS-(amic acid)] network is formed via a polycondensation reaction at the interface between two immiscible solvents, as shown in **Scheme 1-1 (left panel)**. A water-soluble octa-ammonium POSS in alkaline solution and 6FDA in toluene were used as the amine and anhydride sources, respectively. In the second step, the amic acid groups are converted into cyclic imide groups via thermal imidization at temperatures up to 300 °C in either air or an inert atmosphere, as shown in **Scheme 1-1 (right panel)**.



Scheme 1-1. The membrane synthesis process. (a) Interfacial polymerization reaction of octa-ammonium POSS in water and 6FDA in toluene. The ammonium groups are partially deprotonated to primary amines by sodium hydroxide (NaOH, pH = 9.9 ± 0.3). The reaction occurs at the water-toluene interface, with final layer poly[POSS-(amic acid)] thicknesses of ~0.1 μm after 5 min. (b) The subsequent conversion of the amic acid to cyclic imide (imidization) is performed via heat treatment at temperatures up to 300 °C.

2.2. Experimental

2.2.1. Synthesis of poly(POSS-imide)s via interfacial polymerization

Toluene (anhydrous 99.8 wt.%, Sigma-Aldrich), 4,4-(hexafluoroisopropylidene) diphthalic anhydride (6FDA, Sigma-Aldrich), ammonium chloride salt functionalized POSS (OctaAmmonium POSS[®], Hybrid Plastics (USA)) and sodium hydroxide (1.0 mol L⁻¹) were used as received. Free-standing hybrid films were prepared by adjusting the pH of an aqueous solution of 0.9 wt.% octa-ammonium POSS, by adjusting the pH to 9.9 using sodium hydroxide (0.1 mol L⁻¹), and subsequently contacting the aqueous solution with a 6FDA solution in toluene (0.075 wt.%). The reaction at the interface between the aqueous POSS solution and 6FDA in toluene was confirmed by observing the thin-film formation. The mechanical integrity of the films was sufficient for their removal from the interface. The rapid kinetics of the polycondensation reaction allow for the production of a sufficient amount of freestanding film for bulk material characterization, such as infrared spectroscopy. Detailed thin-film characterization was performed on the supported thin films, that were produced directly on ceramic membranes (α -alumina discs with a 3- μ m-thick γ -alumina layer). Film formation atop porous alumina supports was achieved by soaking the porous ceramic material in the aqueous POSS solution, followed by contacting with the 6FDA solution in toluene. The membrane was thermally imidized at 300 °C at a heating rate of 5 °C min⁻¹ under an air atmosphere.

2.2.2. Material characterization.

Static liquid/air contact angles were measured with a goniometer (OCA 15, Data Physics). Drops of 1 μ L milli-Q water were formed at the needle tip and contact angles were measured 5 s after placing the drop on the substrate.

Density measurements were performed using an AccuPyc II 1340 gas displacement density analyzer (Micromeritics, USA), with helium as gas source. The poly[POSS-(amic acid)] and poly(POSS-imide) samples were placed in a vacuum chamber, at 30 °C, prior to the measurement to remove any water from the sample. The standard deviation was determined from 30 individual density measurements.

Scanning electron microscopy (SEM) images were obtained using a LEO-1550 Schottky field emission scanning electron microscope (Carl-Zeiss, Germany), with an accelerating voltage of 2.00 kV. Atomic Force Microscopy (AFM)

measurements were performed using a Multimode 8 AFM instrument equipped with a NanoScope V controller, and a vertical engage J-scanner (Bruker AXS, Santa Barbara, CA). Membrane samples were glued to a metal support using a two component epoxy and dried overnight. Image processing and data analysis were performed with NanoScope software version 8.14 and NanoScope Analysis software version 1.40. Peak force tapping was done in air with Si tips on SiN cantilevers (SCANASYST-AIR, Bruker AXS, Camarillo, CA, nominal spring constant 0.4 N m^{-1}). Cantilever spring constants were determined with the thermal noise method. Imaging was done with a peak force tapping amplitude of 150 nm and at a scan rate of 0.97 Hz.

Membrane single gas permeation experiments were performed in a dead-end mode at a trans-membrane pressure of 2 bar, and atmospheric pressure at the permeate side. Once the helium permeance remained constant, the other gases (N_2 , CH_4 , H_2 , and CO_2 , consecutively) were measured at temperatures between 50-300 °C.

2.3. Results and discussion

Film formation was confirmed using scanning electron microscopy (SEM) cross section images, and top-view atomic force microscopy (AFM) as depicted in **Figure 2-2**. The SEM micrograph reveals a distinct continuous film of approximately $0.1 \mu\text{m}$ atop the ceramic support. The AFM top-view topography image of the poly[POSS-(amic acid)] reveals a smooth top layer with height differences ($0.1 \mu\text{m}$) and a morphology less coarse compared to that of typical layers obtained via interfacial polymerization.²⁹ **Figure 2-2 (b)** and **2-2 (d)** correspond to the poly(POSS-imide) layer obtained after thermal imidization at 300 °C. The SEM micrograph demonstrates that a distinct and continuous film remains on the support. The AFM images do exhibit a change in morphology resulting from stresses in the thin film confined on the porous support. Density measurements via helium pycnometry on the freestanding film material reveal that these stresses originate from densification, with the bulk density increasing from 1.5 g cm^{-3} to 1.67 g cm^{-3} , induced by the chemical conversion of the amic acid groups to cyclic imides. However, no cracks appear to form in the ultrathin films. The high degree of crosslinking and the limited thickness of this layer prevent any pinhole or crack formation that could degrade the membrane's gas separation performance.

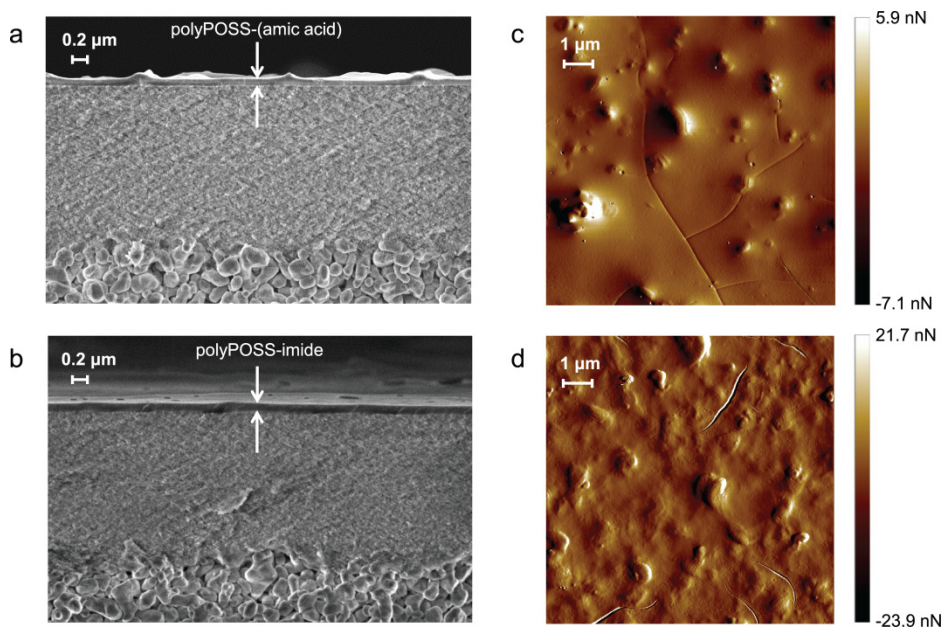


Figure 2-2: Heat treatment induced evolution of membrane layer morphology. (a-b) SEM micrograph of 0.1- μm poly[POSS-(amic acid)] and poly(POSS-imide) layers, on α -alumina discs with a 3- μm -thick γ -alumina layer. The homogeneous supported films exhibit no apparent crack formation due to drying stresses or heat treatment. (c-d) The AFM peak force error images of the supported poly[POSS-(amic acid)] demonstrate that the film formation results in a smooth layer with hills and valleys of lateral dimensions up to 0.2 μm . The poly(POSS-imide) (d) layer exhibits a similar hill-valley structure. The heat-treatment step increases the intrinsic and thermal stress-induced surface roughness.

The formation of the poly[POSS-(amic acid)] and its subsequent conversion to poly(POSS-imide) via thermal treatment are confirmed using Fourier transform infrared spectroscopy with attenuated total reflectance (FTIR-ATR). **Figure 2-3 (a)** presents the spectra of the samples before and after thermal imidization at 300 $^{\circ}\text{C}$. The untreated sample exhibits two typical polyamide bands at 1620 and 1570 cm^{-1} that correspond to C=O stretching and N-H bending, respectively. After thermal treatment, these two bands vanish, and two distinct bands emerge at 1720 and 1780 cm^{-1} that can be attributed to polyimide C=O symmetric and asymmetric stretching, respectively. The thermal conversion to polyimide is not inhibited by the presence of water, whereas trace water removal is a main challenge in the synthesis of polyimides via polymerization in aprotic polar solvents.³⁰ **Figure 2-3 (b)** displays the

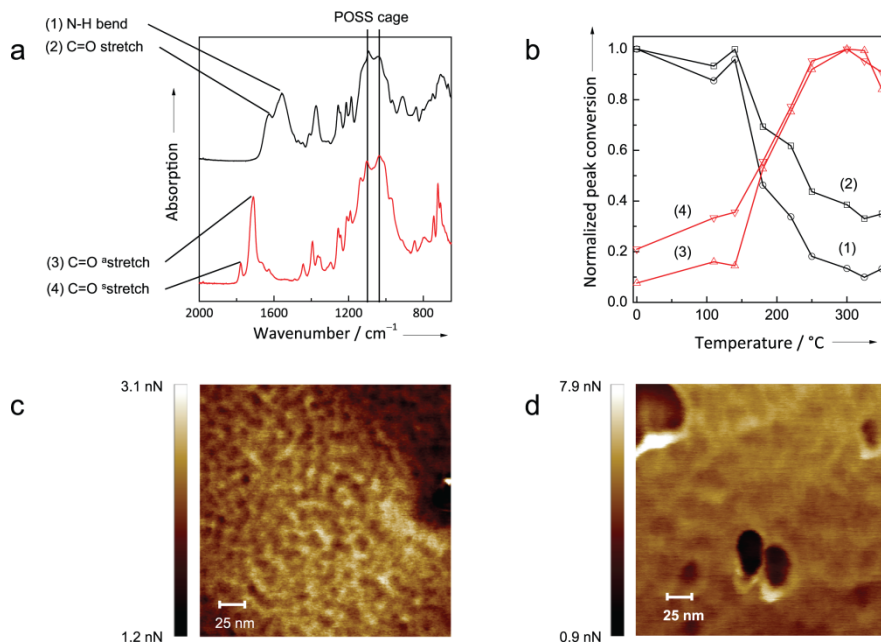


Figure 2-3: Heat treatment induced imidization. a, ATR-FTIR spectra of free-standing poly[POSS-(amic acid)] layers prior to (top line) and after heat treatment for 2 h in air at 300 °C (bottom line), normalized for the CF_3 band at 1254 cm^{-1} . The bands at 1620 and 1570 cm^{-1} are assigned to N-H bending (1) and C=O stretching (2) of the amic acid group. After heat treatment, the bands at 1620 and 1570 cm^{-1} are replaced by bands at 1720 and 1780 cm^{-1} that are assigned to C=O asymmetric (3) and symmetric (4) stretching of the imide group, respectively. The sharp bands at 1125 and 1040 cm^{-1} can be attributed to the Si-O-Si asymmetric stretching vibrations of the polyhedral and ladder silsesquioxane structures, respectively. The results indicate complete conversion of the amic acid groups to cyclic imide groups, and suggest a concurrent partial cleavage of the POSS cage induced by the high pH during synthesis.³¹ b, ATR-FTIR band intensities of (1) and (2) normalized with respect to their initial intensities and the band intensities of (3) and (4) normalized with respect to the imide band intensity of the 300 °C-treated sample as a function of temperature. The results indicate that imidization is initiated at 140–160 °C, reaching a maximum conversion at 300 °C. c-d, AFM adhesion images of poly[POSS-(amic acid)] and poly(POSS-imide) layers. The images reveal homogeneously distributed areas of several nanometers in size with varying adhesion strength that correspond to regions with different chemical compositions.

intensities of the two amic acid bands at 1570 (1) and 1620 cm^{-1} (2) and of the imide bands at 1720 (3) and 1780 cm^{-1} (4). The spectra are normalized with respect to the C-F band intensity at 1254 cm^{-1} . At temperatures below 140 °C, no imidization occurs. The onset of imidization is observed between 140 and 160 °C, and increases up to 300 °C, above which a decrease in band intensity is observed that can be explained by de-imidization and polymer-bond degradation. This result is confirmed via thermogravimetric analysis (TGA) that indicates that there is no weight loss at temperatures up to 300 °C in either air or nitrogen atmospheres (Appendix, Figure A2-3). **Figure 2-3 (c and d)** present the adhesion-force images of poly[POSS-(amic acid)] and poly(POSS-imide). Peak force tapping AFM was used to map the adhesion forces of the poly[POSS-(amic acid)] and poly(POSS-imide) surfaces. The adhesion force was determined from the force-distance curves corresponding to an oscillating AFM tip that contacts the sample upon each oscillation at a rate well below the resonance frequency of the AFM cantilever.³² The images reveal 1–5-nm sized heterogeneities, bearing resemblance to two-dimensional periodic covalent organic frameworks,³³ that can be attributed to the intrinsic molecular local ordering of inorganic and organic moieties. This local intrinsic ordering remains after the amic acid is converted into the imide; however, the force contrast diminishes. This result can be rationalized through the replacement of the strong polar amic acid with a weakly interacting imide. A comparison of the water contact angle measurements of the poly[POSS-(amic acid)] (53°) with those of the poly(POSS-imide) (72°) suggest a similar effect, supporting a nanoscale evolution in the adhesion force.

The hybrid characteristics of the material are manifested in the exceptional gas separation performance at elevated temperatures. Unprecedented performance at temperatures up to 300 °C (the practical limit of the measurement apparatus) is observed from individual gas permeation experiments. **Figure 2-4** illustrates the gas permeation behavior of poly(POSS-imide) on α -alumina discs with a 3- μm -thick γ -alumina layer. **Figure 2-4 (left panel)** depicts a plot of the single gas permeance as a function of the gas molecule kinetic diameter (for He, H₂, CO₂, N₂ and CH₄) at 100, 200 and 300 °C. The permeance decreases with increasing gas molecule kinetic diameter, a trend typical of glassy polymers. **Figure 2-4 (middle panel)** depicts the Arrhenius plot of the permeance on a logarithmic scale as a function of $R^{-1}T^{-1}$ reveals that the gas permeance is thermally activated. The activation energies for the measured gases are in the order CH₄ > N₂ > H₂ > He > CO₂. The poly(POSS-imide) activation energies

for gas permeation are a factor 5-7 higher as compared to conventional polyimides.³⁴ The relatively high activation energies for permeation underline the high energy barriers for gas diffusion in the rigid poly(POSS-imide) network.

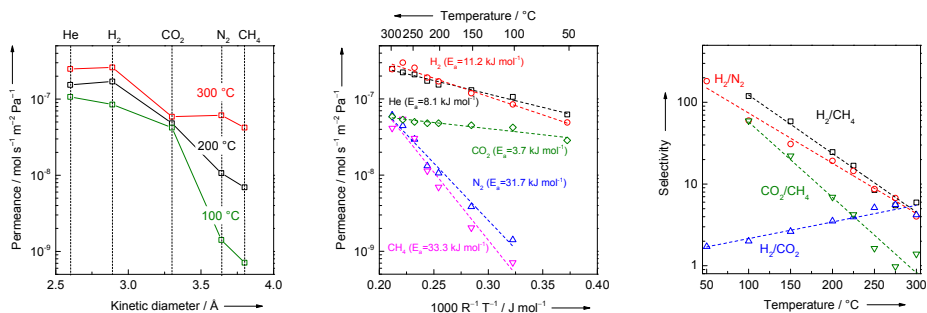


Figure 2-4: Gas permeation characteristics of poly(POSS-imide) membranes. (left panel) Permeance as a function of gas kinetic diameter. The decrease in permeance with increasing kinetic diameter is consistent with the glassy character of the poly(POSS-imide). (middle panel) Arrhenius plot of single gas permeances for He, H₂, CO₂, N₂ and CH₄. For all gases, activated transport is the dominant transport mechanism. The apparent activation energies for transport remain constant over temperatures ranging from 50–300 °C, demonstrating that the membrane does not suffer from temperature-induced chain mobility. (right panel) Ideal selectivity of H₂/CH₄, H₂/N₂, CO₂/CH₄ and H₂/CO₂ as a function of temperature.

The low activation energy for the CO₂ transport results from the high solubility of CO₂ at low temperatures due to the presence of trifluoromethyl (CF₃) groups. At elevated temperatures, this solubility decreases, while the diffusivity increases, cancelling out the effect of temperature on the product of these processes. This is in agreement with gas sorption and diffusion data measured for other 6FDA based polyimide membranes.³⁴⁻³⁶ These studies show that, for increasing temperature, the CO₂ permeation remains constant or even decreases. The correspondingly low activation energy is related to the simultaneous increase in gas diffusivity and decrease in gas sorption, at increasing temperatures. For the other gases, He, N₂ and CH₄, the permeation does increase with temperature. The result is a decrease in selectivity of CO₂ over these other gases. Conventional polyimides without CF₃ groups do not display such behavior.³⁷ The affinity towards CO₂ implies that gas molecules

diffuse in the organic part of the network, which is in agreement with the findings of molecular dynamics simulations.³⁸

Unlike polymer membranes that suffer from chain-rearrangement-induced permeability loss at the elevated temperatures used in this study, this linear trend in the Arrhenius plot suggests that the activation energies of diffusion and sorption do not significantly depend on the temperature. The high thermal stability of the membrane can be rationalized by the large number of covalent bonds between the individual POSS cages. An average POSS/imide ratio of 3.8 was observed using X-ray photoelectron spectroscopy (XPS) of a poly(POSS-imide) membrane on an alumina support (Appendix). **Figure 2-4 (right panel)** presents the ideal selectivities of the H₂/CH₄, H₂/N₂, CO₂/CH₄ and H₂/CO₂ gas pairs as a function of the temperature. The persistence of selectivity at elevated temperatures underlines the moderation of augmented macromolecular dynamics in the hyper-cross-linked poly(POSS-imide) network. The dilation of the network is impeded by the high large number of organic bridges linking the rigid POSS cages, while molecular motions of the organic bridges allow diffusion of gas molecules.³⁹ The selectivity as a function of temperature decreases due to the differences in the activation energies between gases, which results in an increase in the H₂/CO₂ selectivity with temperature and a decrease in the selectivities for the other gas pairs. Most surprisingly, the poly(POSS-imide) membrane retains gas selectivities of approximately 5 for H₂/CH₄ and H₂/N₂ at 300 °C, which are unsurpassed by any other polymeric membrane. Moreover, the CO₂/CH₄ selectivities of approximately 60 at temperatures below 100 °C emphasize the applicability of the poly(POSS-imide) over a broad temperature range.

2.4. Conclusion

In summary, we have described the preparation of poly(POSS-imide) ultrathin gas separation membranes using interfacial polymerization followed by thermal imidization. The interfacial reaction results in an intrinsic homogeneous distribution of inorganic and organic constituents on the molecular scale. The subsequent heat treatment successfully converts the as-formed amic acid into a cyclic imide at temperatures exceeding 180 °C. The hybrid character of the thin film is manifested in its excellent gas separation performance at elevated temperatures, which originate from the hyper-cross-linked periodic network of covalently bound rigid POSS and mobile organic moieties. The presented method can be easily extended to other dianhydride

linkers to yield the next generation of potential gas separation membranes for elevated-temperature applications.

2.5. Acknowledgements

This project has received funding from the European Union's Seventh Framework Programme for research, technological development and demonstration under CARENA grant agreement no. 263007.

2.6. Appendices

2.6.1. Poly(POSS-imide) synthesis

Figure A2-1 shows the reaction scheme of poly[POSS-(amic acid)] and poly(POSS-imide) macromolecular network. Water soluble ammonium chloride salt functionalized POSS is first dissolved in an alkaline aqueous solution, allowing the conversion of ammonium to primary amine.

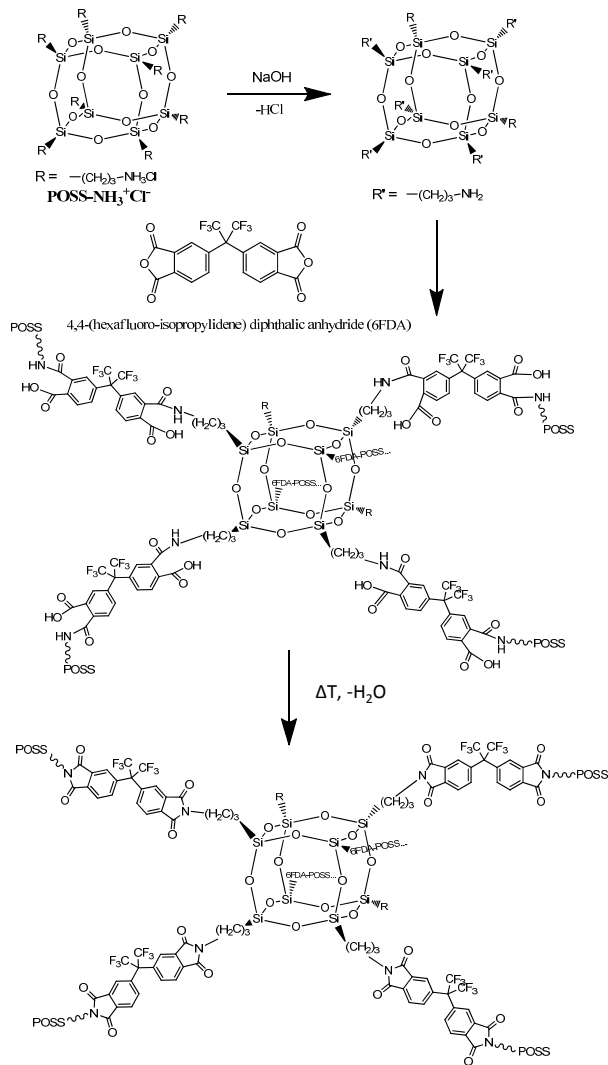


Figure A2-1. Interfacial polymerization reaction of partially deprotonated octa-ammonium POSS and 6FDA. The formed poly[POSS-(amic acid)] is subsequently converted to a poly(POSS-imide) by heat treatment.

The alkaline aqueous POSS solution is brought into contact with a 6FDA solution in toluene; the POSS and dianhydride react at the water/toluene interface, forming the thin film, hybrid poly[POSS-(amic acid)] network. Next, formation of poly(POSS-imide) is achieved by heat treatment at temperatures up to 300 °C, converting the amic acid into cyclic imide bonds. Any unreacted POSS and 6FDA on the sample surface was removed by acetone and water

washes. Samples were dried for 24 hours in dry nitrogen atmosphere to remove any toluene and unbound water.

Supported thin films were produced on α -alumina discs coated with 3 μm thick γ -alumina (porosity of 60 % and a pore size of 2-3 nm). Pre-wetted discs, held fixed on a perforated plate by vacuum, were impregnated with the POSS solution. Following, the discs were left to dry in a nitrogen atmosphere for 30 min and subsequently submersed in the 6FDA in toluene solution (0.075 wt.%).

2.6.2. Material characterization

Differential scanning calorimetry

Differential scanning calorimetry (DSC) was performed using a Perkin Elmer DSC 8000. Free standing poly(POSS-imide) was placed in an aluminum sample pan and cycled from 50 to 300 $^{\circ}\text{C}$ with a heating rate of 20 $^{\circ}\text{C min}^{-1}$. Four subsequent heating and cooling cycles were used to prevent influence from sorbed water on the measurement.

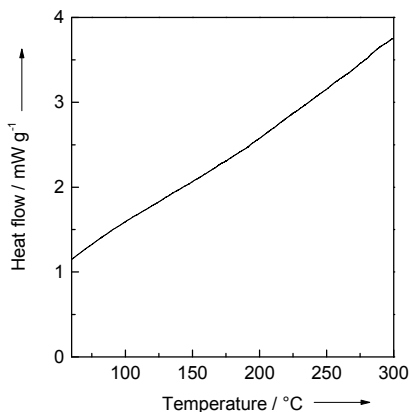


Figure A2-2: DSC analysis of a poly(POSS-imide) powder sample.

The heat flow as function of temperature shown in **Figure A2-2** displays a steady increase of the heat flow with temperature. The absence of any peaks in the heat flow as a function of temperature evidences that there is no glass transition for temperatures up to 300 $^{\circ}\text{C}$.

Thermal gravimetric analysis

Thermal gravimetric analysis (TGA) was performed with NETZSCH STA 449 (Germany). Measurements were done on 1.5 mg samples in alumina pans, under an air and nitrogen atmosphere (50 ml min^{-1}) respectively, with a heating rate of $10 \text{ }^\circ\text{C}$. The thermal gravimetric evolution of freestanding poly(POSS-imide) shown in **Figure A2-3** demonstrates that both under air and nitrogen the onset of weight loss is located above $300 \text{ }^\circ\text{C}$. In air the sample reaches a constant mass at around $600 \text{ }^\circ\text{C}$ while for nitrogen weight loss persists even at $1100 \text{ }^\circ\text{C}$, indicating two distinct degradation mechanisms. Both samples reach a final mass of 35% of the initial mass, having the appearance of a white powder in air atmosphere, and black powder in nitrogen atmosphere.

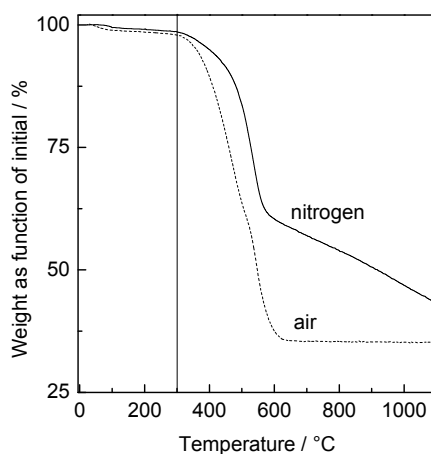


Figure A2-3: TGA analysis in air and nitrogen of a poly(POSS-imide) powder sample

X-ray photoelectron spectroscopy

X-ray photoelectron spectroscopy measurements were performed on a Quantera SXM scanning XPS microprobe (Physical Electronics), using a monochromatic Al $K\alpha$ source (1486.6 eV). The ratio of silica and fluorine elements indicates the presence of 1.9 dianhydride bridging molecules per POSS cage. Assuming complete conversion of the anhydride groups to cyclic imides, each POSS cage is connected with an average of 3.8 bridges. This assumption follows from the absence of anhydride and carboxylic acid peaks

in the FTIR-ATR spectra and is in agreement with the nitrogen and carbon elemental fits.

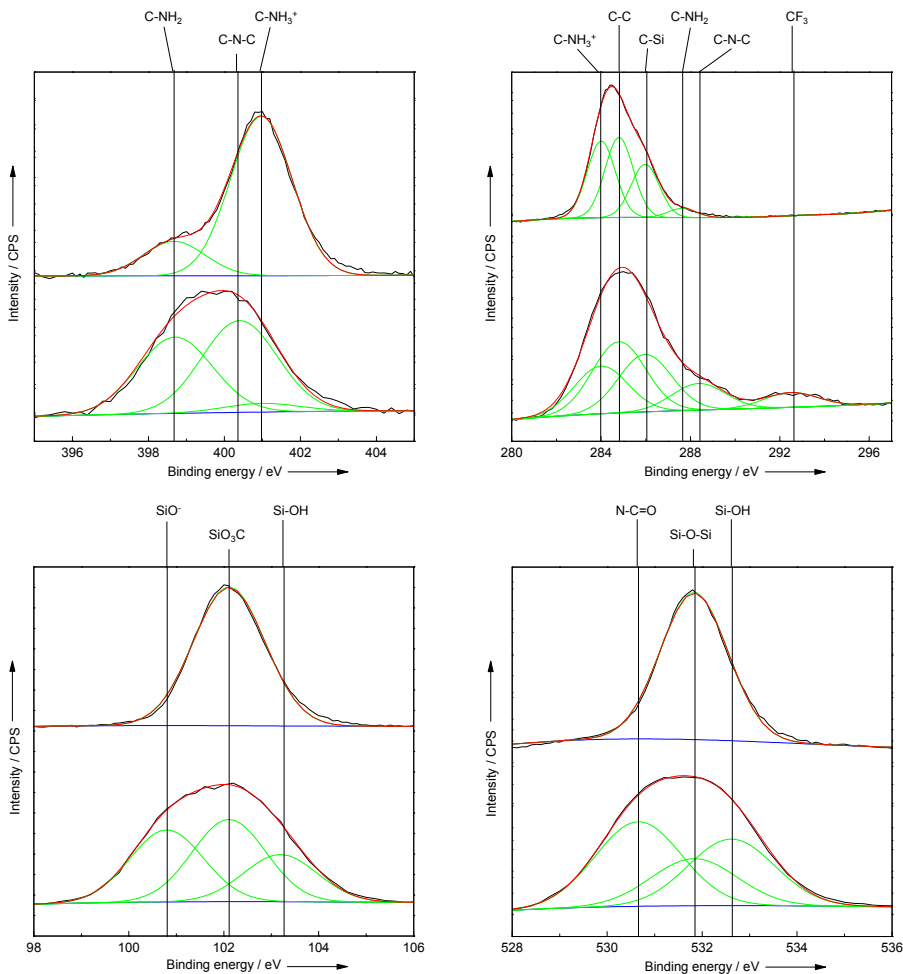


Figure A2-4: XPS elemental spectra for the N1s, C1s, Si2p and O1s signal. The data fitting has been performed using the peak analyzer function of Origin software. The peaks were fitted using Gaussians with similar FWHM values.

The nitrogen, carbon, oxygen and silica elemental fits of octa-ammonium POSS powder and poly(POSS-imide) on α -alumina discs coated with 3 μm thick γ -alumina are shown in **Figure A2-4**. The nitrogen elemental fit of octa-ammonium POSS shows two distinct peaks, attributed to the partially deprotonated ammonia groups. The binding energies of the amine and

ammonia groups were fixed in the poly(POSS-imide) nitrogen peak fit, to determine the number of imide bonds per POSS molecule.

Table A2-1: XPS elemental composition for Octa-ammonium POSS and poly(POSS-imide) samples.

	Octa-NH ₃ POSS (theoretical)	Octa-NH ₃ POSS		Poly(POSS- imide)	
	Element concentration (%)	Element concentration (%)	Standard deviation (%)	Element concentration (%)	Standard deviation (%)
C	40	47.8	3.7	54.7	1.0
N	13.33	9.8	1.1	5.0	0.4
O	20	22.0	2.4	22.5	0.6
Si	13.33	11.5	1.1	6.9	0.1
F	-	-	-	9.8	0.1
Cl	13.33	9.0	1.5	-	-
Na	-	0.8	0.9	0.5	0.3
C/N	3	3.4		10.9	
F/Si	-	-		1.4	
O/N	1.5	1.6		4.5	
Cl/N	1	0.9		-	

The resulting fit indicates that 4 out of 8 groups per POSS molecule have been converted to imide groups. The imide binding energy is in agreement with values found for other polyimides.⁴⁰ The remaining unreacted groups mainly consist of amine groups, indicating that most ammonia groups are deprotonated upon interfacial polymerization. The binding energies of the octa-ammonium POSS were fixed in the carbon elemental fit of the poly(POSS-imide). The poly(POSS-imide) carbon elemental peak fit shows two additional peaks with respect to octa-ammonium POSS. These peaks are attributed to the imide bond (288.6 eV) and CF₃ groups (292.5 eV), in accordance to typical binding energies found for these bonds. The ratio of the imide:CF₃ peak fit area (approximately 2:1) is in good agreement with the supposition that both anhydride groups of the 6FDA are converted to cyclic imide bonds.

The silicon elemental fit of octa-ammonium POSS shows a single peak, attributed to the SiO₃C groups of the POSS cage. The silicon elemental fit of

the poly(POSS-imide) shows two additional peaks at a lower and higher binding energy. These peaks are associated with silanol and SiO⁻ formed by partial hydrolysis of the POSS cage.⁴¹ The formation of silanol is known to both shift the binding energy, and broaden the XPS spectrum.⁴²

The oxygen elemental spectrum of octa-ammonium shows a single peak associated with siloxane bonds in the POSS cages. The poly(POSS-imide) oxygen elemental spectrum shows an additional peak at a binding energy of 530.7 eV, and is associated with the C=O of the imide group. The binding energy peak that emerged at 532.6 eV is considered to be from silanol bonds, in agreement with the peak fit of silicon for the poly(POSS-imide) sample. In summary, the XPS spectra suggests a high degree of cross-linking between the POSS cages, with approximately 4 out of 8 functional groups that have reacted with a dianhydride. Also, the data shows that the POSS cage is partially hydrolyzed during the interfacial polymerization reaction.

Attenuated Total Reflection Fourier Transform Infrared Spectroscopy

The chemical structures of the poly[POSS-(amic acid)] and poly(POSS-imide) were analyzed with Attenuated Total Reflection Fourier Transform Infrared Spectroscopy (ATR-FTIR) on free standing films using an ALPHA FT-IR Spectrometer (Bruker Optics Inc., Germany) equipped with a ZnSe crystal. All spectra were recorded at room temperature. Thermal imidization was done by heat treatment in air for two hours at temperatures ranging from 0-300 °C. A detailed analysis of the poly[POSS-(amic acid)] and poly(POSS-imide) infrared absorption spectra is given in **Table A2-2**. The infrared data confirms the presence of the partially hydrolyzed POSS cage, in accordance with the XPS data. Presence of aliphatic carbon originating from octa-ammonium POSS, CF₃ groups and phenyl groups of the 6FDA bridging molecule is confirmed by the infrared data. The differences between the spectra of the poly[POSS-(amic acid)] and poly(POSS-imide) originate solely from the conversion of the amic acid groups to cyclic imide.

Table A2-2: FTIR-ATR peak analysis data for a poly[POSS-(amic acid)] and poly(POSS-imide) sample

Wavenumber	Poly[POSS-(amic acid)]	Poly(POSS-imide)		
cm^{-1}	<i>Intensity</i>	<i>Intensity</i>	<i>Bond</i>	<i>Vibrational mode</i>
691	high	shoulder	CF ₃	def vib
706	high	high	NH ₂	def vib of primary amine
725	shoulder	high	CF ₃	def vib
750	medium	medium	CH	out of plane 1,2,4, trisubstituted benzene
793	shoulder	medium	NH ₂	out of plane bend
846	medium	medium	NH ₂	out of plane bend
910	medium	shoulder	C-C	rocking
965	medium	medium	C-C	rocking
1000	shoulder	shoulder	C-C	rocking
1040	high	high	Si-O cage	str
1093	high	high	Si-O ladder	str
1122	shoulder	high	CF ₃	str
1185	medium	medium	CF ₃	str
1212	medium	medium	CF ₃	str
1245	medium	medium	CF ₃	str
1255	medium	medium	CF ₃	str
1393	-	medium	C=O or C-N	str
1374	high	-	C-N	str
1445	low	medium	CH ₂	scissoring
1475	low	low	CH ₂	def vib
1560	high	-	N-H	bend amide
1627	high	low	C=O	str amide
1670	-	shoulder	C=O	str carboxylic acid
1710	-	high	C=O	asym str imide
1780	-	low	C=O	sym str imide
2886	shoulder	-	CH ₂	sym str
2939	low	-	CH ₂	asym str
3068–3235	broad	-	H ₂ O/COOH	bend
3380	broad	broad	NH ₂	asym str

2.6.3. Membrane single gas permeation experiments

Membrane single gas permeation experiments were performed in a dead-end mode at a trans-membrane pressure of 2 bar, and atmospheric pressure at the permeate side. Single gas permeation of N₂, CH₄, H₂, and CO₂ were measured at temperatures between 50-300 °C. The apparent activation energy for gas permeance (E_p) was determined using a linear fit using OriginPro 9 software. The activation energies were compared with those of conventional and 6FDA based polyimides, as shown in **Table A2-3**.

Table A2-3: gas permeance activation energy for polyimide membranes

E_p (kJ mol ⁻¹)	E_p (kJ mol ⁻¹)	E_p (kJ mol ⁻¹)	Reference
CO ₂	N ₂	CH ₄	
3.7	31.7	33.3	Current study
-3.3	3.5		³⁴
-1.3			³⁶
0.2	4.45	7.25	³⁵
10.5	24.1		³⁷
14.3	27.3		
21.0	31.2		

2.7. References

1. Niwa, S. I.; Eswaramoorthy, M.; Nair, J.; Raj, A.; Itoh, N.; Shoji, H.; Namba, T.; Mizukami, F. *Science* **2002**, 295, (5552), 105-107
2. Jiang, H.; Cao, Z.; Schirmermeister, S.; Schiestel, T.; Caro, J. *Angew. Chem. Int. Ed.* **2010**, 49, (33), 5656-5660
3. Choudhary, V. R.; Gaikwad, A. G.; Sansare, S. D. *Angew. Chem. Int. Ed.* **2001**, 40, (9), 1776-1779
4. Wind, J. D.; Sirard, S. M.; Paul, D. R.; Green, P. F.; Johnston, K. P.; Koros, W. J. *Macromolecules* **2003**, 36, (17), 6433-6441
5. Koros, W. J.; Woods, D. G. *J. Membr. Sci.* **2001**, 181, (2), 157-166
6. Guiver, M. D.; Lee, Y. M. *Science* **2013**, 339, (6117), 284-285
7. Carta, M.; Malpass-Evans, R.; Croad, M.; Rogan, Y.; Jansen, J. C.; Bernardo, P.; Bazzarelli, F.; McKeown, N. B. *Science* **2013**, 339, (6117), 303-307
8. Du, N.; Park, H. B.; Robertson, G. P.; Dal-Cin, M. M.; Visser, T.; Scoles, L.; Guiver, M. D. *Nat. Mater.* **2011**, 10, (5), 372-375
9. Song, Q.; Cao, S.; Zavala-Rivera, P.; Ping Lu, L.; Li, W.; Ji, Y.; Al-Muhtaseb, S. A.; Cheetham, A. K.; Sivaniah, E. *Nat. Commun.* **2013**, 4,
10. Rezac, M. E.; Koros, W. J.; Miller, S. J. *J. Membr. Sci.* **1994**, 93, (2), 193-201

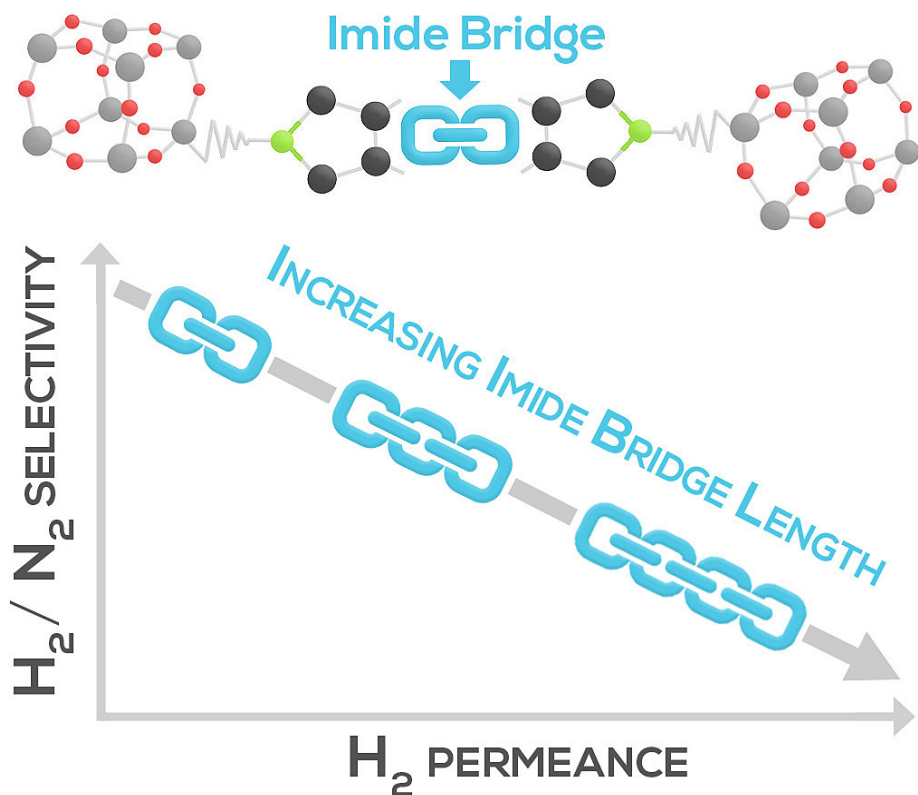
11. Calle, M.; Doherty, C. M.; Hill, A. J.; Lee, Y. M. *Macromolecules* **2013**, *46*, (20), 8179-8189
12. Calle, M.; Lozano, A. E.; Lee, Y. M. *Eur. Polym. J.* **2012**, *48*, (7), 1313-1322
13. Joseph, W. D.; Abed, J. C.; Mercier, R.; McGrath, J. E. *Polymer* **1994**, *35*, (23), 5046-5050
14. Kim, S.; Han, S. H.; Lee, Y. M. *J. Membr. Sci.* **2012**, 403-404, 169-178
15. Angelova, P.; Vieker, H.; Weber, N. E.; Matei, D.; Reimer, O.; Meier, I.; Kurasch, S.; Biskupek, J.; Lorbach, D.; Wunderlich, K.; Chen, L.; Terfort, A.; Klapper, M.; Müllen, K.; Kaiser, U.; Götzhäuser, A.; Turchanin, A. *ACS Nano* **2013**, *7*, (8), 6489-6497
16. Vendamme, R.; Onoue, S. Y.; Nakao, A.; Kunitake, T. *Nat. Mater.* **2006**, *5*, (6), 494-501
17. Peinemann, K. V.; Abetz, V.; Simon, P. F. W. *Nat. Mater.* **2007**, *6*, (12), 992-996
18. Du, N.; Park, H. B.; Dal-Cin, M. M.; Guiver, M. D. *Energy Environ. Sci.* **2012**, *5*, (6), 7306-7322
19. Ho, B. P.; Chul, H. J.; Young, M. L.; Hill, A. J.; Pas, S. J.; Mudie, S. T.; Van Wagner, E.; Freeman, B. D.; Cookson, D. J. *Science* **2007**, *318*, (5848), 254-258
20. Vanherck, K.; Koeckelberghs, G.; Vankelecom, I. F. J. *Prog. Polym. Sci.* **2013**, *38*, (6), 874-896
21. Laine, R. M.; Roll, M. F. *Macromolecules* **2011**, *44*, (5), 1073-1109
22. Nischang, I.; Brüggemann, O.; Teasdale, I. *Angew. Chem. Int. Ed.* **2011**, *50*, (20), 4593-4596
23. Oaten, M.; Choudhury, N. R. *Macromolecules* **2005**, *38*, (15), 6392-6401
24. Wu, G.; Su, Z. *Chem. Mater.* **2006**, *18*, (16), 3726-3732
25. Zhang, C.; Babonneau, F.; Bonhomme, C.; Laine, R. M.; Soles, C. L.; Hristov, H. A.; Yee, A. F. *J. Am. Chem. Soc.* **1998**, *120*, (33), 8380-8391
26. Iyer, P.; Iyer, G.; Coleman, M. J. *J. Membr. Sci.* **2010**, *358*, (1-2), 26-32
27. Leu, C. M.; Chang, Y. T.; Wei, K. H. *Chem. Mater.* **2003**, *15*, (19), 3721-3727
28. Dalwani, M.; Zheng, J.; Hempenius, M.; Raaijmakers, M. J. T.; Doherty, C. M.; Hill, A. J.; Wessling, M.; Benes, N. E. *Journal of Materials Chemistry* **2012**, *22*, (30), 14835-14838
29. Freger, V. *Langmuir* **2003**, *19*, (11), 4791-4797.10.1021/la020920q
30. Sroog, C. E. *Prog. Polym. Sci.* **1991**, *16*, (4), 561-694
31. J. Feher, F.; D. Wyndham, K.; Soulivong, D.; Nguyen, F. *J. Chem. Soc., Dalton Trans.* **1999**, (9), 1491-1498.10.1039/A807302C
32. Schön, P.; Bagdi, K.; Molnár, K.; Markus, P.; Pukánszky, B.; Julius Vancso, G. *Eur. Polym. J.* **2011**, *47*, (4), 692-698
33. Colson, J. W.; Dichtel, W. R. *Nature Chem.* **2013**, *5*, (6), 453-465
34. Duthie, X.; Kentish, S.; Powell, C.; Nagai, K.; Qiao, G.; Stevens, G. J. *J. Membr. Sci.* **2007**, *294*, (1-2), 40-49
35. Lin, W. H.; Chung, T. S. *J. Membr. Sci.* **2001**, 186, (2), 183-193
36. Tanaka, K.; Okano, M.; Toshino, H.; Kita, H.; Okamoto, K.-I. *J. Polym. Sci., Part B: Polym. Phys.* **1992**, *30*, (8), 907-914
37. Villaluenga, J. P. G.; Seoane, B.; Hradil, J.; Sysel, P. *J. Membr. Sci.* **2007**, *305*, (1-2), 160-168

38. Neyertz, S.; Gopalan, P.; Brachet, P.; Kristiansen, A.; Männle, F.; Brown, D. *Soft Mater.* **2014**, 12, (1), 113-123
39. Lin, H.; Van Wagner, E.; Freeman, B. D.; Toy, L. G.; Gupta, R. P. *Science* **2006**, 311, (5761), 639-642
40. Beamson, G.; Briggs, D., *High Resolution XPS of Organic Polymers: The Scienta ESCA300 Database*. John Wiley & Sons: 1992.
41. Feher, F. J.; Wyndham, K. D.; Soulivong, D.; Nguyen, F. *Journal of the Chemical Society - Dalton Transactions* **1999**, (9), 1491-1497
42. Simonsen, M. E.; Sønderby, C.; Li, Z.; Søgaard, E. G. *J. Mater. Sci.* **2009**, 44, (8), 2079-2088

Chapter 3

Hybrid poly(POSS-imide)s with tailored inter-cage spacing for sieving of hot gases

*This chapter has been adapted from: Raaijmakers, M.J.T., Hybrid polyhedral oligomeric silsesquioxanes-imides with tailored inter-cage spacing for sieving of hot gases, *Chem. Mater.*, **2014**, 26, (12), pp 3660-3664 (DOI: 10.1021/cm500691e)*



Abstract

Macromolecular network rigidity of synthetic membranes is essential for sieving of hot gases. Hyper-cross-linked poly(POSS-imide) membranes with tailored inter-cage spacing are presented. The length and flexibility of their imide bridges enables tuning of gas permeability and selectivity in a broad temperature range. The facile synthesis allows for large-scale production of membranes designed for specific process conditions.

3.1. Introduction

Sieving of hot gases requires membranes with moderated macromolecular dynamics at elevated temperatures.¹ Recently, we have presented ultrathin poly(POSS-imide) hybrid membranes that allow gas separation in a broad temperature range.² The poly(POSS-imide) membranes consist of a giant molecular network of polyhedral oligomeric silsesquioxanes (POSS), covalently linked by imide bridges. The hyper-cross-linked network characteristics allow persistence of gas separation performance up to 300 °C. At such temperatures, size-sieving selectivity of organic polymeric membranes disappears due to the loss in their chain rigidity.³ Here, we demonstrate that we can tailor the gas sieving performance of nanoscale hybrid membranes via selection of the imide bridge that connects the POSS cages. The length and flexibility of the imide bridges directly affect the macromolecular dynamics and inter-cage distance of the giant network. In turn, this enables tuning of gas permeability and selectivity in a broad temperature range. The facile nature of the technique used for membrane synthesis allows for large-scale and defect-free membrane production, with properties tailored to fit the process requirements.

Hybrid materials allow integration of the superior thermo-mechanical properties of inorganic materials and versatile organic polymer segments. The physical dispersion of inorganic nanoparticles in polymers allows for materials synthesis with properties that are a combination of the individual components.⁴⁻⁷ Superior properties can be obtained by incorporation of nanoscale inorganic moieties as an intrinsic part of the polymeric network.⁸⁻¹² The octahedral symmetry of polyhedral oligomeric silsesquioxanes (POSS), and the wide array of functional groups they are decorated with, permit covalent bond formation in three dimensions. Here, we use a facile interfacial polymerization reaction that allows for production of nanoscale-hybrid ultrathin films.^{2, 13} The hybrid membranes are prepared by interfacial polycondensation of octa-ammonium POSS in water and a dianhydride in toluene, resulting in the formation of a poly[POSS-(amic acid)] membrane layer. The high reactivity of the monomers allows for rapid formation of inherently defect-free membranes. Inhibition of reactant diffusion upon film formation impedes further film growth, limiting the film thickness to several hundred nanometers.

3.2. Experimental section

3.2.1. Synthesis of poly(POSS-imide)s via interfacial polymerization

Toluene (anhydrous 99.8 wt.%, Sigma-Aldrich), pyromellitic dianhydride (PMDA, Sigma-Aldrich), 3,3',4,4'-biphenyl tetracarboxylic dianhydride (BPDA, Sigma-Aldrich), 4,4'-oxydiphthalic anhydride (ODPA, Sigma-Aldrich), and 4,4'-(4,4'-Isopropylidenediphenoxy)bis(phthalic anhydride) (BPADA) 4,4'-(Hexafluoroisopropylidene) diphthalic anhydride (6FDA, Sigma-Aldrich), ammonium chloride salt functionalized POSS (OctaAmmonium POSS[®], Hybrid Plastics (USA)) and sodium hydroxide (Sigma-Aldrich) were used as received. Free-standing films were prepared using ammonium chloride salt functionalized POSS, that is readily soluble in water. The pH of an aqueous solution of 0.9 wt.% ammonium chloride salt functionalized POSS was adjusted using sodium hydroxide (0.1 mol L⁻¹), and subsequently contacted with the dianhydride solution in toluene (0.075 wt.%). Supported membranes were produced on ceramic membranes (α -alumina discs with a 3- μ m-thick γ -alumina layer by pre-wetting the porous ceramic material under 0.5 bar vacuum in the aqueous POSS solution for 15 min, followed by contacting with the dianhydride solution in toluene for 5 min. The pore size of the γ -alumina is in the order of several nm, and allows for defect-free interfacial polymerization membrane formation. The high hydrophilicity of the γ -alumina allows for facile wetting of the pores with the aqueous phase. Thermal conversion of the poly[POSS-(amic acid)] to poly(POSS-imide) was performed for 2 hours at 300 °C under an air atmosphere, at a heating rate of 5 °C min⁻¹.

3.2.2. Material characterization

Membrane single gas permeation experiments were performed in a dead-end mode at a trans-membrane pressure of 2 bar, and atmospheric pressure at the permeate side. Once the helium permeance remained constant, the other gases (N₂, CH₄, H₂, and CO₂, consecutively) were measured at temperatures between 50-300 °C.

3.3. Results and discussion

After film formation by interfacial polymerization, the poly[POSS-(amic acid)]s are converted to poly(POSS-imide)s by thermal treatment at 300 °C. **Figure 3-1** shows the Attenuated Total Reflection - Fourier Transform Infrared Spectroscopy (ATR-FTIR) spectra of the poly[POSS-(amic acid)] and

poly(POSS-imide) materials. The poly[POSS-(amic acid)] spectra in **Figure 3-1 (left panel)** show common peaks at identical wave numbers, that can be attributed to the POSS cages, the amic acid groups, and the phenyl groups.

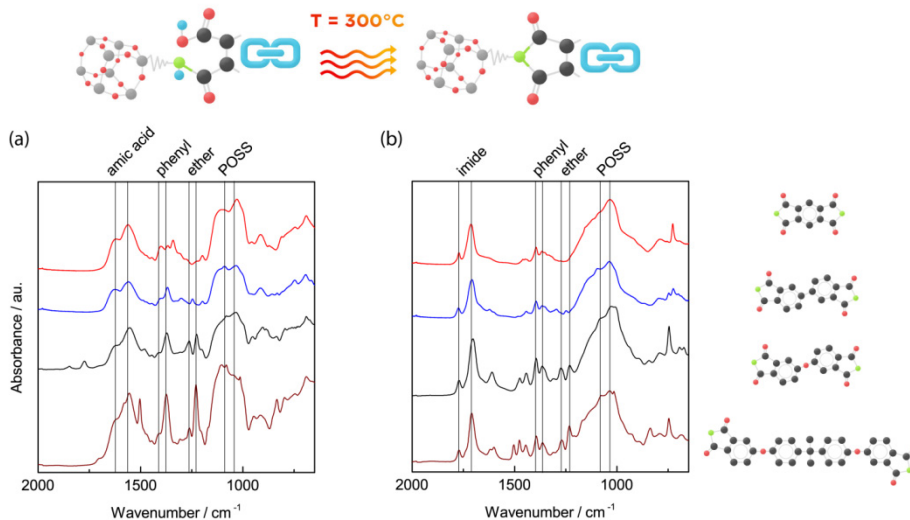


Figure 3-1: ATR-FTIR absorbance spectra of (left panel) poly[POSS-(amic acid)] and (right panel) poly(POSS-imide) (after 300 °C heat treatment) pre-prepared using PMDA (—), BPDA (—), ODPA (—), BPADA (—). The bands at 1620 and 1570 cm^{-1} are assigned to N-H bending (1) and C=O stretching (2) of the amide group. After heat treatment the bands at 1620 and 1570 cm^{-1} are substituted by the bands at 1720 and 1780 cm^{-1} , assigned to C=O asymmetric (3) and symmetric (4) stretching of the imide group, respectively. The sharp bands at 1125 and 1040 cm^{-1} can be attributed to the Si-O-Si asymmetric stretching vibrations of polyhedral and ladder silsesquioxane structures, respectively. Partial cleavage of the POSS cages occurs due to hydrolysis by hydroxyl ions.

The differences between the poly[POSS-(amic acid)] spectra originate from the different functional groups of the dianhydrides; PMDA contains a 1,2,4,5-substituted phenyl, ODPA contains an ether, and BPADA has quaternary carbon and ether bonds (the complete peak analysis can be found in the Appendix, Table A2-1). After thermal treatment two distinct imide bands emerge at 1720 and 1780 cm^{-1} , shown in **Figure 3-1 (right panel)** These peaks are attributed to the imide carbonyl symmetric and asymmetric stretching, respectively. The vanishing of the amic acid bands at 1620 and 1570 cm^{-1}

indicates that complete conversion of the amic acid to imide groups is achieved.¹⁴ Also, the poly(POSS-imide) spectra lack carboxylic acid and dianhydride bands, implying that no detectable unreacted dianhydride moieties remain after imidization. The ratios between the POSS and imide peak intensities are similar for all poly(POSS-imide)s, implying that the number of imide groups on each POSS cage is not strongly affected by differences in reactivity and solubility of the dianhydrides.

The similar degree of POSS interconnectivity is confirmed by X-ray photoelectron spectroscopy (XPS) measurements of ceramic supported poly(POSS-imide) membranes (Appendix, Figure A2-4). Deconvoluted nitrogen elemental spectra reveal that, on average, 4 out of 8 functional groups on each POSS cage are converted to imides. The remaining unreacted functional groups are mostly primary amines, of which a slight fraction is protonated. The nitrogen, silica and carbon elemental compositions derived from the XPS measurement suggest a similar number of imide bridges per POSS molecule, assuming that no unreacted dianhydride groups remain. Both the infrared and XPS spectra reveal that partial hydrolysis of the POSS cage occurs. The wide range of dianhydrides suitable for the interfacial polycondensation of octa-ammonium POSS allows for production of gas separation membranes with a tailored inter-cage spacing. **Figure 3-2** demonstrates the adaptability of the single gas permeance and selectivity over a broad temperature range, by the use of different imide bridges. **Figure 3-2 (left panel)** shows the gas sieving abilities of the membranes. The gas permeance follows a monotonic decrease with increasing kinetic diameter of the molecules, indicating that molecular separation occurs on basis of size exclusion. The diffusivity-controlled selectivity was also observed for the 6FDA based poly(POSS-imide)s, and originates from the hyper-cross-linked network characteristics. The permeance of each gas increases with increasing length of the imide bridges. This indicates that the larger spacing between the POSS cages results in increased permeation. The observation that transport occurs via the organic bridges of the hybrid material is supported by molecular dynamics simulations of gas transport in amino functionalized POSS.¹⁵ **Figure 3-2 (right panel)** shows that the inter-cage distance also affects the permselectivity. The H_2/N_2 selectivity as function of the H_2 permeance shows the typical trade-off for molecular sieving membranes. A decrease in permeance, with decreasing length of the imide bridge, concurs with a

substantial increase in the H₂/N₂ selectivity. At 100, 200 and 300 °C a similar trade-off between selectivity and permeance can be observed.

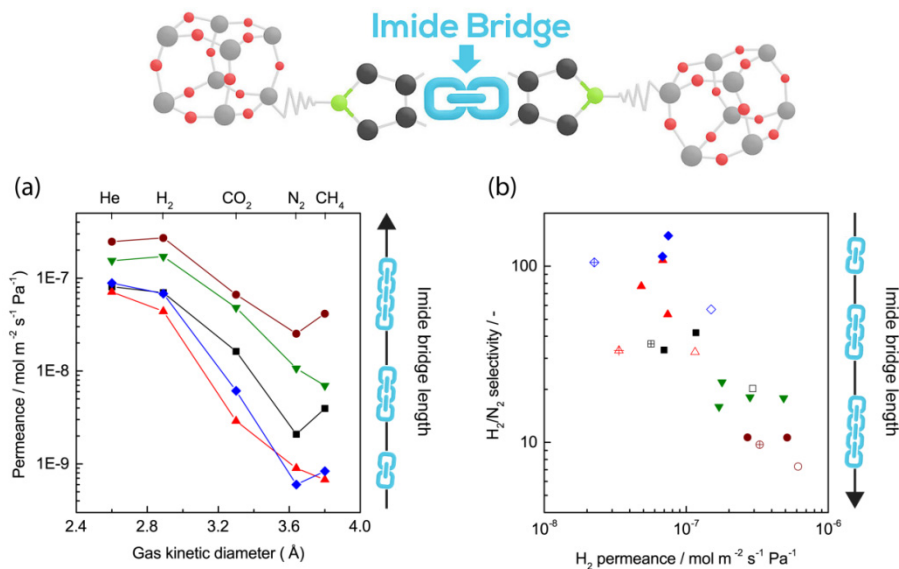


Figure 3-2: (left panel) Single gas permeance at 200 °C as function of gas kinetic diameter for the poly(POSS-imide)s derived from PMDA (▲), BPDA (◆), ODPA (■), 6FDA (▼) and BPADA (●). All poly(POSS-imide)s are selective towards smaller kinetic diameter gases. The gas permeance of all gases increases with increasing dianhydride molecular length, supporting the hypothesis that the inter-POSS spacing is a key parameter for the membrane characteristics. (right panel) The H₂/N₂ ideal gas selectivity as function of hydrogen permeance at 100 °C (open, crossed symbols), 200 °C (closed symbols) and 300 °C (open symbols) for the poly(POSS-imide)s derived from the different dianhydrides. The H₂/N₂ selectivity increases with decreasing imide bridge length, while H₂ permeance is lower for the short imide bridges.

The gas permeation data as function of temperature demonstrates the hyper-cross-linked characteristics of the poly(POSS-imide)s. **Figure 3-3** shows the Arrhenius plots for the membranes prepared with BPDA and BPADA. The Arrhenius plots for the membranes prepared with PMDA and ODPA are given in the Appendix. All membranes showed persistent gas selectivity in the temperature range of 50-300 °C. Thermogravimetric analysis (Figure A3-2, Appendix) confirms that no material degradation occurs below 300 °C for all poly(POSS-imide)s. For all membranes the permeances increase with

temperature, and an Arrhenius-type temperature dependence is observed for most gases. The membranes based on the shortest linkers, BPDA (**Figure 3-3 (left panel)**) and PMDA (Appendix, Figure A3-1), show similar apparent activation energies for all gases.

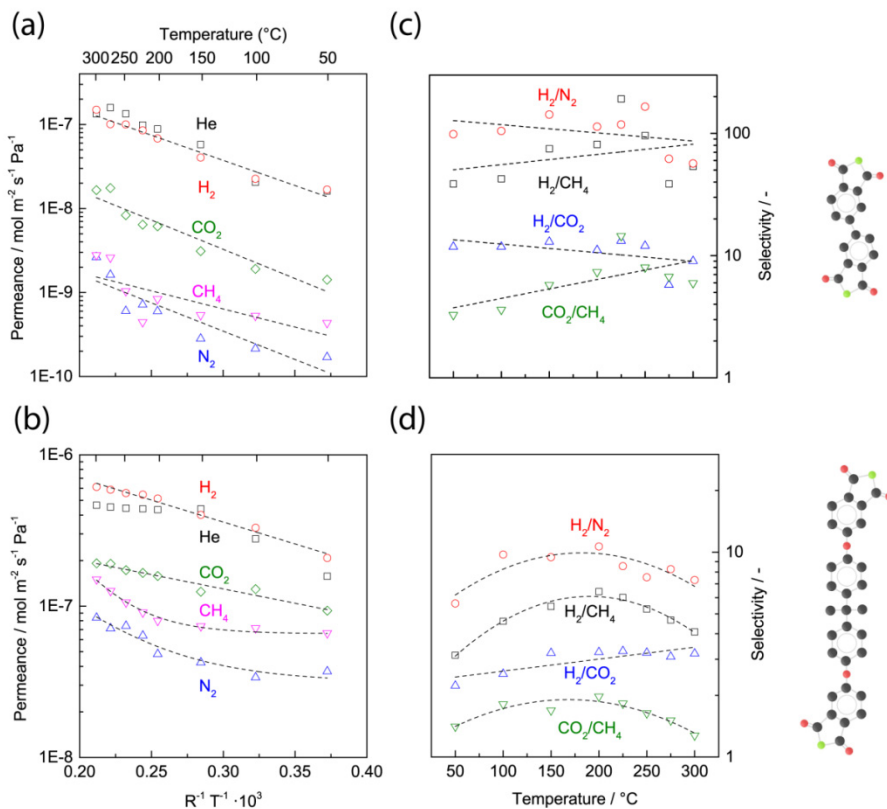


Figure 3-3: Arrhenius plot of the logarithm of the single gas permeance of He, H₂, CO₂, N₂ and CH₄, as a function of 1000 R⁻¹T⁻¹ for the poly(POSS-imide)s derived from BPDA (a), and BPADA (b). The apparent activation energies for gas permeance are given in Table A3-1 in the Appendix, calculated from the slope of ln(permeance) as function of R⁻¹T⁻¹. The corresponding ideal gas selectivities of H₂/N₂, H₂/CH₄, H₂/CO₂ and CO₂/CH₄ as a function of temperature for the poly(POSS-imide)s derived from BPDA (c) and BPADA (d). The dashed lines are drawn as a guide to the eye.

The absence of any significant changes in the activation energy demonstrates the resilience of these membranes with respect to the operating temperature. This translates into the unsurpassed permselectivities that these membranes

display at temperatures up to 300 °C. **Figure 3-3 (right panel)** shows the corresponding permselectivities of H₂/N₂, H₂/CH₄, H₂/CO₂ and CO₂/CH₄ as a function of temperature. Single gas H₂/N₂ and H₂/CH₄ selectivities between 40-190 are observed for BPDA and 10-55 for PMDA based membranes, respectively. Most noteworthy, the H₂/N₂ and H₂/CH₄ selectivity predominantly increases with temperature. The H₂/CO₂ selectivities are above 10 over the complete temperature range of 50-300 °C for the BPDA based poly(POSS-imides). Relatively few membrane materials have been characterized in a similar temperature range, due to the limited membrane performance stability at elevated temperatures. In the last few years, data have become available on polybenzimidazole membranes. These membranes exhibit slightly higher selectivities, but significantly lower permeances. Also, interesting work has been performed on elevated temperature gas separation with polyimides and polyaramides.^{3, 16} The performance of these materials is comparable to our hybrid materials, but does not persist above 200 °C.¹⁷⁻¹⁹ There is a range of rigid polymers, such as poly(benzoxazole)s and poly(benzoxazole-co-imides), that have potential for high temperature gas separation.²⁰⁻²³ Yet, currently there is a lack of membrane performance data at high temperatures.

The poly(POSS-imide)s allow for facile tailoring of the rigidity and spacing of the segments that connect the POSS cages. The short imide bridges constrain macromolecular motions that would allow for permeation of larger kinetic diameter gas molecules. This is in contrast to longer imide bridges, ODPA and BPADA. These longer bridges display temperature-dependent apparent activation energies for the gas permeance of the larger molecules, N₂ and CH₄. At elevated temperature the molecular mobility of the longer bridges is more affected by an increase in temperature, as compared to the mobility of the short imide bridges. This is in line with the variation in the coherence length found for conventional polyimides, obeying the order PMDA > BPDA > ODPA > BPADA.²⁴ The augmented network mobility is manifested by a contribution to the apparent energy of activation, reflected by an increased permeation. This effect is most pronounced for the larger molecules that suffer the most from size exclusion. At lower temperatures the molecular motions of the network are less pronounced and their contribution to the apparent energy of activation diminishes. This is reflected by a lower apparent energies of activation of N₂ and CH₄ permeance at temperatures below 150 °C. Differential scanning calorimetry (DSC) measurements on all

poly(POSS-imide)s (Appendix) do not show any sharp transitions, indicating the network dynamics only change gradually. The absence of a glass transition at temperatures up to 300 °C can therefore not be the origin of the change in apparent activation energy. The transition in activation energies results in a maximum selectivity of H₂/N₂ and H₂/CH₄ of ODPA (Appendix) and BPADA (**Figure 3-3 (bottom left panel)**) based poly(POSS-imide)s at a temperature around 150 °C. The different selectivities of the poly(POSS-imide)s as function of temperature stresses the importance of the network dynamics for membrane performance, even in a system with relatively short flexible moieties. This understanding is essential for selecting the suitable imide bridge, and allows for a broad range of applications and operating conditions.

3.4. Conclusion

In conclusion, the poly(POSS-imide) membranes allow unprecedented gas sieving performance at elevated temperatures. Their facile synthesis allows for large-scale production of membranes designed for specific process conditions. The molecular sieving characteristics can be tailored by varying the inter-cage spacing, via the length of the imide bridge. The persistence of gas separation stability up to 300 °C underlines the hyper-cross-linked periodic network characteristics of the covalently bound rigid POSS. The simple and reliable synthesis method potentially allows for large-scale production of a new generation of tailor-made hybrid membranes for industrial scale applications that require sieving of hot gases.

3.5. Acknowledgements

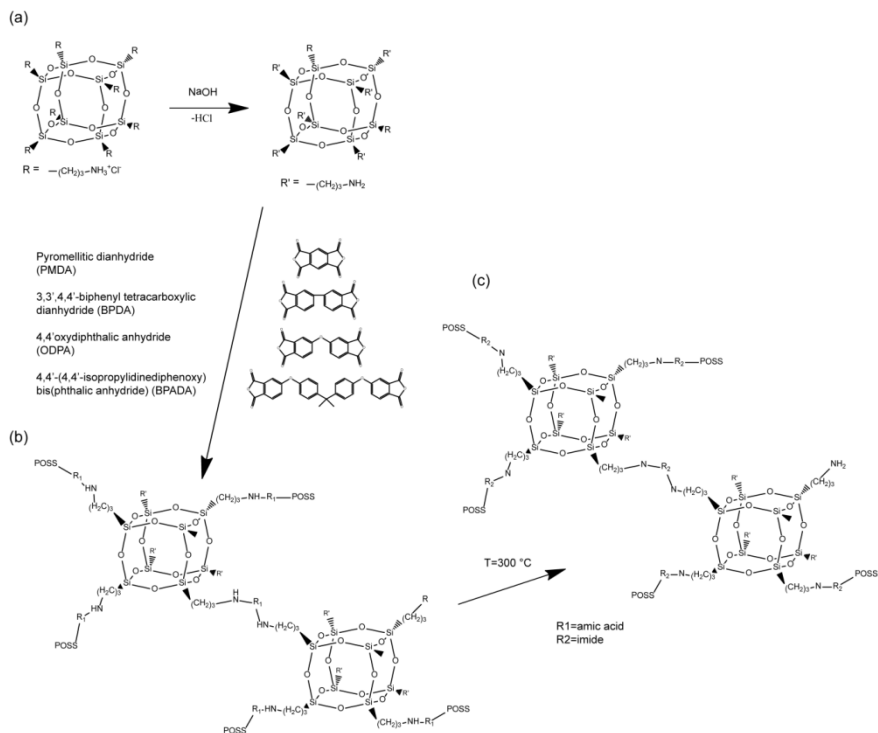
This project has received funding from the European Union's Seventh Framework Programme for research, technological development and demonstration under CARENA grant agreement no. 263007.

3.6. Appendices

3.6.1. Poly(POSS-imide) layer preparation

Scheme A3-1 shows the formation of poly[POSS-(amic acid)] and poly(POSS-imide) network by interfacial polymerization. Ammonium chloride salt functionalized POSS is readily dissolved in water. Subsequently, the pH of the solution is adjusted using sodium hydroxide (1 M) to allow the conversion of ammonium to primary amine functional groups. The alkaline aqueous POSS solution is contacted with a dianhydride solution in toluene for 5 min. The polycondensation reaction at the interface results in rapid and defect-free layer

formation of the hybrid poly[POSS-(amic acid)] network. After removal of the reactants, by flushing with acetone, the layers are heat treated at 300 °C in an air atmosphere to convert the poly[POSS-(amic acid)]s to poly(POSS-imide)s.



Scheme A3-1. Formation of poly[POSS-(amic acid)] and poly(POSS-imide) network by interfacial polymerization. (a) Partial deprotonation of the octa-ammonium POSS by sodium hydroxide to create amine functionalized functional groups. (b) Interfacial polycondensation reaction of the partially amine-functionalized POSS cage and the different dianhydrides, resulting in the formation of poly[POSS-(amic acid)]s. (c) thermal conversion

3.6.2. Material characterization

Gas permeation analysis

Membrane single gas permeation experiments were performed on an in-house developed gas permeation setup, using Kalrez[®] Spectrum 6375 O-rings. All membranes were measured in a dead-end mode at a trans-membrane pressure

of 2 bar, and atmospheric pressure at the permeate side. The membranes were heated under helium atmosphere at a heating rate of $1.5\text{ }^{\circ}\text{C min}^{-1}$. When the helium permeance reached a constant value, the other gases (N_2 , CH_4 , H_2 , and CO_2 , consecutively) were measured at temperatures between $50\text{-}300\text{ }^{\circ}\text{C}$. Equilibration time between measurements was at least 30 min.

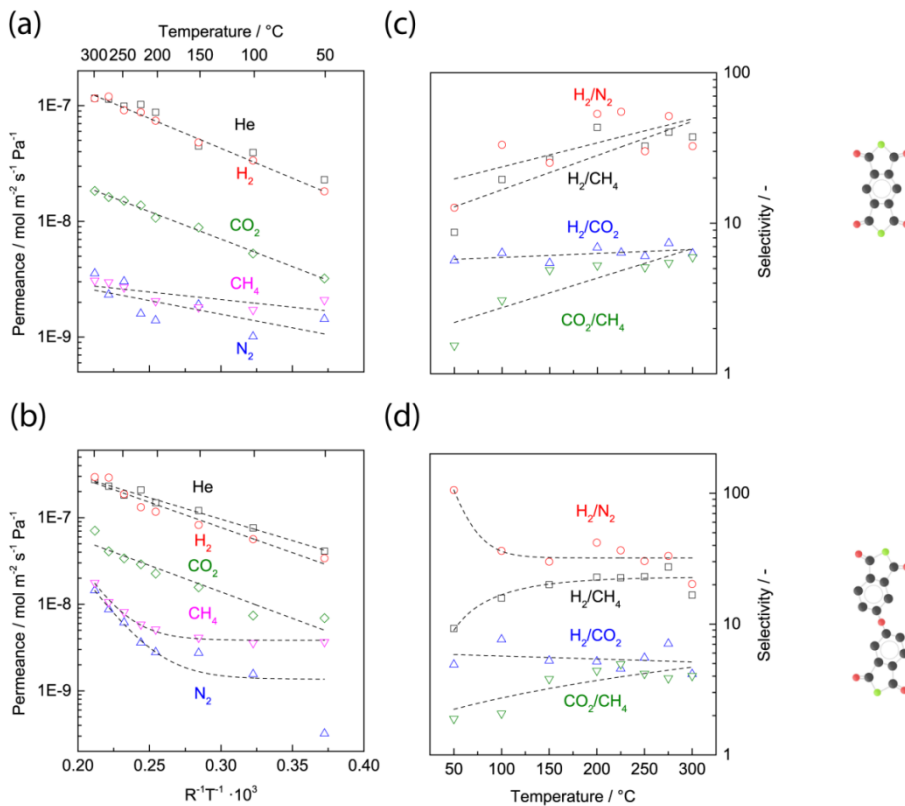


Figure A3-1. Arrhenius plot of the logarithm of the single gas permeance of He, H_2 , CO_2 , N_2 and CH_4 , as a function of $R^{-1}T^{-1} \cdot 10^3$ for the poly(POSS-imide)s derived from PMDA (a), and ODPA (b). The activation energies are calculated from the slope of the $\ln(\text{permeance})$ as function of $1/R^{-1}T^{-1}$. The corresponding ideal gas selectivities of H_2/N_2 , H_2/CH_4 , H_2/CO_2 and CO_2/CH_4 as a function of temperature for the poly(POSS-imide)s derived from PMDA (c) and ODPA (d). The dashed lines are drawn as a guide to the eye.

Figure 3-1 shows the Arrhenius plots of the $\log(\text{permeance})$ as function of $R^{-1}T^{-1} \cdot 10^{-3}$ for the membranes prepared with PMDA and ODPA. Both membranes show higher permeation rate with increasing temperatures. The

activation energies for gas permeation through PMDA based poly(POSS-imide)s remain similar over the complete temperature range. The corresponding ideal gas selectivities of H₂/N₂, H₂/CH₄, H₂/CO₂ and CO₂/CH₄ as a function of temperature for the poly(POSS-imide)s derived from PMDA (**d**) show H₂/N₂ and H₂/CH₄ selectivities between 10-55. The low activation energy for N₂ and CH₄ substantiates that the short imide bridges do not exhibit macromolecular mobility that is required for transport of large kinetic diameter gases. This is in contrast to the apparent activation energies for N₂ and CH₄ for (c) BPADA poly(POSS-imide)s. The higher mobility of the large kinetic diameter gases originates from the larger imide bridge distance.

Table A3-1. The apparent activation energies for gas permeance for all poly(POSS-imide)s prepared with PMDA, BPDA, ODPa and BPADA. The activation for N₂ and CH₄ permeance of ODPa and BPADA based poly(POSS-imide)s were omitted due to changes in the apparent activation energy as function of temperature, in the temperature range of 50-300 °C.

Gas	Activation energy / kJ mol ⁻¹			
	PMDA	BPDA	ODPA	BPADA
He	10.7	16.2	13.4	8.4
H ₂	11.9	15.8	11.2	7.6
CO ₂	10.9	15.26	14.1	4.4
N ₂	5.4	13.17		
CH ₄	3	7.78		

Table A3-1 shows the apparent activation energies for permeance for all poly(POSS-imide)s prepared with PMDA, BPDA, ODPa and BPADA. The apparent activation energies for permeance are relatively high compared to conventional polymeric membranes. BPDA based poly(POSS-imide)s show particularly high activation energies, and underlines the high energy barriers for gas diffusion due to rigidity of the short imide bridge.

Thermogravimetric analysis

Thermogravimetric analysis (TGA) was performed on a STA 449 F3 Jupiter[®] (Netzsch, Germany), equipped with a TG-only sample holder. Measurements were performed under 70 mL min⁻¹ synthetic air (20% O₂ in N₂) or 70 mL min⁻¹ nitrogen from room temperature to 1000 °C, with heating rates of 10 °C min⁻¹. Temperature calibration was performed using melting standards. Blank corrections with an empty cup were carried under the same heating program.

Sample weights were determined ex-situ. **Figure A3-2** shows the relative weight normalized for the initial weight as function of temperature, for the poly(POSS-imide)s thermalized under air and nitrogen atmosphere. All poly(POSS-imide)s in air and nitrogen atmosphere show a similar degradation offset temperature at a temperature above 300 °C. The initial mass loss at temperatures below 300 °C is likely due to evaporation of adsorbed water. The weight loss between 300-500 °C follows a similar degradation mechanism for all poly(POSS-imide)s. The weight loss rate under nitrogen atmosphere is significantly lower than under air atmosphere, suggesting that carbonaceous degradation products are only partially removed in the absence of oxygen. Above 500 °C, the weight loss rate decreases. Under air atmosphere the weight loss stabilizes for all imide bridge types, except for BPADA based poly(POSS-imide)s. The distinct degradation process of the BPADA based poly(POSS-imide) can be rationalized by the presence of the relatively stable quaternary carbon groups that are not present in the other poly(POSS-imide)s. Under nitrogen weight loss persists for all poly(POSS-imide)s, suggesting the degradation kinetics are relatively low in the absence of nitrogen.

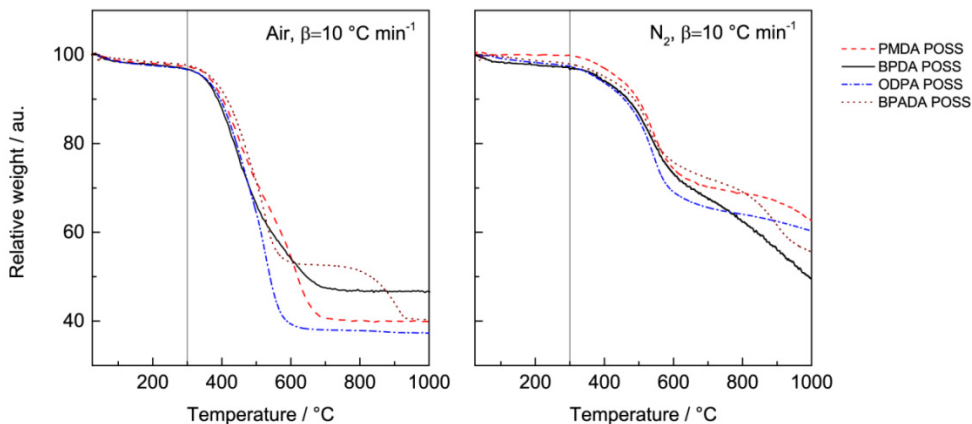


Figure A3-2. TGA mass loss curves of poly(POSS-imide)s prepared using PMDA, BPDA, ODPA and BPADA.

Differential scanning calorimetry

Differential scanning calorimetry (DSC) was performed on a DSC 8000 (Perkin Elmer, USA). Free-standing poly(POSS-imide) was placed in an aluminum sample pan and cycled from 50 to 300 °C with a heating rate of 20

$^{\circ}\text{C min}^{-1}$. Measurements were performed under 70 mL min^{-1} nitrogen. Temperature calibration was performed using melting standards. Blank corrections with an empty cup were carried under the same heating program. Sample weights were determined ex-situ. Four subsequent heating and cooling cycles were used to eliminate the influence of adsorbed water on the measurement. **Figure A3-3** shows the heat flow of all poly(POSS-imide)s as function of temperature, corrected for a blank run and sample weight. The heat flow curves of all poly(POSS-imide)s display no transitions, underlining the lack of a glass transition in the material at temperatures up to $300 \text{ }^{\circ}\text{C}$. The heat capacity, represented by the slope of the curves, is largest for the BPDA based poly(POSS-imide). The ODPDA based poly(POSS-imide) has the lowest calculated heat capacity. The PMDA and BPADA based poly(POSS-imide)s have similar heat flow profiles, suggesting the heat capacities are similar.

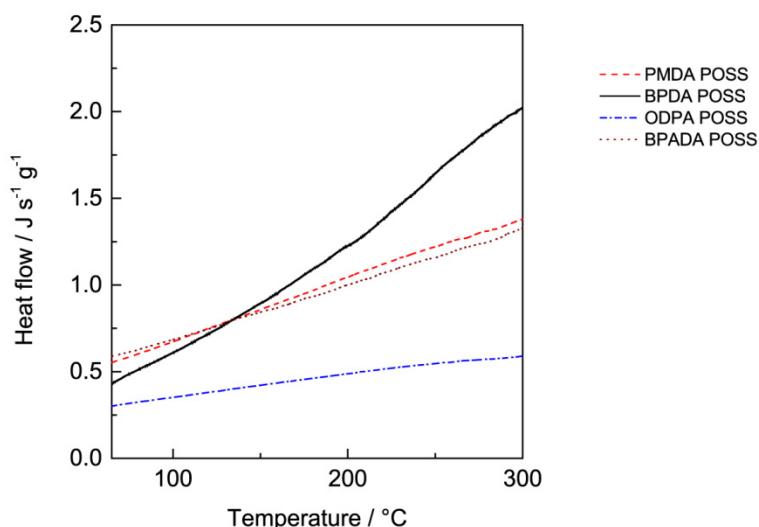


Figure A3-3. DSC curves of poly(POSS-imide) prepared using PMDA, BPDA, ODPDA and BPADA.

X-ray photoelectron spectroscopy

X-ray photoelectron spectroscopy measurements were performed on a Quantera SXM scanning XPS microprobe (Physical Electronics), using a monochromatic Al $K\alpha$ source (1486.6 eV). Octa-ammonium POSS powder and poly(POSS-imide) on α -alumina discs coated with $3 \mu\text{m}$ thick γ -alumina samples were measured. The elemental compositions of the poly(POSS-

imide)s and octa-ammonium POSS powder are given in **Table A3-2**. For all poly(POSS-imide) samples an increase in carbon and oxygen content with respect to the POSS is observed, originating from imide bridge formation. The remaining sodium and chlorine are originating from the aqueous alkaline POSS solution.

Table A3-2 Elemental compositions of the poly(POSS-imide)s and octa-ammonium POSS powder.

Sample	Element					
	C1s	N1s	O1s	Na1s	Cl2p	Si2p
Octa-ammonium POSS	47.8	9.8	22.0	0.8	9.0	11.5
PMDA based poly(POSS-imide)	39.7	4.3	39.7	3.2	0.08	11.3
BPDA based poly(POSS-imide)	42.7	4.8	37.8	2.5	0.1	10.3
OPDA based poly(POSS-imide)	55.4	5.2	29.2	1.1	0.11	7.8
ODPDA based poly(POSS-imide)	61.2	4.3	26.3	0.3	0.03	7.7

The average number of imide bridged per POSS cage is calculated from the Si/C, Si/N and Si/O ratios of the poly(POSS-imide)s. For all poly(POSS-imide)s around 4 out of 8 functional groups on each POSS cage are bridged with an imide moiety. The absence of anhydride and carboxylic acid peaks in the FTIR-ATR spectra suggests that the imide bridges are connected with two POSS moieties. The carbon (C1s) and nitrogen (N1s) elemental spectra of octa-ammonium POSS powder and poly(POSS-imide)s are shown in **Figure A3-4**. The main differences between the C1s elemental spectrum of the poly(POSS-imide)s and the octa-ammonium POSS originates from the imide bonds and additional aliphatic and aromatic carbon groups. The emerged binding energy peak of the imide groups at 288 eV is most pronounced. The deconvoluted peak surface area corresponds to a number of 4 imide groups per POSS cage. This in agreement with the N1s spectral data. The N1s elemental fit of octa-ammonium POSS shows two distinct peaks, attributed to the ammonia (401 eV) and amine (398.7) binding energies of the partially deprotonated ammonia groups. All poly(POSSimide) N1s spectra show a distinct shift towards lower binding energy groups. The shift can be attributed to an increase in amine and imide bond contribution to the N1s spectrum. About 50% of the nitrogen bonds in the deconvoluted N1s spectra

can be attributed to imide groups. **Table A3-3** gives the deconvoluted peak area distribution for the different binding energies associated with imide, amine and ammonia groups. The data suggests that around 4 out of 8 functional groups on each POSS cage are bridged with an imide moiety. This is in good agreement with the calculated numbers from the elemental ratios and with previously found results for 6FDA based poly(POSS-imide)s.

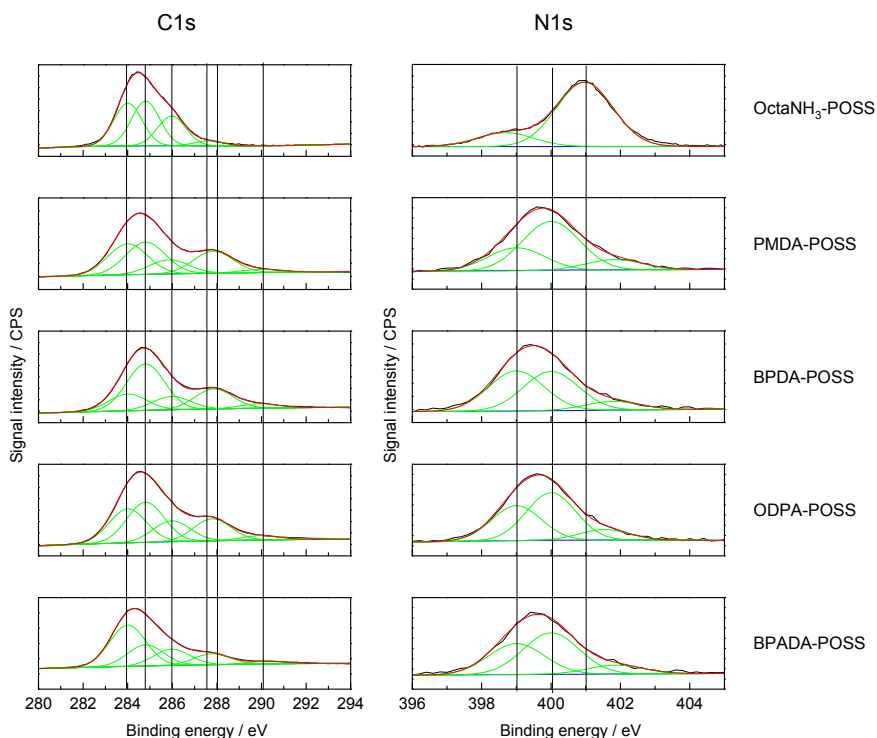


Figure A3-4. Deconvoluted XPS elemental spectra of C1s and N1s for poly(POSS-imide)s prepared using PMDA, BPDA, ODPDA and BPADA.

Table A3-3. Deconvoluted XPS peak area distribution for the binding energies associated with amine, imide and ammonia binding energies

	Deconvoluted peak area		
	imide (%)	amine (%)	ammonia (%)
PMDA	51.1	38.0	10.9
BPDA	59.5	27.8	12.7
OPDA	51.2	37.6	11.2
ODPDA	44.5	45.6	9.9
Octa-NH ₃ -POSS	0	17.7	82.3

Figure A3-5 shows the deconvoluted XPS elemental spectra of Si2p and O1s for octa-ammonium POSS and the poly(POSS-imide)s prepared with the different dianhydrides. The single binding energy of the Si2p spectrum of the octa-ammonium POSS corresponds to the attributed to the SiO_3C groups of the POSS cage.

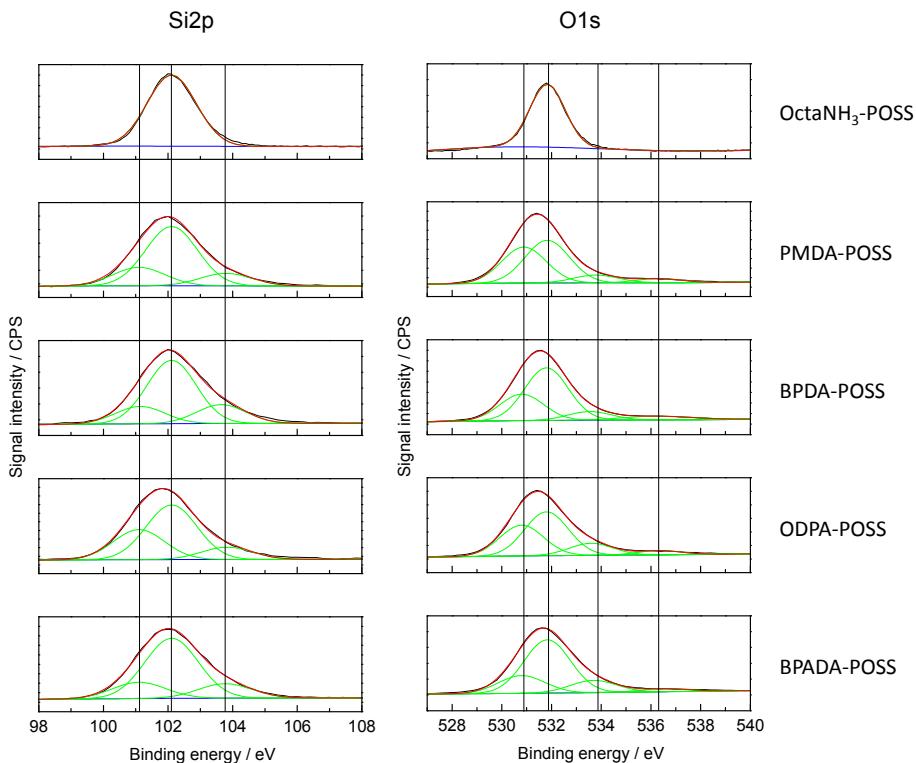


Figure A3-5. Deconvoluted XPS elemental spectra of Si2p and O1s for poly(POSS-imide)s prepared using PMDA, BPDA, ODPDA and BPADA.

The poly(POSS-imide) Si2p spectra display a shift in binding energies towards both lower and higher binding energies. These peaks are associated with silanol and SiO^- formed by partial hydrolysis of the POSS cage. The shift in binding energy and broadening of the XPS spectrum is mainly attributed to the formation of silanol groups. The single binding energy of the O1s spectrum of the octa-ammonium POSS corresponds to the siloxane bonds in the POSS cages. The O1s spectrum of the poly(POSS-imide)s show additional peaks at a binding energy of 530.7 and 532.6 eV, associated with the $\text{C}=\text{O}$ of the imide group and silanol bonds, respectively. The appearance of the silanol peak in

the O1s spectrum is in agreement with the Si2p spectrum of the poly(POSS-imide) samples.

Attenuated Total Reflection – Fourier Transform Infrared Spectroscopy

The chemical structures of the poly[POSS-(amic acid)] and poly(POSS-imide) were analyzed with Attenuated Total Reflection Fourier Transform Infrared Spectroscopy (ATR-FTIR) of free-standing films using an ALPHA FTIR Spectrometer (Bruker Optics Inc, Germany) equipped with a ZnSe crystal. All spectra were recorded at room temperature. **Figure A3-6** shows the FTIR-ATR absorbance spectra of poly(POSS-imide)s prepared with PMDA, BPDA, ODPA and BPADA.

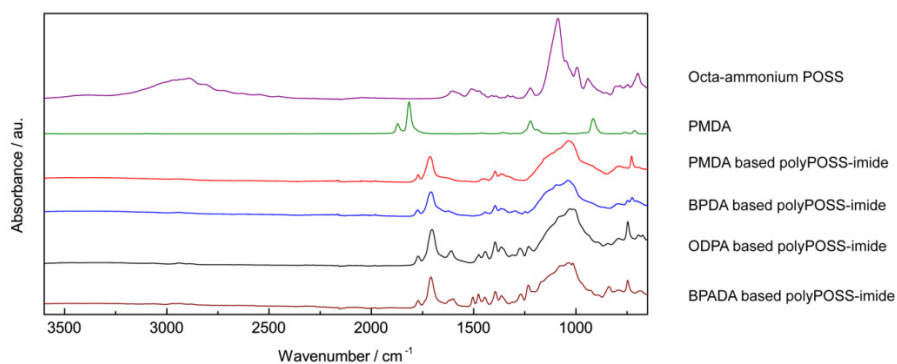


Figure A3-6 FTIR-ATR absorbance spectra of poly(POSS-imide)s prepared with PMDA, BPDA, ODPA and BPADA. The octa-ammonium POSS and PMDA spectra are given as reference. The PMDA spectrum is adapted from the NIST chemistry webpage.²⁵

The octa-ammonium POSS and PMDA spectra are given as reference. The dianhydride peaks at 1820 and 1870 cm^{-1} for PMDA are not reflected in any of the poly(POSS-imide) spectra. The ammonia and water related peaks at 3200-2800 cm^{-1} are clearly visible in the octa-ammonium POSS spectrum. The poly(POSS-imide)s absorbance spectra only show slight absorbance in this region, underlining the absence of any carboxylic acid and ammonia groups in the poly(POSS-imide) layers. **Table A3-4** and **A3-5** show the bond and vibrational mode data as function of peak position for the poly[POSS-(amic acid)] and poly(POSS-imide)s respectively.

Table A3-4. Poly[POSS-(amic acid)] bond and vibrational mode data as function of peak wavenumber position, for the poly(POSS-imide)s prepared with PMDA, BPDA, ODPA and BPADA.

Poly[POSS-(amic acid)]						
	PMDA	BPDA	ODPA	BPADA		
Wavenumber	Intensity	Intensity	Intensity	Intensity	Bond	Vibrational mode
cm ⁻¹						
693	medium	medium	medium	medium	C-H	out of plane bend
727	shoulder	shoulder	shoulder	shoulder		O-substituted benzene
746	-	low	medium	medium	CH	out of plane bend 1,2,4, trisubstituted benzene
773	shoulder	shoulder	shoulder	shoulder	NH	def vib amide
798	medium	medium	medium	medium	NH ₂	out of plane bend of primary amine
837	-	-	low	medium	NH ₂	out of plane bend of primary amine
910	shoulder	shoulder	shoulder	shoulder	C-C	rocking
955	shoulder	shoulder	shoulder	shoulder	C-C	rocking
1000	shoulder	shoulder	shoulder	shoulder	C-C	rocking
1040	high	high	high	high	Si-O cage	str
1093	high	high	high	high	Si-O ladder	str
1120	shoulder	shoulder	shoulder	shoulder	C-H	in plane bending
1203	medium	medium	medium	medium	N-H	def
1228	-	-	medium	high	C-O (ether)	str
1272	-	-	medium	medium	C-O-C (ether)	def vib
1370	low	low	medium	high	C=O or C-N	str
1400	medium	medium	high	high	C=O or C-N	str
1445	low	low	medium	medium	CH ₂	scissoring
1475	-	-	medium	medium	CH ₂	def vib
1504	-	-	-	medium	C=C	str (only for electron donor groups)
1560	high	high	high	high	N-H	bend amide

1620	high	high	high	high	C=O	str amide
1670	high	high	high	high	C=O	str carboxylic acid
1710	-	-	-	-	C=O	asym str imide
1770	-	-	low	-	C-O-C	sym str
1845	-	-	low	-	C-O-C	asym str
2878	medium	medium	medium	medium	CH ₂	sym str
2939	medium	medium	medium	medium	CH ₂	asym str
3068	low	low	low	low	H ₂ O/CO OH	bend
3235	broad	broad	broad	broad	H ₂ O/CO OH	OH str
3380	broad	broad	broad	broad	NH ₂	asym str

Table A3-5. Poly(POSS-imide) bond and vibrational mode data as function of peak wavenumber position, for the poly(POSS-imide)s prepared with PMDA, BPDA, ODPDA and BPADA.

Poly(POSS-imide)						
	PMDA	BPDA	ODPA	BPADA		
Wavenumber cm ⁻¹	Intensity	Intensity	Intensity	Intensity	Bond	Vibrational mode
693	medium	medium	medium	medium	C-H	out of plane bend
725	medium	medium	low	low	N-H	wagging
746	-	low	medium	medium	CH	out of plane 1,2,4, trisubstituted benzene
773	shoulder	shoulder	shoulder	shoulder	NH	def vib amide
793	low	low	low	low	NH ₂	out of plane bend of primary amine
837	-	-	low	medium	NH ₂	out of plane bend of primary amine
910	shoulder	shoulder	shoulder	shoulder	C-C	rocking
965	shoulder	shoulder	shoulder	shoulder	C-C	rocking
1000	shoulder	shoulder	shoulder	shoulder	C-C	rocking
1040	high	high	high	high	Si-O cage	str
1093	high	high	high	high	Si-O ladder	str
1120	shoulder	shoulder	shoulder	shoulder	C-H	in plane bending

1228	-	-	high	high	C-O (ether)	str
1272	-	-	medium	medium	C-O-C	def vib
1364	low	low	medium	medium	C=O or C- N	str
1393	medium	medium	high	high	C=O or C- N	str
1445	low	low	medium	medium	CH ₂	scissoring
1475	-	-	medium	medium	CH ₂	def vib
1504	-	-	-	medium	C=C	srt (only for electron donor groups)
1610	-	-	medium	medium	C=O	str amide
1670	-	-	-	-	C=O	str carboxylic acid
1710	high	high	high	high	C=O	asym str imide
1770	low	low	low	low	C=O	sym str imide
2878	medium	medium	medium	medium	CH ₂	sym str
2939	medium	medium	medium	medium	CH ₂	asym str
3068	low	low	low	low	H ₂ O/CO OH	bend
3235	broad	broad	broad	broad	H ₂ O/CO OH	OH str
3380	broad	broad	broad	broad	NH ₂	asym str

3.7. References

1. Maier, G. *Angewandte Chemie - International Edition* **1998**, 37, (21), 2961-2974
2. Raaijmakers, M. J. T.; Hempenius, M. A.; Schön, P. M.; Vancso, G. J.; Nijmeijer, A.; Wessling, M.; Benes, N. E. *Journal of the American Chemical Society* **2013**, 136, (1), 330-335.10.1021/ja410047u
3. Koros, W. J.; Woods, D. G. *Journal of Membrane Science* **2001**, 181, (2), 157-166
4. Le, N. L.; Chung, T. S. *Journal of Membrane Science* **2014**, 454, 62-73
5. Lee, Y. J.; Huang, J. M.; Kuo, S. W.; Chang, F. C. *Polymer* **2005**, 46, (23), 10056-10065
6. Chua, M. L.; Shao, L.; Low, B. T.; Xiao, Y.; Chung, T. S. *Journal of Membrane Science* **2011**, 385-386, (1), 40-48
7. Li, Y.; Chung, T. S. *International Journal of Hydrogen Energy* **2010**, 35, (19), 10560-10568
8. Laine, R. M.; Roll, M. F. *Macromolecules* **2011**, 44, (5), 1073-1109
9. Nischang, I.; Brüggemann, O.; Teasdale, I. *Angewandte Chemie - International Edition* **2011**, 50, (20), 4593-4596
10. Oaten, M.; Choudhury, N. R. *Macromolecules* **2005**, 38, (15), 6392-6401

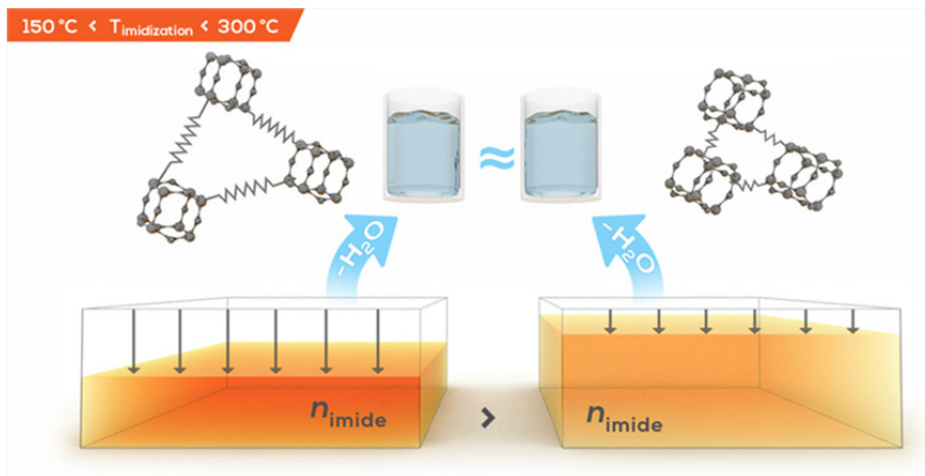
11. Wu, G.; Su, Z. *Chemistry of Materials* **2006**, 18, (16), 3726-3732
12. Zhang, C.; Babonneau, F.; Bonhomme, C.; Laine, R. M.; Soles, C. L.; Hristov, H. A.; Yee, A. F. *Journal of the American Chemical Society* **1998**, 120, (33), 8380-8391
13. Dalwani, M.; Zheng, J.; Hempenius, M.; Raaijmakers, M. J. T.; Doherty, C. M.; Hill, A. J.; Wessling, M.; Benes, N. E. *Journal of Materials Chemistry* **2012**, 22, (30), 14835-14838
14. Diahm, S.; Locatelli, M. L.; Lebey, T.; Malec, D. *Thin Solid Films* **2011**, 519, (6), 1851-1856.
15. Neyertz, S.; Gopalan, P.; Brachet, P.; Kristiansen, A.; Männle, F.; Brown, D. *Soft Materials* **2014**, 12, (1), 113-123
16. Rezac, M. E.; Koros, W. J.; Miller, S. J. *Journal of Membrane Science* **1994**, 93, (2), 193-201
17. Berchtold, K. A.; Singh, R. P.; Young, J. S.; Dudeck, K. W. *Journal of Membrane Science* **2012**, 415-416, 265-270
18. Kumbharkar, S. C.; Liu, Y.; Li, K. *Journal of Membrane Science* **2011**, 375, (1-2), 231-240
19. Li, X.; Singh, R. P.; Dudeck, K. W.; Berchtold, K. A.; Benicewicz, B. C. *Journal of Membrane Science* **2014**, 461, 59-68
20. Calle, M.; Doherty, C. M.; Hill, A. J.; Lee, Y. M. *Macromolecules* **2013**, 46, (20), 8179-8189
21. Calle, M.; Lozano, A. E.; Lee, Y. M. *European Polymer Journal* **2012**, 48, (7), 1313-1322
22. Joseph, W. D.; Abed, J. C.; Mercier, R.; McGrath, J. E. *Polymer* **1994**, 35, (23), 5046-5050
23. Kim, S.; Han, S. H.; Lee, Y. M. *Journal of Membrane Science* **2012**, 403-404, 169-178
24. Ree, M.; Kim, K.; Woo, S. H.; Chang, H. *Journal of Applied Physics* **1997**, 81, (2), 698-708.
25. Stein, S. E., *Infrared Spectra*. NIST Mass Spec Data Center.

Chapter 4

Thermal imidization kinetics of ultrathin films of hybrid poly(POSS-imide)s

This chapter has been adapted from:

Raaijmakers, M.J.T., E.J. Kappert, A. Nijmeijer, N.E. Benes, Thermal imidization kinetics of ultrathin films of hybrid poly(POSS imide)s, *Macromolecules*, DOI 10.1021/acs.macromol.5b00473



Abstract

In the thermal imidization of an alternating inorganic-organic hybrid network, there is an inverse relationship between the length and flexibility of the organic bridges and the extent of the layer shrinkage. The hybrid material studied here consists of polyhedral oligomeric silsesquioxanes that are covalently bridged by amic acid groups. During heat treatment, shrinkage of the materials occurs due to the removal of physically bound water, imidization of the amic acid groups, and silanol condensation. For five different bridging groups with different lengths and flexibilities, comparable mass reductions are observed. For the shorter bridging groups, the dimensional changes are hindered by the limited network mobility. Longer, more flexible bridging groups allow for much greater shrinkage. The imidization step can be described by a decelerating reaction mechanism with an onset at 150 °C and shows a higher activation energy than in the case of entirely organic polyimides. The differences in the imidization kinetics between hybrid and purely organic materials demonstrates the need for close study of the thermal processing of hybrid, hyper-cross-linked materials.

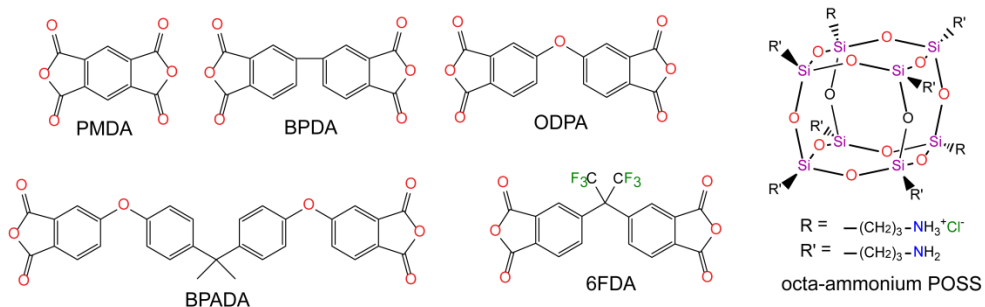
4.1. Introduction

Hybrid network materials exhibit properties that are distinct from their individual organic and inorganic constituents. These unique properties are a result of the interplay between flexible organic bridges and rigid inorganic domains.¹⁻³ Due to their chemical and thermal stability, aromatic imides are relevant candidates for the organic component in hybrid polymers. Most of these hybrid polyimides are based on sol-gel-derived silica-imide networks^{4, 5} or polyhedral oligomeric silsesquioxane (POSS)-derived materials. These POSS-derived materials can consist of a network of alternating POSS and imide groups,⁶⁻⁸ POSS cages that are covalently bound to oligomeric imides,⁹⁻¹³ or POSS cages that are tethered to a polyimide main chain as side or end group.^{14, 15}

To synthesize polyimide-based hybrid polymers, poly(amic acid) precursors are thermally processed to convert the amic acid groups to chemically and thermally robust imide groups. Compared to fully organic poly(amic acid)s, differences in the mobility of the functional groups in the hybrid material can strongly affect the imidization reaction kinetics and structural rearrangements.⁸ Therefore, a thermal processing strategy designed for an organic imide cannot simply be applied to its hybrid counterpart. Only a few studies have reported on the changes in the physical properties during thermal treatment of hybrid polyimides.^{10, 16, 17} Often, only the properties before and after the imidization step are measured, and the mechanisms of the thermally activated processes remain a black box.

Optimization of the thermal treatment step is crucial for obtaining a fully imidized material without significant decomposition of the organic moieties. Thermal imidization of hybrid imides most often needs to be performed in the solid state because of the limited solubility of the highly cross-linked networks. Solid-state thermal imidization has been studied *ex situ* using UV-vis,^{18, 19} infrared,¹⁹ and Raman spectroscopy.²⁰ *In situ* tracking of the imidization can be performed using TGA-MS,²¹ *in situ* infrared spectroscopy,²² and interferometry.²³⁻²⁵ The resulting data can be used to study the reaction kinetics. Past studies on these reactions unanimously agree on a decelerating reactivity;^{20, 26-29} first-order reaction models²⁶⁻²⁸ and diffusion models²⁹ have both been proposed. Most of these studies were performed on bulk materials, but in many applications, the materials are used as thin films. The length-scale confinement in ultrathin films can affect the time scale of diffusion-limited processes and, thus, result in different apparent kinetics.

Here, we explore the concurrent imidization and structural rearrangements of ultrathin POSS-based hybrid materials using a combination of time-resolved techniques. The changes to the materials chemistry in the bulk have been studied via TGA-MS, allowing for the assignment of the mass loss processes to specific chemical reactions. Thermo-ellipsometric analysis (TEA) has been applied to follow the changes in the layer thickness and refractive index during thermal treatment. To assess the influence of the organic moiety on the behavior of the hybrid material, the five different organic linking groups given in **Scheme 4-1** were studied. We conclude that the length and flexibility of the dianhydride precursor is an important factor that influences the network mobility during the imidization reaction, resulting in lower density films for shorter bridges.



Scheme 4-1. Structural formulas of the dianhydrides used as precursors for the crosslinking POSS-cages.

4.2. Experimental section

4.2.1. Synthesis of poly[POSS-(amic acid)]s by interfacial polymerization.

Toluene (anhydrous 99.8%, Sigma-Aldrich), 4,4-(hexafluoroisopropylidene) diphtalic anhydride (6FDA, Sigma-Aldrich), pyromellitic dianhydride (PMDA, Sigma-Aldrich), 3,3',4,4'-biphenyl tetracarboxylic dianhydride (BPDA, Sigma-Aldrich), 4,4'-oxydiphthalic anhydride (ODPA, Sigma-Aldrich), 4,4'-(4,4'-isopropylidene diphenoxy) bis(phthalic anhydride) (BPADA, Sigma-Aldrich), ammonium chloride-functionalized POSS (octa-ammonium POSS[®], Hybrid Plastics) and sodium hydroxide (NaOH, Sigma-Aldrich) were used as received. The POSS was dissolved in water. To partially convert the ammonium groups to reactive amine groups, the pH was adjusted to 9.9 using 1 M NaOH. Bulk poly[POSS-(amic acid)] was prepared by vigorously stirring a mixture of a 0.9 wt-% aqueous solution of

octa-ammonium POSS and a 0.075 wt.% dianhydride solution in toluene, which was filtered to remove any undissolved dianhydride. After reacting for several hours, the poly[POSS-(amic acid)] was removed from the toluene and water by vacuum filtration using a Büchner funnel, followed by rinsing with acetone to remove residual reactants. Poly[POSS-(amic acid)] membranes were prepared via interfacial polymerization on top of γ -alumina-coated α -alumina discs. The α -alumina discs were pre-wetted with the 0.9 wt.% aqueous POSS solution for 15 min under a 500-mbar vacuum, followed by drying for 30 min at room temperature. Subsequently, a solution of the dianhydride in toluene was poured onto the discs. After 5 min, the toluene was removed, and the samples were rinsed with acetone.

The structures and properties of the poly[POSS-(amic acid)] and poly(POSS-imide) samples were determined using infrared spectroscopy, X-ray photoelectron spectroscopy, differential scanning calorimetry, atomic force microscopy and gas permeability at elevated temperatures in previous work on these hybrid materials.^{6, 30}

4.2.2. Characterization of thin films.

Thermogravimetric analysis (TGA) was performed using an STA 449 F3 Jupiter[®] (Netzsch), equipped with a TG-only sample holder. Measurements were performed under 70 mL min⁻¹ N₂ flow with a heating rate of 20 °C min⁻¹ from 50 to 1200 °C. Temperature calibration was performed using melting standards. Measurements were run sample-temperature controlled. The sample masses were determined using an internal balance exactly 30 min after inserting the sample. A consistent residence time in the purge gas prior to measurement was found to be a crucial parameter to obtain reproducible TGA graphs. The gases that evolved during the thermogravimetric analysis were transferred to a mass spectrometer (QMS 403 D Aëolos[®], Netzsch). TGA and MS start times were synchronized, but no correction was applied for the time offset caused by the transfer line time (estimated < 30 sec, systematic offset). First, a bar graph scan for $m/z = 1-100$ amu was recorded for all poly(POSS-amic acid) samples in the N₂ atmosphere to determine the evolving m/z numbers (data not shown). The detected m/z numbers were selected and recorded more accurately in multiple-ion-detection mode with a dwell of 0.5 sec per m/z value at a resolution of 50.

4.2.3. Kinetic analysis

The samples that were designated for kinetic analysis were stored under vacuum at 30 °C for 24 hours prior to analysis to remove any sorbed water. The measurements were performed using a N₂ flow rate of 70 ml min⁻¹ with heating rates (β) of 5, 10, 15, and 20 °C min⁻¹ over the range from 50 to 1200 °C. Blank corrections with an empty cup were performed at every heating rate. The mass loss was converted to the normalized conversion (α). The activation energies were determined using the modified advanced isoconversional method that allows for analyzing non-linear temperature programs and variations in the apparent activation energy with α .³¹⁻³³ The resulting activation energies were used as starting values for multivariate analysis of the kinetics using a multistep parallel reaction model described by

$$\frac{d\alpha_i}{dt} = A_i \exp\left[\frac{-E_{a,i}}{RT(t)}\right] f_i(\alpha) \quad 4-1$$

Equation 4-1 was fit by minimizing the residual sum of squares (*RSS*) between the data and the fit using the *patternsearch* algorithm in Matlab. The individual steps were fitted with 14 different reaction models,³⁴ and the resulting *RSS* were used to determine the most accurate reaction model. Using the selected reaction models, all steps were fitted simultaneously, with A_i , $E_{a,i}$, and w_i as fitting parameters for every individual step i , where the sum of the weights w_i was set to 1.

4.2.4. Characterization of thin films by thermo-ellipsometric analysis (TEA)

The thicknesses and refractive indices of the poly[POSS-(amic acid)] films were measured as a function of time and temperature to track the progress of the thermal imidization. Measurements were performed on an M2000-X ellipsometer (J.A. Woollam Co.) equipped with a temperature-controlled hot-stage (HCS622, INSTEC), calibrated using melting point standards. The spectroscopic ellipsometry measurements were conducted in the full wavelength range of 210 – 1000 nm. For the room temperature measurements, spectra were recorded with 65°, 70°, and 75° angles of incidence; measurements at elevated temperatures were performed under a single angle of incidence of 70°. During the experiments, the hot stage was continuously purged with ultrapure N₂. Prior to the thermal treatment, the films were held under vacuum in the measurement cell for two hours at 100 °C, followed by a

30-minute dwell at 50 °C. Subsequently, the samples were heated to 300 °C at a heating rate of 5 °C min⁻¹. The sample was held at 300 °C for at least 6 hours to ensure completion of the imidization process. After the dwell, the sample was cooled to room temperature at the fastest attainable cooling rate (> 50 °C min⁻¹).

4.2.5. TEA data analysis

CompleteEASE (v.4.86, J.A. Woollam Co.) was used for the data analysis. The optical model used to model the layer on top of the γ -alumina-coated α -alumina disc is visualized in **Figure 4-2**. The layered optical model was constructed by first measuring the bare substrate and, subsequently, measuring each individually applied layer. All layers are characterized by their thickness d and their refractive index $n(\lambda)$. The wavelength-dependency of n is modeled by an optical dispersion. Due to light scattering below $\lambda = 500$ nm, the wavelength range was limited to 500-1000 nm.

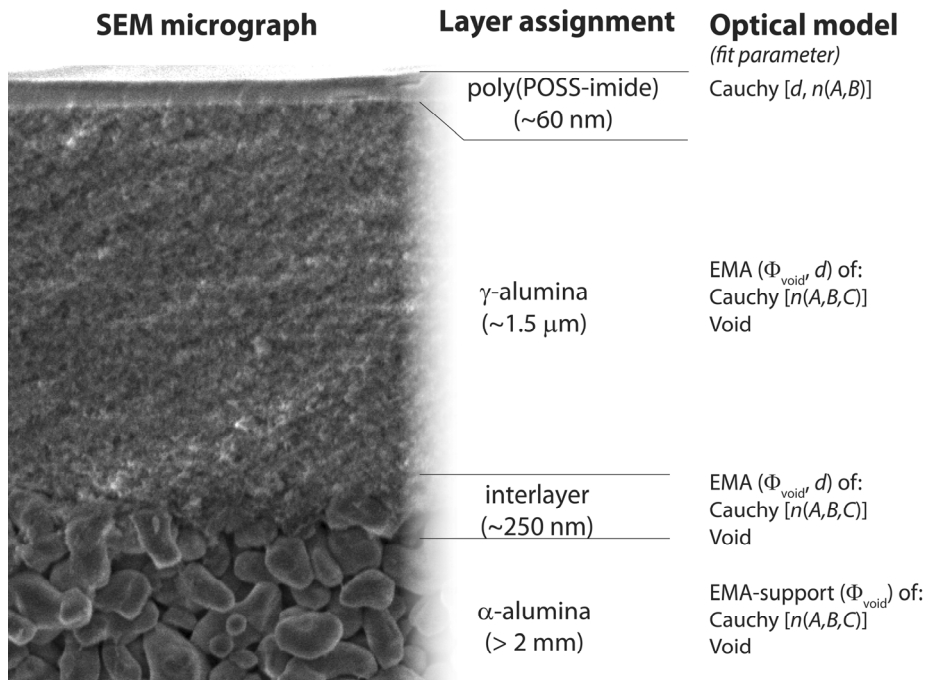


Figure 4-2: Optical model of a poly(POSS-imide) layer on top of a γ -alumina-coated α -alumina disc. The cross-section scanning electron micrograph of the supported layer shows the distinct morphology of the dense poly(POSS-imide) layer, the 1.5- μm γ -alumina layer and the macroporous α -alumina support.

The α -alumina disc was modeled using Bruggeman's Effective Medium Approximation (EMA) of alumina³⁵ and void ($n = 1$) with porosity $\Phi_{\text{void,substrate}}$. The roughness of the ceramic disc is modeled by a gradient in the porosity;³⁶ this layer is converted to an intermix layer between the α -alumina substrate and the γ -alumina coating to model infiltration of the coating layer into the substrate. The γ -alumina layer was also modeled using an EMA of alumina and void ($n = 1$) with porosity $\Phi_{\text{void},\gamma\text{-alumina}}$. The layer thickness and refractive index of the poly[POSS-(amic acid)] layers were modeled by a Cauchy optical dispersion, assuming transparency of the hybrid material in the wavelength range of 500-1000 nm. In the final fit, the thickness and optical dispersion were fit using the porosity of the γ -alumina layer and the porosity of the interlayer. Inclusion of the latter two parameters is required to correct for the changes in the residual water content in the γ -alumina pores.

4.3. Results and discussion

4.3.1. Imidization and thermal stability of the poly[POSS-(amic acid)] groups

The successful synthesis of poly[POSS-(amic acid)]s has been reported previously.^{6, 30} The poly[POSS-(amic acid)] can be converted to poly(POSS-imide)s by heating. The conversion of amic acid groups to imide groups is accompanied by the release of water [Scheme A4-1, Appendix]. **Figure 4-3** shows the mass loss and the primary evolved gases upon heating for five different poly[POSS-(amic acid)]s. All five materials display a mass loss in four different mass steps, indicated by bold numerals (**1**, **2**, **3**, and **4**) throughout the manuscript. Every step involves the loss of water from the material. The first three steps occur below 350 °C and are attributed to the removal of physically bound water (**1**), amic acid condensation and/or imidization (**2**), and dehydroxylation due to silanol condensation (**3**). A fourth step, recorded at temperatures exceeding 350 °C, involves the thermal decomposition of the hybrid material (**4**). These four steps will be discussed in more detail.

The removal of physically bound water (**1**) occurs from room temperature to ~250 °C. The CO₂ that is released during this step can originate from a decarboxylation reaction of either unreacted carboxylic acid groups or non-cyclized amic acid groups. Additionally, CO₂ may have been sorbed by the POSS-material, leading to CO₂ release at low temperatures.

The imidization of the material (2) occurs in the temperature range 150-300 °C, agreeing well with previous observations by infrared spectroscopy of the imidization temperature range of these hybrid polyimides.⁶ This step can overlap with the condensation of amic acid moieties of hydrolyzed or partially reacted organic bridges. Subsequently, these newly formed amic acid groups are available as additional groups for imidization. Mainly water evolves during step 2. The water loss is higher than would be expected based on an imidization step alone. Because the drying overlaps with the imidization (2) step, the mass loss below 300 °C can be associated with both drying and imidization. For the ODPA and 6FDA-based samples, a small amount of organic components is also detected. These components may be the result of the sublimation of unreacted organic groups.

It is unlikely that the water release during step 3 corresponds to a distinct second imidization step. Although the imidization is reported to occur via a two-step reaction (see, e.g.,²⁷), these steps are reported to directly follow each other. This step would then be detected as a unimodal, non-Gaussian peak, rather than a bimodal peak. Therefore, we hypothesize that the water release originates from a condensation reaction of silanol groups. The silanol groups are formed via the partial hydrolysis of POSS cages in the presence of NaOH in the aqueous solution used for interfacial polymerization.^{6, 37, 38} The silanol condensation is supported by the observed disappearance of the silanol absorbance band and simultaneous manifestation of POSS cage and ladder bands in the attenuated total reflection Fourier transform infrared spectroscopy (ATR-FTIR) measurements (Scheme A4-2 and Figure A4-1, Appendix).

The onset of the decomposition (4) at ~350 °C is found at the same temperature for all of the different organic materials. This observation suggests that the weakest link is found in the POSS-precursor. Theoretically, the aliphatic propyl-chain connecting the POSS-cage to the amine group is expected to have the lowest thermal stability.³⁹ The detection of C₃H_x components during the decomposition step in the TGA-MS analysis at lower temperatures than any other evolved organic components suggests that the propyl-group in the POSS-cage indeed forms the weakest link. Although the majority of the decomposition occurs between 350 and 650 °C, a minor mass loss associated with the release of CO₂ and methane is found to continue up to 1200 °C, indicating that organic groups are still present at these temperatures.

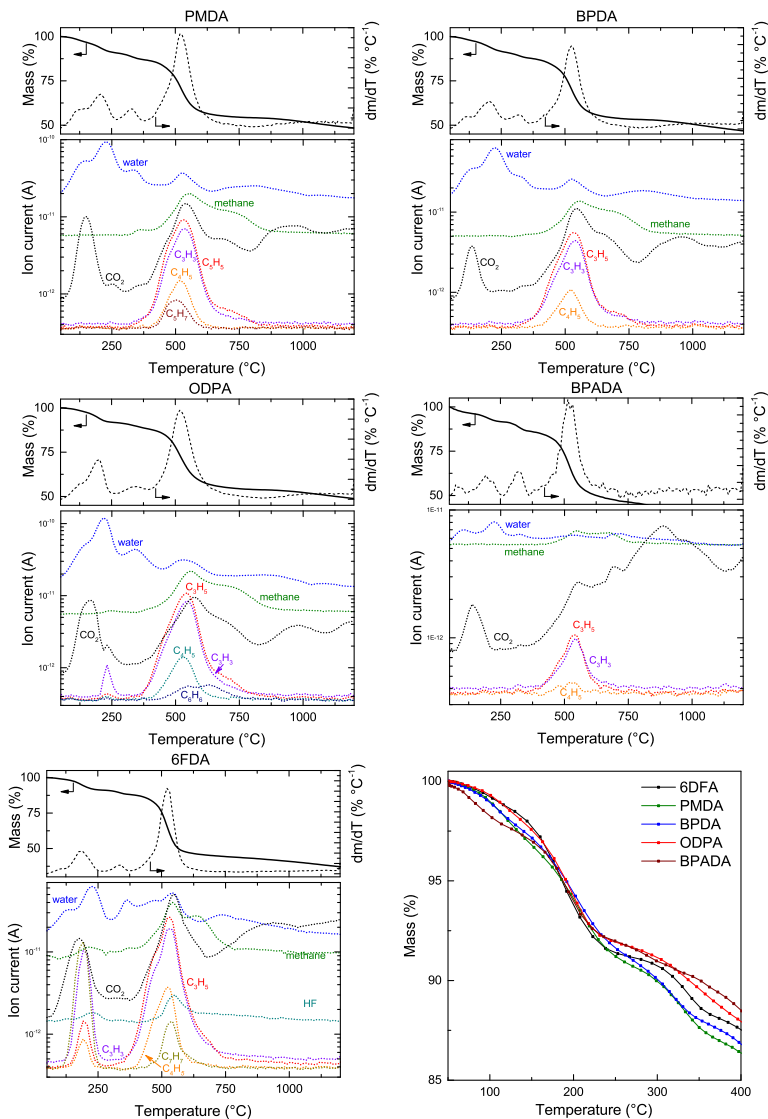


Figure 4-3: (all except for the bottom right graph) TGA-MS data: the relative mass and the differential mass loss (top panels) and the evolved gases (bottom panels) as a function of temperature for the poly[POSS-(amic acid)]s prepared using the different dianhydrides. All samples were heated under N₂ at 20 °C min⁻¹. (bottom right graph) Comparison of the changes in sample mass as function of the temperature for the different bridging groups.

In **Figure 4-3** (bottom right graph), the mass loss curve of the 5 different poly[POSS-(amic acid)]s are compared in the temperature range 50-400 °C.

The relative mass loss up to 300 °C, which is associated with drying (1), imidization (2), and silanol condensation (3), is comparable for all of the poly[POSS-(amic acid)]s. The similarity in the mass losses can be rationalized by the similar number of amic acid, unreacted amine, and silanol groups in all samples, as was apparent from the XPS analysis in previous studies.³⁰ Because the high molar mass of the POSS-cages dominates the mass of the polymer, the differences in the masses of the organic bridges will only have a marginal influence on the differences in the molecular weights of the synthesized network. As a result, the relative amount of mass released during imidization and silanol condensation will also be similar. Moreover, because the physisorbed water will mainly be present at the amic acid and amine groups and the number of these groups is similar for these materials, this amount will be comparable for all of the materials. Therefore, the sum of the drying, imidization, and silanol condensation processes result in similar mass losses, irrespective of which organic bridging groups is considered.

4.3.2. Imidization of thin layers

Accurate determination of the film thickness and density during thermal imidization is required to understand the mechanism of the imidization process in thin films. In particular, the role of the length and flexibility of the organic bridging group on the structural reorganizations is investigated. **Figure 4-4** shows the relative changes in the thicknesses of the different poly[POSS-(amic acid)]s during heating under nitrogen.

Upon heating, the thicknesses of all of the layers decrease. The stepwise shrinkage is in agreement with the stepwise mass loss. The hybrid materials display a smaller shrinkage than their organic counterparts.⁴⁰ For these organic polyimides, shrinkage is governed by the amount of residual solvent remaining after preparation by conventional solution polymerization and casting. In contrast, for the hybrid materials, the dense nature of the interfacial polymerization layer likely results in smaller amounts of residual solvent, resulting in the observed smaller shrinkages. The large degree of shrinkage outweighs the contributions from thermal expansion to the thickness. Only two distinct steps were recorded for the shrinkage: The drying step (1) recorded in the TGA experiment takes place during the pretreatment of the film at 100 °C and is not recorded in this measurement. The onset of the first shrinkage is recorded at 125 °C, and the process continues up to ~225 °C. A larger decrease in the thickness is recorded during further heating to 345 °C, resulting from the concurrent imidization (2) and silanol condensation (3). At this temperature,

the reaction driving the shrinkage is kinetically hampered, as is evident from the shrinkage that persists for several hours of dwelling at 345 °C.

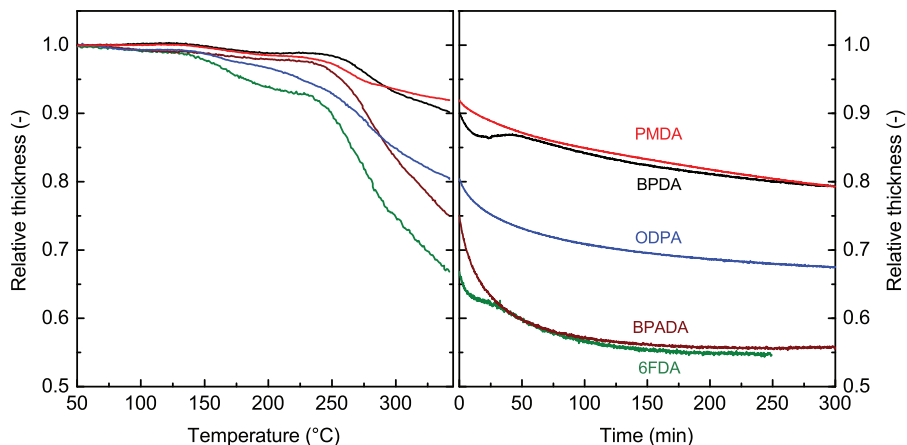


Figure 4-4: (left panel) Relative thickness during conversion of poly[POSS-(amic acid)]s to poly(POSS-imide)s as function of temperature, and (right panel) dwell time at 345 °C after heating from 50 to 345 °C at a heating rate of 5 °C min⁻¹. The optical model is validated by a duplicate measurement of the ODPA based poly[POSS-(amic acid)] (not shown here).

The observation that the shrinkage rate decreases in time during the isothermal treatment is indicative of a decelerating reaction.⁴¹ For the layers prepared with short and rigid dianhydride bridges (PMDA, BPDA and ODPA), the thickness changes last for longer than 10 hours of dwell time (not shown in graph). In contrast, for the longer dianhydride bridges (BPADA, 6FDA), the changes in thickness stabilize within 4 hours of dwell time. The final relative thickness changes the most for 6FDA, followed by the others in the order 6FDA ≈ BPADA > ODPA > BPDA ≈ PMDA. The shrinkages are most pronounced for the longest bridging groups because the larger spacing between the POSS-cages and higher flexibility of the long groups allows for larger and faster structural rearrangements. The lengths of the functional units and flexibility of the chain has been determined for polyimide bridges by the coherence length along the chain axis.⁴² For the studied bridges, the coherence lengths from smallest to largest are PMDA < BPDA < ODPA < BPADA. The coherence length for 6FDA is not measurable because its bulky character significantly distorts the chain of the polyimide. The differences in length and flexibility are also reflected in the linear thermal expansion coefficients that are larger for the longer bridges and smaller for the shorter bridges (Table A4-1, Appendix). For

solid-state reactions, decelerating reactions are typically described using a reaction order or diffusion model. The strong dependency of the shrinkage on the length and flexibility of the dianhydride bridge could indicate that diffusional limitations are the main reason for the decelerating rate.⁴³

The smaller shrinkage displayed by the layers with shorter bridging groups are indicative of more free volume in the imidized material, which is confirmed by a stronger decrease of the refractive index of the materials with short bridging groups. **Figure 4-5** shows the evolution of the relative refractive index of the layers during heating. For all layers, the refractive index decreases upon heating. In agreement with the mass and thickness changes, the refractive index change occurs in a stepwise manner. The concurrent decreases in the refractive index and thickness are a typical indication of the removal of a component from a matrix

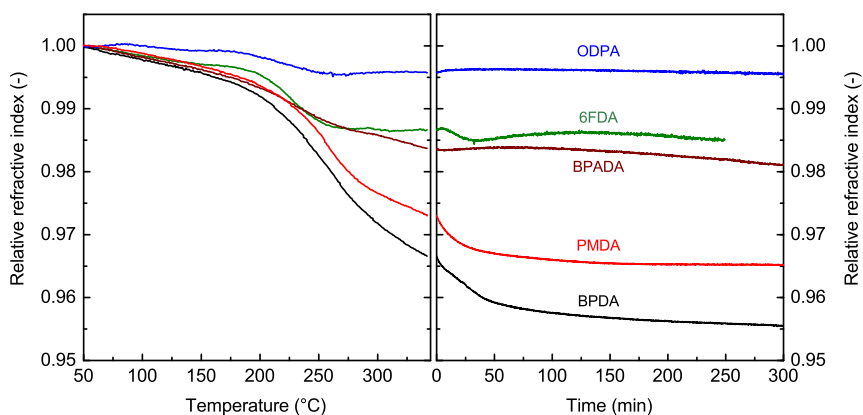


Figure 4-5: (Left panel) Relative refractive index at 632.8 nm wavelength of the poly[POSS-(amic acid)] as a function of the temperature and (right panel) the dwell time at 300 °C after heating from 50 to 300 °C at a heating rate of 5 °C min⁻¹.

The relative refractive index changes differ significantly among the different layers. The relative changes in the refractive index are the largest for BPDA, followed by the others in the order BPDA > PMDA > BPADA > 6FDA > ODPA. The changes in the refractive index due to chemical changes are expected to be similar for the different bridging groups. Therefore, the differences in the mobilities of the networks are the probable cause of the distinct changes in the refractive indices of the different bridging groups. For all networks, a similar amount of water is removed. However, in the more

rigid networks of the BPDA- and PMDA-based layers, the shrinkage is less pronounced. This corresponds to a relatively high free volume in the imidized networks with the short bridging groups, which is further substantiated by a larger change in their refractive index during the imidization step..

4.3.3. Density change upon imidization

The densities of the poly[POSS-(amic acid)] films change during imidization due to shrinkage and water removal. **Figure 4-6** shows a comparison of the changes in refractive index between the poly[POSS-(amic acid)]s and the poly(POSS-imide)s. All measurements were performed at 50 °C and, therefore, include any structural rearrangement that occurs during the cooling step that follows the imidization.

The refractive indices of the amic acids are similar for the materials prepared with the 5 different precursors. A strong decrease in the index was recorded for the short bridging groups PMDA and BPDA, whereas only a minor change was recorded for the BPADA, 6FDA and ODPA samples. Changes in the refractive index can occur due to chemical group conversion, removal of a component and densification. The changes in the refractive index due to imidization and water removal are similar because all materials display a similar mass loss and number of amic acid and silanol groups.

Therefore, the significant difference in layer shrinkage is the only explanation for the differences in the change in refractive index upon imidization. For the BPADA-, 6FDA-, and, to a lesser extent, ODPA-bridging groups, the shrinkage is significant.

For these materials, the overall changes in refractive index due to densification, chemical group conversion and water removal are negligible. For the PMDA- and BPDA-bridging groups, only minor shrinkage is observed because of the decreased mobility of the network. The absence of densification upon removal and chemical group conversion results in the formation of void space. The additional free volume that is created in the PMDA- and BPDA-based materials results in a decrease in the refractive index

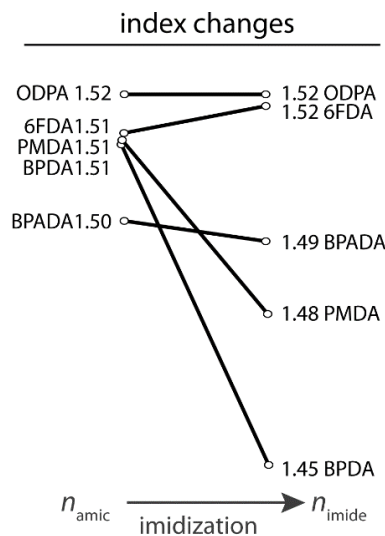


Figure 4-6: Changes in refractive index at 50 °C as a result of imidization, for 5 different dianhydride precursors.

4.3.4. Kinetic analysis of the reactions by isoconversional and multivariate analyses

As discussed in the previous sections, upon heating to 600 °C, four distinct steps are considered for the thermal evolution of the mass of the poly[POSS-(amic acid)]s: drying (1), imidization (2), silanol condensation (3), and decomposition of the organic moieties (4). The imidization step (2) significantly overlaps with the drying step (1); in the kinetic analysis, these steps will be considered a single step, referred to as step 1+2. Step 1+2 is responsible for ~16% of the mass loss, and the imidization step may constitute only a small part of this mass loss. Step 3, which is responsible for ~5% of the mass loss, is associated with water release from the condensation reactions of the silanol groups that were formed via the partial hydrolysis of the POSS cages during the synthesis. Step 3 may partially overlap with the final stages of the imidization reaction (2), but the condensation reactions are anticipated to dominate the observed mass loss. Step 4 is associated with the decomposition of the hybrid materials.

Determination of the activation energy via an isoconversional analysis

Here, the reaction kinetics of the poly(POSS-6FDA) material are analyzed. The reaction kinetics are typically expressed by three parameters for every step i : the pre-exponential constant A , the reaction model $f(\alpha)$, and the activation energy E_a (see Equation 1). First, the activation energy as a function of mass loss is determined without assuming a reaction model, using a model-free isoconversional analysis method proposed in the literature.³¹⁻³³ To accomplish this goal, the mass loss is converted to the normalized conversion α . Drying and imidization (1+2) are detected in the range $\alpha=0-0.16$, silanol condensation (3) is detected for $\alpha=0.16-0.21$, and decomposition (4) for $\alpha=0.21-1$. The results of this analysis, shown in Figure A4-4 in the Appendix, clearly indicate the existence of the three different steps. The combined step 1+2 and step 3 are associated with activation energies of $\sim 225 \text{ kJ mol}^{-1}$ and $\sim 150 \text{ kJ mol}^{-1}$, respectively. Step 4 shows an activation energy that gradually increases with conversion from 225 to 400 kJ mol^{-1} .

In the analysis of step 1+2, the resulting value for the activation energy will be an effective average of the activation energies for the removal of physisorbed water and the imidization reactions. Imidization can only occur after the removal of the physisorbed water from the amic acid group. The apparent activation energy determined in this study is significantly higher than the values typically obtained in previous imidization studies, which are on the

order of ~ 50 to 100 kJ mol^{-1} .^{18, 19, 27-29} The use of a non-isothermal temperature program can be excluded as the cause of this difference,⁴¹ and the difference is too large to result solely from the assumption of a different reaction model.⁴⁴ As the differences cannot be attributed to modeling artefacts, the hybrid nature of the material strongly increases the activation energy of the imidization reaction. It has been suggested that the rotation of the amic acid carbon towards the amide group could be the rate-limiting step during the imidization reaction.⁴⁵ The rigid characteristics and the high degree of network interconnectivity of the POSS cage can hinder the rotational freedom of the amic acid groups.

Determination of the kinetic triplet through a multivariate analysis of the kinetics

The model-free values for the activation energy are subsequently used as inputs for a multivariate analysis of the kinetics, where Equation 1 is integrated for the 3 different reaction steps (**1+2**, **3**, and **4**). In the fitting approach, all steps are first fitted independently in their own temperature range: For step **1+2**, this range is $50\text{-}250 \text{ }^\circ\text{C}$; for step **3**, this range is $250\text{-}380 \text{ }^\circ\text{C}$; and for step **4**, this range is $380 \text{ }^\circ\text{C}$ and above. The optimal fit parameters obtained for the individual reaction steps are subsequently combined and used as starting values for an overall fit of the data over the full temperature range. In this overall fit, the relative weights of the individual steps are included as a fit parameter as well.

Fitting of the drying and imidization steps (1+2)

For step **1+2**, when a single step reaction is fitted to the data in the range $\alpha=0.02\text{-}0.16$, none of the 14 reaction models given in Table A4-2 (Appendix) adequately capture the data. The reaction order model F1 and the diffusional models D2, D3, and D4 describe the shape of the curve better than the other models. The inadequacy of the fit, when assuming a single reaction step, is in line with the previous suggestion that, for imidization, a diffusional term needs to be added to the commonly employed F1-model.²⁹ Fitting the data with two reactions in parallel also does not capture the data accurately. To improve the fit, a distributed activation energy can be assumed. This approach has been shown to be adequate for a wide range of parallel reactions.⁴⁶ By combining the D4 reaction model (best description of the data from the first fitting attempt) with a Weibull distribution of the activation energy, the data can be fitted accurately. The mean activation energy of $\sim 225 \text{ kJ mol}^{-1}$, obtained from

the model fit, is in agreement with the value obtained from the isoconversional analysis. The suitability of the diffusional model can indicate that densification of the material limits the reaction rate with increasing conversion.

Fitting of the silanol condensation (3)

For the silanol condensation (3), when a single step reaction is fitted to the data in the range $\alpha=0.16-0.21$, the reaction-order model F1 most accurately describes the data. The corresponding activation energy is $\sim 150 \text{ kJ mol}^{-1}$. The fit results are found to be completely independent of the starting values used for the fit. The suitability of the F1 model implies that the reactivity decreases due to a decrease in the concentration of reactive groups.

Fitting of the decomposition (4)

For the decomposition step (4), the strong dependency of the activation energy on the conversion hints at multiple processes taking place. Therefore, a distributed activation energy is required to properly fit the measured data. The onset of the decomposition processes is captured adequately using a Weibull-distributed activation energy. This approach does not accurately capture the complete degradation process. Because only the onset of decomposition is of interest in this study, no further attempts at optimizing a quantitative fit of the data were performed.

Overall fit of the reaction kinetics

The values obtained for the pre-exponential constant, activation energy, and reaction model for the individual steps were used as initial guess values for a fit of the data over the entire temperature and conversion ranges. In addition, the weights, w_i , of the individual steps are included as an extra fit parameter, for which w_4 is set equal to $1 - w_{1+2} - w_3$. The results of the overall fit are shown in **Figure 4-7**, and the values corresponding to the resulting fit are given in **Table 4-1**. The resulting values are insensitive to the starting values and do not deviate strongly from the values obtained when fitting the individual steps. This result supports the appropriateness of considering the individual steps in the analysis. The high weight of reaction **1+2** over reaction **3** confirms the strong mass losses during the drying and imidization steps.

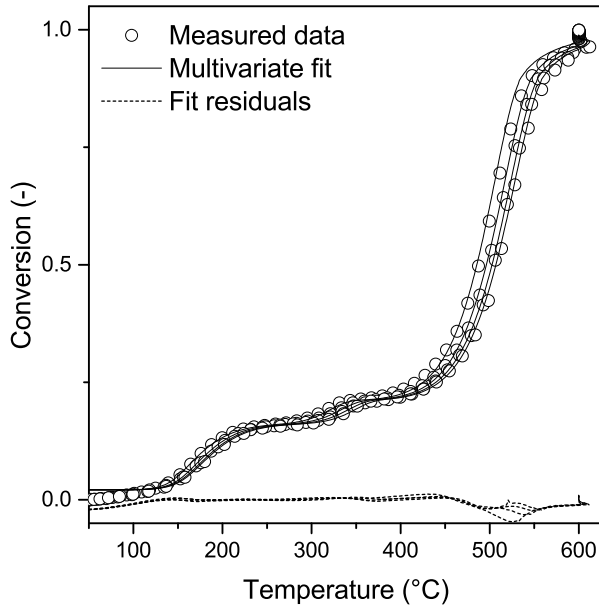


Figure 4-7: Multivariate fit for the thermal treatment of 6FDA-based poly[POSS-(amic acid)] under a N₂ atmosphere. The symbols depict the experimental data and solid lines represent the fit; the dashed lines show the fit residuals.

Table 4-1: Kinetic parameters for the thermal treatment of 6FDA-based poly[POSS-(amic acid)] under a N₂ atmosphere. Step 1+2 and 4 are fitted using a Weibull-distributed activation energy, and step 3 was fitted to an F1 reaction model.

Conversion	Drying and imidization (1+2, w = 0.141)	Silanol condensation (3, w = 0.054)	Decomposition (4, w = 0.785)
A (min ⁻¹)	2.62·10 ²⁴	5.12·10 ¹²	3.77·10 ¹⁸
Ea threshold (kJ mol ⁻¹)	200	n/a	295
□ (-)	1.65	n/a	3.29
□ (kJ mol ⁻¹)	26.8	n/a	4.9
Ea average (kJ mol ⁻¹) ^a	224	151.4	299
Reaction model	$\frac{3}{2}(1-\alpha)^{2/3} [1-(1-\alpha)^{1/3}]$	$1-\alpha$	$\frac{3}{2}(1-\alpha)^{2/3} [1-(1-\alpha)^{1/3}]^{-1}$

^a The activation energy indicated for step 2 is the single activation energy used for the fit

4.4. Conclusion

Four steps were identified in the thermal processing of poly[POSS-(amic acid)]s: drying of physisorbed water (1), imidization (2), silanol condensation (3), and decomposition (4). The imidization was found to occur between 150 and 300 °C, independent of the bridging group. Because of the comparatively low contribution of the organic bridging groups to the total mass of the material, the mass loss during all steps is similar. In contrast to the mass loss, the linking group does strongly influence the shrinkage and, therefore, the densification that occurs during imidization of the layer. The most pronounced shrinkage is found for the poly[POSS-(amic acid)]s with long bridges. In materials with short bridges, the network densification is hindered by the rigidity of the bridges. Therefore, the use of shorter bridges results in hybrid polyimides with significantly higher free volumes and, thus, lower densities.

A kinetic analysis of the imidization step reveals a very high value for the activation energy compared to imidization of fully organic poly(amic acid)s. This result is attributed to the high degree of interconnectivity and the rigidity of the POSS cages, which impedes the rate-limiting rotation of the amic acid groups. The appropriateness of the decelerating reaction model suggests that the decelerating reaction rate is due to network densification.

The combination of TGA-MS and TEA provides unique insights into the structural rearrangements in the hybrid materials that can be used for further optimization of thermal treatments of hybrid organic-inorganic network materials.

4.5. Acknowledgements

This project has received funding from the European Union's Seventh Framework Programme for research, technological development and demonstration under CARENA grant agreement no. 263007.

4.6. Appendices

4.6.1. Conversion processes during thermal imidization

During the heat treatment of the poly[POSS-(amic acid)]s, reaction steps associated with drying and imidization (1+2), silanol condensation (3) and decomposition (4) are observed. Scheme S2 shows the reaction mechanism of step 2 and 3 that occur. During step 2 of the heat treatment process, mainly conversion of amic acid to imide groups occurs (blue).

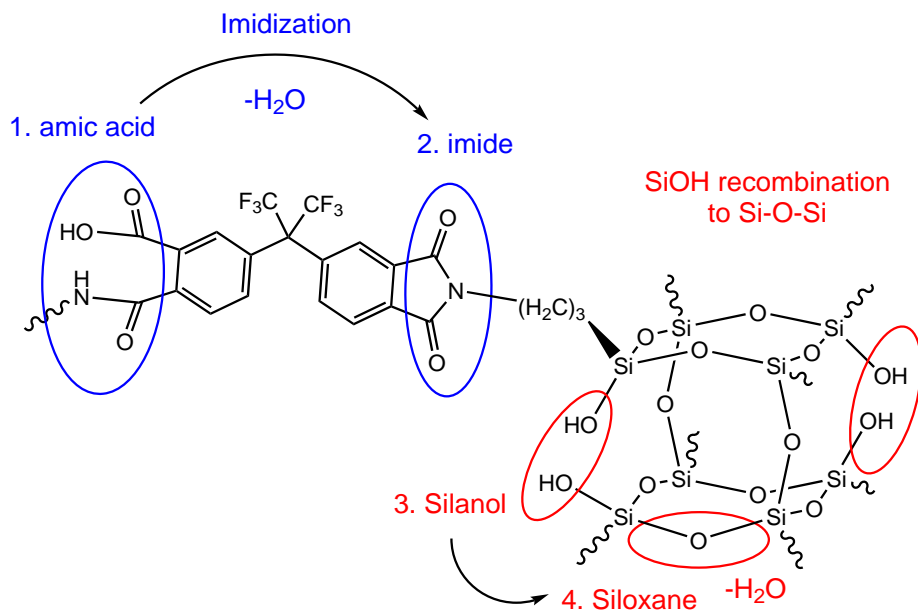


Figure 4-A9: Overview of the water loss originating from imidization and silanol condensation reactions.

During step 3, additional water loss is observed that originates from recombination of silanol groups to form siloxane groups (red). The silanol condensation reaction is observed from attenuated total reflection – Fourier transform infrared spectroscopy (ATR-FTIR) measurements of poly[POSS-(amic acid)] samples that were heat treated at different temperatures. Figure 4-A10 shows the relative intensity of infrared peaks that are characteristic for Si-O bonds in a cage or ladder (i.e., a broken POSS cage) structure, and peaks that are characteristic for silanol groups. The peak at 3230 cm^{-1} could include vibrations from water present in the material. Although the scatter in the data makes a quantitative analysis difficult, the data shows a trend of increasing ladder and cage formation with increasing treatment temperatures, at the expense of silanol groups.

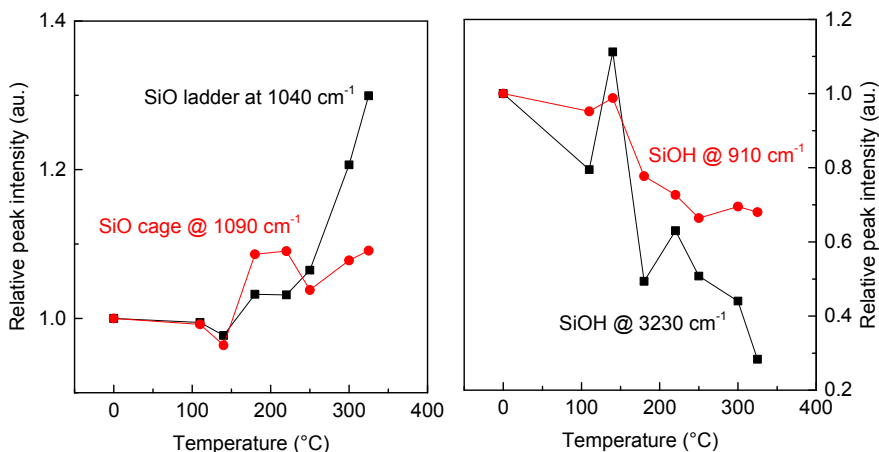


Figure 4-A10: (left panel) Relative intensity of the infrared peaks at 1040 and 1090 cm^{-1} for 6FDA-based samples, corresponding to a Si-O-Si bond in ladder and cage configuration, respectively; (right panel) Relative intensity of the infrared peaks at 910 and 3230 cm^{-1} , both corresponding to silanol groups. All infrared spectra were normalized with respect to the CF_3 band at 1254 cm^{-1} . All peak intensities are normalized with respect to their initial peak intensity.

4.6.2. Thickness and refractive indices

The thickness and refractive index have been measured using spectroscopic ellipsometry. **Figure A4-2** shows the evolution of the thickness (top panels) and refractive index (bottom panels) of poly[POSS-(amic acid)]s prepared using PMDA, BPDA, ODPDA, BPADA and 6FDA precursors, as function of temperature (left panel) and as function of time during the subsequent dwell at 345 °C (right panel). The data in Figure A4-2 correspond to the relative thickness data in Figure 4-3 and relative refractive index data in Figure 4-4.

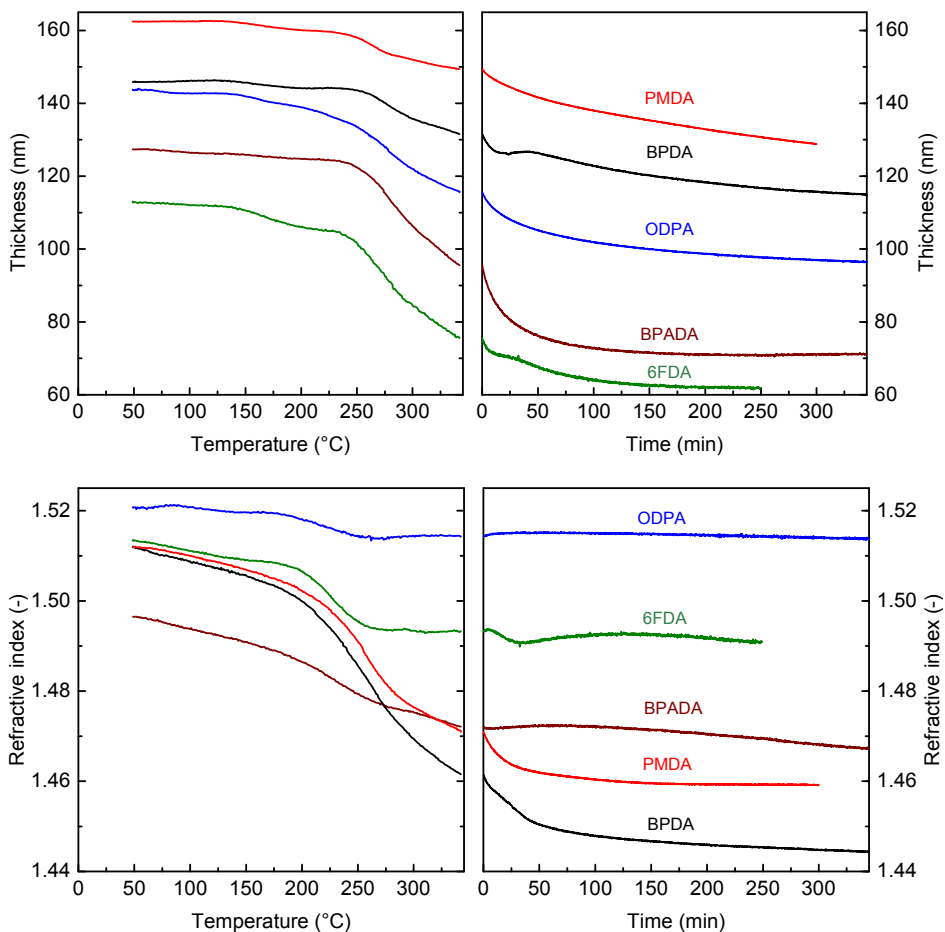


Figure A4-2. (top panels) Thickness and (bottom panels) refractive index of the poly[POSS-(amic acid)] layers as function of temperature (left), and dwell time at 345 °C after heating from 50 to 345 °C at a heating rate of 5 °C min⁻¹. The poly[POSS-(amic acid)] layers were prepared atop a γ -alumina coated α -alumina disc using PMDA, BPDA, ODPa, BPADA and 6FDA precursors.

Duplicate measurements were performed to validate the optical model of the spectroscopic ellipsometry measurements. **Figure A4-3** shows the refractive index and thickness data of two poly[POSS-(amic acid)] prepared using ODPa (left panel). The data shows a similar evolution in thickness and refractive index. The absolute values of the thickness are slightly different, which can be related to the reproducibility of the interfacial polymerization reaction.

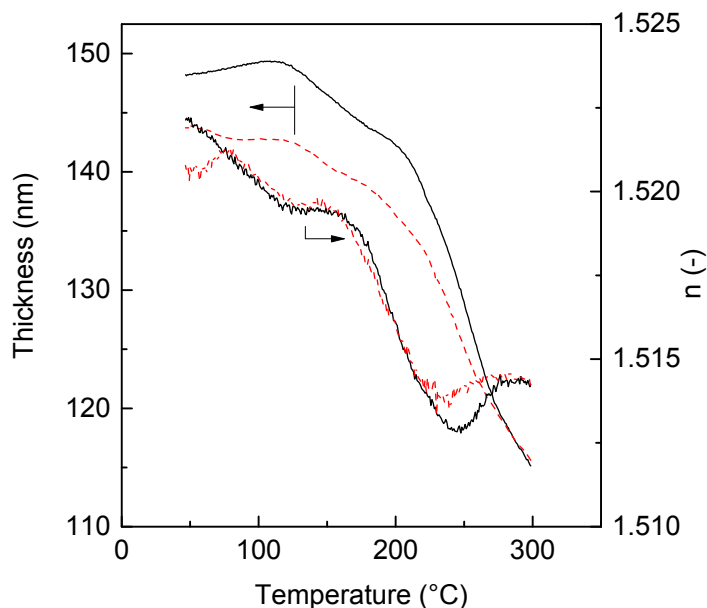


Figure A4-3. Refractive index and thickness data of two poly[POSS-(amic acid)]s prepared using ODPa (left panel).

The linear thermal expansion coefficient of the poly(POSS-imide)s has been determined by measuring the thicknesses between 50 °C and 345 °C. **Table A4-1** shows the linear thermal expansion coefficients of the poly(POSS-imide)s.

Table A4-1. Linear thermal expansion coefficient of poly(POSS-imide)s prepared using PMDA, BPDA, ODPa, BPADA and 6FDA

	Thickness at 50 °C	Thickness at 345 °C	Linear thermal expansion coefficient
Dianhydride linker	(nm)	(nm)	(10^{-6} C^{-1})
PMDA	118.6	121.3	76
BPDA	113.2	114.6	44
ODPA	91.9	95.7	141
BPADA	64.4	70.5	317
6FDA	59.2	61.9	154

4.6.3. Kinetic analysis

Figure A4-4 (left panel) shows the conversion of the mass loss of 6FDA-POSS as a function of temperature for heating rates $\beta=5,10,15$ and $20\text{ }^{\circ}\text{C min}^{-1}$. The shift in the curves introduced by the different heating rates is an indication of kinetically limited processes. A plateau in the conversion curves is related to the absence of mass loss processes. The curves before and after the plateau can therefore be appointed to distinct, serial reaction steps. The conversion profile demonstrates 3 distinct mass loss steps: step 1 from $\alpha = 0-0.16$, step 2 from $\alpha = 0.16-0.21$, and step 3 from $\alpha = 0.21-1$. The effective activation energy for mass loss as a function of the conversion can be calculated by performing an isoconversional analysis.⁴¹

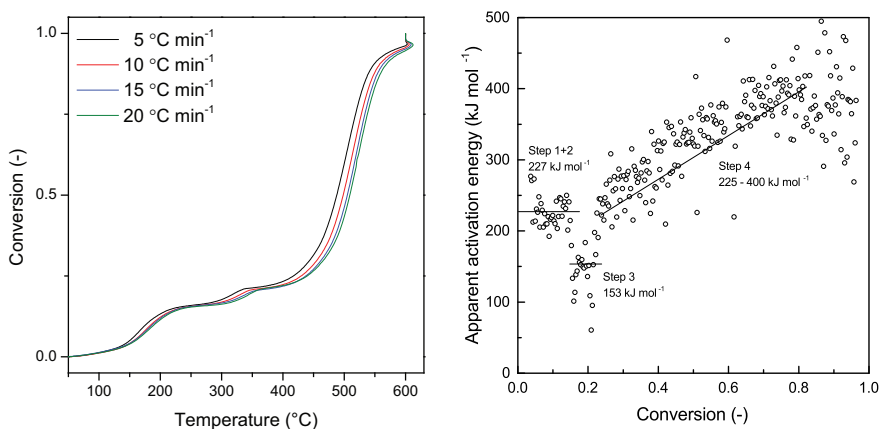


Figure A4-4. (left panel) Conversion of the mass loss of 6FDA-based poly[POSS-(amic acid)] as function of temperature, for heating rates $\beta=5,10,15$ and $20\text{ }^{\circ}\text{C min}^{-1}$ under N_2 atmosphere. **(right panel)** Apparent activation energy as function of conversion, determined by the isoconversional analysis of TGA-data for the thermal treatment of 6FDA based poly[POSS-(amic acid)].

This activation energy is referred to as an ‘effective’ activation energy, as it is in fact an average over the activation energies of the different reactions taking place at a specific value of the conversion. The occurrence of multiple reactions within the distinct steps is apparent from the release of different fragments that is observed in the TGA-MS data. Step 1 is dominated by the loss of water from the material, accompanied by the release of small amounts of CO_2 and aromatic fragments. Step 2 is only coupled to the loss of water. In step 3, aromatics, CO_2 and water are released. **Figure A4-4 (right panel)**

shows the effective activation energy for the thermal imidization steps of poly(POSS-amic acid) prepared with 6FDA. The three distinct steps result in three plateaus in the effective activation energy: For step 1, $E_a \sim 225 \text{ kJ mol}^{-1}$; for step 2, $E_a \sim 150 \text{ kJ mol}^{-1}$; for step 3, E_a increased from ~ 225 to $\sim 400 \text{ kJ mol}^{-1}$. Only an activation energy is insufficient for performing kinetic calculations, as the reaction rate is typically expressed as a function of A , the pre-exponential constant, and $f(\alpha)$. An overview of possible reaction models is given in **Table A4-2**.

Table A4-2. Overview of possible reaction models, taken from ³⁴

Reaction model (name + abbreviation)	$f(\alpha)$
Power law – P4	$4\alpha^{3/4}$
Power law – P3	$3\alpha^{2/3}$
Power law – P2	$2\alpha^{1/2}$
Power law – P2/3	$2/3\alpha^{1/2}$
Mampel (first order) – F1	$1-\alpha$
Avrami-Erofeev – A4	$4(1-\alpha)[- \ln(1-\alpha)]^{3/4}$
Avrami-Erofeev – A3	$3(1-\alpha)[- \ln(1-\alpha)]^{2/3}$
Avrami-Erofeev – A2	$2(1-\alpha)[- \ln(1-\alpha)]^{1/2}$
Contracting sphere – R3	$3(1-\alpha)^{2/3}$
Contracting cylinder – R2	$2(1-\alpha)^{1/2}$
One-dimensional diffusion – D1	$1/2\alpha^{-1}$
Two-dimensional diffusion – D2	$[- \ln(1-\alpha)]^{-1}$
Three-dimensional diffusion (Jander) – D3	$3/2(1-\alpha)^{2/3}[1-(1-\alpha)^{1/3}]^{-1}$
Three-dimensional diffusion (Ginstling-Brounshtein) D4	$3/2[(1-\alpha)^{-1/3}-1]^{-1}$

In order to get insight into the reaction model, a temperature program containing isothermal dwells was ran. The temperatures of the isothermals were chosen such that in every isothermal step, one of the reactions was taking place. In line with previous observations, the profile of the conversion versus the time revealed a decelerating reaction profile that is commonly associated to the reaction order (F) or diffusion (D) models from Table A4-2. ^{20, 26-29}

To determine which reaction model captures the data most adequately, and to obtain the value for the pre-exponential constant, the data given in Figure A4-4 (left panel) was fit by a multivariate kinetic model. To perform this analysis, the 3 steps in the activation energy were first fitted individually, using the activation energies obtained from Figure A4-4 right panel) as starting values. The data was fit 14 times, one time for each reaction models given in Table

A4-2. These individual fits were followed by a combined fit of the full conversion range.

For the fitting of the first step, it was found that the data could not be captured using a single kinetic triplet (A , E_a , and $f(\alpha)$). This is of no surprise, as the MS-data gave clear evidence for multiple reactions occurring in this step. Surprisingly, however, fitting of the data with a combination of two individual reactions did not result in a good fit either. Therefore, it was tried to fit the data with a distributed activation energy. Here, a Weibull-distribution was chosen to model the distributed activation energy. For certain values of the parameters, this distribution can be mathematically equivalent to a Gamma-distributed activation energy or a n th order reaction.⁴⁶ Using the Weibull-distribution, the data could be accurately fit, as long as the fitting was started from a conversion value of $\alpha = 0.02$. Below this value, the individual curves do not demonstrate a shift with heating rate, implying a thermodynamic equilibrium. Step **2** could be captured accurately using a single kinetic triplet. Tests for the different reaction models revealed that a first order reaction (F1) model captured the data most accurately. For step **3**, again a distribution in the activation energy was required for the fitting. Again this is with no surprise, since the degradation of the organic fragments typically consist of many different reactions, smeared out over a broad temperature range. These reaction distributions are commonly fit with distributed kinetic parameters.⁴⁶

4.7. References

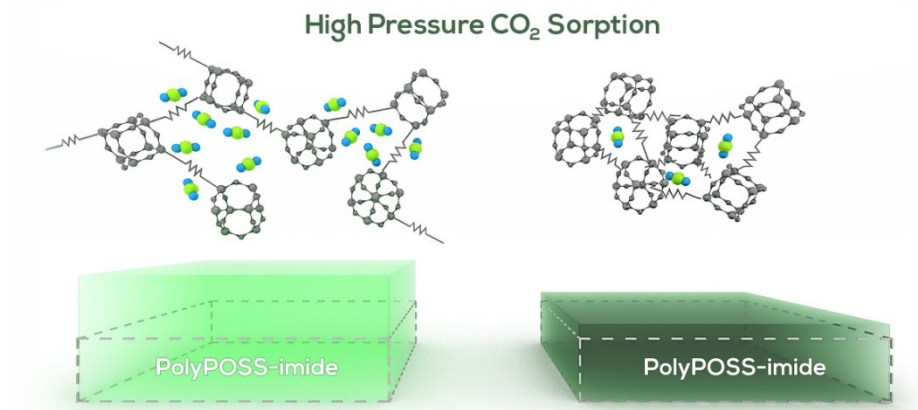
1. Pielichowski, K.; Njuguna, J.; Janowski, B.; Pielichowski, J., Polyhedral oligomeric silsesquioxanes (POSS)-containing nanohybrid polymers. In *Advances in Polymer Science*, 2006; Vol. 201, pp 225-296.
2. Ruiz-Hitzky, E.; Aranda, P.; Darder, M.; Ogawa, M. *Chemical Society Reviews* **2011**, 40, (2), 801-828
3. Sanchez, C.; Soler-Illia, G. J. D. A. A.; Ribot, F.; Lalot, T.; Mayer, C. R.; Cabuil, V. *Chemistry of Materials* **2001**, 13, (10), 3061-3083
4. Beecroft, L. L.; Johnen, N. A.; Ober, C. K. *Polymers for Advanced Technologies* **1997**, 8, (5), 289-296
5. Khalil, M.; Saeed, S.; Ahmad, Z. *Journal of Applied Polymer Science* **2008**, 107, (2), 1257-1268
6. Raaijmakers, M. J. T.; Hempenius, M. A.; Schön, P. M.; Vancso, G. J.; Nijmeijer, A.; Wessling, M.; Benes, N. E. *Journal of the American Chemical Society* **2014**, 136, (1), 330-335
7. Asuncion, M. Z.; Laine, R. M. *Macromolecules* **2007**, 40, (3), 555-562

8. Choi, J.; Tamaki, R.; Kim, S. G.; Laine, R. M. *Chemistry of Materials* **2003**, *15*, (17), 3365-3375
9. Devaraju, S.; Vengatesan, M. R.; Alagar, M. *High Performance Polymers* **2011**, *23*, (2), 99-111
10. Huang, J. C.; He, C. B.; Xiao, Y.; Mya, K. Y.; Dai, J.; Siow, Y. P. *Polymer* **2003**, *44*, (16), 4491-4499
11. Leu, C. M.; Chang, Y. T.; Wei, K. H. *Macromolecules* **2003**, *36*, (24), 9122-9127
12. Leu, C. M.; Chang, Y. T.; Wei, K. H. *Chemistry of Materials* **2003**, *15*, (19), 3721-3727
13. Seçkin, T.; Köytepe, S.; Adigüzel, H. I. *Materials Chemistry and Physics* **2008**, *112*, (3), 1040-1046
14. Wright, M. E.; Petteys, B. J.; Guenther, A. J.; Fallis, S.; Yandek, G. R.; Tomczak, S. J.; Minton, T. K.; Brunsvold, A. *Macromolecules* **2006**, *39*, (14), 4710-4718
15. Monticelli, O.; Fina, A.; Ullah, A.; Waghmare, P. *Macromolecules* **2009**, *42*, (17), 6614-6623
16. Wright, M. E.; Schorzman, D. A.; Feher, F. J.; Jin, R. Z. *Chemistry of Materials* **2003**, *15*, (1), 264-268
17. Wright, M. E.; Petteys, B. J.; Guenther, A. J.; Fallis, S.; Yandek, G. R.; Tomczak, S. J.; Minton, T. K.; Brunsvold, A. *Macromolecules* **2006**, *39*, (14), 4710-4718.10.1021/ma060372d
18. Pyun, E.; Mathisen, R. J.; Sung, C. S. P. *Macromolecules* **1989**, *22*, (3), 1174-1183.10.1021/ma00193a031
19. Dickinson, P. R.; Sung, C. S. P. *Macromolecules* **1992**, *25*, (14), 3758-3768
20. Seo, Y.; Lee, S. M.; Kim, D. Y.; Kim, K. U. *Macromolecules* **1997**, *30*, (13), 3747-3753.10.1021/ma961482v
21. Kim, B. H.; Park, H.; Park, H.; Moon, D. C. *Thermochimica Acta* **2013**, *551*, 184-190
22. Kim, S. K.; Kim, H. T.; Park, J. K. *Polymer Journal* **1998**, *30*, (3), 229-233
23. Ree, M.; Shin, T. J.; Park, Y. H.; Kim, S. I.; Woo, S. H.; Cho, C. K.; Park, C. E. *Journal of Polymer Science, Part B: Polymer Physics* **1998**, *36*, (8), 1261-1273
24. Kook, H. J.; Kim, D. *Journal of Materials Science* **2000**, *35*, (12), 2949-2954
25. Shin, T. J.; Ree, M. *Langmuir* **2005**, *21*, (13), 6081-6085
26. Yilmaz, T.; Güçlü, H.; Özarslan, Ö.; Yildiz, E.; Kuyulu, A.; Ekinci, E.; Güngör, A. *Journal of Polymer Science, Part A: Polymer Chemistry* **1997**, *35*, (14), 2981-2990
27. Seo, Y. *Polymer Engineering and Science* **1997**, *37*, (5), 772-776
28. Kim, Y. J.; Glass, T. E.; Lyle, G. D.; McGrath, J. E. *Macromolecules* **1993**, *26*, (6), 1344-1358
29. Lu, H.; Zhou, J.; He, T. *Journal of Applied Polymer Science* **2001**, *79*, (11), 2052-2059
30. Raaijmakers, M. J. T.; Wessling, M.; Nijmeijer, A.; Benes, N. E. *Chemistry of Materials* **2014**, *26*, (12), 3660-3664
31. Vyazovkin, S.; Dollimore, D. *Journal of Chemical Information and Computer Sciences* **1996**, *36*, (1), 42-45
32. Vyazovkin, S. *Journal of Computational Chemistry* **2001**, *22*, (2), 178-183
33. Vyazovkin, S. *Journal of Computational Chemistry* **1997**, *18*, (3), 393-402
34. Vyazovkin, S.; Chrissafis, K.; Di Lorenzo, M. L.; Koga, N.; Pijolat, M.; Roduit, B.; Sbirrazzuoli, N.; Suñol, J. J. *Thermochimica Acta* **2014**, *590*, 1-23

35. Lichtenstein, T., *Handbook of Thin Film Materials*. College of Engineering and Applied Science, University of Rochester: University of Rochester. College of Engineering and Applied Science, 1979.
36. Ogieglo, W.; Wormeester, H.; Wessling, M.; Benes, N. E. *ACS Applied Materials and Interfaces* **2012**, 4, (2), 935-943
37. J. Feher, F.; D. Wyndham, K.; Soulivong, D.; Nguyen, F. *Journal of the Chemical Society, Dalton Transactions* **1999**, (9), 1491-1498.10.1039/A807302C
38. Dalwani, M.; Zheng, J.; Hempenius, M.; Raaijmakers, M. J. T.; Doherty, C. M.; Hill, A. J.; Wessling, M.; Benes, N. E. *Journal of Materials Chemistry* **2012**, 22, (30), 14835-14838
39. Van Krevelen, D. W.; Te Nijenhuis, K., *Properties of Polymers*. 2009.
40. Unsal, E.; Cakmak, M. *Macromolecules* **2013**, 46, (21), 8616-8627.10.1021/ma401361w
41. Vyazovkin, S.; Burnham, A. K.; Criado, J. M.; Pérez-Maqueda, L. A.; Popescu, C.; Sbirrazzuoli, N. *Thermochimica Acta* **2011**, 520, (1-2), 1-19
42. Ree, M.; Kim, K.; Woo, S. H.; Chang, H. *Journal of Applied Physics* **1997**, 81, (2), 698-708
43. Khawam, A.; Flanagan, D. R. *The Journal of Physical Chemistry B* **2006**, 110, (35), 17315-17328.10.1021/jp062746a
44. Lesnikovich, A. I.; Levchik, S. V. *Journal of Thermal Analysis* **1983**, 27, (1), 89-93
45. Ghosh, M. K.; Mittal, K. L., *Polyimides : fundamentals and applications* New York etc. : Marcel Dekker: 1996.
46. Burnham, A. K.; Braun, R. L. *Energy & Fuels* **1999**, 13, (1), 1-22.10.1021/ef9800765

Chapter 5
**Sorption behavior of compressed CO₂
and CH₄ in ultrathin hybrid
poly(POSS-imide) layers**

This chapter has been submitted for publication: Raaijmakers, M.J.T., Ogieglo, W., Wiese, M., Wessling M., Nijmeijer, A., Benes, N.E. Sorption behavior of compressed CO₂ and CH₄ in ultrathin hybrid poly(POSS-imide) layers



Abstract

Membrane gas separation of CO₂ from other gases is a key enabling technique for carbon capture and storage as well as natural gas sweetening. Large-scale implementation of synthetic membranes for CO₂ separation requires membranes with high CO₂ permeability. Glassy polymeric membranes are suitable for CO₂ separation applications, but in particular ultrathin polymeric films with high CO₂ permeabilities suffer from penetrant induced changes such as plasticization and physical ageing. Here, we investigated the effects of high pressure CO₂ and CH₄ on the dilation and sorption behavior of ultrathin membrane layers of a hybrid inorganic-organic network material that consists of alternating polyhedral oligomeric silsesquioxane and imide groups. The imide precursor, containing fluoroalkane groups, provides affinity towards CO₂ sorption, while the octa-functionalized silsesquioxane provides a high degree of cross-linking. The combination of these properties allows for extremely high sorption capacities, while maintaining the glassy characteristics of a network material. We succeeded to quantify the uptake of CO₂ in the selective layer of a composite membrane only by determining the effective layer thickness and refractive index changes obtained by spectroscopic ellipsometry measurements at high CO₂ and CH₄ pressures. Spectroscopic ellipsometry can be used to accurately determine the sorption characteristics, whereas gravimetric or volumetric do not allow for accurate sorption measurements on swelling, ultrathin films. The sorption behavior of the ultrathin hybrid layers depends on the fluoroalkane group content. At low pressure, the apparent molar volume of the gases is low as compared to the liquid molar volume of CO₂ and CH₄, respectively. At high gas concentrations

in the polymer film, the apparent molar volume of CO₂ and CH₄ exceeds that of the liquid molar volume, and approaches that of the fluid phase. The high sorption capacity and network characteristics of the presented materials provide a new direction for membrane development for CO₂ separation applications.

5.1. Introduction

Membrane gas separation is a key technology for CO₂ separation and capture applications.¹ Potential CO₂ membrane separation applications range from post-combustion flue gas treatment, pre-combustion capture systems, oxy-fuel processes, natural gas sweetening and biogas refineries.²⁻⁶ Conventional techniques such as solvent scrubbing and physical adsorption processes are technologically well developed, but incur a large energy penalty on the CO₂ capture. Membrane gas separation potentially lowers the energy requirements for CO₂ removal, but large-scale implementation is hampered by the insufficient membrane permeability⁷ and the limited stability at high CO₂ partial pressures.⁸⁻¹⁰

Polyimides currently represent the state-of-the-art for industrial membrane applications, owing to their rigid backbone that provides selectivity and stability at high pressures.^{11, 12} Their stability at high pressure CO₂ conditions is generally further improved by cross-linking and thermal annealing of polymers in the vicinity of the glass transition temperature.^{10, 13-15} However, the improved stability is usually at the cost of permeability due to loss of free volume required for transport. Membrane developers therefore aim to further improve gas permeabilities, while maintaining the rigid characteristics of the glassy polymers.¹ In recent years, the development of highly permeable polymers has brought about new classes of polymers, including polymers of intrinsic microporosity (PIMs),¹⁶⁻¹⁹ thermally rearranged (TR) polymers,²⁰⁻²³ hybrid inorganic-organic network polymers,²⁴⁻²⁷ polyethers²⁸ and substituted polyacetylenes.²⁹ Their high excess free volume (EFV) content and high affinity towards gases allows for high solubility and rapid diffusion of gases through the membrane layers. Especially polymeric membranes with high EFV suffer from penetrant induced changes such as plasticization and physical ageing, as a result of increased macromolecular dynamics.³⁰ Moreover, the changes of membrane performance in time are particularly pronounced for ultrathin films that suffer from nano-confinement effects and accelerated aging.³⁰⁻³⁹ The increased macromolecular dynamics in highly permeable polymers are caused by the high solubility of a penetrant in the polymer

matrix. Strategies to decelerate the macromolecular chain mobility include the use of hyper-cross-linked^{25, 40} or interpenetrating networks⁴¹ and the physical dispersion of nanoparticles in the polymer.⁴² The hybridization allows for material synthesis that provides a synergistic combination of the highly permeable polymer and rigid inorganic constituents.⁴³ Particularly hybrid networks that consist of alternating organic and inorganic groups allow for material design with properties that are distinct from those of the individual components. Here, we investigate the CO₂ sorption and swelling behavior of an ultrathin hybrid network polymer using spectroscopic ellipsometry (SE). SE can be used to accurately determine the sorption, sorbed gas molar volume and penetrant-induced changes in the network polymer. Other gravimetric techniques used to determine sorption do not allow for accurate sorption measurements on ultrathin films, because the buoyancy correction that is required for calculation of the sorption depends on the polymer volume, which is an unknown parameter when strong swelling of the polymer occurs.

The network is based on polyhedral oligomeric silsesquioxanes (POSS) that are covalently bound by aromatic imide bridges. The POSS molecules restrict the macromolecular dynamics at elevated CO₂ pressures, while the fluoroalkane-functionalized imide bridges provide affinity towards CO₂ sorption. The properties of the ultrathin poly(POSS-imide) films have been systematically investigated with respect to their sorption, dilation and macromolecular dynamics at high CO₂ pressures. We show that the degree of network connectivity is crucial for moderating dilation at very high CO₂ concentrations. The presented poly(POSS-imide)s display very high CO₂ sorption capacities, while the network rigidity restricts short- and long-term dynamics.

5.2. Experimental

5.2.1. Membrane synthesis

Network formation occurs via a facile interfacial polymerization reaction between an aqueous solution of POSS and a dianhydride solution in toluene. Here, the monomer concentration in the aqueous solution was varied to obtain films with different thicknesses and imide:POSS ratios. The pH of the POSS solution was fixed at 9.9, after optimization of the pH with respect to thickness and refractive index (Appendix, Figure A5-1). Poly(POSS-imide) membranes were prepared by interfacial polymerization of water-soluble ammonium chloride-functionalized POSS (octa-ammonium POSS[®], Hybrid Plastics) and a

0.075 wt.% 4,4-(hexafluoroisopropylidene) diphthalic anhydride (6FDA, Sigma-Aldrich) solution in toluene. The partial conversion of ammonium to primary amine groups was achieved by addition of NaOH until the solution reached a pH of 9.9. Supported thin films were produced on α -alumina discs (Pervatech, Netherlands) coated with 1.5 μm thick γ -alumina (porosity of $\sim 40\%$ and a pore size of 2-3 nm). First, the α -alumina discs, held fixed on a perforated plate by vacuum, were impregnated with the POSS solution. Next, the discs were left to dry in a nitrogen atmosphere for 30 min and subsequently submerged in the 6FDA in toluene solution. After 5 min reaction time the toluene was removed from the interface and the discs were washed with acetone to remove any residual reactants. After drying for at least 2 hours in air atmosphere the samples were heat-treated for 2 hours at 300 $^{\circ}\text{C}$ to achieve conversion of the amic acid groups to cyclic imide groups. The concentration of the POSS solution, a critical parameter in the interfacial polymerization reaction, were varied to obtain membranes with different thicknesses, refractive indices and chemical composition.

The Matrimid films were deposited on both silicon wafers and γ -alumina-coated discs to mimic the sample structure of the poly(POSS-imide)s.⁴⁴ Matrimid membranes atop silicon wafers were prepared by spin coating (WS-400B-6NPP/LITE, Laurell Technologies Corporation) of a 7 wt.% Matrimid (type 5218, Huntsman) solution in cyclopentanone, under N_2 atmosphere. Silicon wafers (100, front side polished, CZ test grade, Silchem) were used as a substrate for the spin-coated layer. The wafers were stored under clean-room conditions until being cut. The spin coating recipe consisted of a single step of 60 seconds at 3000 rpm. Matrimid membranes atop γ -alumina coated α -alumina discs were prepared by floating of a spin coated, air-dried Matrimid layer deposited on a silicon wafer.⁴⁴ Detachment of the Matrimid layer from the silicon wafer was accomplished by placing the sample in milli-Q water for 30 min. A γ -alumina coated α -alumina discs was carefully moved below the floating layer and moved upwards until full coverage of the disc was accomplished. Removal of water was accomplished by placing the samples in vacuum at 30 $^{\circ}\text{C}$ for at least 24 hours. In the ellipsometry cell, slight vacuum was applied on the substrate side to assure the presence of a sharp interface between Matrimid and the γ -alumina layer that was required for a resolvable ellipsometry model. The samples were annealed at 300 $^{\circ}\text{C}$ to remove any residual solvent and to improve the plasticization resistance. For samples that were not annealed, residual solvent results in non-physical CO_2 sorption

behavior. The thickness and refractive index data of non-annealed Matrimid are given in Figure A5-4 (Appendix).

5.2.2. Spectroscopic ellipsometry

The thickness and refractive index of poly(POSS-imide)s atop γ -alumina coated α -alumina discs were determined using spectroscopic ellipsometry (M-2000X, J.A. Woollam Co., Inc.). The psi (Ψ) and delta (Δ) spectra were recorded over a wavelength range of 340–1000 nm, with a spectral resolution of about 2 nm, using light reflected at 65°, 70° and 75° angles of incidence. The optical model of the poly(POSS-imide) layer atop a γ -alumina coated α -alumina disc is visualized in **Figure 5-1**.

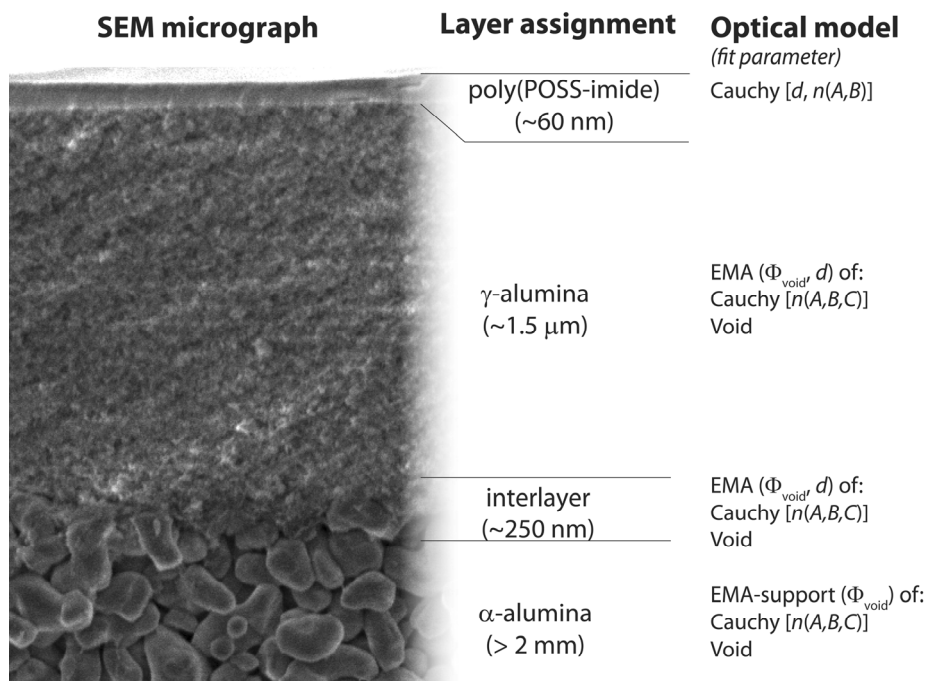


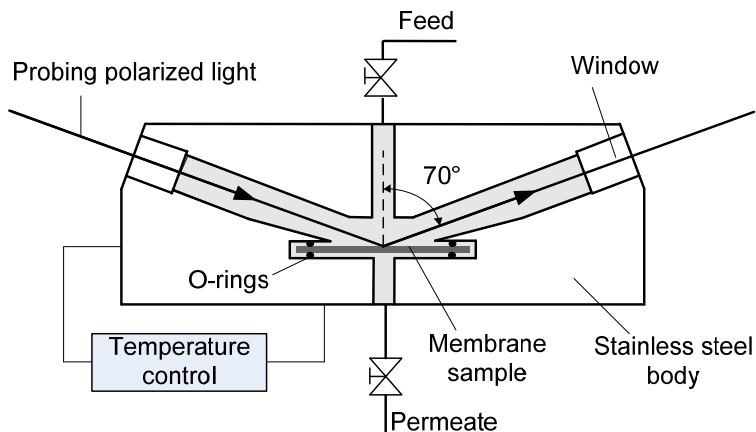
Figure 5-1. Optical model of a poly(POSS-imide) layer atop a γ -alumina coated α -alumina disc. The cross-section scanning electron micrograph of the membrane shows the distinct morphology of the dense poly(POSS-imide) layer, γ -alumina and α -alumina.

The layered optical model was constructed by a stepwise measurement of each individually added layer. The α -alumina disc was modelled using an Effective Medium Approximation (EMA) of three-parameter Cauchy-type optical dispersion of Al_2O_3 $n(\lambda) = A + B/\lambda^2 + C/\lambda^4$ with $A = 1.751$, $B = 0.00632 \mu\text{m}^2$, C

= $-0.00010152 \mu\text{m}$ ⁴⁵ and void ($n=1$) with a graded EMA layer atop corresponding to the roughness of the ceramic disc. Justification for the optical model and its validation versus Atomic Force Microscopy and Mercury Porosimetry is given elsewhere ⁴⁴. The samples were again measured after coating of the γ -alumina layer. The interlayer between the γ -alumina and the α -alumina was assumed to have a thickness similar to the thickness of the graded EMA layer that reflects the roughness of the α -alumina disc, but its porosity was left as a fitting parameter accounting for the possible intrusion of the γ -alumina layer. The γ -alumina thickness and porosity were modelled using an EMA of Al_2O_3 and void. Finally, poly(POSS-imide) formation atop the γ -alumina was achieved by a procedure described in the synthesis section. The poly(POSS-imide) layer thickness and refractive index were determined using a two-parameter Cauchy optical dispersion (fit parameters A and B), assuming transparency of the hybrid material in the used wavelength range. The porosity of the γ -alumina and the interlayer were set as fit parameters, to account for the water that remains in the γ -alumina after poly(POSS-imide) synthesis. The wavelength range for all optical models was limited to 500–1000 nm to reduce the influence of light scattering as a result of the non-uniformity of the porous α -alumina discs.⁴⁴

5.2.3. Spectroscopic ellipsometry – high pressure CO_2 sorption

Spectroscopic ellipsometry measurements at elevated gas pressures were conducted with an Alpha-SE[®] ellipsometer (J.A. Woollam Co. Inc.). All measurements were done at a fixed angle of incidence (70°) in the wavelength range from 370 to 900 nm. Samples were placed in a home-built stainless steel cell ($p_{\text{max}}=20 \text{ MPa}$, $T_{\text{max}}=473.15 \text{ K}$) equipped with a temperature and pressure control system, as depicted in **Scheme 5-1**.



Scheme 5-1. Schematic of the stainless steel cell used in the spectroscopic ellipsometry analysis of CO₂ adsorption and swelling dynamics of poly(POSS-imide)s and Matrimid membranes.

Accurate control and stability (within 0.1 bar) of the gas pressure was achieved using a syringe pump (Teledyne ISCO, 500D). The system temperature was maintained at 35 °C by a glycol bath connected to the cylinder of the syringe pump and by an induction heating belt connected to the measurement cell, in order to correct temperature changes due to CO₂ Joule-Thompson effects upon incremental pressure change. Light entered and exited the cell through 1 cm thick quartz windows positioned perpendicular to the polarized light beam source and detector. Pressure induced birefringence of the cell windows was measured via a high-pressure helium calibration on a 25 nm SiO₂/Si wafer, and used for correction of during further high pressure measurements.

5.2.4. Magnetic suspension balance

The poly(POSS-imide) CO₂ sorption isotherms were measured in µg resolution using a gravimetric sorption analyzer with magnetic suspension balance (Rubotherm). The temperature of the chambers was controlled at 35 °C by an external thermostat. In order to correct for drift, the magnetic suspension balance decouples the sample holder from the balance every 2 min, measures the zero point and automatically corrects the deviation. To compensate the buoyancy effect introduced by quick changes of the reigning pressure in the pressure vessel, the precise volume of the sample container (filled and empty) is required. The determination of the sample container mass and volume starts with a degassing step at elevated temperatures. Sequential purging with helium guarantees the removing of all moisture and stable mass

in the end. As soon as the mass is constant the temperature is regulated to the desired measurement temperature. The degassing step has been conducted for almost 2 days. Plotting the mass as a function of the gas density (helium) reveals the volume of the empty sample container which corresponds to the slope of the line. In addition the mass of the sample container is equal to the mass when no helium through flow is applied (interception at the y axis).

The density of helium and CO₂ are calculated and integrated using ASPEN Properties. In order to determine the volume and mass of the sample container filled with sample, the same procedure is adapted. Before starting with the sorption and desorption measurements vacuum is applied to the pressure vessel and if necessary the temperature level corrected. The sorption and desorption measurements presented here are conducted at a constant temperature of 35°C and range between 0 and 30 bar. The gas chosen for the sorption is CO₂. As mentioned above all measurements need to be corrected due to the buoyancy effect. Lorenz and Wessling derived the HSC algorithm which compensates this effect.⁴⁶

5.2.5. X-ray photoelectron spectroscopy

Elemental composition and functional group binding energies were measured using X-ray photoelectron spectroscopy (XPS). The measurements were performed on a Quanterra SXM scanning XPS microprobe (Physical Electronics), using a monochromatic Al K α source (1486.6 eV) with a beam size of 200 μm . On every sample 4 different areas were probed with an area size of 300 x 200 μm . XPS depth profiling was done by Argon ion sputtering at 2 kV, corresponding to a sputter speed of 5.4 nm min⁻¹ on SiO₂.

5.2.6. Scanning electron microscopy

Scanning electron microscopy (SEM) images were obtained using a LEO-1550 Schottky field emission scanning electron microscope (Carl-Zeiss, Germany), with an accelerating voltage of 1.40 kV. The cross-section micrographs were used to determine the poly(POSS-imide) layer thickness.

5.3. Results and discussion

The poly(POSS-imide) membranes consist of a network of alternating POSS and imide moieties. The imide:POSS ratio, corresponding to the degree of network cross-linking, determines the membrane properties to a great extent. The layer growth and imide:POSS ratio are functions of the reactant concentration, reactivity, diffusivity and solubility in either phase. **Figure 5-2**

(left panel) shows the reaction scheme of the formation of poly(POSS-imide) membranes by interfacial polymerization of octa-ammonium POSS and 6FDA. Each POSS cage is decorated with eight ammonium functional groups, that can potentially be converted to amine groups using a base such as sodium hydroxide. Formation of a poly[POSS-(amic acid)] layer is accomplished by contacting an aqueous solution of the partially deprotonated octa-ammonium POSS with a 6FDA solution in toluene. Finally, the amic acid groups are converted to cyclic imides by a heat treatment at 300 °C.⁴⁷ **Figure 5-2 (right panel)** shows the micrographs of the poly(POSS-imide) membranes atop ceramic discs, prepared with 5.0, 2.5 and 0.9 wt.% POSS solutions.

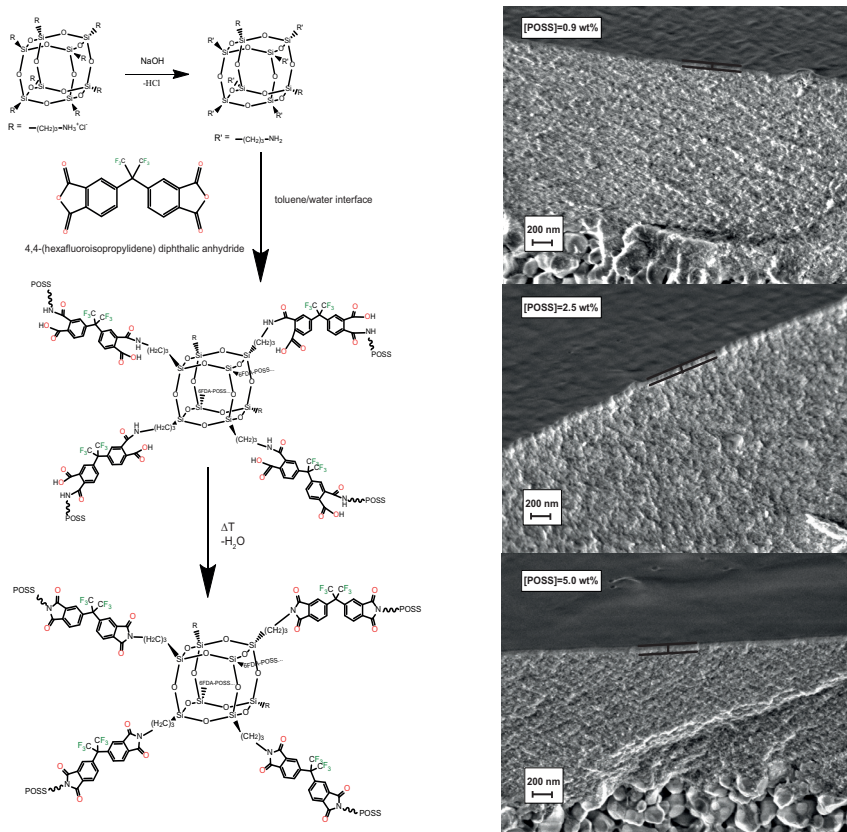


Figure 5-2. (left panel) Reaction scheme of the formation of poly(POSS-imide) membranes by interfacial polymerization of octa-ammonium POSS in water and 6FDA in toluene. (right panel) Scanning electron micrographs of poly(POSS-imide)s prepared with 5.0, 2.5 and 0.9 wt.% POSS solutions.

The thickness of the poly(POSS-imide) layer increases with increasing concentration of the POSS solution used for synthesis. The poly(POSS-imide) layers display relatively smooth surfaces compared to conventional interfacial polymerization membranes.⁴⁸ The regular surface is likely a result of the limited solubility of the charged POSS molecules in the organic phase, and limited diffusivity of the large reactants upon formation of the dense membrane layer.⁴⁹ The irregularities found for films prepared with lower POSS concentrations likely originate from the roughness of the γ -alumina layer. For thicker poly(POSS-imide) layers, the fingerprint of the γ -alumina substrate fades.

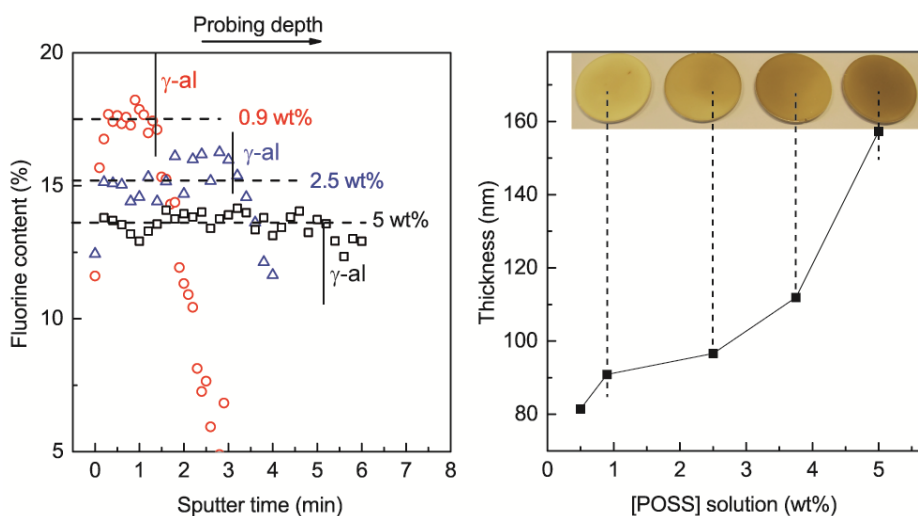


Figure 5-3. (left panel) The poly(POSS-imide) fluorine atom%, determined by XPS as a function of etching time by argon ion sputtering. The sputter time is approximately proportional to the probing depth of the films. The sputtering depth at which the γ -alumina layer emerges in the XPS depth profile data is indicated with a horizontal line. (right panel) Poly(POSS-imide) refractive index (red, open circles) and layer thickness (black, closed squares) as function of POSS concentration of the aqueous POSS solution used for interfacial polymerization. The photograph displays the top view of the ceramic discs with the corresponding poly(POSS-imide) layers. All lines are drawn as a guide for the eye.

The poly(POSS-imide)s prepared with different concentrations were further analyzed with respect to chemical composition and optical properties. **Figure 5-3 (left panel)** displays the ratio of fluorine content determined by X-ray photoelectron spectroscopy as function of argon sputter time. The

sputter time relates to the probing depth. The fluorine content data show that the number of imide groups is higher for the membranes prepared with lower POSS concentrations. The average number of imide groups per POSS cage, calculated from the fluorine content, equals about 3.7, 4.3 and 4.9 imide groups per POSS cage for the 5, 2.5 and 0.9 wt.% layers, respectively. The imide:POSS group ratios are in accordance with the reactant stoichiometry during interfacial polymerization. Membranes prepared with higher POSS concentrations result in higher POSS content. Membranes prepared with lower POSS concentrations have a higher fluorine content.

The fluorine content of the poly(POSS-imide) membranes is relatively constant over the probing depth, indicating that the number of imide groups per POSS cage is similar throughout the membrane. This implies that the cross-linking density is independent of the side at which the reactants are offered during interfacial polymerization reaction, different from the gradients found in conventional interfacial polymerization membranes.⁵⁰ However, because different elements display a different propensity towards removal by argon ion etching it is not possible to determine the imide:POSS ratio as function of etching depth with certainty. The differences in the rate of element removal by sputtering are reflected by the gradients in Si/F and C/F ratios as function of sputtering depth (Figure A5-2, Appendix). The observation with respect to the absence of gradients in the fluorine content should therefore be treated with caution.

The lower fluorine content in layers prepared with increasing wt.% POSS solutions corresponds well with the thickness and refractive index data obtained from spectroscopic ellipsometry experiments. **Figure 5-3 (right panel)** displays the thicknesses and refractive indices of the poly(POSS-imide) films as a function of the POSS solution concentration used for synthesis. Both the thickness and the refractive index increase with increasing POSS solution concentration. The refractive index is a measure for the optical density of the material, and depends on the imide:POSS group ratio and the group packing density. The lower refractive index for layers prepared with lower concentrations is related to the higher imide group content and number of fluorine groups. High fluorine concentrations are known to result in a lower refractive index due to their large contribution to free volume elements.⁵¹ Because the fluorine content strongly influences the refractive index, a straightforward correlation of the refractive index and group packing density is not possible. However, the lower number of imide groups per POSS cage is

indicative of a higher packing density. A similar effect has been reported for alkyl-POSS thin films, where the shorter alkyl groups led to higher refractive indices of the films due to higher packing densities.⁵² In summary, a high POSS concentration used for interfacial polymerization results in a more dense network, while a low POSS concentration results in a more open network.

The increase in thickness with increasing POSS concentration corresponds with the thickness trend found by SEM analysis of the same membranes. In addition, visual observation of the poly(POSS-imide) membranes reveals that membranes prepared with higher POSS concentrations have a darker color, indicative for a thicker layer. The lower thicknesses observed for films prepared with low POSS concentration solutions could indicate that the reaction is strongly limited due to depletion of reactants and reactant diffusion limitations upon layer formation. The absolute value of the thickness determined by ellipsometry are higher than those observed by SEM, which can be due to partial intrusion of the poly(POSS-imide) in the γ -alumina support layer. The layer intrusion, not easily discernable in SEM analysis, is confirmed by the gradual increase of aluminum and oxygen element concentrations with increasing etching depth, measured using XPS analysis (Figure A5-2 and A5-3, Appendix). Also, the complexity of the optical model might result in an overestimation of layer thickness. Nonetheless, the agreement between spectroscopic ellipsometry, XPS and SEM data supports the optical model used for modelling to poly(POSS-imide)s atop γ -alumina coated α -alumina discs.

In conclusion, the poly(POSS-imide) layer formation can be controlled using the POSS concentration in the aqueous solution used for interfacial polymerization. The membrane thickness, the POSS and fluorine fractions and network density can be tailored to optimize membrane performance with respect to stability under high pressure conditions.

5.3.1. CO₂ and CH₄ sorption isotherms – high pressure ellipsometry

The CO₂ sorption isotherms of Matrimid and poly(POSS-imide)s prepared at POSS concentrations of 0.9, 2.5 and 5 wt.% were measured using high pressure SE. The change in polarization state of light upon reflection from the layers allows for precise measurement of changes in film thickness and refractive index as a function of pressure. From these changes, the concentration of the sorbed gas can be estimated using the Clausius – Mossotti approach.^{39, 53-55}

CO₂ sorption in Matrimid 5218

The CO₂ sorption behavior of ultrathin Matrimid layers was measured for comparison with the poly(POSS-imide) samples. Matrimid was chosen because it is a high EFV, relatively plasticization-resistant glassy polymer widely used for gas separation.^{14, 56-58} This polyimide can serve as a benchmark for other potential gas separation materials, since it is characterized by a relatively large CO₂ sorption capacity and a good CO₂/CH₄ membrane selectivity. It is also known to respond well to annealing below and in the vicinity of its glass transition to improve plasticization resistance.^{14, 59} The Matrimid films were deposited on both silicon wafers and γ -alumina-coated discs to mimic the sample structure of the poly(POSS-imide)s.⁴⁴ The samples were annealed at 300 °C to remove any residual solvent and to improve the plasticization resistance. For samples that were not annealed, residual solvent resulted in non-physical CO₂ sorption behavior. **Figure 5-4** shows the thickness (left panel), refractive index (middle panel) and CO₂ concentration (right panel) of annealed Matrimid on a silicon wafer (top panels) and a γ -alumina coated disc (bottom panels) as function of pressure upon sorption and desorption.

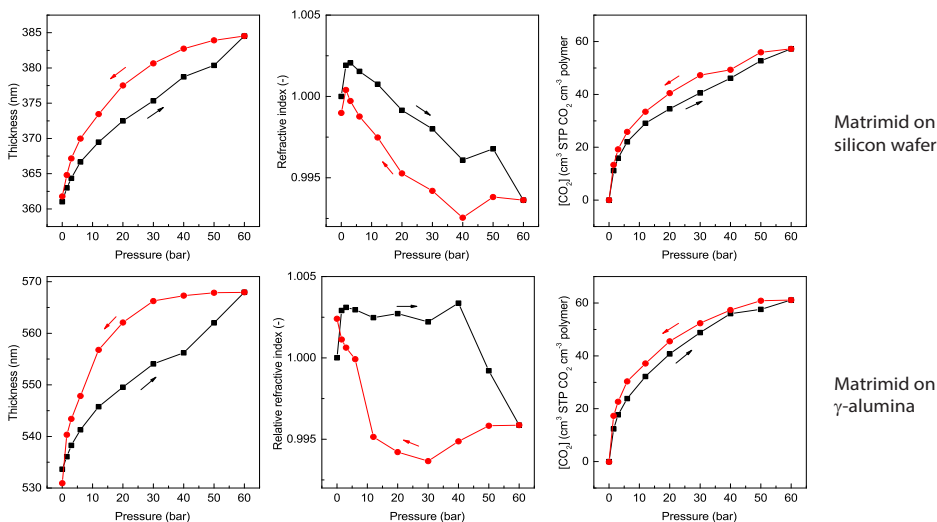


Figure 5-4. (left panel) Thickness, (middle panel) relative refractive index and (right panel) CO₂ concentration upon sorption (■) and desorption (●) of a 300 °C annealed Matrimid film on a silicon wafer (top panels) and a γ -alumina coated disc (bottom panels) as function of pressure.

The more complex optical model for Matrimid on the γ -alumina-coated disc is validated by measurements of Matrimid on silicon wafers. The similarity between the thickness and refractive index data as function of pressure confirms the validity of the ellipsometry model for the Matrimid layer on top of the γ -alumina coated disc. Both thickness graphs display a concave shape of the isotherm, which is typical for gas sorption in glassy polymers, having a free volume distribution with frozen-in free volume.^{58, 60} Upon increasing CO₂ pressure from 0 to 1.5 bar, a simultaneous thickness increase and relative refractive index increase occurs. At higher CO₂ pressures, the relative refractive index predominantly decreases. For a relative refractive index larger than 1, the frozen-in free volume elements of the polymer ($n = 1.000$) are being filled by the adsorbing gas molecules. A relative refractive index below 1 indicates predominant dissolution of the adsorbing gas molecules in the polymer matrix, and results in a reduction of the refractive index of the mixture. This is because the refractive index of the liquid CO₂ (estimated at $n \approx 1.23$ ^{10, 54, 61, 62}) is much lower than the refractive index of the analyzed polymers. Matrimid displays predominantly free volume filling at low pressures, followed by dilation of the matrix at high CO₂ pressures.

Upon desorption, the thickness and refractive index revert, without recovering to the original values that were found during sorption. The large hysteresis effect can be rationalized by the structural rearrangements upon dilation and lack of necessary chain mobility required to return the polymer to its original state. In fact, such hysteresis effects are known to be strongly depend on the sample's swelling history.⁶³ The hysteresis effect in the refractive index are most pronounced for annealed Matrimid with respect to the non-annealed samples (Figure A5-4, Appendix). The suppressed mobility of the annealed Matrimid is likely related to the absence of residual solvent and chain reorganization upon heat treatment. The pronounced hysteresis in thickness and refractive index underline the non-equilibrium glassy nature of Matrimid.

The CO₂ concentration in Matrimid as function of pressure, derived from the thickness and refractive index data, shows a typical glassy polymer sorption curve. Initially, a steep increase of CO₂ concentration is observed, related to CO₂ sorption in the easily accessible EFV of the polymer. At higher pressures, the sorption is dominated by CO₂ uptake that requires polymer dilation. The CO₂ sorption capacities of Matrimid agree very well with those reported in literature.^{39, 53}

CO₂ sorption in poly(POSS-imide)s

The poly(POSS-imide)s have properties that are distinct from organic polymers, due to their hyper-cross-linked network characteristics. As a consequence, the CO₂ sorption behavior of poly(POSS-imide)s is completely different than that of Matrimid. **Figure 5-5** shows the CO₂ sorption-induced swelling (left panel), the relative refractive indices (middle panel) and adsorbed CO₂ concentration (right panel) as function of pressure for poly(POSS-imide)s prepared with 0.9, 2.5 and 5 wt.% POSS solutions. As a reference, the corresponding data for Matrimid and 6FDA-DAM:DABA-based polyimide are also shown.

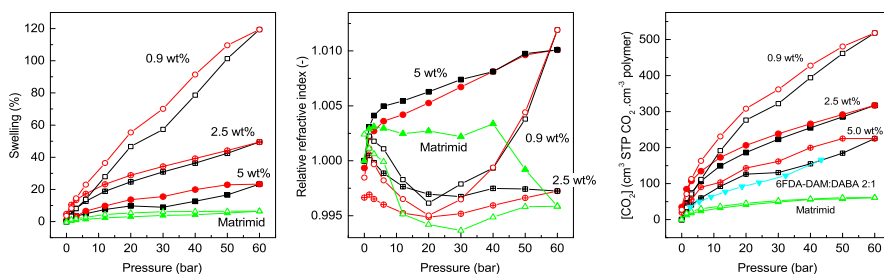


Figure 5-5. (left panel) Swelling degree, (middle panel) relative refractive index and (right panel) CO₂ concentration as function of pressure for the poly(POSS-imide) membranes on γ -alumina coated discs, prepared at different POSS concentrations. Matrimid swelling degree, relative refractive index and sorption data and 6FDA-DAM:DABA-based polyimide sorption data are shown as reference.¹⁰

All poly(POSS-imide)s show significant degrees of swelling (left panel) that are associated with the high CO₂ concentrations. The highest swelling is observed for the layers prepared with low POSS concentration solutions. The large degree of swelling, as much as 120 % at 60 bar for the 0.9 wt.% sample, demonstrates that the network has a flexible response to CO₂ exposure. This is in contrast with the membranes prepared with high POSS concentrations that show a much less pronounced swelling.

The CO₂ concentration data (right panel) shows that all three poly(POSS-imide)s are characterized by CO₂ sorption capacities that are much larger than that of Matrimid. The most pronounced CO₂ sorption and swelling is observed for the poly(POSS-imide)s with the highest fluorine content. The high CO₂ uptake, also observed for 6FDA based polymers, is attributed to the presence

of CF₃ groups in the structure.^{10, 64, 65} The data from Wind et al. for an ester modified 6FDA-DAM:DABA-based polyimide has a similar order of magnitude CO₂ concentration. The magnitude of CO₂ uptake increases with a decreasing concentration of the POSS solution used for the synthesis. The higher CO₂ solubility can be rationalized by the higher concentration of fluorine for the layers prepared with lower POSS concentrations, as determined by SE in combination with XPS.

Despite the high swelling degrees, the swelling of all poly(POSS-imide)s under vacuum upon desorption returns very closely to the initial values before sorption. This indicates a good high pressure stability of the materials and is related to their highly cross-linked, giant macromolecular network character. The sorption-induced hysteresis of swelling, especially for 2.5 and 5 wt.% samples is comparable to that for Matrimid. In the case of the 0.9 wt.% sample the hysteresis is larger. This might be due to the possibility of some macromolecular rearrangements as a result of the largest swelling and the lowest cross-linking density of this material.

The lack of significant sorption-desorption hysteresis for the poly(POSS-imide)s, in comparison to Matrimid, is particularly evident from the refractive index isotherms. While the excess free volume structure of the Matrimid changes significantly in the course of the experiment, the poly(POSS-imide) based membranes seem remarkably stable. This again is in agreement with the highly cross-linked nature of the system, as opposed to the non-cross-linked structure of Matrimid, which allows for long range macromolecular rearrangements. The free volume characteristics of the poly(POSS-imide)s are therefore also different from conventional polymeric membranes. The free volume is not present as frozen-in free volume between the polymer chains, but as open spaces between the network elements.

The relative refractive index is calculated from the values of the refractive index of the CO₂-exposed films divided by the refractive index of the films at vacuum. This type of sorption corresponds to the regular solution behavior. In the case of Matrimid, the refractive index during the sorption initially increases, corresponding to the filling of the EFV of the polymer. At higher pressures, the regular solution mechanism dominates and the index of the film decreases. Upon desorption, a pronounced, plasticization-related hysteresis is apparent as discussed earlier. In contrast, in the case of the 5 wt.% poly(POSS-imide) sample, the index increases during the sorption cycle up to the

maximum reached pressure of 60 bar. This indicates, that even though this material swells about 4 times more than Matrimid, the regular sorption behavior still dominates the gas uptake. Such rather unusual behavior indicates the very high amount of penetrant-accessible open spaces in the network. This seems consistent with the observed significant increases of the free volume fractions for systems, where POSS is dispersed within the polymer network, as is determined from dielectric constant measurements.⁶⁶ Nonetheless, such dispersions can also result in a decrease in sorption capacity, as is supported both by results of density and gas sorption measurements.⁶⁷ The covalent bonds between the alternating POSS and imide groups in this work prevent loss of the open spaces in the network.

At lower POSS group concentrations, the network flexibility increases. The relative refractive index changes of the 2.5 wt.% sample, after showing an initial increase, decrease as function of pressure. The decrease in relative refractive index is indicative for strong dilation of the network, while a large part of the open spaces in the network have already been filled. Nonetheless, the dilation does have limitations: the refractive index of the 0.9 wt.% sample shows a strong increase above 20 bar. Such a behavior of the refractive index may be explained by a swelling-limiting effect of cross-links; the large affinity of the fluorine groups results in an increased sorption at higher pressures, but the matrix simply does not dilate further because the higher energy required for deformation.

CO₂ sorption isotherms – magnetic suspension balance

The CO₂ sorption isotherms of Matrimid and free-standing poly(POSS-imide) film prepared using a POSS concentrations of 0.9 wt.% were measured using a magnetic suspension balance (MSB). Figure A5-5 in the Appendix displays the CO₂ sorption of (left panel) Matrimid and (right panel) poly(POSS-imide) powders as a function of CO₂ pressure. For Matrimid, results are comparable to literature values are observed. For the poly(POSS-imide) samples, values that are much lower than those measured with SE are observed. A lower CO₂ uptake in the poly(POSS-imide)s can be related to differences between powder reaction times (several hours reaction time are required to obtain sufficient powder volume for MSB measurements) and the change in reactant stoichiometries in the bulk can change the sample properties. More importantly, due to the swelling of the hybrid polymer, the calculations of the buoyancy effect are inherently incorrect (i.e., volume and mass calculations are dependent). The buoyancy correction requires precise knowledge of the

sample volume. Since the volume is an unknown parameter for swelling samples such as the poly(POSS-imide)s, the gas sorption cannot be quantified from measurements based on volume displacement or mass changes.

CH₄ sorption in poly(POSS-imide)s

Figure 5-6 (left panel) shows the swelling degree of the poly(POSS-imide) layers as function of CH₄ pressure. The swelling degree increases with an increasing methane pressure, with swelling degrees up to about 60 %. The highest swelling is observed for the layers prepared with low POSS concentration solutions. The swelling degrees are significant compared to conventional polymers, but are less high as compared to swelling by CO₂ at similar pressures.

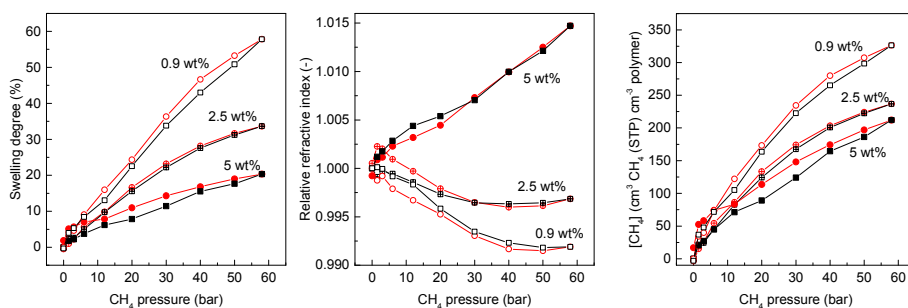


Figure 5-6. (left panel) Swelling degree, (middle panel) relative refractive index and (right panel) CH₄ concentration upon sorption (■) and desorption (●) of poly(POSS-imide)s prepared with 0.9, 2.5 and 5.0 wt.% POSS solutions and a 300 °C annealed Matrimid film, on γ -alumina coated discs, as function of pressure.

The CH₄ concentration data, shown in **Figure 5-6 (right panel)**, shows that all three poly(POSS-imide)s are characterized by CO₂ sorption capacities that are much larger than that of conventional polyimides. The CH₄ concentrations are about half of the CO₂ concentrations, similar to other 6FDA-based polyimides. The high CH₄ concentration originates from the large amount of open space in the poly(POSS-imide) network and the flexible response of the network upon CH₄ exposure that results in swelling of the network. The most pronounced CH₄ sorption and swelling is observed for the poly(POSS-imide)s with the highest fluorine content. The relative refractive index data for CH₄ sorption is similar to that of the CO₂ sorption data. For the samples with a low fluorine content, the relative refractive index increases over the complete pressure range. The increasing refractive index is indicative for a high degree of

network rigidity. For the poly(POSS-imide)s with a higher fluor content, the relative refractive index slightly decreases, indicating that the network rigidity is lower.

5.3.2. CO₂ and CH₄ partial molar volume and penetrant induced dynamics

The apparent molar volumes, V_m , of the dissolved gases can be determined from the slope of the swelling versus the CO₂ or CH₄ concentrations.⁵³ **Figure 5-7** (top panels) shows the swelling degree as a function of the CO₂ (left panels) and CH₄ (right panels) concentrations in the poly(POSS-imide)s. **Figure 5-7 (bottom panels)** shows the apparent V_m derived from the slope of the swelling as function of the gas concentration data, as a function of the CO₂ (left panels) and CH₄ (right panels) concentrations in the poly(POSS-imide)s. At low CO₂ concentrations, the poly(POSS-imide)s follow the same trend as Matrimid. Consequently, the apparent V_m at lower CO₂ concentrations for the poly(POSS-imide)s and Matrimid are similar. The V_m of CO₂ at low concentrations is about 27 cm³ mol⁻¹, which is less than the approximate V_m value for liquid CO₂. This value is typical for glassy polymers⁶⁸, where gas molecules fill the space between the polymer chains (sorption into access free volume) as well as dilating the polymer matrix (regular solution sorption). In the absence of the former mechanism (e.g. sorption in rubbery polymers or liquids) the CO₂ V_m would be close to its liquid value, as is found for PDMS.⁶⁹

As the CO₂ concentration increases, the slope of the curves inclines towards values that are close to the approximate V_m value for CO₂ in liquids of about 46 cm³ mol⁻¹. At very high CO₂ concentrations, the apparent V_m increases to above that of liquid CO₂. The same observations are made for apparent V_m values of CO₂ in PDMS and PES, albeit at different CO₂ concentrations. In PES, similarly high molar volumes of CO₂ are attributed to long range polymer matrix reorganizations, also referred to as plasticization.⁷⁰ Because only a small amount of EFV is present in PES, the apparent V_m reaches high values at relatively low CO₂ concentrations. For the poly(POSS-imide) layers a much higher degree of open space is present, which is reflected by the low apparent V_m values at high CO₂ concentrations. In PDMS, the upswing in the CO₂ molar volume is attributed to a change in CO₂ activity at high concentrations, also observed for CO₂/butane mixtures near the critical point (which is at 31 °C for CO₂). However, the explanation of the near-supercritical behavior of CO₂ is not satisfactory to explain the apparent V_m changes in the ultrathin poly(POSS-imide)s.

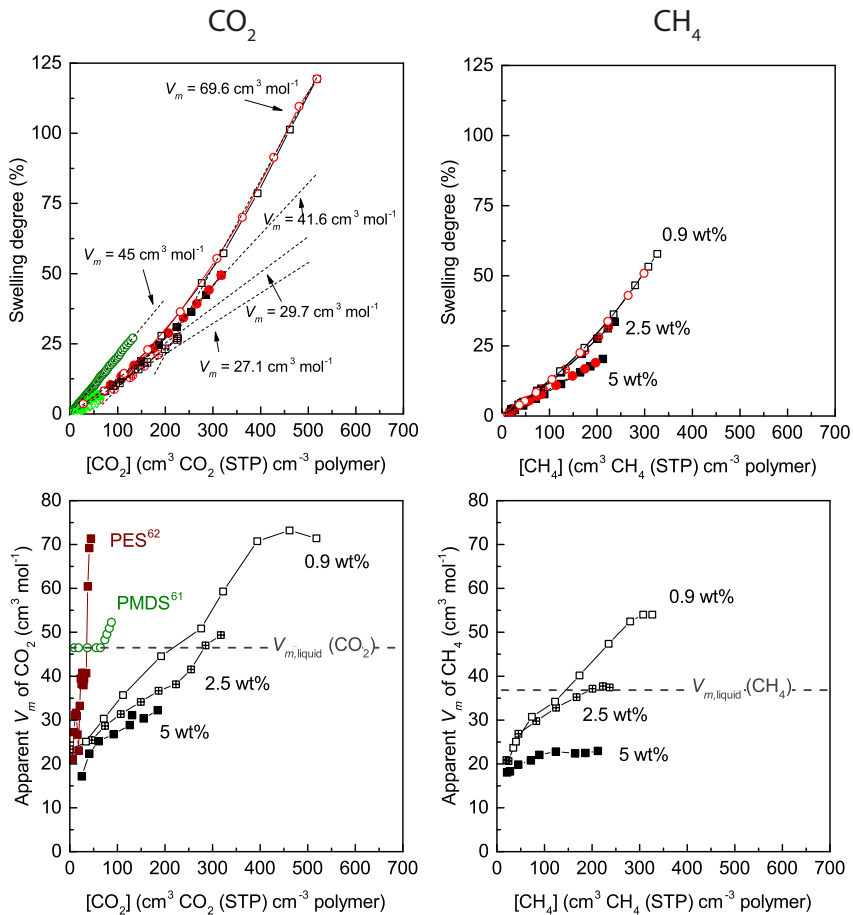


Figure 5-7. (top panels) Swelling as a function of the (left panel) CO₂ and (right panel) CH₄ concentrations in the poly(POSS-imide) layers prepared at (open symbols) 0.9, (crossed symbols) 2.5 and (closed symbols) 5.0 wt.%, upon sorption (black squares) and desorption (red circles). Matrimid (light green triangles) and polydimethylsiloxane (PDMS, green circles, data from⁶⁹) are added as a reference. (bottom panels) the V_m of (left panel) CO₂ and (right panel) CH₄ as function of gas concentration in the poly(POSS-imide) layers prepared at different POSS concentrations. The V_m of CO₂ in PDMS (data from⁶⁹) and polyethersulfone (PES, data from⁷⁰) are added as a reference.

The apparent V_m of CH₄ displays a similar increase with increasing gas concentration. The apparent V_m of CH₄ similar as compared to CO₂ at similar gas concentrations, except for the 5.0 wt.% that shows a lower V_m value of CH₄ as compared to CO₂. The lower V_m values might be related to the lower

V_m of liquid CH₄ (37 cm³ mol⁻¹) as compared to CO₂ (46 cm³ mol⁻¹). At high CH₄ concentrations, the apparent V_m increases to above that of liquid CH₄, similar as the observations in CO₂. The high V_m values are not related to supercritical behavior, because CH₄ at 35 °C is not near its supercritical point. We suggest the changes in the CO₂ and CH₄ apparent V_m are coupled to the high gas concentrations. When most of the initially available free volume has been filled, each CO₂ or CH₄ molecule added to the polymer matrix has to result in dilation. As the gas concentration increases, the interactions between CO₂ or CH₄ molecules and the polymer will become less relevant and the V_m will approach that of the fluid phase. An infinitely diluted polymer matrix would approach the V_m of CO₂ or CH₄ at a given pressure. For example, at 60 bar and 35 °C the V_m of CO₂ is about 280 cm³ mol⁻¹ (calculated using ASPEN Properties 7.3, using a Soave-Redlich-Kwong property set for CO₂ to predict the thermodynamic behavior of these gases within a range of 0 to 60 bars at 35 °C), which is still much higher as the apparent V_m of CO₂ in the poly(POSS-imide), PES or PDMS samples at 60 bar.

Unlike for the PES sorption, the increasing apparent V_m of CO₂ in the poly(POSS-imide)s is not related to time-dependent plasticization effects, since the sorption-desorption hysteresis is limited. This effect is particularly pronounced for the poly(POSS-imide) layer prepared with 5.0 wt.% POSS solution. The layer shows only a small increase in the apparent V_m , indicating that the network rigidity prevails over plasticizing effects of the gas. In addition, the lower CH₄ concentrations and lesser extent of interactions between CH₄ and the polymers might limit the plasticizing effect of the penetrant on the polymer matrix. Long-term, CO₂-induced chain relaxations have been determined by the long-term thickness changes upon a sudden pressure increment. **Figure 5-8 (left panel)** displays the swelling degree as function of time for matrimid and poly(POSS-imide) thin films prepared at different POSS concentration on γ -alumina coated disc, after an incremental pressure increase from 0 to 50 bar CO₂ pressure. Upon exposure to 50 bar CO₂, the layers almost instantaneously attain the high swelling degree. The swelling degrees are highest for 0.9 wt.% based poly(POSS-imide)s, followed by the others in the order 0.9 wt.% > 2.5 wt.% > 5.0 wt.% > Matrimid. The swelling degrees at 50 bar are in accordance with the stepwise sorption experiments displayed in Figure 5-4. Any slight discrepancies are probably caused by the difference in the CO₂ exposure route. During the subsequent dwell, the thickness of the layers increases due to slow rearrangements of the

network that are referred to as secondary relaxations. **Figure 5-8 (right panel)** displays the magnitude of secondary relaxations, given by the slope of the swelling change as function of the initial swelling value at 50 bar. The swelling change is obtained from a linear fit of the swelling degree data as function of time.

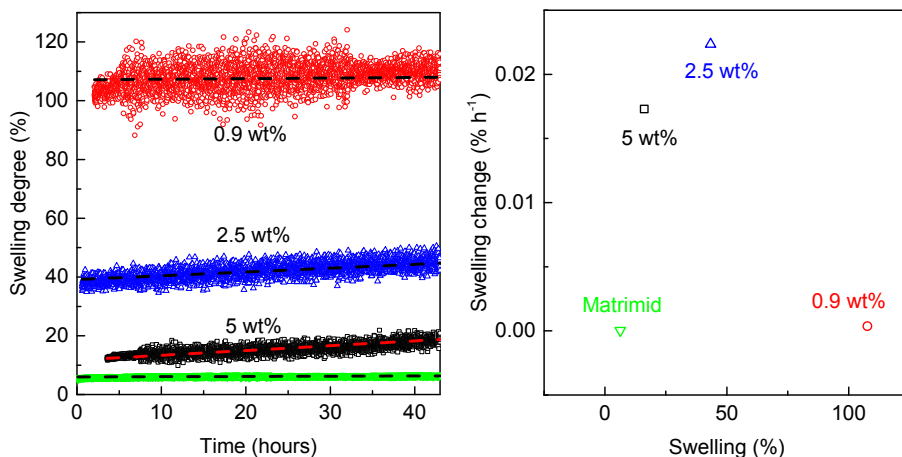


Figure 5-8. (left panel) Swelling degree as function of time for Matrimid and poly(POSS-imide) thin films on γ -alumina coated disc prepared using 0.9, 2.5 and 5.0 wt.% POSS solutions, after an incremental pressure increase from 0 to 50 bar CO_2 pressure. (right panel) Thickness increment of the slope of the swelling degree as function of time, as function of the initial swelling value at 50 bar.

The swelling change is most pronounced for the 2.5 and 5 wt.% samples, indicating that these samples show the highest degree of secondary relaxations. For Matrimid and the 0.9 wt.% samples, secondary relaxations are much less pronounced. For Matrimid, the absence of large relaxations can be rationalized by the relatively low CO_2 concentration as compared to the poly(POSS-imide) samples. The macromolecular mobility increases with CO_2 concentration, and therefore shows a more pronounced change in the poly(POSS-imide) layers. For the 0.9 wt.% sample, the high CO_2 concentration likely accelerates the dynamics of the network to such an extent that the structure quickly attains a state close to equilibrium after exposure to 50 bar CO_2 . Thus any secondary relaxations are absent.

5.4. Conclusions

Here, we compare the effects of high pressure CO₂ and CH₄ on the dilation and sorption behavior of ultrathin hybrid layers and conventional polyimide layers. The gas uptake was determined from thickness and refractive index changes obtained by spectroscopic ellipsometry measurements at high CO₂ pressures. For the hybrid polymers we found sorption behavior that is distinct from the conventional polyimide. The dilation behavior hybrid polymers depends mainly on the fluorine group content. The CO₂ and CH₄ sorption in the hybrid poly(POSS-imides) are very high compared to conventional polyimides, due to the large amount of open space in the network and the flexible response of the network upon exposure to a high pressure gas. Because the open space gradually fills, additional sorption can only occur due to additional swelling. This large swelling degree prevents characterization of the sorption of these materials by using gravimetric methods that require accurate knowledge on the sample volume. Because of the gradual filling of the open space and increasing gas concentration in the poly(POSS-imide) films at higher pressures, the sorbing gases occupy an increasingly large molar volume. At high gas concentrations in the polymer film, the apparent molar volume of CO₂ and CH₄ exceeds that of the liquid molar volume, and approaches that of the fluid phase. The here determined structure-property relationship between the gas sorption behavior and hybrid material composition allows for optimization of the layers for CO₂-related applications.

5.5. Acknowledgements

This project has received funding from the European Union's Seventh Framework Programme for research, technological development and demonstration under CARENA grant agreement no. 263007.

5.6. Appendices

5.6.1. Spectroscopic ellipsometry

The interfacial polymerization reaction parameters were analyzed using spectroscopic ellipsometry (SE) to determine the thickness and refractive index. **Figure A5-1** shows the poly(POSS-imide) thickness and refractive index as function of pH of the aqueous POSS solution used for interfacial polymerization.

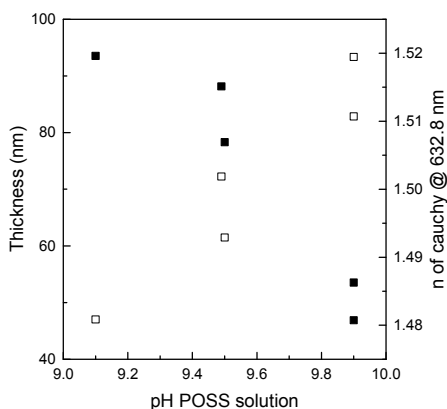


Figure A5-1. Thickness and refractive index as function of pH, for poly(POSS-imide)s prepared with 0.9 wt.% POSS solution.

With increasing pH, the number of deprotonated ammonia group on each POSS cage increases, allowing more groups on each POSS cage to participate in the interfacial polymerization reaction. At low pH values, the lack of reactive amine groups on the POSS cages results in a high fraction of POSS cages with respect to the imide bridged groups. This is reflected by the high refractive index at low pH values. Alternatively, high pH values allow for many imide bridges to form on each POSS cage, resulting in a lower fraction of POSS cages. Because layer thicknesses need to be sufficiently high to resolve spectroscopic ellipsometry measurements at elevated pressures, only membranes prepared with a high pH were used for further analysis.

5.6.2. X-ray photoelectron spectroscopy

X-ray photoelectron spectroscopy (XPS) measurements were performed to determine the element concentration. XPS measurements were performed on a Quanterra SXM scanning XPS microprobe (Physical Electronics), using a monochromatic Al K α source (1486.6 eV) with a beam size of 200 μm . XPS depth profiling was done by Argon ion sputtering at 2kV, corresponding to a sputter speed of 5.4 nm min^{-1} on SiO $_2$. The element concentrations without Argon sputtering are given in **Table A5-1**.

Table A5-1. Element concentrations and element ratios of poly(POSS-imide) layers and powder prepared with different concentration POSS solutions. The element concentrations of 6FDA and octa-ammonium POSS are given as a reference.

	Poly(POSS-imide) (0.9 wt.%)	Poly(POSS-imide) (2.5 wt.%)	Poly(POSS-imide) (5.0 wt.%)	Poly(POSS-imide) (0.9 wt.%) powder	6FDA	Octa-ammonium POSS
	Element concentration (%)	Element concentration (%)	Element concentration (%)	Element concentration (%)	Element concentration (%)	Element concentration (%)
C	44.2	44.4	48.2	44.0	65.5	47.8
N	4.4	4.4	4.5	3.9		9.8
O	28.8	28.1	16.4	24.6	13.8	22
Si	8.1	9.2	16.1	15.1		11.5
F	10.9	12.0	13.5	12.4	20.7	-
Cl						9
Na	2.1	0.9	0.8			
Al	1.5	1.0	0.6			0.8
C/N	10.1	10.2	10.8	11.2		
F/Si	1.3	1.3	0.8	0.8		
C/F	4.0	3.7	3.6	3.5	3.2	

Figure A5-2 displays the ratio of carbon/fluorine (left panel) and silicon/fluorine ratio (right panel) as function of etching time by argon ion sputtering for poly(POSS-imide) layers prepared using 0.9, 2.5 and 5.0 wt.% POSS solutions.

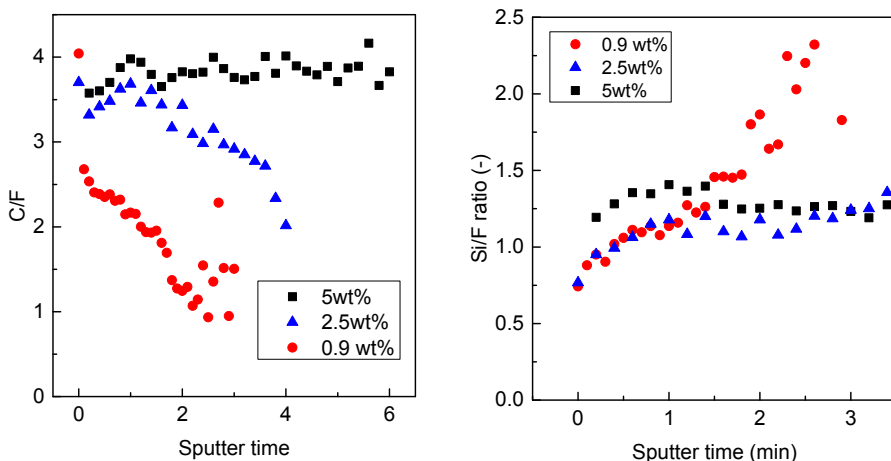


Figure A5-2. (left panel) ratio of carbon/fluorine and (right panel) silicon/fluorine ratio determined by XPS as function of etching time by argon ion sputtering for poly(POSS-imide) layers prepared using 0.9, 2.5 and 5.0 wt.% POSS solutions.

Figure A5-3 shows the element concentration as function of etching time by argon sputtering for poly(POSS-imide) layers prepared using 0.9 (left panel), 2.5 (middle panel) and 5.0 wt.% POSS solutions. The gradual concurrent increase of the O1s and Al2p signals as function of sputter time indicates that the poly(POSS-imide)s intrudes the γ -alumina layer.

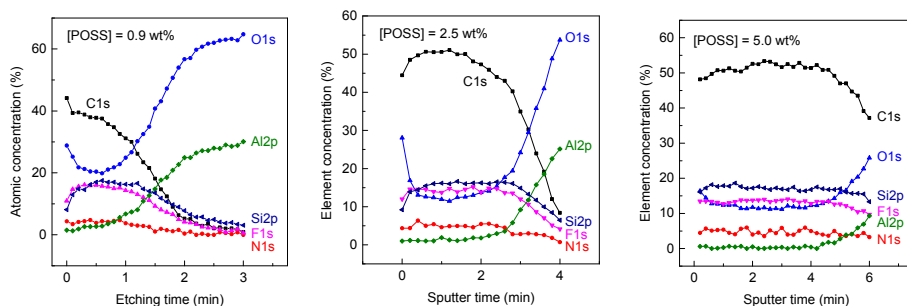


Figure A5-3. Element concentration determined by XPS as function of etching time by argon sputtering for poly(POSS-imide) layers prepared using 0.9 (left panel), 2.5 (middle panel) and 5.0 wt.% POSS solutions.

Figure A5-4 shows the thickness and refractive index as a function of gas pressure for a non-annealed Matrimid film deposited on a silicon wafer and a γ -alumina coated disc, respectively. The more complex optical model for

Matrimid on the γ -alumina-coated disc is validated by the similarity between the thicknesses and refractive indices as function of pressure. Both thickness graphs display a concave shape of the isotherm, which is typical for dual mode gas sorption in glassy polymers.^{58, 71}

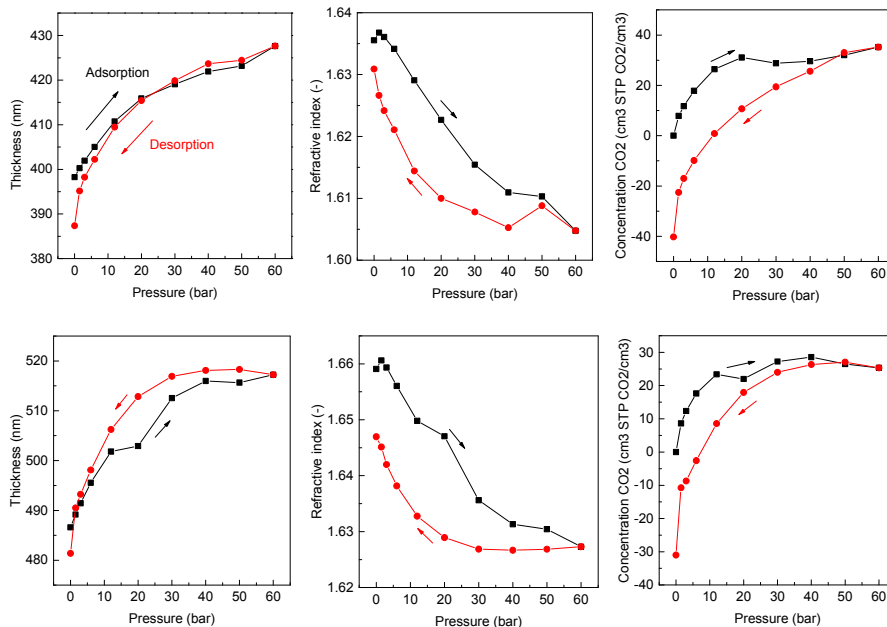


Figure A5-4. Thickness (left panel), refractive index (middle panel) and CO₂ concentration upon sorption (■) and desorption (●) of non-annealed Matrimid on a silicon wafer (top panels) and γ -alumina coated disc (lower panels) as function of pressure.

Upon CO₂ adsorption, a simultaneous thickness increase and refractive index decrease occurs, corresponding to dilation of the polymer matrix. Upon desorption, the thickness and refractive index revert, without recovering to the original values upon sorption. The large hysteresis effects can be rationalized by the structural rearrangements upon dilation and lack of necessary chain mobility required to return the polymer to its original state. Moreover, both thickness and refractive index are lower upon returning to vacuum. The difference in thickness and refractive index before and after sorption can only be explained by removal of residual solvent upon CO₂ adsorption. Even under vacuum, the solvent used for spin coating remains trapped in the polymer matrix. Expansion of the polymer matrix by CO₂ allows liberation of the kinetically trapped solvent.⁷² The solvent removal yields a polymer with larger

excess fractional free volume as compared to the structure at the beginning of the sorption cycle. The pronounced non-equilibrium characteristics indicate the high tendency of the non-annealed Matrimid towards CO₂-induced plasticization. The thickness mismatch at vacuum before and after the sorption measurements renders CO₂ concentration calculations meaningless.

5.6.3. CO₂ sorption measurements measured by a magnetic suspension balance

Sorption behavior was investigated in a magnetic suspension balance (MSB) with pressures up to 30 bars at 35°C. **Figure A5-5** displays the CO₂ sorption of (left panel) Matrimid and (right panel) poly(POSS-imide) powders as a function of CO₂ pressure. Both sorption isotherms display a steep initial incline in CO₂ sorption that gradually flattens at higher pressure, as is typical for dual mode sorption.

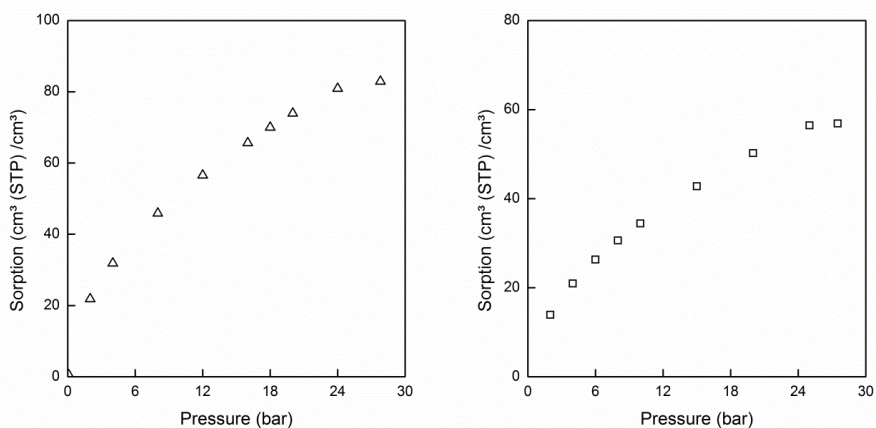


Figure A5-5. CO₂ sorption as function of pressure for Matrimid (left panel) and poly(POSS-imide) powder (right panel), measured using a magnetic suspension balance.

For Matrimid the observed behavior and CO₂ uptake of ~ 80 cm³ CO₂ (STP) cm⁻³ polymer at 28 bar is in good agreement with literature results for powders.⁵⁸ The CO₂ sorption in Matrimid is higher as compared to the ellipsometry results (about 40% higher as compared to spectroscopic ellipsometry results shown in Figure 4 (right panel), which has been observed by others^{38, 39} and can be attributed to the differences in layer thickness, measurement technique and polymer history. The results shown in The

poly(POSS-imide) powder has a lower CO₂ sorption as compared to the Matrimid sample and a much lower CO₂ uptake as compared to the ellipsometry measurements in Figure 5 (right panel). The lower CO₂ uptake in the poly(POSS-imide) can be related to several factors. Differences between powder reaction times (several hours reaction time are required to obtain sufficient powder volume for MSB measurements) and the change in reactant stoichiometries in the bulk can change the sample properties. The POSS powder used for CO₂ measurements in the magnetic suspension balance was prepared with 0.9 wt.% POSS solution. However, XPS data, shown in Table A5-1, indicates that the element composition resembled that of the poly(POSS-imide) layer prepared with a 5.0 wt.% POSS solution. Because the measurement depth of XPS is limited to several tens of nanometers, the powder composition can significantly differ from the layer composition. In addition, only a small amount of powder mass could be measured using the magnetic suspension balance. The sample mass was lower than the buoyancy effect of CO₂, for which the measured weight needs to be corrected. Small discrepancies in the sample volume and mass will therefore significantly affect the calculated CO₂ sorption. An underestimation of the buoyancy effect might lead to an underestimation of the sample volume, mass and CO₂ uptake. Because the sample volume might change due to CO₂ sorption, as observed by the large swelling degrees of the poly(POSS-imide)s, the buoyancy calculations are by definition incorrect. Because the magnetic suspension balance results are influenced by large number of experimental errors, the results should be interpreted with caution.

5.7. References

1. Du, N.; Park, H. B.; Dal-Cin, M. M.; Guiver, M. D. *Energy and Environmental Science* **2012**, 5, (6), 7306-7322
2. Czaperek, M.; Zapp, P.; Bouwmeester, H. J. M.; Modigell, M.; Ebert, K.; Voigt, I.; Meulenbergh, W. A.; Singheiser, L.; Stöver, D. *Journal of Membrane Science* **2010**, 359, (1-2), 149-159
3. Favre, E.; Bounaceur, R.; Roizard, D. *Journal of Membrane Science* **2009**, 328, (1-2), 11-14
4. Jones, C. W. *Annual Review of Chemical and Biomolecular Engineering* **2011**, 2, 31-52
5. Smart, S.; Lin, C. X. C.; Ding, L.; Thambimuthu, K.; Diniz Da Costa, J. C. *Energy and Environmental Science* **2010**, 3, (3), 268-278
6. Scholz, M.; Melin, T.; Wessling, M. *Renewable and Sustainable Energy Reviews* **2013**, 17, (0), 199-212
7. Blomen, E.; Hendriks, C.; Neele, F. In *Capture technologies: Improvements and promising developments*, Energy Procedia, 2009; 2009; pp 1505-1512.

8. Baker, R. W., *Membrane Technology and Applications*. 2012.
9. Duthie, X.; Kentish, S.; Powell, C.; Nagai, K.; Qiao, G.; Stevens, G. *Journal of Membrane Science* **2007**, 294, (1-2), 40-49
10. Wind, J. D.; Sirard, S. M.; Paul, D. R.; Green, P. F.; Johnston, K. P.; Koros, W. J. *Macromolecules* **2003**, 36, (17), 6433-6441
11. Sridhar, S.; Veerapur, R. S.; Patil, M. B.; Gudasi, K. B.; Aminabhavi, T. M. *Journal of Applied Polymer Science* **2007**, 106, (3), 1585-1594
12. Visser, T.; Masetto, N.; Wessling, M. *Journal of Membrane Science* **2007**, 306, (1-2), 16-28
13. Duthie, X.; Kentish, S.; Pas, S. J.; Hill, A. J.; Powell, C.; Nagai, K.; Stevens, G.; Qiao, G. *Journal of Polymer Science, Part B: Polymer Physics* **2008**, 46, (18), 1879-1890
14. Bos, A.; Pünt, I. G. M.; Wessling, M.; Strathmann, H. *Separation and Purification Technology* **1998**, 14, (1-3), 27-39
15. Hillock, A. M. W.; Koros, W. J. *Macromolecules* **2007**, 40, (3), 583-587
16. Budd, P. M.; Elabas, E. S.; Ghanem, B. S.; Makhseed, S.; McKeown, N. B.; Msayib, K. J.; Tattershall, C. E.; Wang, D. *Advanced Materials* **2004**, 16, (5), 456-459
17. Hashem, M.; Bezzu, C. G.; Kariuki, B. M.; McKeown, N. B. *Polymer Chemistry* **2011**, 2, (10), 2190-2192
18. Budd, P. M.; McKeown, N. B.; Fritsch, D. *Journal of Materials Chemistry* **2005**, 15, (20), 1977-1986
19. Bezzu, C. G.; Carta, M.; Tonkins, A.; Jansen, J. C.; Bernardo, P.; Bazzarelli, F.; McKeown, N. B. *Advanced Materials* **2012**, 24, (44), 5930-5933
20. Han, S. H.; Misdan, N.; Kim, S.; Doherty, C. M.; Hill, A. J.; Lee, Y. M. *Macromolecules* **2010**, 43, (18), 7657-7667
21. Han, S. H.; Kwon, H. J.; Kim, K. Y.; Seong, J. G.; Park, C. H.; Kim, S.; Doherty, C. M.; Thornton, A. W.; Hill, A. J.; Lozano, Á. E.; Berchtold, K. A.; Lee, Y. M. *Physical Chemistry Chemical Physics* **2012**, 14, (13), 4365-4373
22. Sanders, D. F.; Smith, Z. P.; Ribeiro, C. P.; Guo, R.; McGrath, J. E.; Paul, D. R.; Freeman, B. D. *Journal of Membrane Science* **2012**, 409-410, 232-241
23. Calle, M.; Doherty, C. M.; Hill, A. J.; Lee, Y. M. *Macromolecules* **2013**, 46, (20), 8179-8189
24. Raaijmakers, M. J. T.; Hempenius, M. A.; Schön, P. M.; Vancso, G. J.; Nijmeijer, A.; Wessling, M.; Benes, N. E. *Journal of the American Chemical Society* **2013**, 136, (1), 330-335
25. Raaijmakers, M. J. T.; Wessling, M.; Nijmeijer, A.; Benes, N. E. *Chemistry of Materials* **2014**, 26, (12), 3660-3664
26. Cornelius, C. J.; Marand, E. *Journal of Membrane Science* **2002**, 202, (1-2), 97-118
27. Suzuki, T.; Yamada, Y.; Itahashi, K. *Journal of Applied Polymer Science* **2008**, 109, (2), 813-819
28. Sarbu, T. T. E. *Nature* **2000**, 405, (6783), 165
29. Consolati, G.; Genco, I.; Pegoraro, M.; Zanderighi, L. *Journal of Polymer Science, Part B: Polymer Physics* **1996**, 34, (2), 357-367
30. Dorkenoo, K. D.; Pfromm, P. H. *Macromolecules* **2000**, 33, (10), 3747-3751
31. Punsalan, D.; Koros, W. J. *Journal of Applied Polymer Science* **2005**, 96, (4), 1115-1121
32. Punsalan, D.; Koros, W. J. *Polymer* **2005**, 46, (23), 10214-10220

33. Huang, Y.; Paul, D. R. *Journal of Membrane Science* **2004**, 244, (1-2), 167-178
34. Huang, Y.; Paul, D. R. *Polymer* **2004**, 45, (25), 8377-8393
35. Huang, Y.; Paul, D. R. *Macromolecules* **2005**, 38, (24), 10148-10154
36. Huang, Y.; Paul, D. R. *Macromolecules* **2006**, 39, (4), 1554-1559
37. Cui, L.; Qiu, W.; Paul, D. R.; Koros, W. J. *Polymer* **2011**, 52, (15), 3374-3380
38. Horn, N. R.; Paul, D. R. *Polymer* **2011**, 52, (7), 1619-1627
39. Horn, N. R.; Paul, D. R. *Macromolecules* **2012**, 45, (6), 2820-2834
40. Raaijmakers, M. J. T.; Hempenius, M. A.; Schön, P. M.; Vancso, G. J.; Nijmeijer, A.; Wessling, M.; Benes, N. E. *Journal of the American Chemical Society* **2014**, 136, (1), 330-335
41. Low, B. T.; Chung, T. S.; Chen, H.; Jean, Y. C.; Pramoda, K. P. *Macromolecules* **2009**, 42, (18), 7042-7054
42. Gomes, D.; Nunes, S. P.; Peinemann, K. V. *Journal of Membrane Science* **2005**, 246, (1), 13-25
43. Lau, C. H.; Nguyen, P. T.; Hill, M. R.; Thornton, A. W.; Konstas, K.; Doherty, C. M.; Mulder, R. J.; Bourgeois, L.; Liu, A. C. Y.; Sprouster, D. J.; Sullivan, J. P.; Bastow, T. J.; Hill, A. J.; Gin, D. L.; Noble, R. D. *Angewandte Chemie - International Edition* **2014**, 53, (21), 5322-5326
44. Ogieglo, W.; Wormeester, H.; Wessling, M.; Benes, N. E. *ACS applied materials & interfaces* **2012**, 4, (2), 935-43
45. Lichtenstein, T.; Engineering, U. o. R. C. o.; Science, A., *Handbook of Thin Film Materials*. College of Engineering and Applied Science, University of Rochester: 1979.
46. Lorenz, K.; Wessling, M. *Adsorption* **2013**, 19, (6), 1117-1125
47. Raaijmakers, M. J. T.; Kappert, E. J.; Nijmeijer, A.; Benes, N. E. *Macromolecules* **2015**, 48, (9), 3031-3039
48. Pacheco, F. A.; Pinnau, I.; Reinhard, M.; Leckie, J. O. *Journal of Membrane Science* **2010**, 358, (1-2), 51-59
49. Zhang, Y.; Benes, N. E.; Lammertink, R. G. H. *Lab on a Chip* **2015**,
50. Freger, V. *Langmuir* **2003**, 19, (11), 4791-4797
51. Hougham, G.; Tesoro, G.; Viehbeck, A. *Macromolecules* **1996**, 29, (10), 3453-3456
52. Tanaka, K.; Chujo, Y. *Journal of Materials Chemistry* **2012**, 22, (5), 1733-1746
53. Simons, K.; Nijmeijer, K.; Sala, J. G.; van der Werf, H.; Benes, N. E.; Dingemans, T. J.; Wessling, M. *Polymer* **2010**, 51, (17), 3907-3917
54. Sirard, S. M.; Green, P. F.; Johnston, K. P. *J Phys Chem B* **2001**, 105, (4), 766-772
55. Wind, J. D.; Sirard, S. M.; Paul, D. R.; Green, P. F.; Johnston, K. P.; Koros, W. J. *Macromolecules* **2003**, 36, (17), 6442-6448
56. Rowe, B. W.; Freeman, B. D.; Paul, D. R. *Macromolecules* **2007**, 40, (8), 2806-2813
57. Wessling, M.; Lidon Lopez, M.; Strathmann, H. *Separation and Purification Technology* **2001**, 24, (1-2), 223-233
58. Visser, T.; Koops, G. H.; Wessling, M. *Journal of Membrane Science* **2005**, 252, (1-2), 265-277
59. Dong, G.; Li, H.; Chen, V. *Journal of Membrane Science* **2011**, 369, (1-2), 206-220
60. Wang, J. S.; Kamiya, Y. *Journal of Polymer Science, Part B: Polymer Physics* **2000**, 38, (6), 883-888

61. Sirard, S. M.; Ziegler, K. J.; Sanchez, I. C.; Green, P. F.; Johnston, K. P. *Macromolecules* **2002**, *35*, (5), 1928-1935
62. Sirard, S. M.; Castellanos, H.; Green, P. F.; Johnston, K. P. *J Supercrit Fluid* **2004**, *32*, (1-3), 265-273
63. Wessling, M.; Huisman, I.; Boomgaard, T.; Smolders, C. *Journal of Polymer Science Part B: Polymer Physics* **1995**, *33*, (9), 1371-1384
64. Cheng, S.-X.; Chung, T.-S.; Wang, R.; Vora, R. H. *Journal of Applied Polymer Science* **2003**, *90*, (8), 2187-2193
65. Duthie, X.; Kentish, S.; Powell, C.; Nagai, K.; Qiao, G.; Stevens, G. *Journal of Membrane Science* **2007**, *294*, (1-2), 40-49
66. Leu, C.-M.; Chang, Y.-T.; Wei, K.-H. *Chemistry of Materials* **2003**, *15*, (19), 3721-3727
67. Iyer, P.; Iyer, G.; Coleman, M. *Journal of Membrane Science* **2010**, *358*, (1-2), 26-32
68. Böhning, M.; Springer, J. *Polymer* **1998**, *39*, (21), 5183-5195
69. Fleming, G. K.; Koros, W. J. *Macromolecules* **1986**, *19*, (8), 2285-2291
70. Böhning, M.; Springer, J. *Polymer* **1998**, *39*, (21), 5183-5195
71. Scholes, C. A.; Chen, G. Q.; Stevens, G. W.; Kentish, S. E. *Journal of Membrane Science* **2010**, *346*, (1), 208-214
72. Ogieglo, W.; Upadhyaya, L.; Wessling, M.; Nijmeijer, A.; Benes, N. E. *Journal of Membrane Science* **2014**, *464*, 80-85

Chapter 6
**High pressure CO₂ permeation
behavior of hybrid poly(POSS-imide)s**

Abstract

Polyimide membranes based on fluoroalkanes display high CO₂ permeances due to the sorption affinity of the fluorine groups towards CO₂. Here, we studied the relationship between the CO₂ sorption and permeability at high pressure differences across the membrane, for ultrathin fluoroalkane functionalized hybrid membranes. The hybrid membranes consist of a network of alternating imide and polyhedral oligomeric silsesquioxanes. The fluoroalkane groups on the imide bridge are responsible for the high sorption capacities, that range from 100-350 cm³ CO₂ (STP) cm⁻³ polymer at 26 bar. The CO₂ permeability coefficient increases with increasing CO₂ concentration in the membrane. The permeability coefficient increase is due to an increase in both solubility and diffusivity of the CO₂ at higher pressures. The diffusivity of CO₂ increases because the network swells, resulting in a higher apparent molar volume of CO₂ and a reduced interaction of CO₂ with the hybrid network. The presented work allows for optimization of the sorption behavior of the membrane with respect to the membrane permeability.

6.1. Introduction

Membrane gas separation is considered a key technology for carbon dioxide (CO₂) separation for carbon capture and sequestration applications,¹⁻³ natural gas sweetening⁴⁻⁷ and biogas upgrading.⁸⁻¹⁰ Membranes that selectively permeate CO₂ can be used for the removal of CO₂ from high pressure gas mixtures such as methane or higher alkanes.^{6, 11-13} The valuable, retained component will remain at high pressure, while the permeated CO₂ is at low pressure. In the development of highly permeable CO₂ membranes the aim is to either increase the amount of excess free volume (EFV) in the polymer, or to improve the affinity of the polymer towards the permeating component.¹⁴ Examples of high EFV polymers include of polymers of intrinsic microporosity (PIMs),¹⁵ thermally rearranged (TR) polymers¹⁵⁻¹⁸ or substituted polyacetylenes such as poly[1-(trimethylsilyl)-1-propyne]. Although these materials show much promise due to their combination of high permeability and selectivity, inherent loss of EFV and permeance due ageing is observed.¹⁹

Incorporating affinity groups in the polymer matrix potentially allows for higher CO₂ sorption, without the requirement of a high EFV content. The most common groups used for improved affinity towards CO₂ are fluoroalkanes. The fluoroalkanes are usually incorporated by using 4,4'-(hexafluoro isopropylidene) diphthalic anhydride (6FDA) or 4,4'-(hexafluoro isopropylidene) dianiline (6FpDA) as precursors during synthesis.²⁰⁻²⁴ Polyimides that are functionalized with fluoroalkanes are known to have both a high permselectivity and permeability with respect to other polyimides.²⁵ The electronegative character of the fluorine groups creates sites on the polyimide backbone that preferentially sorb CO₂.²⁶ Nonetheless, the high sorption affinity for CO₂ also makes the layers more sensitive towards plasticization and physical ageing effects,²⁷⁻³⁰ particularly for ultrathin films.^{30, 31} To suppress these effects, chemical cross-linking^{20, 32-34} and thermal annealing³⁵⁻³⁷ have been successfully applied, although at the cost of CO₂ permeance.²⁰ Recently, we presented hybrid polyhedral oligomeric silsesquioxane-imides (poly(POSS-imide)s)³⁸ that have permeances that are comparable PIMs and TR polymers, but have the network rigidity^{38, 39} that is required to prevent plasticization and ageing effects. Here, we studied the CO₂ sorption and permeation behavior of hybrid poly(POSS-imide)s that are functionalized with fluoroalkanes. The CO₂ permeation depends strongly on the fluorine and POSS content of the membrane. Fundamental understanding of the structure-property-performance relationships of the membrane allows

for optimization of the membrane properties for CO₂ separation applications. Here, we studied the sorption behavior of ultrathin poly(POSS-imide) films in compressed CO₂ atmospheres and determined the relationship between permeation and sorption data.

6.2. Experimental

6.2.1. Poly(POSS-imide) membrane synthesis

Poly(POSS-imide) membranes were prepared by interfacial polymerization of water-soluble ammonium chloride-functionalized POSS (octa-ammonium POSS, Hybrid Plastics) and a 0.075 wt.% 4,4-(hexafluoroisopropylidene) diphthalic anhydride (6FDA, Sigma-Aldrich) solution in toluene. The partial conversion of ammonium to primary amine groups was achieved by addition of NaOH until the solution reached a pH of 9.9. Supported thin films were produced on α -alumina discs (Pervatech, Netherlands) coated with 1.5 μ m thick γ -alumina (porosity of \sim 40 % and a pore size of 2-3 nm). First, the α -alumina discs, held fixed on a perforated plate by vacuum, were impregnated with the POSS solution. Next, the discs were left to dry in a N₂ atmosphere for 15 min and subsequently submerged in the 6FDA in toluene solution. After 5 min reaction time, the toluene was removed from the interface and the discs were washed with acetone to remove any residual reactants. After drying for at least 2 h in air atmosphere the samples were heat-treated for 2 h at 300 °C in air atmosphere to achieve conversion of the amic acid groups to cyclic imide groups. The concentration of the POSS solution, a critical parameter in the interfacial polymerization reaction, were varied to obtain membranes with different thicknesses, refractive indices and chemical composition. The concentrations of fluorine groups in the final polyPOSS-imide layer was determined elsewhere.⁴⁰

6.2.2. Membrane characterization

Spectroscopic ellipsometry

The thickness and refractive index of poly(POSS-imide)s atop γ -alumina coated α -alumina discs were determined using spectroscopic ellipsometry (M-2000X, J.A. Woollam Co., Inc.). The psi (Ψ) and delta (Δ) spectra were recorded over a wavelength range of 340–1000 nm, with a spectral resolution of about 2 nm, using light reflected at 65°, 70° and 75° angles of incidence. The optical model of the poly(POSS-imide) layer atop a γ -alumina coated α -alumina disc is visualized in **Figure 6-1**. The layered optical model was

constructed by a stepwise measurement of each individually added layer. The α -alumina disc was modelled using an Effective Medium Approximation (EMA) of three-parameter Cauchy-type optical dispersion of Al_2O_3 ⁴¹ with $n(\lambda) = A + B/\lambda^2 + C/\lambda^4$ with $A = 1.751$, $B = 0.00632 \mu\text{m}^2$, $C = -0.00010152 \mu\text{m}^4$ and void ($n=1.000$) with a graded EMA layer atop corresponding to the roughness of the ceramic disc.

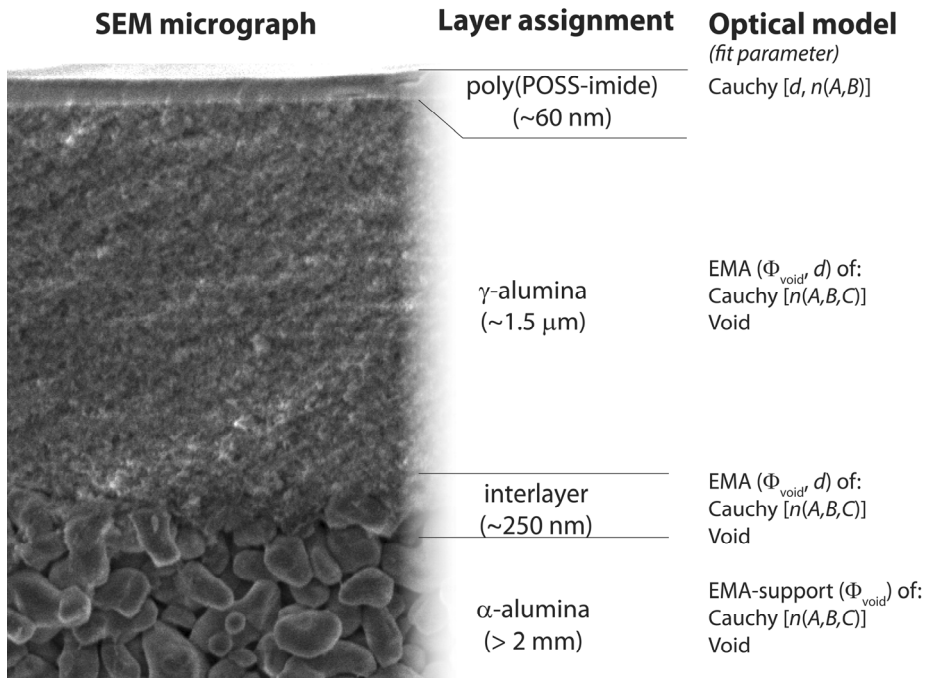


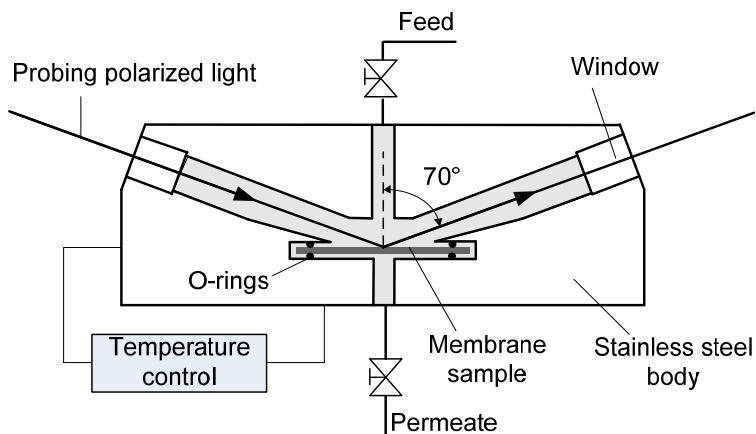
Figure 6-1. Optical model of a poly(POSS-imide) layer atop a γ -alumina coated α -alumina disc. The cross-section scanning electron micrograph of the membrane shows the distinct morphology of the dense poly(POSS-imide) layer, γ -alumina and α -alumina.

Justification for the optical model and its validation versus Atomic Force Microscopy and Mercury Porosimetry is given elsewhere.⁴² The samples were again measured after coating of the γ -alumina layer. The interlayer between the γ -alumina and the α -alumina was assumed to have a thickness similar to the thickness of the graded EMA layer that reflects the roughness of the α -alumina disc, but its porosity was left as a fitting parameter to account for the possible intrusion by γ -alumina. The γ -alumina thickness and porosity were modelled using an EMA of Al_2O_3 and void. Finally, poly(POSS-imide) formation atop the γ -alumina was achieved by a procedure described in the

synthesis section. The poly(POSS-imide) layer thickness and refractive index were determined using a two-parameter Cauchy optical dispersion (fit parameters A and B), assuming transparency of the hybrid material in the used wavelength range. The porosity of the γ -alumina and the interlayer were set as fit parameters, to account for the water that remains in the γ -alumina after poly(POSS-imide) synthesis. The wavelength range for all optical models was limited to 600–1000 nm to reduce the influence of light scattering as a result of the non-uniformity of the porous α -alumina discs.⁴²

Spectroscopic ellipsometry – high pressure CO₂ sorption

Spectroscopic ellipsometry measurements at elevated gas pressures were conducted with an Alpha-SE[®] ellipsometer (J.A. Woollam Co. Inc.). All measurements were done at a fixed angle of incidence (70°) in the wavelength range from 370 to 900 nm. Samples were placed in a home-built stainless steel cell ($p_{\max}=20$ MPa, $T_{\max}=473.15$ K) equipped with a temperature and pressure control system, as depicted in **Scheme 6-1**.



Scheme 6-1. Schematic of the stainless steel cell used in the spectroscopic ellipsometry analysis of CO₂ adsorption and swelling dynamics of poly(POSS-imide)s and Matrimid membranes.

Accurate control and stability (within 0.1 bar) of the gas pressure was achieved using a syringe pump (Teledyne ISCO, 500D). The system temperature was maintained at 35 °C by a glycol bath connected to the cylinder of the syringe pump and by an induction heating belt connected to the measurement cell, in order to correct temperature changes due to Joule-Thompson effects upon incremental pressure change. Light entered and exited the cell through 1 cm thick quartz windows positioned perpendicular to the polarized light beam

source and detector. Pressure induced birefringence of the cell windows was measured via a high-pressure helium calibration on a 25 nm SiO₂/Si wafer, and used for correction of the birefringence during further high pressure measurements. Static sorption experiments were performed by opening a valve between the feed and permeate side, equalizing the pressure on both sides of the membrane. Permeation experiments were performed by closing the valve between the feed and permeate side, and slowly opening the permeate side to atmosphere.⁴³ The membrane permeance was determined by measuring the change in volume of CO₂ in the syringe pump as function of time. The poly(POSS-imide) layer thickness and refractive index were determined using a two-parameter Cauchy optical dispersion (fit parameters *A* and *B*), assuming transparency of the hybrid material in the used wavelength range. The porosity of the γ -alumina and the interlayer were set as fit parameters, to account for the water that remains in the γ -alumina after poly(POSS-imide) synthesis. The wavelength range for all optical models was limited to 600–900 nm to reduce the influence of light scattering as a result of the non-uniformity of the porous α -alumina discs.⁴² The change in refractive index of CO₂ at elevated pressures was taken into account by changing the ambient refractive index according to data from^{44, 45}.

6.2.3. Membrane CO₂ permeability

Figure 6-2 shows the CO₂ permeance as function of the pressure difference across the ultrathin poly(POSS-imide) membranes. All poly(POSS-imide) membranes have permeances between about $1\text{-}3\cdot 10^{-7}$ mol m⁻² s⁻¹ Pa⁻¹ (or 300–900 GPU), close to the permeance requirements for economically viable, large-scale CO₂ membrane separation processes.⁴⁶ The membrane thicknesses of the dry polymer are 93, 87 and 150 nm for the 0.9, 2.5 and 5.0 wt.% samples respectively. The lower permeance of the 5.0 wt.% as compared to the other samples is partly due to the higher layer thickness. The CO₂ permeance of the poly(POSS-imide) membrane prepared with a 5.0 wt.% POSS solution remains constant for pressures differences up to 26 bar. For the membranes prepared with 2.5 and 0.9 wt.% POSS solutions, the CO₂ permeance increases with increasing CO₂ transmembrane pressure. The increasing CO₂ permeances can be due to an increased solubility and/or diffusivity of CO₂ at higher pressure. The permeance behavior is distinct from that of conventional fluoroalkane based polyimides, that show a pronounced minimum in the permeance at the so-called plasticization pressure.^{27, 31, 47} Below the plasticization pressure, polymers become saturated by the gaseous penetrant.

As a result, the permeability coefficient as function of pressure decreases. Above the plasticization pressure, the gas diffusivity increases due to plasticization of the matrix. The poly(POSS-imide)s differ from conventional polyimides: the solubility and/or diffusivity of CO₂ likely increase with respect to pressure.

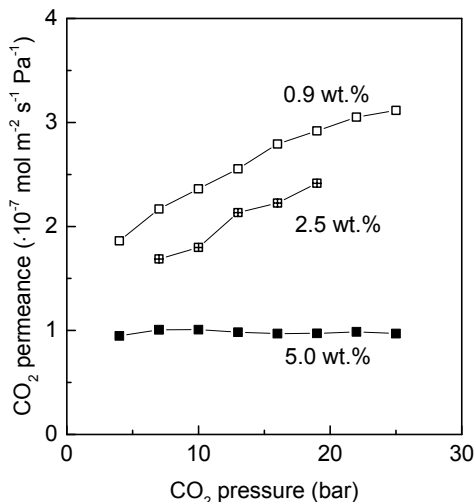


Figure 6-2. CO₂ permeance at 35 °C as function of trans-membrane pressure for poly(POSS-imide)s prepared with 0.9, 2.5 and 5.0 wt.% POSS solutions. A permeance of $1 \cdot 10^{-7} \text{ mol m}^{-2} \text{ s}^{-1} \text{ Pa}^{-1}$ equals about 300 GPU.

6.2.4. Thickness, refractive index and CO₂ concentrations

The solubility and diffusivity of CO₂ in the ultrathin poly(POSS-imide) layers has been determined by performing in-situ sorption measurements of a membrane, using spectroscopic ellipsometry. The thicknesses and refractive indices of the ultrathin poly(POSS-imide) layers are measured during static sorption experiments (i.e., no pressure difference across the membrane) and during permeation experiments (i.e., high pressure at the feed side and atmospheric pressure at the permeate side). **Figure 6-3 (top left panel)** shows the swelling degree as function of pressure of the poly(POSS-imide) membranes. The swelling degree of all poly(POSS-imide)s increases with increasing CO₂ pressure. The swelling degrees are highest for the membranes prepared with 0.9 wt.% POSS solutions.

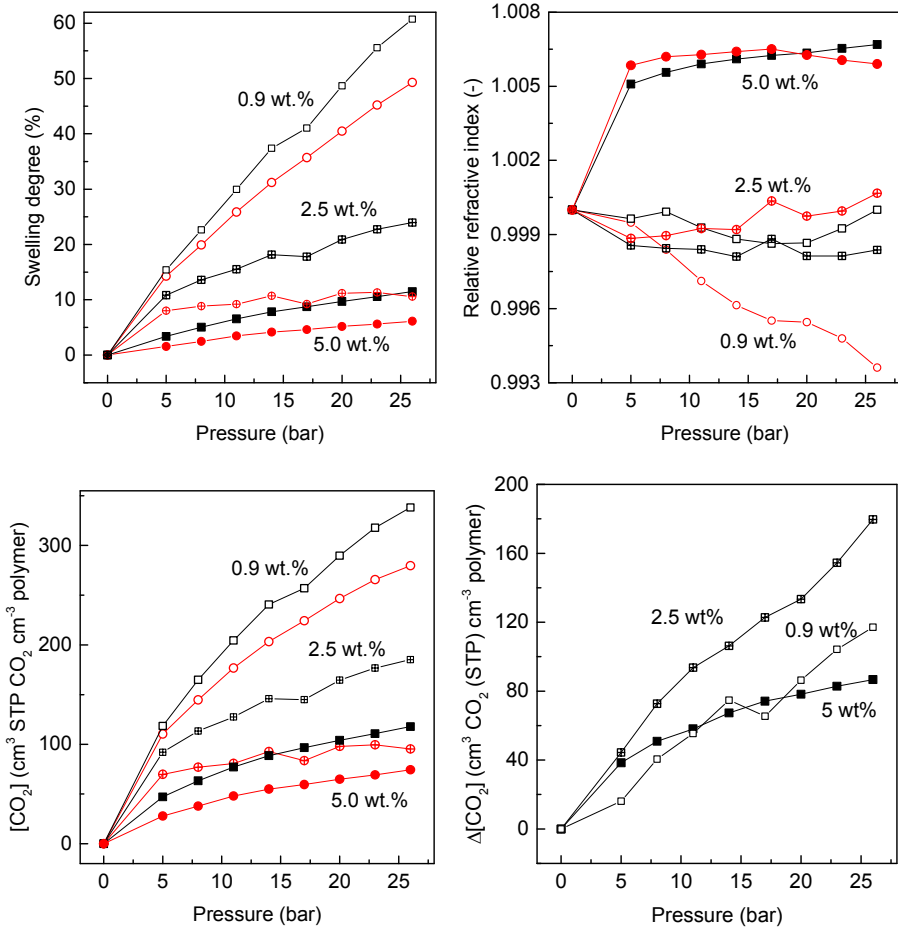


Figure 6-3. Top left panel: swelling degree as function of feed pressure of the membranes during static sorption (black squares) and permeation with atmospheric pressure at permeate side (red circles). Top right panel: relative refractive index of the membranes during static sorption (black squares) and permeation with atmospheric pressure at permeate side (red circles). Bottom left panel: CO₂ concentrations as function of feed pressure, of the membranes during static sorption (black squares) and permeation with atmospheric pressure at permeate side (red circles). Bottom right panel: CO₂ concentration gradient across the membrane layer as function of feed pressure, during the permeation experiment with atmospheric pressure at permeate side. The membranes were prepared using (open symbols) 0.9, (crossed symbols) 2.5 and (closed symbols) 5.0 wt.% POSS solutions.

The higher swelling degrees are associated with the larger fluorine content for the poly(POSS-imide)s prepared with lower concentration POSS solutions, which is discussed in detail elsewhere.⁴⁰ The swelling degrees during a static sorption experiment are always higher as compared to the permeation experiment. During static sorption, the CO₂ activity throughout the membrane layer is equal. The pressure difference across the membrane in permeation mode, resulting in a gradient in CO₂ activity across the membrane, decreases the overall swelling degree of the membrane layers. The layers with lower swelling degrees display a higher relative refractive index, as shown in **Figure 6-3 (top right panel)**. A relative refractive index above 1 indicates predominant filling of free volume spaces in the hybrid network, and results in an increase of the refractive index of the mixture. This is because the refractive index of the liquid CO₂ (estimated at $n \approx 1.23$ ⁴⁸⁻⁵¹) is much higher than the refractive index of void space ($n = 1$). Relative refractive indices below 1 indicate predominant dilation of the network as compared to filling of free void spaces in the network. The layers prepared with 5.0 wt.% POSS solution show a relative refractive index higher than 1 that increases with increasing pressure. For the 0.9 wt.% sample, the relative refractive index decreases with increasing pressure, in line with the high swelling degrees. The differences in relative refractive index can be rationalized by differences in network composition: a higher POSS content increases the rigidity of the network and prevents dilation of the matrix upon CO₂ sorption. The CO₂ concentration as function of pressure, shown in **Figure 6-3 (bottom left panel)** display a concave isotherm shape that is typical for glassy polymers.^{52, 53} The CO₂ concentration is in the order, from high to low, for membranes prepared with $0.9 > 2.5 > 5.0$ wt.% POSS solution. The CO₂ concentration measured during permeation is the average CO₂ concentration. The complexity of the model used to fit the SE data does not allow for analysis of gradients in the CO₂ concentration in the poly(POSS-imide) layers. However, assuming that the feed side concentration equals the CO₂ sorption measured during static sorption, the SE data can be used to calculate a concentration profile across the membrane. By assuming that the concentration gradient is either linear or non-linear, two concentration profiles can be estimated from the difference between the concentration measured during static sorption (feed side concentration) and the concentration determined during permeation (average concentration). **Figure 6-3 (bottom right panel)** shows the calculated differences CO₂ in concentration between the retentate and permeate sides of the films, assuming linear concentration gradients inside the films. The

concentration differences across the membrane are similar for the membranes prepared with 0.9 and 5.0 wt.% POSS solutions. The highest concentration difference is observed for the 2.5 wt.% sample. For the membrane prepared with 0.9 wt.% POSS the sorption isotherm of CO₂ is the highest; in the absence of a transport resistance over the support this implies that for this membrane the highest concentration differences over the membrane are expected. The observed lower values indicate that the assumption of a linear concentration profile is not valid, or that the transport resistance through the ceramic support is not negligible. Because the permeances of the three membranes are in the same order of magnitude, and the negligible resistance of the ceramic support is confirmed by viscous flow calculations and permeance measurements of a bare support, it is most likely that non-linear concentration gradients exist across the membrane thickness.

Theoretical linear and non-linear concentration profiles across the layer thickness are visualized in **Figure 6-4**. The large discrepancy between the linear and non-linear profiles for the 0.9 wt.% based sample is apparent. For the 2.5 and 5.0 wt.% samples, the similarity between the concentration profiles indicate that the linear profile might well describe the CO₂ concentration across the membrane layer. The difference in swelling degree change and concentration gradient profiles likely originates from differences in poly(POSS-imide) network rigidity: at high fluorine content, the network displays a high degree of flexibility that allows for high CO₂ sorption.⁴⁰ Consequently, a gradient in the CO₂ concentration equals a gradient in the swelling degree, potentially resulting in large differences in solubility and diffusivity across the membrane. Because the membrane sorption is lower at the permeate side, lower dilation of the network occurs and the diffusivity of CO₂ decreases. A higher CO₂ diffusivity at higher concentrations, results in the absence of large concentration gradients at the feed side of the layer. For the other samples, sufficient network rigidity remains to prevent the excessive swelling differences across the layer.

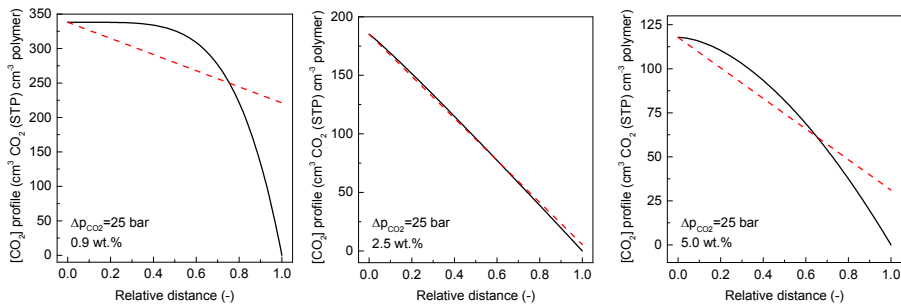


Figure 6-4. (top, left panel) Relative swelling degree change upon changing from static sorption to permeation. (other panels) CO₂ concentration profile as function of relative distance across the membrane layer (feed side = 0, permeate side = 1) for poly(POSS-imide)s prepared with (top, right panel) 0.9, (bottom, left panel) 2.5 and (bottom, right panel) 5.0 wt.% POSS solutions. The linear (dotted, red line) and non-linear (black, solid line) concentration profiles are calculated assuming that the CO₂ concentration at the feed side equals that of the static sorption experiment, and that the average CO₂ concentration is given by the CO₂ concentration measured during permeation experiments.

6.2.5. Apparent gas molar volumes

The apparent molar volumes, V_m , of the dissolved gases can be determined from the slope of the swelling versus the CO₂ concentrations.⁵⁴ **Figure 6-5 (left panel)** displays the swelling degree as a function of the CO₂ concentration in the poly(POSS-imide) membranes. For all membranes, the swelling degree as function of concentration during static sorption and permeation experiments follows the same increase in swelling as function of the CO₂ concentration. The similarity between the sorption and permeation data indicates the absence of pronounced hysteresis effects upon changing from static sorption to a pressure gradient during permeation. Only the 0.9 wt.% sample displays hysteresis, which is reflected by the higher CO₂ V_m during permeation and the large difference in relative refractive index shown in Figure 3 (top, right panel). The V_m of CO₂, shown in **Figure 6-5 (right panel)** increases significantly, from 12.5 to 65 cm³ mol⁻¹, with increasing CO₂ concentration. The increase in V_m can be rationalized by the progressive filling of the network. At low concentrations, the CO₂ molecules can fill free spaces in the network without much dilation. At higher concentrations, sorption of the CO₂ molecules requires additional dilation because the available free space is occupied more and more. Because the environment of the CO₂ molecules

changes, from a completely polymeric network to an environment that is partially filled with CO₂, the V_m will also progressively change. At high CO₂ concentrations, the apparent V_m values will start to resemble that of the fluid phase.⁴⁰

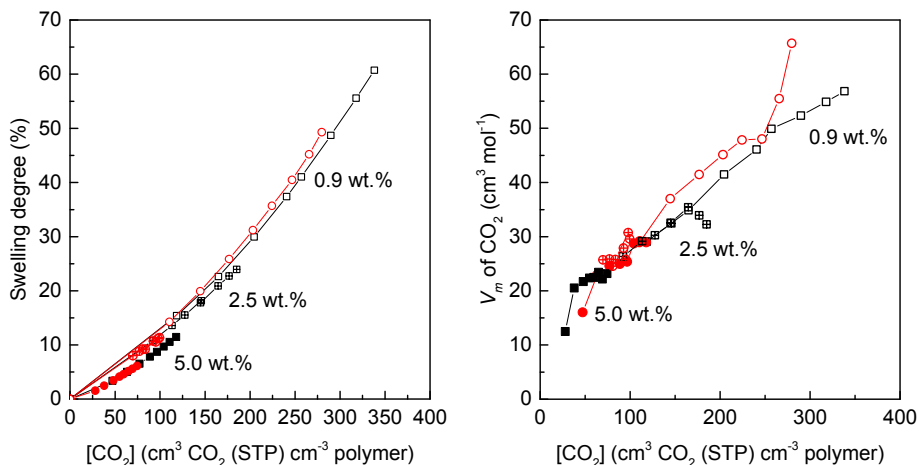


Figure 6-5. Swelling degree (left panel) and apparent V_m of CO₂ (right panel) as function of CO₂ concentration, during static sorption experiments (black squares) and permeation experiments (red circles) for the poly(POSS-imide)s prepared with (open symbols) 0.9, (crossed symbols) 2.5 and (closed symbols) 5.0 wt.% POSS solutions.

6.2.6. CO₂ permeability and diffusivity

The change of the V_m with CO₂ concentration illustrates the influence of the penetrant on the nature of the network. The changes in network properties are reflected by the gas sorption and permeation behavior of the poly(POSS-imide)s. **Figure 6-6 (left panel)** shows the permeability coefficient as function of CO₂ concentration in the membranes. The permeability coefficient of CO₂ is calculated from the permeance and thickness data measured by SE. The permeability coefficient increases with increasing CO₂ concentration, due to the higher sorption and diffusion. Nonetheless, the slope of the curves is distinct for the different compositions. The 5.0 wt.% sample does not show an increase in permeability coefficient due to the high network rigidity. The 2.5 wt.% sample does show a strong increase, without loss of network rigidity. The 0.9 wt.% sample does result in much higher CO₂ concentrations and permeability, but at the cost of network rigidity. **Figure 6-6 (right panel)** shows the diffusion coefficient of CO₂ in the poly(POSS-imide) layer as

function of sorbed CO_2 concentration. The diffusion coefficients are in the range of about $2\text{-}12 \cdot 10^{-8} \text{ cm}^2 \text{ s}^{-1}$, which is in a similar range as found for conventional polyimides.⁵⁵ The diffusion coefficients increase with increasing CO_2 concentration. The order of magnitude change of the diffusion coefficients as function of CO_2 concentration are also observed for polybenzylmethacrylate,⁵⁶ polysulfone,⁵⁷ natural methyl cellulose and sodium carboxymethyl cellulose,⁵⁸ and carbon molecular sieve membranes.⁵⁹

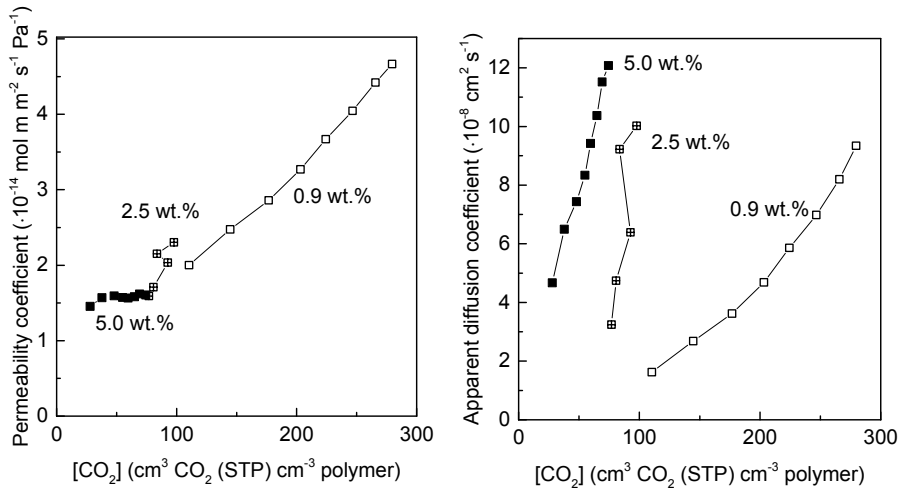


Figure 6-6. (left panel) CO_2 concentration gradient as function of the average CO_2 concentration during permeation. $1 \cdot 10^{-14} \text{ mol m m}^{-2} \text{ s}^{-1} \text{ Pa}^{-1}$ equals about 30.3 barrer ($= 10 \cdot 10^{-10} \text{ cm}^3 \text{ (STP) cm cm}^{-2} \text{ s}^{-1} \text{ cmHg}^{-1}$). (right panel) Diffusion coefficient as function of the average CO_2 concentration during permeation.

The increase in diffusion coefficient can be rationalized by the increased swelling and apparent V_m at higher CO_2 concentrations. The interactions of CO_2 with the polymer network decrease, because the swollen, filled network starts to resemble the gas phase. The diffusion coefficient in the 0.9 wt.% sample are lower as compared to the 2.5 and 5.0 wt.% samples. Likely, the higher degree of cross-linking of the 0.9 wt.% sample reduces the diffusivity of the gas, even though the higher fluorine content results in a higher CO_2 sorption.

6.3. Conclusion

In conclusion, the CO_2 permeability in ultrathin poly(POSS-imide) membranes is determined by the sorption characteristics. The CO_2 permeability coefficient

increase with increasing CO₂ concentration in the membrane. At high fluoroalkane content, the persistent increase in sorption due to flexibility of the network increases the permeability. Moreover, swelling of the network results in a higher apparent V_m of CO₂ and reduced interaction of CO₂ with the hybrid network. As a result, the diffusion coefficient of CO₂ increases strongly with increasing CO₂ concentration. The fundamental understanding on the CO₂ permeation allows for design of optimized membrane performance for CO₂ separation applications.

6.4. Acknowledgements

This project has received funding from the European Union's Seventh Framework Programme for research, technological development and demonstration under CARENA grant agreement no. 263007.

6.5. References

1. Czyperk, M.; Zapp, P.; Bouwmeester, H. J. M.; Modigell, M.; Ebert, K.; Voigt, I.; Meulenbergh, W. A.; Singheiser, L.; Stöver, D. *Journal of Membrane Science* **2010**, 359, (1-2), 149-159
2. Jones, C. W. *Annual Review of Chemical and Biomolecular Engineering* **2011**, 2, 31-52
3. Smart, S.; Lin, C. X. C.; Ding, L.; Thambimuthu, K.; Diniz Da Costa, J. C. *Energy and Environmental Science* **2010**, 3, (3), 268-278
4. Hao, J.; Rice, P. A.; Stern, S. A. *Journal of Membrane Science* **2008**, 320, (1-2), 108-122
5. Omole, I. C.; Adams, R. T.; Miller, S. J.; Koros, W. J. *Industrial and Engineering Chemistry Research* **2010**, 49, (10), 4887-4896
6. Safari, M.; Ghanizadeh, A.; Montazer-Rahmati, M. M. *International Journal of Greenhouse Gas Control* **2009**, 3, (1), 3-10
7. Wind, J. D.; Paul, D. R.; Koros, W. J. *Journal of Membrane Science* **2004**, 228, (2), 227-236
8. Du, N.; Park, H. B.; Dal-Cin, M. M.; Guiver, M. D. *Energy and Environmental Science* **2012**, 5, (6), 7306-7322
9. Favre, E.; Bounaceur, R.; Roizard, D. *Journal of Membrane Science* **2009**, 328, (1-2), 11-14
10. Scholz, M.; Melin, T.; Wessling, M. *Renewable and Sustainable Energy Reviews* **2013**, 17, (0), 199-212
11. Bos, A.; Pünt, I. G. M.; Wessling, M.; Strathmann, H. *Separation and Purification Technology* **1998**, 14, (1-3), 27-39
12. Hasan, R.; Scholes, C. A.; Stevens, G. W.; Kentish, S. E. *Industrial and Engineering Chemistry Research* **2009**, 48, (11), 5415-5419
13. Reijerkerk, S. R.; Nijmeijer, K.; Ribeiro, C. P.; Freeman, B. D.; Wessling, M. *Journal of Membrane Science* **2011**, 367, (1-2), 33-44

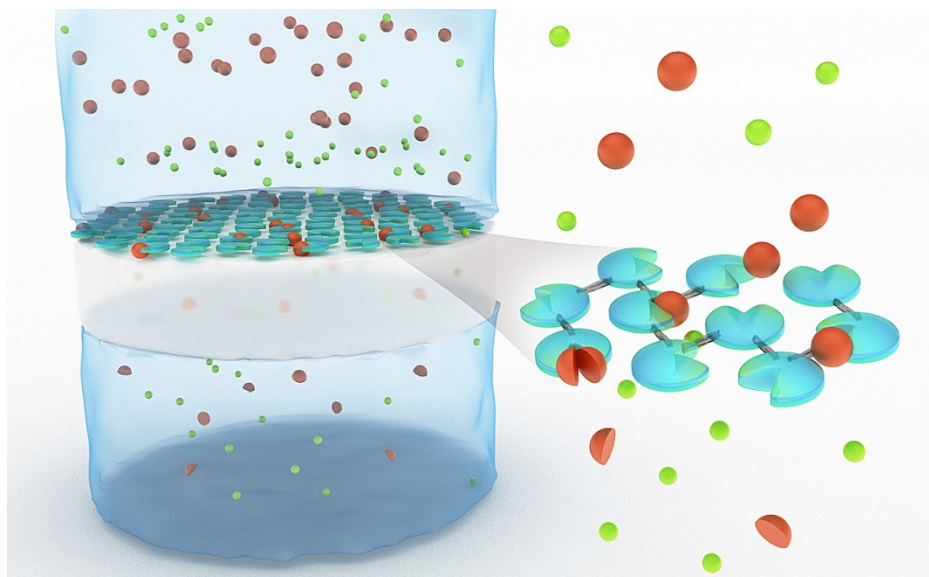
14. Zhao, Y.; Qiu, C.; Li, X.; Vararattanavech, A.; Shen, W.; Torres, J.; Hélix-Nielsen, C.; Wang, R.; Hu, X.; Fane, A. G.; Tang, C. Y. *Journal of Membrane Science* **2012**, 423-424, 422-428
15. Swaidan, R.; Ma, X.; Litwiller, E.; Pinnau, I. *Journal of Membrane Science* **2013**, 447, 387-394
16. Kim, S.; Jo, H. J.; Lee, Y. M. *Journal of Membrane Science* **2013**, 441, 1-8
17. Kim, S.; Woo, K. T.; Lee, J. M.; Quay, J. R.; Keith Murphy, M.; Lee, Y. M. *Journal of Membrane Science* **2014**, 453, 556-565
18. Scholes, C. A.; Ribeiro, C. P.; Kentish, S. E.; Freeman, B. D. *Journal of Membrane Science* **2014**, 450, 72-80
19. Consolati, G.; Genco, I.; Pegoraro, M.; Zanderighi, L. *Journal of Polymer Science, Part B: Polymer Physics* **1996**, 34, (2), 357-367
20. Cao, C.; Chung, T. S.; Liu, Y.; Wang, R.; Pramoda, K. P. *Journal of Membrane Science* **2003**, 216, (1-2), 257-268
21. Cheng, S. X.; Chung, T. S.; Wang, R.; Vora, R. H. *Journal of Applied Polymer Science* **2003**, 90, (8), 2187-2193
22. Duthie, X.; Kentish, S.; Powell, C.; Nagai, K.; Qiao, G.; Stevens, G. *Journal of Membrane Science* **2007**, 294, (1-2), 40-49
23. Sanders, D. F.; Smith, Z. P.; Ribeiro, C. P.; Guo, R.; McGrath, J. E.; Paul, D. R.; Freeman, B. D. *Journal of Membrane Science* **2012**, 409-410, 232-241
24. Suzuki, T.; Yamada, Y.; Itahashi, K. *Journal of Applied Polymer Science* **2008**, 109, (2), 813-819
25. Matsumoto, K.; Xu, P. *Journal of Membrane Science* **1993**, 81, (1-2), 23-30
26. Pandiyan, S.; Brown, D.; Neyertz, S.; Van Der Vegt, N. F. A. *Macromolecules* **2010**, 43, (5), 2605-2621
27. Kawakami, H.; Nakajima, K.; Shimizu, H.; Nagaoka, S. *Journal of Membrane Science* **2003**, 212, (1-2), 195-203
28. Neyertz, S.; Brown, D.; Pandiyan, S.; Van Der Vegt, N. F. A. *Macromolecules* **2010**, 43, (18), 7813-7827
29. Neyertz, S.; Brown, D. *Macromolecules* **2013**, 46, (6), 2433-2449
30. Kim, J. H.; Koros, W. J.; Paul, D. R. *Journal of Membrane Science* **2006**, 282, (1-2), 32-43
31. Cui, L.; Qiu, W.; Paul, D. R.; Koros, W. J. *Polymer* **2011**, 52, (24), 5528-5537
32. Liu, Y.; Wang, R.; Chung, T. S. *Journal of Membrane Science* **2001**, 189, (2), 231-239
33. Ma, C.; Koros, W. J. *Industrial and Engineering Chemistry Research* **2013**, 52, (31), 10495-10505
34. Eguchi, H.; Kim, D. J.; Koros, W. J. *Polymer (United Kingdom)* **2015**, 58, 121-129
35. Kawakami, H.; Mikawa, M.; Nagaoka, S. *Journal of Membrane Science* **1996**, 118, (2), 223-230
36. Duthie, X.; Kentish, S.; Pas, S. J.; Hill, A. J.; Powell, C.; Nagai, K.; Stevens, G.; Qiao, G. *Journal of Polymer Science, Part B: Polymer Physics* **2008**, 46, (18), 1879-1890
37. Swaidan, R.; Ghanem, B.; Litwiller, E.; Pinnau, I. *Journal of Membrane Science* **2015**, 475, 571-581

38. Raaijmakers, M. J. T.; Hempenius, M. A.; Schön, P. M.; Vancso, G. J.; Nijmeijer, A.; Wessling, M.; Benes, N. E. *Journal of the American Chemical Society* **2014**, 136, (1), 330-335
39. Raaijmakers, M. J. T.; Wessling, M.; Nijmeijer, A.; Benes, N. E. *Chemistry of Materials* **2014**, 26, (12), 3660-3664
40. Raaijmakers, M. J. T.; Ogieglo, W.; Wiese, M.; Wessling, M.; Nijmeijer, A.; Benes, N. E. *Submitted* **2015**,
41. Lichtenstein, T.; Engineering, U. o. R. C. o.; Science, A., *Handbook of Thin Film Materials*. College of Engineering and Applied Science, University of Rochester: 1979.
42. Ogieglo, W.; Wormeester, H.; Wessling, M.; Benes, N. E. *ACS applied materials & interfaces* **2012**, 4, (2), 935-43
43. Ogieglo, W.; van der Werf, H.; Tempelman, K.; Wormeester, H.; Wessling, M.; Nijmeijer, A.; Benes, N. E. *Journal of Membrane Science* **2013**, 437, 313-323
44. Michels, A.; Hamers, J. *Physica* **1937**, 4, (10), 995-1006
45. Besserer, G. J.; Robinson, D. B. *Journal of Chemical & Engineering Data* **1973**, 18, (2), 137-140
46. Baker, R. W., *Membrane Technology and Applications*. 2012.
47. Cui, L.; Qiu, W.; Paul, D. R.; Koros, W. J. *Polymer* **2011**, 52, (15), 3374-3380
48. Sirard, S. M.; Green, P. F.; Johnston, K. P. *J Phys Chem B* **2001**, 105, (4), 766-772
49. Sirard, S. M.; Ziegler, K. J.; Sanchez, I. C.; Green, P. F.; Johnston, K. P. *Macromolecules* **2002**, 35, (5), 1928-1935
50. Wind, J. D.; Sirard, S. M.; Paul, D. R.; Green, P. F.; Johnston, K. P.; Koros, W. J. *Macromolecules* **2003**, 36, (17), 6433-6441
51. Sirard, S. M.; Castellanos, H.; Green, P. F.; Johnston, K. P. *J Supercrit Fluid* **2004**, 32, (1-3), 265-273
52. Wang, J. S.; Kamiya, Y. *Journal of Polymer Science, Part B: Polymer Physics* **2000**, 38, (6), 883-888
53. Visser, T.; Koops, G. H.; Wessling, M. *Journal of Membrane Science* **2005**, 252, (1-2), 265-277
54. Simons, K.; Nijmeijer, K.; Sala, J. G.; van der Werf, H.; Benes, N. E.; Dingemans, T. J.; Wessling, M. *Polymer* **2010**, 51, (17), 3907-3917
55. Tanaka, K.; Kita, H.; Okano, M.; Okamoto, K. i. *Polymer* **1992**, 33, (3), 585-592
56. Wang, J. S.; Naito, Y.; Kamiya, Y. *Journal of Polymer Science, Part B: Polymer Physics* **1996**, 34, (12), 2027-2033
57. Wang, J. S.; Kamiya, Y. *Journal of Membrane Science* **1995**, 98, (1-2), 69-76
58. Perko, T.; Markočič, E.; Knez, Z.; Škerget, M. *Journal of Chemical and Engineering Data* **2011**, 56, (11), 4040-4044
59. Wang, K.; Suda, H.; Haraya, K. *Industrial and Engineering Chemistry Research* **2001**, 40, (13), 2942-2946

Chapter 7

Enzymatically-active, ultrathin pepsin membranes

*This chapter has been adapted from: Raaijmakers, M.J.T., Schmidt, T., Barth, M., Tutus, M., Benes, N.E., Wessling, M. Enzymatically-active, ultrathin pepsin membranes, *Angewandte Chemie International Edition*.*



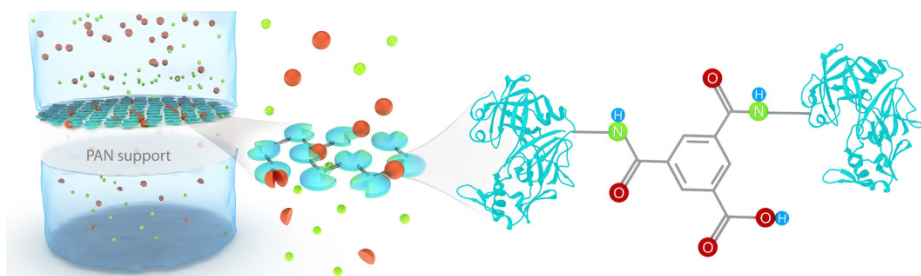
Abstract

Enzymatically active proteins enable efficient and specific cleavage reactions of peptide bonds. Covalent coupling of the enzymes permits immobilization, which in turn reduces autolysis-induced deactivation. Ultrathin pepsin membranes were prepared by facile interfacial polycondensation of pepsin and trimesoyl chloride. The pepsin membrane allows for simultaneous enzymatic conversion and selective removal of digestion products. The large water fluxes through the membrane expedite the transport of large molecules through the pepsin layers. The presented method enables the large-scale production of ultrathin, cross-linked, enzymatically active membranes.

7.1. Introduction

The unique architecture of enzymatic proteins allows for hydrolysis of peptide bonds in mild conditions.¹ The high enzyme specificity and activity are attractive for isolation of peptides and in food upgrading processes. However, enzyme re-usage is complicated by self-cleavage induced deactivation and difficulties in recovery of dilute enzyme solutions used in relevant processes.² Immobilized enzyme can be used instead, potentially reducing deactivation and increasing conversion specificity and activity.³⁻⁸ Enzyme mobility can be restricted by covalent coupling to a substrate or by self-cross-linking of the

enzyme. Enzyme immobilization allows for simultaneous enzymatic conversion and removal of the converted products, while maintaining the enzyme activity of the immobilized proteins.⁹⁻¹¹ The most common approach to achieve enzyme immobilization is formation of a polymer-protein bioconjugate.¹²⁻¹⁴ Current methods to make self-cross-linked freestanding or supported protein layers are based on template or self-assembly assisted crosslinking, generally using glutaraldehyde as cross-linking agent. Examples include freestanding protein films by assembly of proteins on sacrificial cadmium hydroxide templates for controlled drug release or nanofiltration purposes.^{15, 16} More recently, enzymatically active protein films have been prepared based on hierarchical self-assembly of protein-polymer conjugates cross-linked in glutaraldehyde vapor, confirming that the native protein function can remain despite the high degree of covalent bonding between proteins.¹⁷ Nonetheless, the production of freestanding protein films in this manner is not easily scalable and a large amount of precious protein is required for small membrane surface areas.



Scheme 7-1. Schematic representation of the pepsin membrane formation. The pepsin membrane is atop a porous PAN support, represented by the white area. The pepsin membrane consists of pepsin molecules that are randomly cross-linked by TMC, forming amide bridges between the pepsin molecules. The pepsin layer simultaneously acts as enzymatic surface and membrane sieve. The larger molecules are retained by the membrane and selectively cleaved by the pepsin. The large water flux through the membrane increases transport of solute molecules to the membrane surface area and removal of digestion product by membrane permeation.

Here, we propose to use a facile interfacial polycondensation reaction for the production of ultrathin enzymatically active pepsin membranes.¹⁸ Pepsin is a nonspecific acidic endopeptidase that preferentially cleaves proteins at carboxylic groups of aromatic amino acids such as phenylalanine, tryptophan,

leucine and tyrosine.¹⁹ The ultrathin cross-linked pepsin membranes, with a thickness of 50-150 nm, show molecular retention for polyethylene glycol (PEG) at a molecular weight above 10 kDa and exhibit enzymatic activity comparable to pristine pepsin. **Scheme 7-1** shows the schematic representation of the pepsin membrane on top of a porous PAN support (left). The ultrathin pepsin layer allows simultaneous retention and selective cleavage of large molecules. The high water permeability allows for expeditious removal of digestion products.

7.2. Experimental section

Pepsin film formation by interfacial polymerization is achieved using a 0.46 wt% pepsin in phosphate buffered saline (PBS, pH 7) solution and a trimesoyl chloride (TMC) solution in hexane. The pH of the buffer solution, reaction time and reactant concentrations were identified as critical parameters for effective film formation. Optimal pepsin and TMC concentrations were found to be higher than for conventional interfacial polymerization processes. This can be attributed to the large size of the pepsin, low reactivity of the functional groups and the nature of the formed film. In acidic environment the protein reactivity is limited by the high degree of protonated, unreactive ammonia groups. The neutral pH of the PBS buffer is critical for sufficient availability of reactive amines, while preventing permanent pepsin deactivation. Pepsin film formation atop a flat-sheet polyacrylonitril ultrafiltration membrane (PAN, SolSep, Netherlands) was achieved by prewetting the support with the aqueous pepsin solution and subsequent contacting the support with a solution of TMC in hexane.

7.3. Results and discussion

7.3.1. Pepsin film formation

Pepsin film formation was confirmed using X-ray photoelectron spectroscopy (XPS) and attenuated total reflection - Fourier transform infrared spectroscopy (ATR-FTIR). **Figure 7-2 (left panel)** shows the ATR-FTIR absorbance spectrum of pepsin powder and PAN supported ultrathin pepsin membranes prepared with 5 and 15 min reaction time. The absorbance spectra of pepsin membranes show peaks corresponding with the pepsin powder infrared absorbance signature, indicating the nature of the pepsin does not change upon crosslinking. As film formation advances, absorbance bands associated with phenyl rings and amide bonds emerge at 1240 and 1400 cm^{-1} . The intensity of the pepsin related peaks increases with interfacial polymerization reaction

time, which is due to the continued progress of the pepsin film growth. Film growth is sustained by the open character of the formed film that allows for diffusion of the monomer reactant. This is different from conventional interfacial polymerization film formation, where reactant diffusion inhibition limits film growth.²⁰ The scanning electron micrographs shown in **Figure 7-2 (right panel)** substantiate film formation atop the porous PAN support. Whereas the PAN support top view micrograph clearly reveals pores, the pepsin membrane micrographs have the appearance of a dense layer with a distinct morphology that is unlike conventional interfacial polymerization membranes. Layer thickness determined from cross-section micrographs (Appendix, Figure A7-1) is in the range of 50-150 nm.

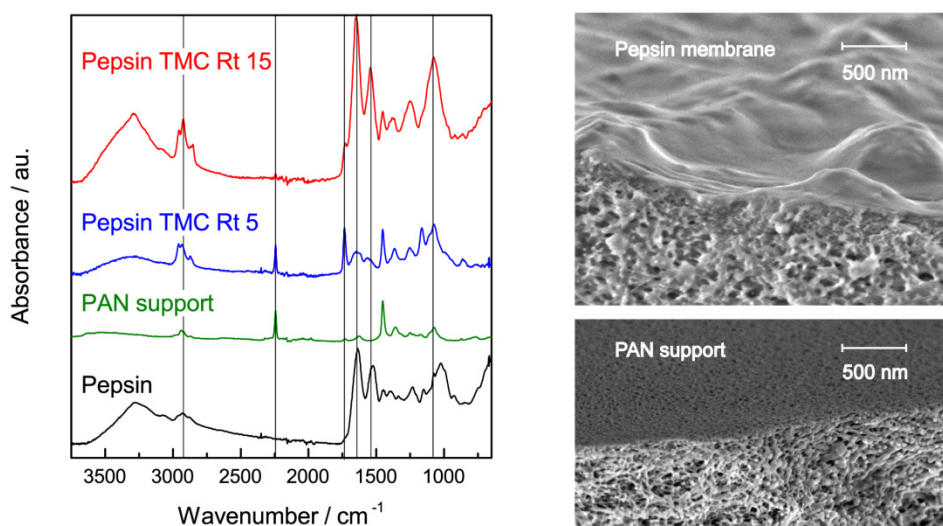


Figure 7-2. (left panel) ATR-FTIR absorbance spectrum of pepsin powder, PAN-PO supported ultrathin pepsin membranes prepared with 5 and 15 min reaction time (Rt). The absorbance peaks around 3000-3500 cm⁻¹ represent the different C-C, C-H and O-H bonds present in the pepsin. Amino acid bonds are located at 1650 (N-H bending) and 1540 (C=O stretching) cm⁻¹. (right panel) Scanning electron micrograph of a pepsin membrane atop a PAN support (top panel) and a bare PAN support (bottom panel). The pores present on the top side of the PAN support are not visible in the pepsin membrane PAN support.

7.3.2. Pepsin layer characterization

A reaction time of 15 min was used to obtain sufficiently thick membranes for further characterization. The degree of pepsin crosslinking by the TMC groups was determined by XPS analysis of the supported films. **Figure 7-3** shows the deconvoluted C1s and O1s binding energy spectrum of pepsin powder and pepsin membranes prepared by reacting presoaked PAN supports with 0.2 and 0.5 wt.% TMC in hexane solutions, respectively. The C1s and O1s binding energy spectrum of the PAN support are given as a reference. The C1s spectra shown in **Figure 7-3 (left panel)** confirm the covalent bond formation between the pepsin and TMC atop the PAN support. The C1s binding energy peak locations of the pepsin membranes at 285, 286.5 and 288 eV, associated with saturated hydrocarbon, amine and amide groups, respectively correspond to the binding energy peaks of the pepsin powder. The increase of the binding energy peak surface area at 285 eV (A) with respect to the 286.5 (B) and 288 eV peaks can be rationalized by an increase in aromatic carbon content. The degree of reaction between the pepsin and TMC can be calculated from the change in the A/B ratio of the C1s peak surface areas. Moreover, the carbon to nitrogen elemental ratio gives an indication of the relative increase in aliphatic carbon in the pepsin membranes. The number of reacted TMC groups per pepsin molecule was estimated to be 40 for the pepsin membrane prepared using 0.2 wt% TMC in hexane. The high degree of crosslinking results in effective immobilization of the pepsin, although it is unlikely that all TMC molecules connect two different pepsin molecules. This is reflected by the C1s binding energy peak at 285.8 eV in the pepsin membrane spectra, associated with carbonyl groups that are formed by reaction of excess acyl chloride groups and water. The membranes prepared using 0.5 wt% TMC in hexane have an estimated 5 reacted TMC groups per pepsin, which is significantly lower than membranes prepared with lower TMC concentrations. This is likely due to the acidification of the aqueous phase upon contact with the excess TMC monomers, hampering the amine group reactivity that is required for effective pepsin polycondensation. The absence of a peak in the pepsin membrane spectra at 287.1 eV, associated with the PAN C1s binding energy spectrum, indicates that the membrane layer thickness is above the X-ray beam penetration depth of ~10 nm. This observation is in accordance with the thickness observed from SEM analysis. The O1s spectra shown in **Figure 7-3 (right panel)** underline the partial conversion of acyl chloride groups to carboxylic acid groups upon interfacial polymerization. The peaks associated with carbonyl (531.5) and hydroxyl groups (532.9 eV) increase with respect to

the amide peaks upon pepsin membrane formation, suggesting that a relatively large fraction of the reactive groups on the TMC are converted to carboxylic acids. Nonetheless, the determination of the fraction of unconnected TMC groups is complicated by the pronounced shift in the fitted binding energy peak maxima and overlap in binding energy peaks of the different functional groups.

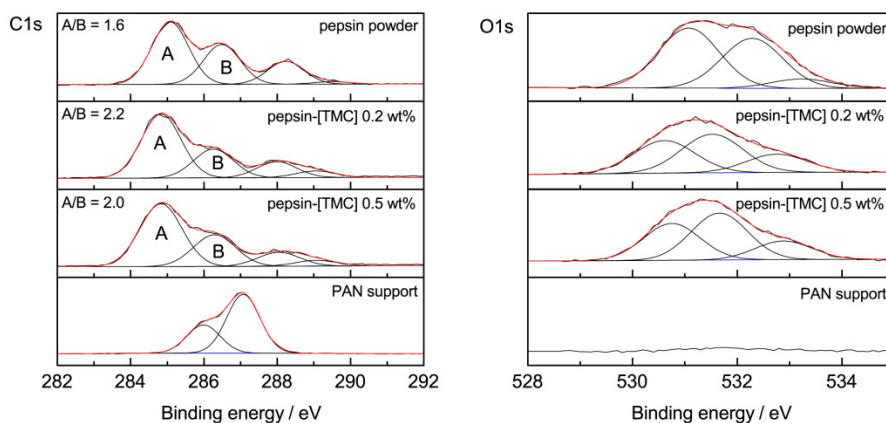


Figure 7-3. Deconvoluted C1s (left panel) and O1s (right panel) spectra of the PAN support, pepsin powder and PAN supported pepsin membranes prepared using 0.2 and 0.5 wt% TMC solutions in hexane with a reaction time of 15 min. The spectra were fitted using Gaussians with similar full width at half maximum (FWHM) values. The complete C1, N1s and O1s binding energy relative peak areas analysis for pepsin powder, the PAN support and pepsin membranes prepared using 0.2 and 0.5 wt% TMC solutions is given in the Appendix.

7.3.3. Assay digestion

Pepsin activity was tested in two consecutive digestion runs using hemoglobin and bovine serum albumin (BSA, fraction V) as substrate, at a temperature of 37 °C and pH 2 (HCl adjusted). Multi angle laser light scattering (MALLS), ultraviolet light absorption (UV) and refractive index (RI) measurements are used to determine protein and digestion product molecular weight distribution. Hemoglobin and BSA digestion kinetics for the TMC cross-linked pepsin membranes on PAN support were compared with pepsin in solution. **Figure 7-4** shows the molecular weight distribution of hemoglobin in solution after different contact times with the pepsin membranes prepared using 0.2 and 0.5 wt.% TMC solutions. The digestion kinetics of pepsin in solution have been determined as a reference (Appendix, Figure A7-3). To determine the

degree of pepsin deactivation, two consecutive assay digestion runs were performed using the same membrane sample. The initial hemoglobin molecular weight distribution, represented by the dotted line at $t=0$, is given by a single peak with a maximum at 36 kDa. After 1 hour, there is a significant decrease in the hemoglobin peak while a second peak at 8 kDa emerges. Further evolution of the molecular weight distribution in time shows a continued decrease of hemoglobin concentration and increase in digestion product concentration. The membranes prepared with a 0.2 wt.% TMC solution show the highest apparent activity. The low activity of the membranes prepared with a 0.5 wt.% TMC solution is likely a result of the lower pepsin reactivity, due to acidification of the aqueous solution during interfacial polymerization.

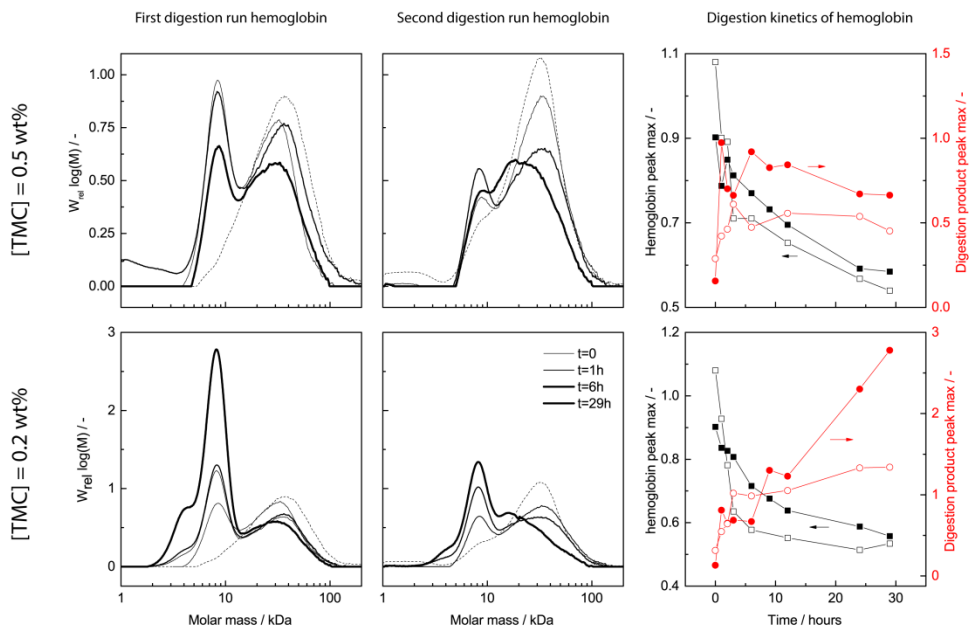


Figure 7-4. Molar mass distribution of hydrolysate products after 1, 6, 29 hours contact of a 1 g L^{-1} hemoglobin solution (pH 2, HCl adjusted) with a pepsin membrane at a temperature of $37 \text{ }^\circ\text{C}$. Two consecutive runs were performed with membranes prepared using 0.5 wt% TMC (top panels) and 0.2 wt% TMC (bottom panels) on PAN support. To see the extent of pepsin deactivation the second runs (middle panels) were performed with the same membrane samples used in the first run (left panels). (right panels) Hemoglobin digestion kinetics as function of time, derived from the hemoglobin peak maximum (■) digestion product peak evolution (●).

Because it is not possible to quantify the amount pepsin in the layer, an exact determination of the degree of deactivation was not possible. However, the hemoglobin digestion for both layers is slightly higher in the second run compared to the first run, indicating that little deactivation occurs over the course of each run (~30 hours each). The digestion product formation, on the other hand, is more pronounced in the first runs (●) compared to the second runs (○). Moreover, the digestion product formation does not correspond to the continuous hemoglobin removal. The undervalued product formation is likely caused by absorption of digestion products to the membranes (Appendix, Figure A7-6). The digestion kinetics of BSA are similar to those measured for hemoglobin (Appendix, Figures A7-4 and A7-5).

7.3.4. Pepsin layer membrane performance

Molecular weight cut-off (MWCO) measurements of pepsin membranes on PAN support were performed using a stirred dead-end permeation cell. The feed and permeate concentrations were sampled to determine degree of retention of PEG molecules with a range of molar masses. The retention was calculated from the ratio of the concentration in the permeate over the concentration in the feed. A more detailed description of the setup is given in the Appendix. Permeation experiments were performed at 2 bar pressure difference using an aqueous feed solution of polyethylene glycol with mean molar masses of 2, 6, 8, 10, 20 and 40 kDa respectively (each fraction 1 g L⁻¹). Permeate composition was sampled after 30, 60, 90 and 120 min. Gel permeation chromatography (GPC) was used for analysis of feed and permeate compositions. **Figure 7-5** displays the molar mass distribution of the feed compared to two membranes prepared with 0.2 and 0.5 wt% TMC solutions, respectively. The flux was around 50 L m⁻² h⁻¹ for all pepsin membranes and around 400 L m⁻² h⁻¹ for the PAN support layer. The concentration of PEG molecules in the feed at 120 min filtration time increases with respect to the initial PEG concentration of the feed. Also, the permeate concentration is lower than the feed concentration. The enrichment of the PEG molecules in the feed implicate that the pepsin membranes retain large molecules. The PAN support without pepsin layer does not show any retention for the same range of PEG molar masses (Appendix, Figure A7-7). The retention data, calculated for a permeation time of 120 min, shows that the membranes prepared with a lower TMC concentration (0.2 wt.%) show a stronger retention of large molecules compared to higher concentrations (0.5 wt.%). The membranes prepared with 0.2 wt.% TMC solution retain 90% of the PEG with a molar

mass above 9.5 kDa. The feed and permeate compositions for the PAN support were the same, implicating that the PEG molecule retention can be ascribed to the ultrathin cross-linked pepsin layer. This is in agreement with the XPS data that suggest a higher crosslink density for the membranes produced using lower TMC concentrations.

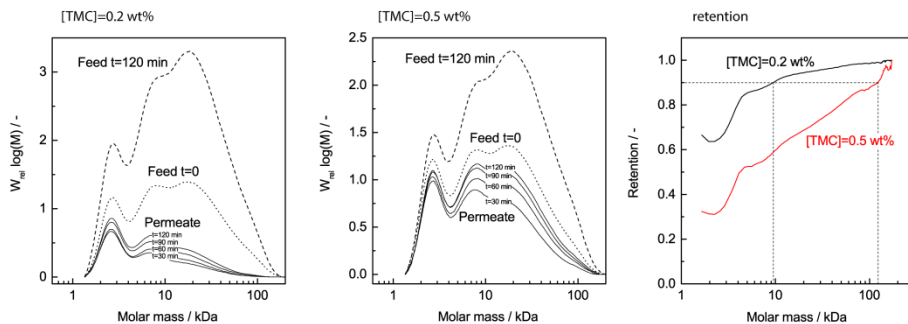


Figure 7-5. Molar mass distribution of the feed at $t=0$ and 120 min and permeate samples taken every 30 min during dead-end filtration of an aqueous PEG solution with a mean molar masses of 2-40 kDa. Permeate compositions of the samples from membranes prepared with 0.2 (left panel) and 0.5 wt% (middle panel) TMC concentrations. (right panel) Retention as a function of PEG molar mass in the permeate fraction calculated from the molar mass distribution. The MWCO of the membranes prepared with 0.2 and 0.5 wt% TMC are 9.5 kDa and 120 kDa, respectively.

The range in which the membranes show retention is in the same range as the molecular weight of the proteins used for the digestion experiments. Integration of the protein thin film on a membrane support would allow for selective removal of enzymatic conversion products, while retaining larger molecules such as proteins.

7.4. Conclusion

In conclusion, we present a method to produce ultrathin pepsin membranes that show persistent enzymatic activity. Further study of the membrane formation process should be considered to determine the degree of active enzymes in the layer and the nanoscale enzyme distribution in the film. The interfacial polymerization technique can easily be applied to other proteins and other covalent organic linkers with different size, number of reactive groups and reactivity.

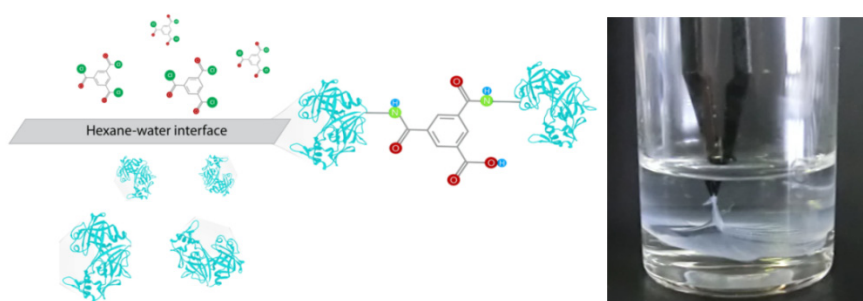
7.5. Acknowledgements

MW, MB and MT acknowledge support through the Alexander von Humboldt Foundation. This work was performed in part at the Center for Chemical Polymer Technology CPT, which is supported by the EU and the federal state of North Rhine-Westphalia (grant no. EFRE 30 00 883 02).

7.6. Appendix

7.6.1. Pepsin film formation

Pepsin film formation by interfacial polymerization is achieved using a 0.46 wt% pepsin (Carl Roth) in phosphate buffered saline (PBS, pH 7) and a trimesoyl chloride (TMC) solution in hexane. TMC concentrations of 0.2 and 0.5 wt% in hexane were used for the synthesis of the pepsin membranes. The membranes were prepared by interfacial polymerization atop porous polyacrylonitril (PAN, SolSep, Netherlands) supports, subsequently presoaked using an ethanol/water (50/50 wt%) and the aqueous pepsin solution. In addition, the interfacial polymerization reaction was performed without the use of a substrate. The formation of a layer at the hexane-water interface could visually be confirmed. The free-standing layer had sufficient mechanical strength to be removed from the interface using tweezers. **Scheme A7-1** shows the formation of a pepsin membrane by polycondensation of amino acid groups and trimesoyl chloride.



Scheme A7-1. (left) Formation of a pepsin membrane by interfacial polycondensation of an aqueous pepsin solution and a TMC solution in hexane. (right) Photograph of a cross-linked pepsin film formed at the hexane-water interface.

Membranes were prepared with various concentrations of pepsin (aq. phase) and TMC (hexane). At low TMC concentrations, no layer formation could be observed by imaging using scanning electron microscopy. Low protein concentrations similarly resulted in absence of clear layer formation. Moreover, one would not expect strong absorption of pepsin on PAN, given that pepsin and the PAN support both have a negative zeta potential at pH 7 (the conditions at which the interfacial polymerization reactions were performed).

7.6.2. Pepsin layer characterization

Scanning electron microscopy

Scanning electron microscopy (SEM) images were obtained using a LEO-1550 Schottky field emission scanning electron microscope (Carl-Zeiss, Germany), with an accelerating voltage of 2.00 kV. The membrane thickness was determined from cross-section micrographs of the PAN supported pepsin membranes.

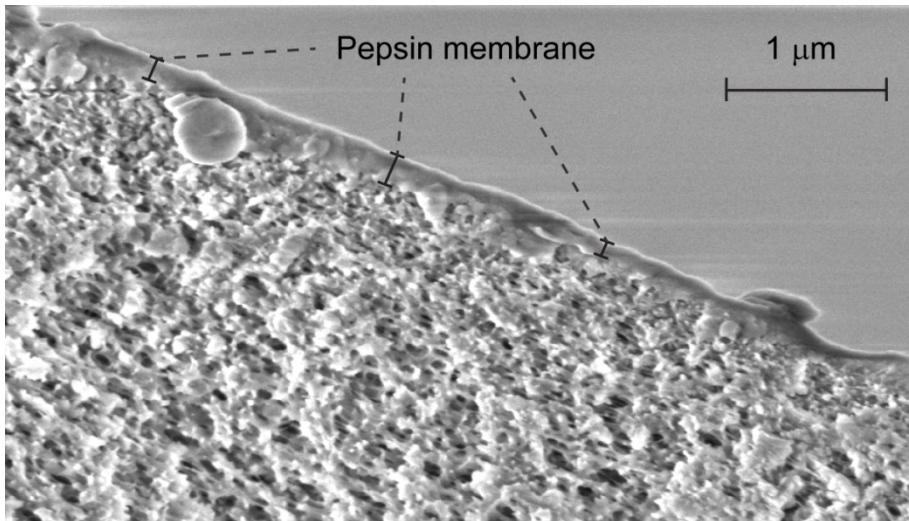


Figure A7-1. Cross-section scanning electron micrograph of a pepsin membrane atop a porous PAN support.

Attenuated Total Reflection Fourier Transform Infrared Spectroscopy

The chemical structures of the pepsin membrane were analyzed with Attenuated Total Reflection Fourier Transform Infrared Spectroscopy (ATR-FTIR) on PAN supported membranes using an ALPHA FT-IR Spectrometer

(Bruker Optics Inc, Germany) equipped with a ZnSe crystal. All spectra were recorded at room temperature. Pepsin films were prepared by interfacial polymerization of aqueous pepsin solution and a 0.2 wt.% TMC solution in hexane, with reaction times of 5 and 15 min.

X-ray photoelectron spectroscopy

XPS (X-ray Photoelectron Spectroscopy) measurements were carried out in an Ultra Axis™ spectrometer, (manufacturer: Kratos Analytical, Manchester UK). The samples were irradiated with monoenergetic Al K^{*1,2} radiation (1486.6 eV) and the spectra were taken at a power of 144 W (12 kV x 12 mA). The aliphatic carbon (C-C, C-H) at a binding energy of 285 eV (C1s photoline) was used to determine the charging. The spectral resolution - i.e., the Full Width of Half Maximum (FWHM) of the Ester carbon from PET - was better than 0.68 eV for the elemental spectra. The information depth is about 10 nm for polymers. The elemental composition of the pepsin membranes, PAN support and pepsin powder are given in **Table A7-1**.

Table A7-1. Elemental composition of pepsin powder, bare PAN support and pepsin membranes on PAN prepared using 0.2 and 0.5 wt% TMC solutions. The element ratios are calculated from the elemental compositions.

Element	Pepsin membrane [TMC] 0.2 wt%	Pepsin membrane [TMC] 0.5 wt%	PAN support	pepsin powder
Elemental fraction (%)				
Na1s	1.09	0.72		
O1s	17.49	15.24	1.52	20.53
N1s	9.76	11.53	21.88	11.16
C1s	70.6	70.56	76.6	66.82
Cl2p	0.49	0.69	-	0.37
Si2p	0.58	1.27	-	0.77
P2p	-	-	-	0.36
Element ratio				
O/N	1.79	1.32	0.07	1.84
C/N	7.23	6.12	3.50	5.99
C/O	4.04	4.63	50.39	3.25

The oxygen/nitrogen/carbon elemental ratios give an indication of the change in composition upon reaction of the TMC with the pepsin. The higher carbon/oxygen of the TMC groups compared to the pepsin powder attributes to the increase in carbon/nitrogen and carbon/oxygen ratio. Surprisingly, the oxygen/nitrogen elemental ratio is lower for the pepsin membranes compared to the pristine membranes. This can be due to a difference in the pepsin hydration state before and after membrane preparation, giving rise to uncertainty in the oxygen content. The carbon/nitrogen elemental ratio was used to estimate the number of TMC groups. The number of reacted TMC groups per pepsin molecule was estimated to be 40 for the pepsin membrane prepared using 0.2 wt.% TMC in hexane. The high number of TMC groups per pepsin molecule substantiates the immobile character of the pepsin in the ultrathin membrane layer. The membranes prepared using 0.5 wt.% TMC in hexane have an estimated 5 reacted TMC groups per pepsin. These results are counterintuitive, as one would expect a higher crosslinking degree for membranes prepared with the higher TMC concentrations. The discrepancy between degree of crosslinking and reactant crosslinking can be rationalized by the acidic nature of the TMC groups. Hydrogen chloride liberated upon contact of TMC with the aqueous solution lowers the pH at the reaction interface, lowering the pepsin reactivity and resulting in a lower degree of crosslinking of the pepsin. This stresses the importance of the reactant stoichiometry for the pepsin membrane properties, and is in line with observations on the importance of reactant ratios in conventional interfacial polymerization processes. The minor fractions of sodium and chloride in the pepsin membrane are attributed to the PBS buffer used to prepare the pepsin solution for interfacial polymerization. It is unlikely that any acid chloride groups have remained on partially unreacted TMC, as the chloride group is readily exchanged with an hydroxyl group upon contact with water.

Figure A7-2 shows the deconvoluted N1s spectra of the PAN support, pristine pepsin powder and PAN supported pepsin membranes prepared using 0.2 and 0.5 wt.% TMC in hexane. The binding energy for nitrogen atoms shifts from 396.98 eV for pristine pepsin to 399 and 401 eV for film 1 and 400 and 401 eV for film 2 respectively. The 397 eV binding energy is typically found for amino acids. The 399-400 eV is associated with the amide bond (N-C=O). The 401 eV is associated with NH-Cl, which can be formed from liberation of HCl upon crosslinking with TMC. H⁺ protonates the amino acids, and simultaneously forms a ionic bond with the Cl.

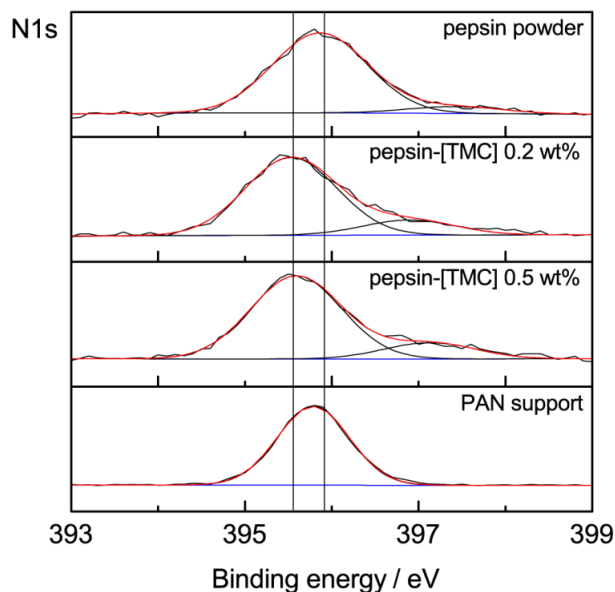


Figure A7-2. Deconvoluted N1s spectra of the PAN support, pristine pepsin powder and PAN supported pepsin membranes prepared using 0.2 and 0.5 wt% TMC in hexane. Both pepsin membranes were prepared using a reaction time of 15 min. The peaks were fitted using Gaussians with similar full width at half maximum (FWHM) values.

Table A7-2, A7-3 and A7-4 show the C1, N1s and O1s binding energy peak deconvolution areas for pepsin powder, PAN support and pepsin membranes prepared using 0.2 and 0.5 wt% TMC solutions. Minor shifts in the binding energy of the functional groups of the pepsin membranes with respect to pepsin are observed. This is likely related to the binding energy peak overlap that complicates the peak fitting procedure.

Table A7-2. C1s binding energy peak deconvolution for pepsin powder, bare PAN support and pepsin membranes on PAN prepared using 0.2 and 0.5 wt% TMC solutions. The functional group associated with the binding energies are in accordance with literature values.²¹

C1s binding energy peak deconvolution							
Binding energy	pepsin powder	PAN support	Binding energy	Pepsin-[TMC] 0.2 wt%	Pepsin-[TMC] 0.5 wt%	Functional group	
eV	peak surface area		eV	peak surface area			
285.1	49.0	-	284.8	55.7	55.1	C*C	saturated hydrocarbon
286.0	-	32.4	286.0	-	-	C*C-C≡N	saturated hydrocarbon
286.5	31.2	-	286.3	24.9	27.8	NH ₂	amine
287.1	-	67.6	287.1	-	-	C*C≡N and C≡N	nitril
288.2	17.9	-	288.0	13.7	12.2	N-C=O	amide
289.5	2.0	-	289.1	5.7	5.0	COOH	carboxylic acid

Table A7-3. N1s binding energy peak deconvolution for pepsin powder, PAN support and pepsin membranes on PAN prepared using 0.2 and 0.5 wt% TMC solutions. The functional group associated with the binding energies are in accordance with literature values.²¹

N1s binding energy peak deconvolution							
Binding energy	pepsin powder	PAN support	Binding energy	Pepsin-[TMC] 0.2 wt%	Pepsin-[TMC] 0.5 wt%	Functional group	
eV	peak surface area		eV	peak surface area			
527.5	50.9	-	527.0	36.9	35.9	N-C=O	amide
528.7	42.2	-	528.3	42.8	45.7	OH	hydroxyl
529.7	6.9	-	528.9	20.3	18.4	C=O	carboxyl

Table A7-4. O1s binding energy peak deconvolution for pepsin powder, bare PAN support and pepsin membranes on PAN prepared using 0.2 and 0.5 wt.% TMC solutions. The functional group associated with the binding energies are in accordance with literature values.²¹

N1s binding energy peak deconvolution							
Binding energy	pepsin powder	PAN support	Binding energy	Pepsin-[TMC] 0.2 wt.%	Pepsin-[TMC] 0.5 wt.%	Functional group	
eV	peak surface area		eV	peak surface area			
395.9	92.1	-	395.5	83.8	83.7	NH ₂	amine
395.8	-	100	395.8	-	-	C≡N	nitril
397.4	7.9	-	397.0	16.2	16.3	N-C=O	amide

7.6.3. Assay digestion

Assay digestion by the pepsin membranes on PAN and pepsin in solution were performed using hemoglobin (Horse, DWI Aachen, 36 kDa, 1 g L⁻¹) and bovine serum albumin (BSA, Sigma-Aldrich, fraction V, 66 kDa, 1 g L⁻¹). Control reactions were performed with pepsin in solution (Stock 5 g L⁻¹, final conc. 0.3 g L⁻¹) mixed with the solutions of hemoglobin and BSA respectively. All experiments were performed at 37 °C, in a pH 2 adjusted 0.2M buffer solution of sodium acetate (NaAc trihydrate, Merck). Samples were taken at set sampling intervals. The sample volume was cooled to room temperature and the pH was raised to pH 7 using sodium hydroxide (0.1 M) to quench the digestive process. The composition of the digested assays was determined using gel permeation chromatography equipped with a Superose column (Superose 6 10/300 GL, GE Healthcare, USA). Multi angle laser light scattering (MALLS), ultraviolet light absorption (UV) and refractive index (RI) measurements were used to determine the molar mass distribution. The calibration curve for the Superose column was performed using 100 µL injects of solutions of Vitamin B12 (13 mg L⁻¹), Insulin human (9 mg L⁻¹), Ovalbumin C (8 mg L⁻¹), Ribonuclease A (4 mg L⁻¹), Myoglobin (3 mg L⁻¹), Ovalbumin (6 mg L⁻¹), β-lactoglobulin (14 mg L⁻¹), Covalbumin (2 mg L⁻¹), Blue Dextran (12 mg L⁻¹). The dn/dc values of BSA (0.1578), dextran (0.147) and casein (0.1880) were used.

Digestion by pepsin in solution occurs by preferential cleavage of phenylalanine, tryptophan, leucine and tyrosine in position P1 or P1'.¹⁹ Cleavage is more specific at pH 1.3, where pepsin preferentially cleaves at

phenylalanine and leucine in position P1 with negligible cleavage for all other amino acids in this position. This specificity is lost at pH >2. **Figure A7-3 (left panel)** shows the molar mass distribution of a 1 g L⁻¹ hemoglobin solution (pH 2, HCl adjusted) and pepsin at a temperature of 37 °C after 0, 1, 6, 29 hours. The initial molar mass distribution, represented by the dotted line at t=0, is given by a single peak with a maximum at 50 kDa, corresponding to the hemoglobin. After 5 min, a significant decrease in the hemoglobin peak is observed, while a second peak emerges at 29 kDa. The M_w values are shifted to higher than hemoglobin in solution (36 kDa), because of residual pepsin in the solution. Further evolution of the molar mass distribution in time shows a continued decrease of hemoglobin concentration and increase in digestion product concentration. **Figure A7-3 (right panel)** shows the hemoglobin digestion kinetics as function of time, derived from the peak maximum evolution as function of time.

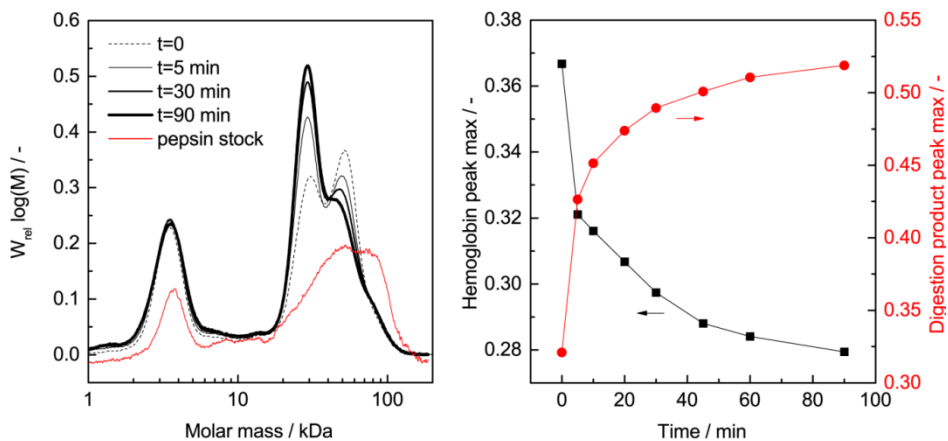


Figure A7-3. (left panel) Molar mass distribution of a 1 g L⁻¹ hemoglobin solution (pH 2, HCl adjusted) and pepsin at a temperature of 37 °C after 0, 5, 30, 90 min. **(right panel)** Hemoglobin digestion kinetics as function of time, derived from the peak maximum evolution as function of time. The hemoglobin peak evolution (■) and digestion product peak evolution (●) show pseudo-first order reaction kinetics.

The hemoglobin peak evolution (■) and digestion product peak evolution (●) show pseudo-first order reaction kinetics. The increase in digestion product peak corresponds to the decrease in hemoglobin peak intensity, suggesting that hemoglobin is preferably cleaved at a single location.

Figure A7-4 (left panel) shows the molar mass distribution of a 1 g L⁻¹ BSA solution (pH 2, HCl adjusted) and pepsin at a temperature of 37 °C after 0, 1, 6, 29 hours. Membrane surface areas of the samples were; 2.6 x 5.4 cm = 14.04 cm² (BSA, [TMC] = 0.5wt%); A = 2.8 x 5.4 cm = 15.12 cm² (Hemoglobin, TMC 0.5wt%); 2.3 x 5.5 cm = 12.65 cm² (BSA [TMC] = 0.2 wt.); 2.3 x 5.5 cm = 12.65 cm² (Hemoglobin, [TMC] = 0.2 wt.%). The initial molar mass distribution, represented by the dotted line at t=0, is given by a single peak with a maximum at 66 kDa, corresponding to the pristine BSA molar mass. After 5 min, a significant decrease in the BSA peak can be observed, while a peak at 44 kDa emerges. An additional broad peak with a maximum around 20 kDa emerges. Further evolution of the molar mass distribution in time shows a continued decrease of BSA concentration and increase in digestion product concentration. **Figure A7-4 (right panel)** shows the BSA digestion kinetics as function of time, derived from the peak maximum evolution as function of time.

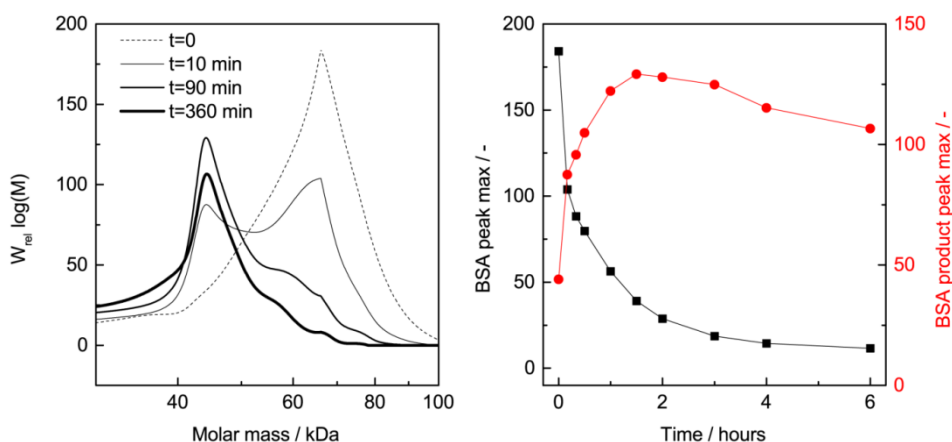


Figure A7-4. (left panel) Molar mass distribution of a 1 g L⁻¹ hemoglobin solution (pH 2, HCl adjusted) and pepsin at a temperature of 37 °C after 0, 1, 6, 29 hours. **(right panel)** Hemoglobin digestion kinetics as function of time, derived from the peak maximum evolution as function of time. The hemoglobin peak evolution (■) and digestion product peak evolution (●) show pseudo-first order reaction kinetics.

The BSA peak evolution (■) and hydrolysate product peak evolution (●) initially show pseudo-first order reaction kinetics. After long digestion times the 44 kDa peak starts to decrease again, suggesting a number of cleavage routes are responsible for the digestion of BSA. The non-specific digestion of

BSA at these conditions is in good agreement with the limited specificity of pepsin at pH 2.

Figure A7-5 shows the molar mass distribution of a 1 g L⁻¹ BSA solution (pH 2, HCl adjusted) after 0, 1, 6 and 29 hours contact with a pepsin membrane at a temperature of 37 °C.

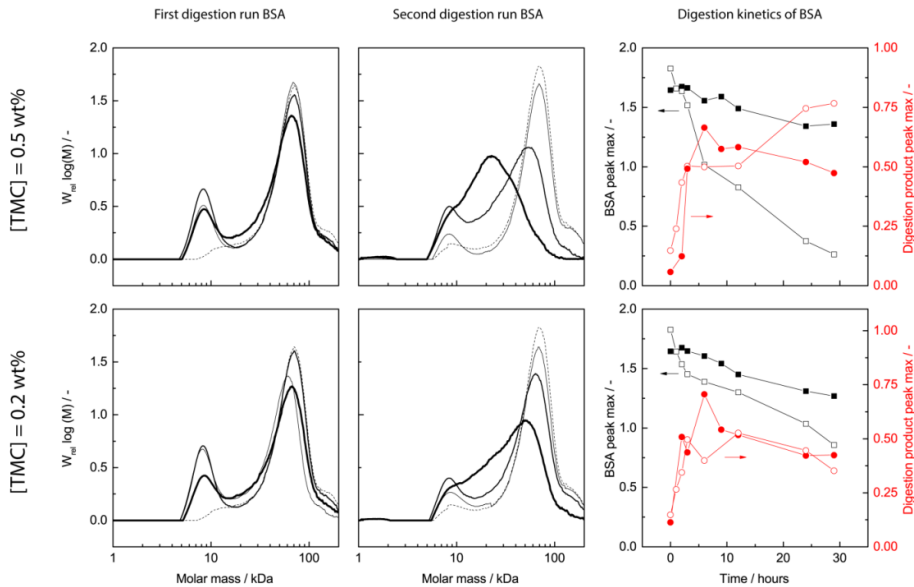


Figure A7-5. Molar mass distribution of a 1 g L⁻¹ BSA solution (pH 2, HCl adjusted) after 0, 1, 6 and 29 hours contact with a pepsin membrane at a temperature of 37 °C. Two consecutive runs were performed with membranes prepared using 0.5 wt.% TMC (top panels) and 0.2 wt.% TMC (bottom panels) on PAN supports. The second runs (middle panels) were performed with the same membrane samples used in the first run (left panels), to see the extent of pepsin deactivation. (right panels) The BSA digestion kinetics derived from the peak maximum evolution as function of time. The first run (●) shows a more pronounced evolution of degradation product than the second run (○). The hemoglobin peak evolution (■) on the other hand, shows a lower digestion rate for the first run than the second run (□).

Two consecutive runs were performed with membranes prepared using 0.2 wt.% TMC (top panels) and 0.5 wt.% TMC (bottom panels) on PAN supports. The second runs (middle panels) were performed with the same membrane samples used in the first run (left panels), to see the extent of pepsin deactivation. The BSA digestion kinetics (right panels) are derived from the

peak maximum evolution as function of time. The first run (●) shows a more pronounced evolution of degradation product than the second run (○). The hemoglobin peak evolution (■) on the other hand, displays a lower digestion rate for the first run compared to the second run (□).

Hemoglobin and BSA digestion by the pepsin membranes shows similar pseudo-first order digestion kinetics. However, the hemoglobin and BSA digestion product peaks shown in Figure 3 and **Figure A7-5** do not show a corresponding increase in the digestion products. Visual observation of the membranes used for the assay digestion experiments revealed adsorption of digestion products. **Figure A7-6** shows a PAN supported pepsin membrane after 29 hours of contact with hemoglobin in solution at a temperature of 37 °C and pH 2 (HCl adjusted). The brown color originates from the hemoglobin digestion products that are adsorbed onto the membrane layer. The brownish colored layer could not be rinsed off with water. Energy-dispersive X-ray spectroscopy (EDX) analysis of the membranes showed the presence of iron atoms that originates from the hemoglobin and its digestion product, underlining the visual observations of Figure A7-6.



Figure A7-6. PAN supported pepsin membrane after 29 hours of contact with hemoglobin in solution at a temperature of 37 °C and pH 2 (HCl adjusted). The brown color originates from the hemoglobin digestion products that are adsorbed into the membrane layer.

7.6.4. Pepsin layer membrane performance

Molecular weight cut-off (MWCO) measurements were evaluated using an aqueous solution of polyethylene glycols with mean molar masses of 2, 6, 8, 10, 20 and 40 kDa respectively (each fraction 1 g L⁻¹). Gel permeation chromatography (GPC) was used for analysis of feed and permeate

compositions. **Figure A7-7 (left panel)** shows the molar mass distribution of a PEG solution of 2, 6, 8, 10, 20 and 40 kDa. The higher molar mass PEG's have a higher molar mass than specified by the manufacturer. **Figure A7-7 (right panel)** shows the molar mass distribution of the feed, permeate and retentate samples taken after 15 min dead-end filtration with the PAN support using an aqueous PEG solution with a mean molar masses of 2-40 kDa. There is no significant difference between the feed and permeate compositions, implicating that the PAN support has negligible PEG retention and a MWCO higher than 100 kDa.

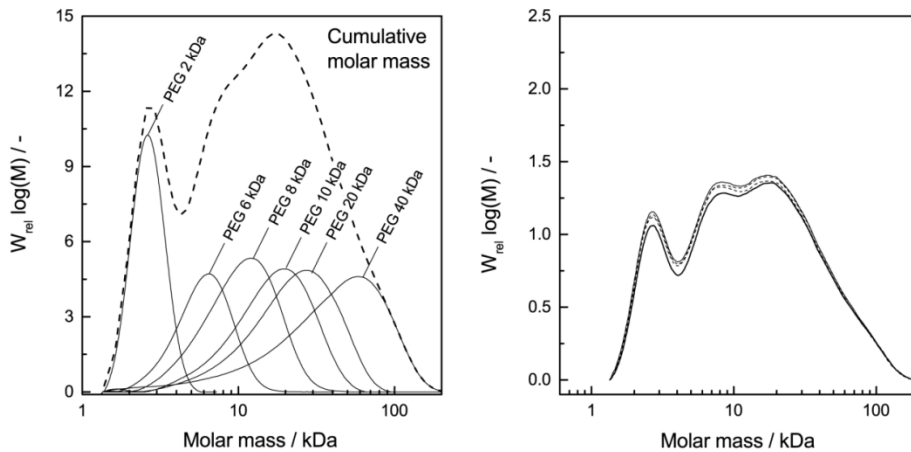


Figure A7-7. (left panel) Molar mass distribution of a PEG solution of 2, 6, 8, 10, 20 and 40 kDa. (right panel) Molar mass distribution of the feed and permeate samples taken after 15 min dead-end filtration with the PAN support using an aqueous PEG solution with a mean molar masses of 2-40 kDa.

The membrane dead-end permeation setup is shown in **Figure A7-8**. The feed solution is supplied to the stirred dead-end permeation cell by pressurizing a PEG solution in a feed tank using nitrogen back-pressure.

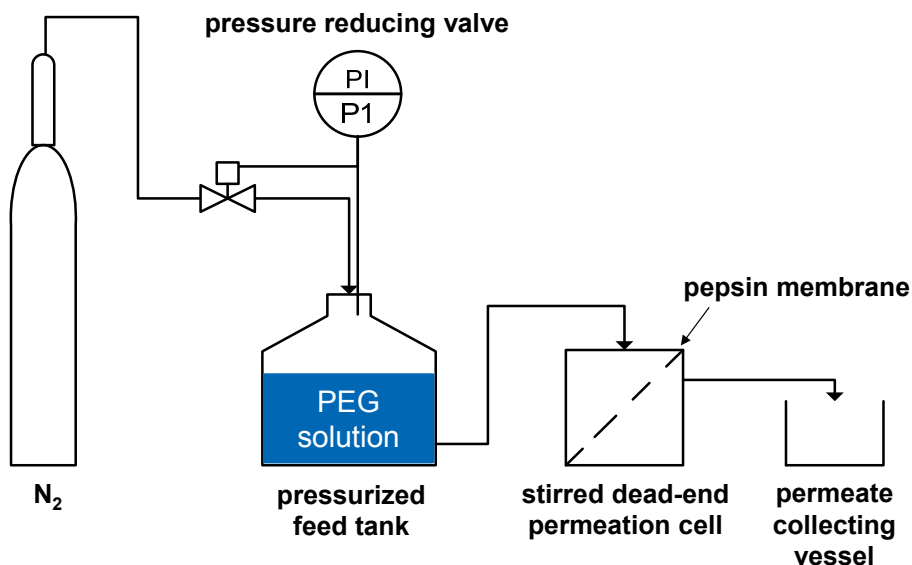


Figure A7-8. Schematic representation of the membrane dead-end permeation setup.

The permeated volume in the stirred dead-end permeation cell is replaced by the PEG solution from the feed tank. Because the PEG molecules are retained by the membrane, the concentration of PEG in the feed increases. The permeate collecting vessel, pressurized feed tank and stirred dead-end permeation cell are sampled for molar mass determination using GPC

7.7. References

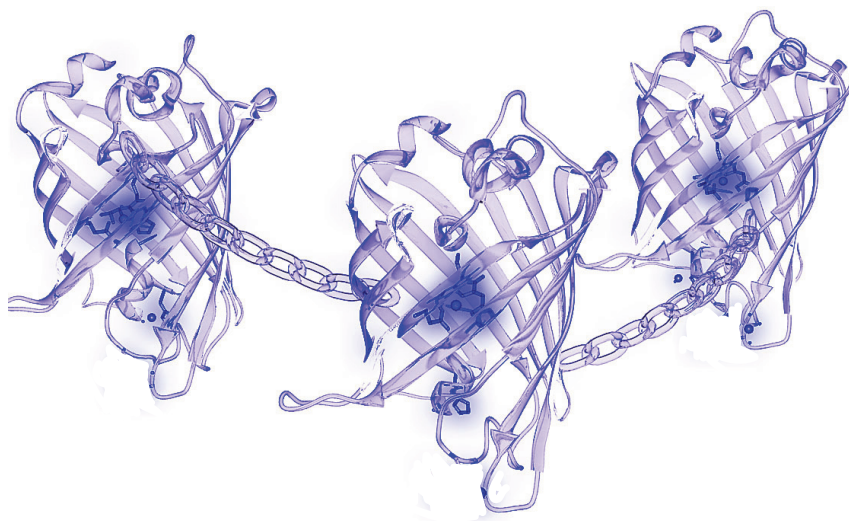
1. Rao, M. B.; Tanksale, A. M.; Ghatge, M. S.; Deshpande, V. V. *Microbiology and Molecular Biology Reviews* **1998**, 62, (3), 597-635
2. Qiao, Y.; Gumpertz, M.; Van Kempen, T. *Journal of Food Biochemistry* **2002**, 26, (4), 355-375.10.1111/j.1745-4514.2002.tb00759.x
3. Chaitali, P. D.; Bahadur, A.; Shah, B. A. *Cellulose Chemistry and Technology* **1997**, 31, (5-6), 315-320
4. Phadtare, S.; Vinod, V. P.; Wadgaonkar, P. P.; Rao, M.; Sastry, M. *Langmuir* **2004**, 20, (9), 3717-3723
5. Shukla, S. P.; Devi, S. *Journal of Applied Polymer Science* **2005**, 96, (5), 1544-1549
6. Hu, J.; Li, S.; Liu, B. *Biotechnology Journal* **2006**, 1, (1), 75-79
7. Li, J.; Wang, J.; Gavalas, V. G.; Atwood, D. A.; Bachas, L. G. *Nano Letters* **2003**, 3, (1), 55-58
8. Poojari, Y.; Palsule, A. S.; Clarson, S. J.; Gross, R. A. *Silicon* **2009**, 1, (1), 37-45

9. Broz, P.; Driamov, S.; Ziegler, J.; Ben-Maim, N.; Marsch, S.; Meier, W.; Hunziker, P. *Nano Letters* **2006**, 6, (10), 2349-2353
10. Palivan, C. G.; Fischer-Onaca, O.; Delcea, M.; Itel, F.; Meier, W. *Chemical Society Reviews* **2012**, 41, (7), 2800-2823.10.1039/C1CS15240H
11. Nardin, C.; Widmer, J.; Winterhalter, M.; Meier, W. *European Physical Journal E* **2001**, 4, (4), 403-410
12. Tao, L.; Xu, J.; Gell, D.; Davis, T. P. *Macromolecules* **2010**, 43, (8), 3721-3727
13. Phadtare, S.; Kumar, A.; Vinod, V. P.; Dash, C.; Palaskar, D. V.; Rao, M.; Shukla, P. G.; Sivaram, S.; Sastry, M. *Chemistry of Materials* **2003**, 15, (10), 1944-1949
14. van Rijn, P.; Tutus, M.; Kathrein, C.; Mougín, N. C.; Park, H.; Hein, C.; Schürings, M. P.; Böker, A. *Advanced Functional Materials* **2014**,
15. Peng, X.; Jin, J.; Ericsson, E. M.; Ichinose, I. *Journal of the American Chemical Society* **2007**, 129, (27), 8625-8633
16. Peng, X.; Jin, J.; Nakamura, Y.; Ohno, T.; Ichinose, I. *Nat Nano* **2009**, 4, (6), 353-357.http://www.nature.com/nnano/journal/v4/n6/supinfo/nnano.2009.90_S1.html
17. Sharma, K. P.; Collins, A. M.; Perriman, A. W.; Mann, S. *Advanced Materials* **2013**, 25, (14), 2005-2010.10.1002/adma.201204161
18. Zhao, J.; Zhang, Y.; Su, Y.; Liu, J.; Zhao, X.; Peng, J.; Jiang, Z. *J. Membr. Sci.* **2013**, 445, 1-7
19. Keil, B., *Specificity of proteolysis*. Springer-Verlag Berlin-Heidelberg-NewYork: 1992; p 335.
20. Freger, V. *Langmuir* **2005**, 21, (5), 1884-1894.10.1021/la048085v
21. Beamson, G.; Briggs, D., *High Resolution XPS of Organic Polymers: The Scienta ESCA300 Database*. John Wiley & Sons: 1992.

Chapter 8

Fluorescent protein thin films via interfacial polymerization

This chapter has been submitted for publication: Raaijmakers, M.J.T., Iyer, A., Subramaniam, V., Blum, C., Wessling, M., Benes, N.E., Fluorescent protein thin films by interfacial polymerization.



Abstract

We report the interfacial polymerization of proteins into a thin all-protein film with preservation of protein functionality. The intrinsic fluorescence of visible fluorescent proteins (VFPs) allows for visualization of their structural integrity upon cross-linking. The cross-linked fluorescent protein films made of EGFP and mRFP display a high degree of immobilization. The retention of significant fluorescence demonstrates that interfacial polymerization of proteins can be performed without major loss of the protein structural integrity. This proof that the protein tertiary structure is preserved during the film fabrication into all-protein films encourages the fabrication of new functional biomacromolecular thin films without the need for embedding of the protein into a protein-polymer conjugate.

8.1. Introduction

Hybrid assemblies of proteins permit design of interfaces with complex biological functionalities.^{1, 2} Covalent immobilization of the proteins in a thin film is generally achieved by self-organization of the proteins at a suitable interface, followed by cross-linking using reagents such as glutaraldehyde.³ Examples include free-standing, highly water permeable, protein films by assembly of proteins on sacrificial cadmium hydroxide templates⁴ and free-standing fluorescent and enzymatic protein layers prepared via a partial charge-neutralization self-assembly mechanism.⁵ The protein functionalities are expressed by their biological activity,⁶ switchable properties as function of the surrounding medium^{7, 8} and biocompatibility.⁹ The unique properties of these layers originate from the interplay between the protein functionality and their nanoscale assembly. Cross-linking the proteins into the integral films while maintaining protein functionality is however difficult: the immobilization is mainly based on conjugation of the proteins using block-copolymers^{10, 11} and Pickering emulsions.^{11, 12} Both methods have limitations with respect to scalability towards the synthesis of thin films with large lateral dimensions. Moreover, typical cross-linking agents such as glutaraldehyde can affect protein function^{5, 13} and require accurate control of the process conditions for successful layer formation.³ Non-covalent strategies have been used to immobilize proteins without affecting their native conformation. Examples include the immobilization of EGFP by layer-by-layer assembly¹⁴ and nanoparticles¹⁵. Challenges of such non-covalent methods arise from limited binding capability of the protein structure to its surrounding, limiting the protein immobilization capability within the layer.¹⁴ Large-scale thin protein layer preparation, with preservation of the protein functionality upon immobilization, remains a major challenge. The techniques used for templating and cross-linking of proteins are relatively time-consuming and not easily scalable. These issues can potentially be overcome by using interfacial polymerization, a technique used for large-scale production of ultrathin films. The technique is based on the rapid polycondensation reaction that occurs at the interface of two immiscible liquids containing two reactive monomers.¹⁶ Commonly used monomers include diamines as aqueous phase reactant and acid chlorides in the organic phase. The reaction is used on large industrial scale to produce most of the desalination membranes. Recently, it was extended to more intricate reactions producing interfacially polymerized POSS-amides, POSS-imides and pepsin.¹⁷⁻²⁰ Interfacial polymerization of

proteins has also been demonstrated by polycondensation of bovine serum albumin⁸ and copolymerization of aquaporin with conventional m-phenyl diamine.²¹ However, it is unclear to what extent the protein structural integrity and functionality is influenced by the polymerization reaction. While pepsin maintained some of its enzymatic activity, the extent to which other proteins maintain their functionality is unknown. Here, we used the intrinsic fluorescence of visible fluorescent proteins (VFPs) to demonstrate the retention of structural integrity of the proteins upon cross-linking. VFPs possess a fluorophore that can absorb and emit light in a range of excitation and emission wavelengths. In VFPs the protein backbone forms a well-defined β -barrel structure around the fluorophores, whose structural integrity is essential for effective fluorescence emission. Denaturing the protein, resulting in destruction of the β -barrel structure, causes a loss of fluorescence.^{22, 23} More subtle changes in the protein encapsulating the fluorophore result in changes in measurable photophysical properties (spectra, lifetimes) of the fluorophore.²⁴⁻²⁹ Single molecule experiments have shown that the fluorescence spectra of fluorescent proteins sensitively depend on the exact nature of the nanoenvironment of the fluorophore formed by the protein backbone.^{30, 31} The intrinsic fluorescence of VFPs has thus been used as a convenient reporter of the structural integrity of the proteins.³² When confronted with denaturation or extensive conformational change the fluorophore activity will change or vanish, and is therefore an excellent check for the effect of cross-linking on protein function.

8.2. Experimental section

Film formation was accomplished by interfacial condensation of solutions of the VFPs enhanced green fluorescent protein (EGFP) and monomeric red fluorescent protein (mRFP) in water with and a trimesoyl chloride (TMC) solution in hexane. Hexane (anhydrous 99.8 %, Sigma-Aldrich) and 1,3,5-Benzenetricarboxylic acid chloride (TMC, Sigma-Aldrich) were used as received. EGFP and mRFP were recombinantly produced and purified according to standard protocols.

The TMC was stored and added to hexane in nitrogen atmosphere to prevent any hydrolysis of the acid chloride by moist from the air. Free-standing films were prepared by adding 10 mL of TMC solution in hexane (0.05 wt.%) to 10 mL aqueous protein solution (0.087 wt.%, Tris buffered). The thin films had sufficient mechanical strength to be transferred to a cuvette for fluorescence microscopy analysis. **Figure 8-1** shows the reaction scheme of

TMC and EGFP. Network formation at the interface of two immiscible solvents containing the monomer reactants occurs via a polycondensation reaction.

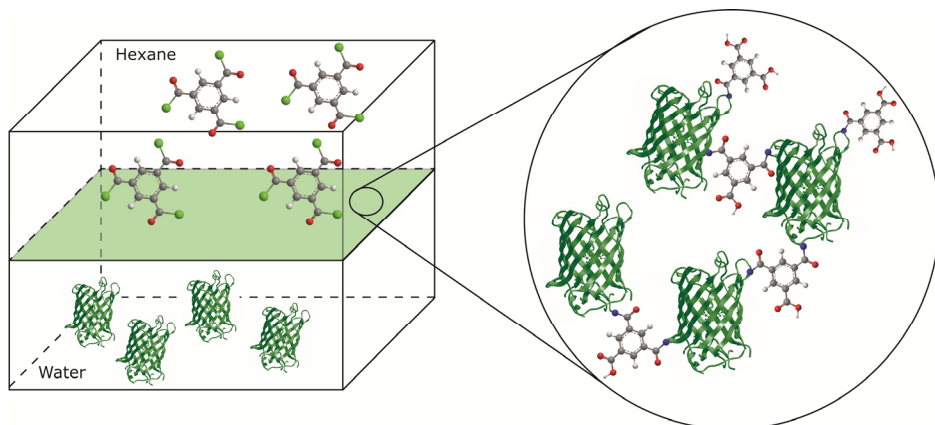


Figure 8-1. Reaction scheme of the interfacial polymerization reaction between EGFP and TMC.

The amine groups of the α -amino acids of the two fluorescent proteins, EGFP and mRFP, are prone to react with trimesoyl chloride (TMC).³³ The abundance of amino acid residues enables high degree of cross-linking, fixating the proteins as a thin film. The TMC can react with one or more proteins, forming a covalent bridge that provides mechanical stability to the film. The films are sufficiently strong to be transferred from the interface to a silicon wafer or a second aqueous phase.

8.2.1. Fluorescence Recovery After Photobleaching

Fluorescence recovery after photobleaching (FRAP) was used to determine the diffusion coefficient within the thin film to gauge the cross linking efficiency. FRAP was performed with a Nikon A1 confocal microscope equipped with a Perfect Focus System. A 100-mW Argon ion laser (488 nm, Coherent, CA) was used to both bleach and monitor the protein fluorescence. In the FRAP experiment fluorescence from a circular region of interest (ROI) was bleached and the increase in fluorescence intensity in the ROI was monitored. Prior to the FRAP experiments the EGFP film was rinsed with Milli-Q water to remove any unreacted protein. During the experiment there was only a minimal drop in the fluorescence intensity in the reference ROI. All FRAP data were fitted using the Soumpasis fit which has been shown to better model

membrane/protein diffusivity than a single exponential fit.³⁴ This provides the diffusion coefficients and mobile fractions of the probed entity.

8.2.2. Excitation and emission

The excitation and emission spectra were measured using a FluoroMax-4 spectrofluorometer (Horiba Jobin Yvon) equipped with a 150 W xenon arc lamp as excitation source. The obtained spectra were analyzed using DAS6 software from Horiba Jobin Yvon. The emission and excitation spectra were recorded for EGFP and mRFP in solution and the interfacial polymerization layer that was cross-linked with TMC. The excitation spectra of EGFP and mRFP were measured by recording the emitted intensity at 510 nm and 610 nm, respectively. The emission spectra of EGFP and mRFP were measured by excitation at 475 nm and 560 nm, respectively.

8.2.3. Lifetime spectroscopy

Fluorescence decays of EGFP and mRFP were recorded by using a custom-built single-photon counting setup. Excitation of EGFP and mRFP by a pulsed laser was done at 475 nm and 560 nm, respectively.³⁵

8.3. Results and discussion

8.3.1. Fluorescence recovery after photobleaching

Upon cross-linking, the fluorescent molecules are immobilized by the covalent bonds between the proteins. The visual appearances of the protein films are light green and red for EGFP and mRFP, respectively. **Figure 8-2 (left panel)** shows the confocal microscopy image of the photobleached circular spot, the non-bleached fluorescent thin film and the background signal as reference. The brighter fluorescent spots in the thin protein layer are likely a result of thickness non-uniformity in the film. The thickness non-uniformity is also observed for conventional interfacial polymerization membranes.^{16, 36} Moreover, the propensity of proteins to lower the surface tension can increase the solubility of reactants in either phase.³⁷ The reactant solubility and interface are known to influence layer morphology.³⁸ **Figure 8-2 (right panel)** shows emitted light intensity from a photobleached spot before and after photobleaching and from a reference spot that was not photobleached. The bleached sample displays an exceedingly slow recovery of fluorescence as a function of time, confirming that the degree of cross-linking between the proteins almost completely immobilizes the proteins. The intensity of a non-bleached sample is added as reference to determine the photobleaching

during measuring. When the intensity data is fitted using a Soumpasis fit model³⁹ averaged over 4 measurements, an estimated immobile fraction of 78% is obtained. The mobile fraction has a diffusion value of $10 \mu\text{m}^2 \text{s}^{-1}$, which is higher than those found for the lateral diffusion of membrane proteins in lipids⁴⁰, but much lower as compared to proteins in solution.⁴¹ This could be indicative of a small fraction of fluorescent proteins that are entrapped in the layer, while being only minimally cross-linked. The low level of recovery allowed for photobleaching of the logos of the MESA⁺ and MIRA institute. The confocal microscopy image demonstrates that even over a long time span of several hours there was only little observable recovery, indicating that the remaining active proteins cannot diffuse back due to their permanent immobilization in the protein network.

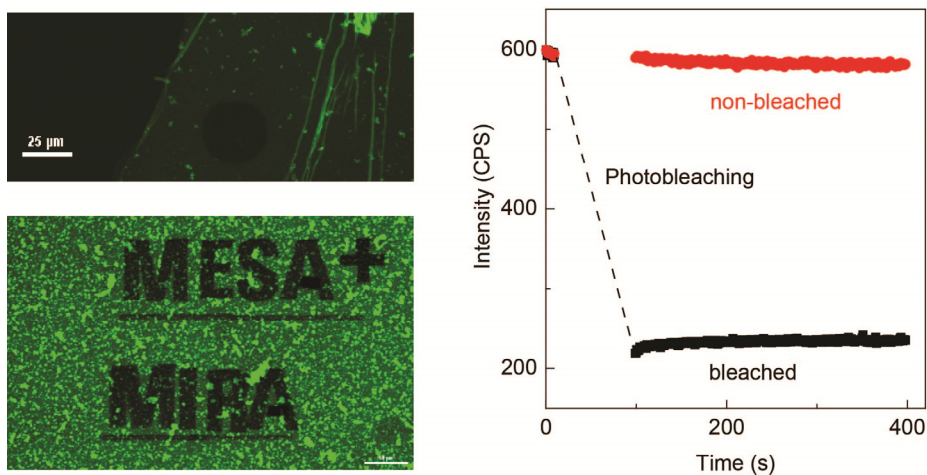


Figure 8-2. (left panel) Confocal microscopy image of a photobleached circular spot and logos of the MESA⁺ Institute for Nanotechnology and MIRA Institute for Biomedical Technology and Technical Medicine. (right panel) Emitted light intensity as function of time before and after photobleaching of a $40 \mu\text{m}^2$ diameter spot.

8.3.2. Fluorescence spectroscopy; excitation and emission

Excitation and emission spectra of TMC cross-linked EGFP and mRFP were taken to determine changes in the nature of the proteins' fluorescence. Changes in the fluorophores or the fluorophores nanoenvironment are known to result in substantial spectral shifts in the excitation and emission maxima. For mRFP, changes in the excitation at lower wavelengths with respect to the excitation maximum can be observed. **Figure 8-3** shows the spectra of EGFP

(left panel) and mRFP (right panel) in solution and after cross-linking. The excitation and emission peaks of EGFP and mRFP in solution are in good agreement with literature.⁴² Upon cross-linking, the excitation peak of EGFP remains at 489 nm and emission peak remain at 508 nm, underlining that structural integrity of the VFP is not compromised. This is in contrast with changes in the excitation spectrum upon glutaraldehyde cross-linking, manifested by a partial conversion of the permanently ionized fluorophore of EGFP to a neutral ionization state.⁵ Small shifts in the excitation and emission maxima have been shown to be related to changes in the surroundings of the protein^{31, 43} Cross-linking clearly changes the protein's environment compared to solution conditions, and we attribute small changes in the spectral maximum positions to the change induced in the environment of the protein and the fluorophore. Similar to EGFP, the excitation peak of mRFP at 580 nm and emission peak at 604 nm remain essentially unchanged after cross-linking. At lower wavelengths, mRFP shows an evident change in the shape of the excitation curve, which might be related to increased exposure of the fluorophore to a more polar environment^{43, 44}. The observed spectral changes indicate that some of the proteins undergo (partial) denaturation upon cross-linking.

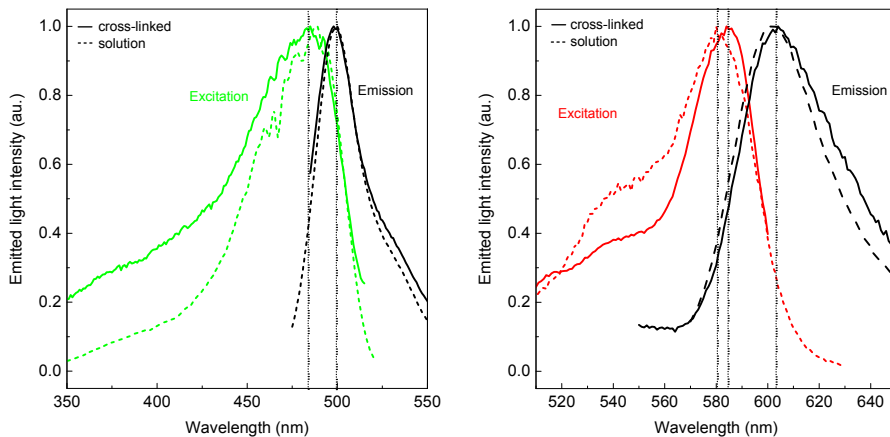


Figure 8-3. Normalized excitation and emission spectra of an EGFP solution and free floating EGFP (left panel) and mRFP (right panel) layers cross-linked with TMC.

8.3.3. Fluorescence lifetime spectroscopy

Fluorescence lifetime spectroscopy was used to probe subtle changes in the protein encapsulating the fluorophore. **Figure 8-4 (left panel)** shows the fluorescence decay of EGFP in solution and of a free-floating EGFP cross-linked layer.

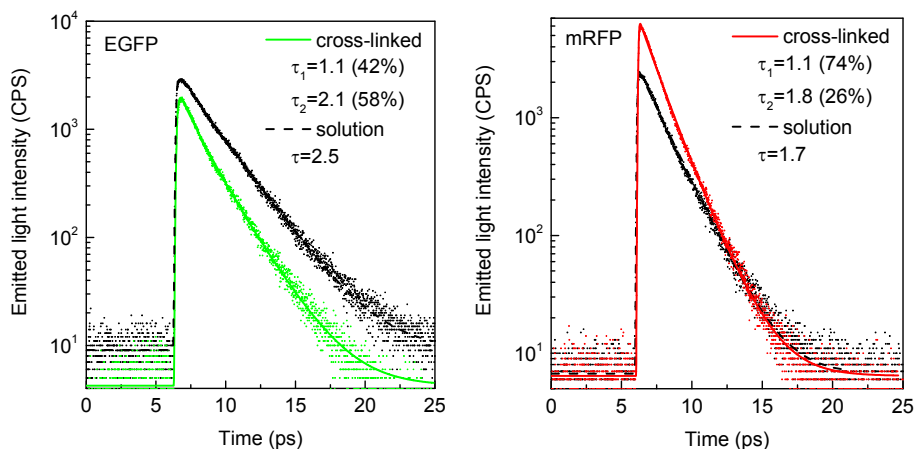


Figure 8-4. Lifetime spectra of an EGFP (left panel) and mRFP (right panel) in solution and cross-linked with TMC.

The intensity loss as function of time, represented by the slope of the fitted emission data, is a measure of the fluorophore lifetime. The lifetime for the EGFP solution is 2.5 ns, which is in accordance with literature values.⁴⁵ After cross-linking with TMC, we observe a decrease in fluorescence lifetime. To determine whether the heterogeneous population of cross-linked EGFP results in a number of different decay rates, we systematically fitted the data with single and multi-exponential decays. The lifetime data from the cross-linked EGFP could not be fitted using a single exponential decay. Fitting with a double exponential function gave lifetimes of 2.1 ns and 1.1 ns. The TMC cross-linked mRFP layers display a similar decrease in fluorophore lifetime, as shown in **Figure 8-4 (right panel)**. We find a double exponential decay with lifetimes of 1.1 and 1.8 nanoseconds for the TMC cross-linked mRFP, and a single exponential decay with lifetime of 1.7 nanoseconds for mRFP in solution. Fitting a third component did not increase the quality of the fit. However, it should be noted that especially the fast component is unlikely to arise from a uniform emitting species, but from a distribution of species of short lifetime.

For both proteins the slow decay component agrees well with the lifetime measured from uncross-linked proteins in solution. The lifetime data thus suggests that the bulk of these proteins is not affected by the cross-linking, and that the structural integrity of these proteins is largely conserved. However, the appearance of a fast decaying component upon cross-linking shows that a fraction of the proteins is affected by the cross-linking and formation of the membrane. We see two possible mechanisms for the appearance of the fast decaying component. First, cross-linking could lead to subtle changes in the chromophore environment. Previous single molecule studies have shown that the emission properties sensitively depend on the nanoenvironment, that is, on the embedding of the fluorophore in the protein barrel. Although fluorescent proteins are known to be very stable, cross-linking might result in stress on the protein barrel that changes the flexibility and chemical environment of the chromophore, leading to the faster non-radiative decay of the fluorophore. Second, the fast decay observed might be related to the formation of quenched, dark fluorophores in the membrane. Denaturation of the fluorescent proteins results in these fully quenched, absorbing, but not emitting fluorophores. The close proximity of the concentrated fluorescent protein network allows for transfer of energy from the excited fluorophores to the dark fluorophores, resulting in the observed short decay component. In practice, both mechanisms are likely to play a role.

8.4. Conclusions

Interfacial polymerization can be used to produce ultrathin protein films without destroying or significantly diminishing the fluorescence of the fluorescent proteins immobilized in the protein network. The fluorescence recovery after photobleaching shows that there is a high degree of cross-linking between the proteins, restricting mobility of proteins within the layer. Fluorophore activity remains, although a fraction of the VFPS in the layer can be dark fluorophores as a result of partial denaturation. The presented method can potentially be extended for fabrication of new functional biomacromolecular thin films without the use of protein conjugates.

8.5. References

1. Tangirala, R.; Hu, Y.; Joralemon, M.; Zhang, Q.; He, J.; Russell, T. P.; Emrick, T. *Soft Matter* **2009**, *5*, (5), 1048-1054
2. Presley, A. D.; Chang, J. J.; Xu, T. *Soft Matter* **2011**, *7*, (1), 172-179

3. Migneault, I.; Dartiguenave, C.; Bertrand, M. J.; Waldron, K. C. *BioTechniques* **2004**, 37, (5), 790-802
4. Peng, X.; Jin, J.; Nakamura, Y.; Ohno, T.; Ichinose, I. *Nat Nano* **2009**, 4, (6), 353-357
5. Sharma, K. P.; Collins, A. M.; Perriman, A. W.; Mann, S. *Advanced Materials* **2013**, 25, (14), 2005-2010
6. Peng, X.; Jin, J.; Ericsson, E. M.; Ichinose, I. *Journal of the American Chemical Society* **2007**, 129, (27), 8625-8633
7. Huang, H.; Yu, Q.; Peng, X.; Ye, Z. *Journal of Materials Chemistry* **2011**, 21, (35), 13172-13179
8. Zhao, J.; Zhang, Y.; Su, Y.; Liu, J.; Zhao, X.; Peng, J.; Jiang, Z. *Journal of Membrane Science* **2013**, 445, 1-7
9. Vaz, C. M.; Fossen, M.; Van Tuil, R. F.; De Graaf, L. A.; Reis, R. L.; Cunha, A. M. *Journal of Biomedical Materials Research - Part A* **2003**, 65, (1), 60-70
10. Lin, Y.; Böker, A.; He, J.; Sill, K.; Xiang, H.; Abetz, C.; Li, X.; Wang, J.; Emrick, T.; Long, S.; Wang, Q.; Balazs, A.; Russell, T. P. *Nature* **2005**, 434, (7029), 55-59
11. Jutz, G.; Böker, A. *Journal of Materials Chemistry* **2010**, 20, (21), 4299-4304
12. Russell, J. T.; Lin, Y.; Böker, A.; Su, L.; Carl, P.; Zettl, H.; He, J.; Sill, K.; Tangirala, R.; Emrick, T.; Littrell, K.; Thiyagarajan, P.; Cookson, D.; Fery, A.; Wang, Q.; Russell, T. P. *Angewandte Chemie - International Edition* **2005**, 44, (16), 2420-2426
13. Chui, W. K.; Wan, L. S. C. *Journal of Microencapsulation* **1997**, 14, (1), 51-61
14. Kozlovskaya, V.; Ankner, J. F.; O'Neill, H.; Zhang, Q.; Kharlampieva, E. *Soft Matter* **2011**, 7, (24), 11453-11463
15. Fuenzalida, J. P.; Weikert, T.; Hoffmann, S.; Vila-Sanjurjo, C.; Moerschbacher, B. M.; Goycoolea, F. M.; Kolkenbrock, S. *Biomacromolecules* **2014**, 15, (7), 2532-2539
16. Freger, V. *Langmuir* **2003**, 19, (11), 4791-4797
17. Dalwani, M.; Zheng, J.; Hempenius, M.; Raaijmakers, M. J. T.; Doherty, C. M.; Hill, A. J.; Wessling, M.; Benes, N. E. *Journal of Materials Chemistry* **2012**, 22, (30), 14835-14838
18. Raaijmakers, M. J. T.; Hempenius, M. A.; Schön, P. M.; Vancso, G. J.; Nijmeijer, A.; Wessling, M.; Benes, N. E. *Journal of the American Chemical Society* **2014**, 136, (1), 330-335
19. Raaijmakers, M. J. T.; Wessling, M.; Nijmeijer, A.; Benes, N. E. *Chemistry of Materials* **2014**, 26, (12), 3660-3664
20. Raaijmakers, M. J. T.; Benes, N. E. *Submitted* **2015**,
21. Zhao, Y.; Qiu, C.; Li, X.; Vararattanavech, A.; Shen, W.; Torres, J.; Hélix-Nielsen, C.; Wang, R.; Hu, X.; Fane, A. G.; Tang, C. Y. *Journal of Membrane Science* **2012**, 423-424, 422-428
22. Ward, W. W.; Bokman, S. H. *Biochemistry* **1982**, 21, (19), 4535-4540
23. Tsien, R. Y. *Annual Review of Biochemistry* **1998**, 67, (1), 509-544
24. Vrzheschch, P. V.; Akovbian, N. A.; Varfolomeyev, S. D.; Verkhusa, V. V. *FEBS Letters* **2000**, 487, (2), 203-208
25. Enoki, S.; Saeki, K.; Maki, K.; Kuwajima, K. *Biochemistry* **2004**, 43, (44), 14238-14248
26. Khan, F.; Kuprov, I.; Craggs, T. D.; Hore, P. J.; Jackson, S. E. *Journal of the American Chemical Society* **2006**, 128, (33), 10729-10737

27. Wielgus-Kutrowska, B.; Narczyk, M.; Buszko, A.; Bzowska, A.; Clark, P. L. *Journal of Physics Condensed Matter* **2007**, *19*, (28),
28. Huang, J. r.; Danny Hsu, S. T.; Christodoulou, J.; Jackson, S. E. *HFSP Journal* **2008**, *2*, (6), 378-387
29. Xie, J. B.; Zhou, J. M. *Biochemistry* **2008**, *47*, (1), 348-357
30. Blum, C.; Meixner, A. J.; Subramaniam, V. *Journal of the American Chemical Society* **2006**, *128*, (26), 8664-8670
31. Schleifenbaum, F.; Blum, C.; Subramaniam, V.; Meixner, A. J. *Molecular Physics* **2009**, *107*, (18), 1923-1942
32. Fabié, L.; Agostini, P.; Stopel, M.; Blum, C.; Lassagne, B.; Subramaniam, V.; Ondarçuhu, T. *Nanoscale* **2015**, *7*, (10), 4497-4504
33. Habeeb, A. F. S. A.; Hiramoto, R. *Archives of Biochemistry and Biophysics* **1968**, *126*, (1), 16-26
34. Seu, K. J.; Cambrea, L. R.; Everly, R. M.; Hovis, J. S. *Biophysical Journal* **2006**, *91*, (10), 3727-3735
35. Blum, C.; Cesa, Y.; Escalante, M.; Subramaniam, V., *Multimode microscopy: spectral and lifetime imaging*. 2009; Vol. 6, p S35-S43.
36. Pacheco, F. A.; Pinnau, I.; Reinhard, M.; Leckie, J. O. *Journal of Membrane Science* **2010**, *358*, (1-2), 51-59
37. Beverung, C. J.; Radke, C. J.; Blanch, H. W. *Biophysical Chemistry* **1999**, *81*, (1), 59-80
38. Zhang, Y.; Benes, N.; Lammertink, R. *Lab on a Chip* **2014**,
39. Soumpasis, D. M. *Biophysical Journal* **1983**, *41*, (1), 95-97
40. Ramadurai, S.; Holt, A.; Krasnikov, V.; van den Bogaart, G.; Killian, J. A.; Poolman, B. *Journal of the American Chemical Society* **2009**, *131*, (35), 12650-12656
41. Petrášek, Z.; Schwille, P. *Biophysical Journal* **2008**, *94*, (4), 1437-1448
42. Shaner, N. C.; Steinbach, P. A.; Tsien, R. Y. *Nature Methods* **2005**, *2*, (12), 905-909
43. Abbyad, P.; Childs, W.; Shi, X.; Boxer, S. G. *Proceedings of the National Academy of Sciences* **2007**, *104*, (51), 20189-20194
44. Dong, J.; Solntsev, K. M.; Tolbert, L. M. *Journal of the American Chemical Society* **2006**, *128*, (37), 12038-12039
45. Jakobs, S.; Subramaniam, V.; Schönle, A.; Jovin, T. M.; Hell, S. W. *FEBS Letters* **2000**, *479*, (3), 131-135

Chapter 9
Reflections & Perspectives

9.1. Introduction

This thesis deals with the design and characterization of novel hybrid (membrane) materials via interfacial polymerization. This chapter reflects on the general structure-property relationships of hybrid materials. In addition, it provides perspectives for future research on membrane material design and the structure-property-performance of hyper-cross-linked, hybrid network materials.

9.2. Reflections

9.2.1. Reflections on hyper-cross-linked, hybrid materials

Here, two types of hybrid materials have been studied: hybrid inorganic-organic network polymers and biological hybrids. Although the structure-properties of these two types of materials are dissimilar, the material concepts are complementary: ultrathin films that consist of hyper-cross-linked networks of two alternating moieties with a distinct functionality. The concept is easily extended towards other new materials, as is illustrated by Figure 9-1.

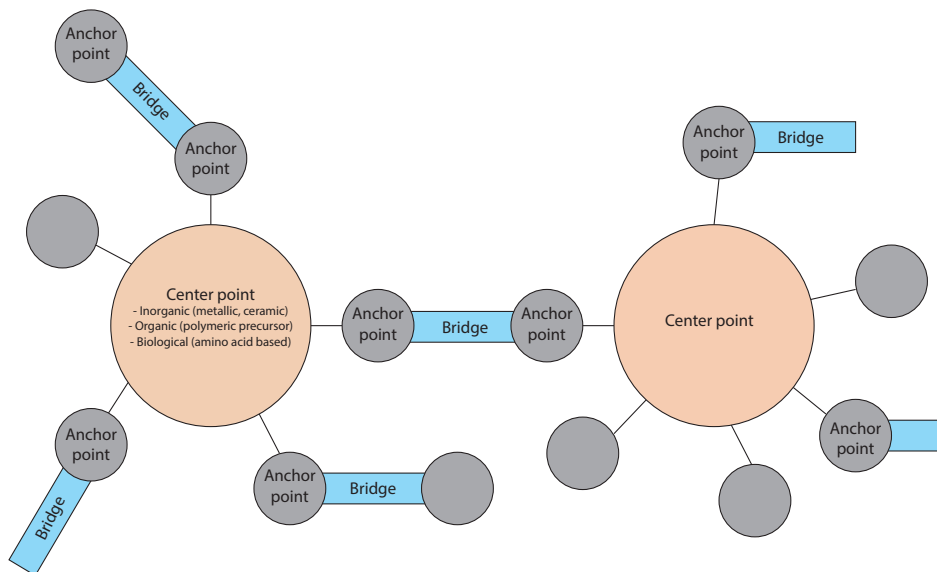


Figure 9-1. Conceptual structure of a hyper-cross-linked, hybrid material. The type of center point, anchor point and bridge moieties can be an inorganic, organic or biological group.

The center point of a hyper-cross-linked material is either an inorganic, organic or biological moiety with a multi-functionality that allows for covalent

bond formation. This includes precursors such as polyhedral oligomeric silsesquioxanes, oligomers such as polyethyleneimine, and proteins. The center points are connected by a bridging moiety via an anchor point, that again have either an inorganic, organic or biological nature. The anchor point connecting the center point and bridging moieties can be any type covalent of bond. The overview on hybrid materials and the current trends in interfacial polymerization chemistry, that is given in Chapter 1, illustrates the broad range of suitable precursors and polymer types. The collection of polymers that can be synthesized via interfacial polymerization includes polyamides, polyurethanes, polyureas, polyanilines, polyimides, and polycarbonates. In addition, the technique has been used to prepare defect-free, ultrathin films of metal organic frameworks, organic-inorganic hybrids, and bio-hybrids. The properties of the center point, anchor point and bridge moieties can be selected to create materials with a distinct structure-property relationship, as is illustrated in Chapters 2-8.

9.2.2. Reflections on structure-property relationships

In this thesis, the selected center points are polyhedral oligomeric silsesquioxanes and proteins. The anchor points are imides (for the POSS based materials) and amides (for the protein based materials). The POSS provides rigidity that is required for membrane separation, while the proteins provide an active functionality (enzymatic or fluorescent activity) to the membrane layer.

Poly(POSS-imide)s

The structure-property relationships of the poly(POSS-imide)s are extensively studied in Chapters 2-6. Chapter 2 and 3 introduce the synthesis of a range of poly(POSS-imide)s. The length and flexibility of the imide bridge, given by the symbol X in Figure 9-2, can be varied by using different precursors during preparation. By doing so, the gas permeance and permselectivity at temperatures between 50-300 °C could be tailored. The systematic change of material structure-properties demonstrates how effective the synthesis approach is for membrane preparation.

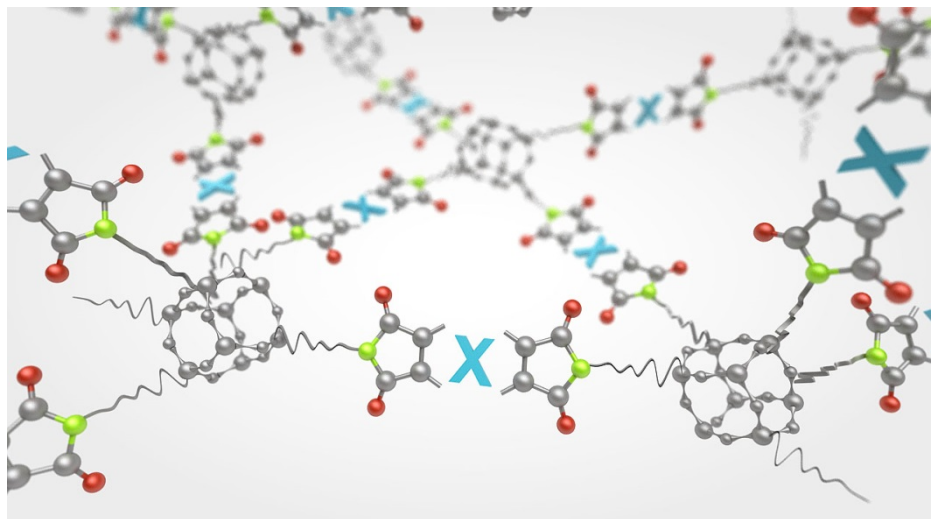


Figure 9-2. Poly(POSS-imide) network that is based on alternating POSS and imide groups.

The differences in structure-property relationships for the different bridges are further emphasized in Chapter 4. The changes in material properties during the heat treatment that is required to convert the poly[POSS-(amic acid)]s into poly(POSS-imide)s depend on the bridge length and flexibility. Moreover, the large change in chemical structure, layer thickness and refractive index demonstrates how important the heat treatment is for the properties of the poly(POSS-imide)s.

The general trend from Chapters 2-4 is clear: poly(POSS-imide)s with short imide bridges are glassy, rigid materials. Even at temperatures up to 300 °C, macromolecular dynamics of the hybrid networks based on short imide bridges is limited. This is illustrated by the relatively small shrinkage during heat treatment of the poly[POSS-(amic acid)]s and the high permselectivities at a broad temperature range. Poly(POSS-imide)s with long, flexible imide bridges display a higher degree of network flexibility. Upon heat treatment, the layers allow for shrinkage that reaches up to 45% of the initial thickness. In addition, permselectivities drop at elevated temperatures due to enhanced macromolecular dynamics. Such observations are in line with other network polymers based on POSS.¹

At elevated temperatures, the Van Der Waals interactions between small non-condensable gases and the membrane material are very small. At ambient temperatures, sorption of gases such as CO₂ and CH₄ plays a larger role in the

gas separation properties. The temperature dependency of gas sorption is illustrated by the low apparent activation energies for CO₂ permeation for a poly(POSS-imide) with an imide bridge that contains fluoroalkanes, shown in Chapter 2. The sorption behavior of the fluoroalkane based poly(POSS-imide) is further elaborated in Chapters 5 and 6. The sorption behavior shows that the characteristics of the poly(POSS-imide)s are distinct from conventional polyimides. The membrane layers sorb large amounts of CO₂ and CH₄, up to an extent that the molar volume of the adsorbed gas exceeds that of the liquid molar volume of these gases. The exceedingly high gas concentrations, at elevated gas pressures, dilute the polymer matrix to such an extent, that the properties of the sorbed gas start to resemble that of the gas phase. The pronounced effect of the high CO₂ sorption capacity is underlined by the increased gas diffusivity with increasing solubility, observed in Chapter 6: the swelling of the polymer decreases the resistance for diffusion, allowing for faster gas permeation.

In summary, the unique characteristics of the poly(POSS-imide)s originate from the hyper-cross-linked network structure. The spacing and molecular flexibility of the network can be adjusted by changing the imide bridge. The introduction of affinity groups such as fluoroalkanes has a pronounced influence on the behavior of the poly(POSS-imide)s. Although this thesis identifies a number of important structure-properties relationships, various questions remain. We have consistently compared to properties of the poly(POSS-imide)s with linear glassy polymers. However, it is not likely that the characteristics of network polymers are comparable to those of linear polymers. Linear glassy polymers display long-range relaxations due to the non-equilibrium state of the glassy state that decrease the free volume content in time. In network polymers, long-range reorganizations are constrained by the high degree of cross-linking, retaining the frozen-in free volume. Moreover, although the sorption isotherms at low concentrations of sorbed gas in the poly(POSS-imide) might resemble the concave sorption isotherm shape of a linear glassy polymer, completely distinct sorption phenomena are observed at high gas concentrations.

Cross-linked protein layers

Cross-linking of proteins via interfacial polymerization into an all-protein layer was performed to immobilize the proteins and to unite the protein activity with membrane performance. Both Chapter 7 and 8 demonstrate that the protein functionality can remain upon cross-linking. Chapter 7

demonstrates that membrane performance and enzymatic activity can be combined into an ultrathin film with thicknesses around 50 nm. The high water flux through the membranes allows for transport to the surface, where retained solutes can be degraded. Chapter 8 demonstrates that most of the proteins are immobilized (about 80%), using similar reaction conditions as for the pepsin layers. The synthesis approach can easily be extended to other proteins, although for each individual protein careful assessment of the stability upon cross-linking is required: some proteins are more prone to unfold as compared to others.

In retrospect, the cross-linker that has been used (trimesoyl chloride) is not the most suitable one. The large number of residual carboxylic acid groups, formed by hydrolysis of unreacted acid chloride groups, indicates that steric hindrance of the proteins plays an important role in the film formation. Longer bridging molecules could potentially improve the cross-linking degree, although inter-molecular bond formation on a single protein could also increase.

The MWCO values are relatively high as compared to other nanofiltration membranes, and further optimization of the interfacial polymerization reaction conditions might be required. A simple way of improving membrane performance is the co-polymerization of other precursors that form membrane layers with a lower MWCO. In the latter case, optimization of reactant reactivity is of importance to obtain membrane layers with a desired protein content.

9.3. Perspectives

9.3.1. Membrane material design for gas separation applications

Design of a membrane material that is suitable for large-scale applications goes beyond the selection of a material with a high permeability and selectivity. Above all, the membrane material is only applicable in a membrane process if the following requirements are met:

- **The membrane material must be suitable for relevant operating conditions.**
- **The technique used to prepare the membranes must be scalable for large surface areas.**

- **Fundamental understanding of structure-property-performance relationships is required to optimize the membrane process performance.**

Literature provides us with a wide array of membrane materials, of which only a very limited number is actually commercialized. In my opinion, it remains relevant to work on the development of new membrane materials. This does not only provide new candidates for membrane separation processes, but it also leads to a better fundamental understanding of the structure-property requirements for desired membrane performance. By systematically characterizing a large number of material candidates, we can come up with design rules for membranes that are fit for large-scale processes. Relevant work has been done in the past, including the realization that membranes display an inherent trade-off between permeability coefficient and selectivity (ref Robeson). The realization that the trade-off can be shifted by playing with the frozen-in free volume content of the material has surged the development of new material concepts such as polymers of intrinsic microporosity (PIMs),²⁻⁵ thermally rearranged (TR) polymers⁶⁻⁹ and substituted polyacetylenes.¹⁰ Nonetheless, a number of membrane design criteria is often overlooked by solely focusing on high permeability and selectivity:

- Permeance is the permeability coefficient divided by thickness. Thus, a membrane needs to be **ultrathin** to minimize the membrane surface area required for permeation.
- The membrane layer must remain stable in the presence of **penetrants** over long periods of time. Particularly **ultrathin films** of highly permeable, high free volume polymers are **prone to changes by physical ageing or plasticization**.
- Permeability depends on temperature. With increasing temperature, the diffusivity increases, but the solubility decreases. Therefore, the **changes in permeability with temperature are not straightforward**.

These criteria impose a set of characteristics on the membrane; the high selectivity and permeability, in combination with long-term stability at high temperatures and high penetrant pressures, can only be accomplished by design of a membrane with an extremely glassy character. The high degree of frozen-in free volume that is required for membrane performance needs to be frozen in by the rigidity of the material matrix. This poses the ultimate challenge: how can we produce a defect-free, ultrathin membrane layer that

has a large, frozen-in free volume. Here, interfacial polymerization is proposed as an ideal starting point to meet the demands of membrane preparation for gas separation applications. The technique allows for preparation of defect-free ultrathin layers that consist of polymer networks. The (hyper-cross-linked, hybrid) polymer network constrains long-range polymer chain reorganizations that are responsible for loss of membrane performance by ageing and plasticization in conventional polymeric membranes.

The preparation and optimization of a hyper-cross-linked network is not straightforward. In this thesis, we have optimized the gas separation performance with a number of parameters: monomer reactant type, concentration and reactivity. In addition, two completely different membrane types (i.e., hybrid inorganic-organic and bio-hybrids) have been prepared. Here, we identify a number of critical parameters that determine the properties of the network.

- **Number of functional groups on each of the reactants.** The degree of branching of the network depends strongly on the number of reactive groups on the monomer reactants. A higher degree of branching can be expected from reactants with a higher number of reactive groups. However, a higher number of reactive groups will also result in more unreacted groups. The poly(POSS-imide)s of Chapters 2-6 had around 50% unreacted amine groups. The pepsin-TMC layers contained a large number of unreacted carboxylic acid groups. The number of optimal groups might well be in between 2-4 functional groups per reactant. Preferably, one of the reactants should have only 2 reactive functional groups.
- **Monomer reactivity.** A high monomer reactivity will result in faster film formation. For monomer reactants with low reactivity, such as pepsin, the layer growth is slow. Therefore, higher reactant concentrations are generally required for successful film formation in case the monomer reactivity is low.
- **Size of the reactant.** The size of the reactants will be reflected in the membrane performance. Two large reactants will form a more open membrane layer due to steric hindrance of the reactants. This is reflected by the high MWCO of cross-linked pepsin membranes, whereas smaller molecules such as POSS allow separation performance in gas separation applications.

- **Monomer influence on the interface.** Proteins consist of both hydrophilic and hydrophobic group, and are known to assemble at the interface. Layer formation and membrane properties are strongly dependent on the surfactant type and concentration.¹¹
- **Length and flexibility of the bridging group.** Chapter 3 and 4 clearly illustrate the influence of the length and flexibility on membrane properties. Distinct properties can be expected from materials that have longer, more flexible bridges. While the poly(POSS-imide)s display glassy characteristics, one could design a more rubbery-like network using longer precursors.
- **Side groups** have a different effect on layer properties as bridging groups. In particular, side groups such as fluoroalkanes that influence the electronegativity will have a large impact on layer properties.
- **Type of chemistry.** The range of monomer reactants that can be used for interfacial polymerization is practically unlimited (Chapter 1). The center point, anchor point and bridge rigidity, hydrophilicity and chemical affinity can be predicted from polymeric counterparts. In addition, the chemical and thermal stability will depend on the type of groups, either aliphatic or with aromatic or other resonance structures.

Although these parameters provide guidelines for rational design of hyper-cross-linked networks, optimization of the reaction conditions for each individual combination of monomer reactants is required. Moreover, a fair comparison of membrane layers prepared via interfacial polymerization can only be accomplished by comparing structure-property-performance relationships, and not by solely comparing membrane performance data.

9.3.2. Structure-property-performance relationships

Fundamental knowledge on structure-property-performance relationships of the membrane material in a process is imperative for the determination of key material parameters. Often, a new membrane material is prepared and its permeability and selectivity are determined. This is particularly the case for membranes prepared via interfacial polymerization. Commonly, polyamides prepared via interfacial polymerization are characterized in terms of salt rejection or MWCO, water permeance, structure analysis by for example infrared spectroscopy or Rutherford backscattering spectrometry¹² and layer morphology. This allows for empirical data analysis (e.g. a higher layer roughness results in higher water permeability, or precursor A gives better

membranes than precursor B), but provides limited mechanistic insight into the membrane system. The difficulty in analysis of the membrane layers prepared via interfacial polymerization lies in the ultrathin nature of the films. Whereas most polymers can easily be prepared and analyzed as thin film and in bulk, preparation of mg sample masses of interfacial polymerization layers (of sub- μm thickness) is already a tedious task. The systematic structure-property analysis is further complicated by the rough morphology and the asymmetric nature of such ultrathin films. Synthesis of free-standing films is possible, and allows for synthesis of larger samples masses. However, it is questionable whether the layer properties of a free-standing film are similar to a layer prepared on a porous support. While film formation on top of a porous support results in a 100 nm layer thickness, we could obtain μm -thick films by free-standing film formation using similar reaction conditions. It is therefore preferential to characterize layers prepared via interfacial polymerization by using techniques that are applicable for thin films.

The only manner to obtain knowledge on the structure-property-performance relationships, is to combine membrane performance measurements with another in-situ characterization technique. Although simultaneous measurements are not a prerequisite, careful simulation of the membrane operating conditions is key to obtain accurate data. Because the temperature and presence of a penetrant (at a certain concentration and pressure) are of great influence on the membrane properties, we should accustom ourselves to measuring the membrane material properties at these conditions. In this thesis we have extensively analyzed the membrane thickness and refractive index (as an analogue to the layer density) by using spectroscopic ellipsometry at elevated temperature and pressure conditions (Chapters 4, 5 and 6). Although this provided useful insight on the membrane material properties in contact with a single component, the data will not reflect the membrane behavior under mixed feed conditions. The discrepancies between single and mixed gas experiments originates from effects such as:

- **Competitive sorption and diffusion.** The sorption and diffusion of a components is influenced by other components. Permeance of one component might decrease due to preferential sorption of the other component. Alternatively, the permeance might increase due to swelling induced by another component.
- **Concentration polarization.** Membranes preferentially permeate one component over the other. In doing so, the retained component is

concentrated at the membrane surface. The concentration reduction of the permeating component decreases the driving force, and reduces process selectivity and permeability of the preferential component.

- **Pressure ratio effects.** when the ideal membrane selectivity is much larger than the pressure ratio across the membrane, the process can be in a pressure-ratio-limited regime. The process selectivity will therefore limit the separation, and the intrinsic membrane material selectivity will be irrelevant.¹³
- **Stage-cut.** The purity of the permeating and retained components are coupled by the membrane process selectivity. Along the length of the membrane, the selectivity can change due to competitive sorption, concentration polarization and pressure ratio effects. The driving force of the permeating component will only decrease across the membrane length, and therefore the permeance and selectivity will also drop along the membrane length. It is therefore crucial to establish the specifications of the retained and permeating components, and to verify whether these can be matched with the given process parameters.

Although membrane material researchers focus on ever-higher membrane permeance and selectivity, the process can be limiting the final membrane performance. It is therefore key to design a membrane material with respect to a specific process. Future research should focus more on the interaction of penetrants with the membrane material, at relevant temperatures and pressure conditions. Spectroscopic ellipsometry is an excellent tool to measure the changes in thickness and refractive index as function of time, temperature, pressure and penetrant type. The technique allows for estimation of penetrant fractions, molar volumes and changes in the polymer as function of time. Nonetheless, it does not give direct information on the physical properties such as macromolecular chain dynamics and the visco-elastic properties of the material. Techniques that allow for direct measurement of the physical properties of ultrathin films are:

- **Atomic force microscopy (AFM)** measures the interaction between a surface and a nano-sized probe. By using different modes (contact, tapping, non-contact) the surface roughness, mechanical properties and adhesion properties can be determined. AFM can be performed in an liquid or gas atmosphere, and can therefore be used to track in situ changes in ultrathin films.

- **Dielectric relaxation spectroscopy** (DRS) measures the dielectric response of an ultrathin film at a broad frequency range (10^2 - 10^{10} Hz). The dielectric response is a function of the electronic, atomic and molecular interactions within a system. In particular, the changes in inter- and intra-molecular chain interactions at elevated temperature and by presence of a penetrant provide mechanistic insight on physical behavior of (network) polymers.
- **Quartz crystal microbalance** (QCM) measures the visco-elastic response of a material that is coated on a resonating quartz crystal. The frequency dependency of the response can be measured in-situ and in the presence of a liquid or gas atmosphere.

In-situ measurement of the thin membrane film properties can be used for optimization of the membrane material properties. After optimization of the physical and chemical properties of the membrane, scale-up of the membrane preparation can be optimized.

9.3.3. Scale-up the membrane production process

All commercial membrane processes require a relatively large surface area. A single disposable hemodialysis module contains about 1.5 m² of surface area, and yearly > 360 million¹⁴ of such modules are produced (with an ultrathin, defect free separation layer on a robust substrate with a high specific surface area!). Reverse osmosis plants operate modules of 35 m² each, and total membrane surface areas can range up to multiple thousands of square meters.

- Membranes need to be **defect-free** to get a process selectivity that resembles the intrinsic membrane selectivity, for gas separation in particular. Defects are more likely to occur when the membrane layer is ultrathin.
- Ultrathin membranes need to be mechanically supported by a **robust**, porous substrate with a **high specific surface area**.

Interfacial polymerization allows for defect-free layer synthesis with potentially unlimited lateral dimensions. Membrane preparation via interfacial polymerization can be performed on hollow fibers and on planar supports that are used in spiral wound modules. Interfacial polymerization is most commonly employed for spiral wound membrane modules, because the layers are mainly used for aqueous applications. However, for gas separation

applications a hollow fiber configuration is often more suitable, due to the higher surface-to-volume ratio of such a configuration.

Hollow fibers are commonly prepared via dry-wet spinning of a polymer solution into a non-solvent containing coagulation bath. At the right conditions, an asymmetric gas separation membrane that consists of a porous substructure and a thin, dense top layer can be obtained. Alternatively, one could prepare a gas separation membrane by using a porous hollow fiber or tube as a substrate for an interfacial polymerization reaction. For this purpose, we have done preliminary tests on membrane performance of poly(POSS-imide)s prepared via interfacial polymerization on tubular ceramic supports. Figure 9-3 shows the hydrogen/nitrogen permselectivity as function of the hydrogen permeance. Clearly, the permselectivities that are obtained for tubular supports are lower as compared to the planar supports, while the permeances through the tubular supports are much higher.

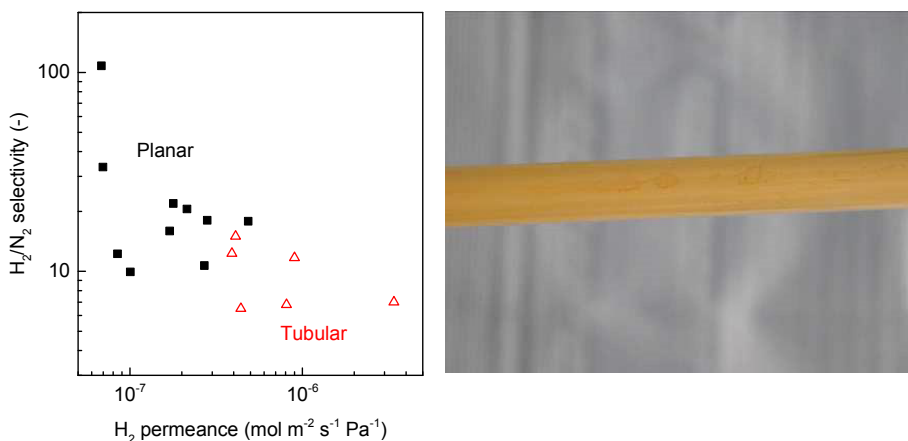


Figure 9-3. (left panel) Hydrogen/nitrogen permselectivity as function of the hydrogen permeance, for poly(POSS-imide)s prepared on planar (black squares) and tubular (red triangles). (right panel) Image of the γ -alumina coated α -alumina tubes with a poly(POSS-imide layer). The yellow-brown color is characteristic for the poly(POSS-imide) layers. Layer thicknesses are about 50-300 nm.

The differences in membrane performance can be caused by a number of reasons:

- The heat treatment of the planar supports was done on the same day as the membranes were prepared. The tubular supports were heat treated

several days after preparation. In case of the tubular supports, poly(amic acid) hydrolysis could have altered the membrane performance.¹⁵

- The pore size distribution of the γ -alumina layers used on the tubular supports might be different from the planar membranes. The pore size is known to influence the membrane performance of layers prepared via interfacial polymerization.¹⁶
- The planar supports are coated with two γ -alumina layers, while the tubular supports are only coated with a single γ -alumina layer. The number of defects can therefore be higher in the tubular supports. Defects are detrimental for the membrane permselectivity.

Further optimization of interfacial polymerization reaction parameters will be required for the preparation of poly(POSS-imide) membranes on tubular supports. The critical parameters that determine the membrane performance have to be determined by systematic investigation of reactant concentrations, support pore size (distribution) and poly(amic acid) stability prior to the heat treatment.

Although tubular supports are suitable for membrane gas separation application, they have a relatively high cost price¹⁷ and low surface-to-volume ratio with respect to hollow fibers. A higher surface to volume ratio can be accomplished using ceramic or metallic hollow fiber membranes.^{18, 19} In addition, by substituting the heat treatment at 300 °C that is necessary to convert the poly[POSS-(amic acid)] precursor into poly(POSS-imide) with a chemical imidization step²⁰ it is possible to use polymeric hollow fiber membranes as support.

9.4. Conclusions

Membrane development requires both fundamental material development and process knowledge. The integral design process is key for successful implementation of membranes in large-scale separation processes. In this thesis, we presented a generic synthesis route for preparation of hyper-cross-linked, hybrid membranes. Future research should move towards extension of the generic synthesis route for other material types and the testing of the membrane materials at relevant process conditions.

9.5. References

1. Choi, J.; Tamaki, R.; Kim, S. G.; Laine, R. M. *Chemistry of Materials* **2003**, 15, (17), 3365-3375
2. Budd, P. M.; Elabas, E. S.; Ghanem, B. S.; Makhseed, S.; McKeown, N. B.; Msayib, K. J.; Tattershall, C. E.; Wang, D. *Advanced Materials* **2004**, 16, (5), 456-459
3. Hashem, M.; Bezzu, C. G.; Kariuki, B. M.; McKeown, N. B. *Polymer Chemistry* **2011**, 2, (10), 2190-2192
4. Budd, P. M.; McKeown, N. B.; Fritsch, D. *Journal of Materials Chemistry* **2005**, 15, (20), 1977-1986
5. Bezzu, C. G.; Carta, M.; Tonkins, A.; Jansen, J. C.; Bernardo, P.; Bazzarelli, F.; McKeown, N. B. *Advanced Materials* **2012**, 24, (44), 5930-5933
6. Han, S. H.; Misdan, N.; Kim, S.; Doherty, C. M.; Hill, A. J.; Lee, Y. M. *Macromolecules* **2010**, 43, (18), 7657-7667
7. Han, S. H.; Kwon, H. J.; Kim, K. Y.; Seong, J. G.; Park, C. H.; Kim, S.; Doherty, C. M.; Thornton, A. W.; Hill, A. J.; Lozano, Á. E.; Berchtold, K. A.; Lee, Y. M. *Physical Chemistry Chemical Physics* **2012**, 14, (13), 4365-4373
8. Sanders, D. F.; Smith, Z. P.; Ribeiro, C. P.; Guo, R.; McGrath, J. E.; Paul, D. R.; Freeman, B. D. *Journal of Membrane Science* **2012**, 409-410, 232-241
9. Calle, M.; Doherty, C. M.; Hill, A. J.; Lee, Y. M. *Macromolecules* **2013**, 46, (20), 8179-8189
10. Consolati, G.; Genco, I.; Pegoraro, M.; Zanderighi, L. *Journal of Polymer Science, Part B: Polymer Physics* **1996**, 34, (2), 357-367
11. Mansourpanah, Y.; Madaeni, S. S.; Rahimpour, A. *Journal of Membrane Science* **2009**, 343, (1-2), 219-228
12. Matthews, T. D.; Yan, H.; Cahill, D. G.; Coronell, O.; Mariñas, B. J. *Journal of Membrane Science* **2013**, 429, (0), 71-80
13. Wijmans, J. G. *Journal of Membrane Science* **2003**, 220, (1-2), 1-3
14. Krause, B., Keynote lecture 1: "Membranes in Medical Applications". Gambro Dialysatoren GmbH: NMG-DMG-BMG meeting, Aachen, 2015.
15. Kreuz, J. A. *Journal of Polymer Science Part A: Polymer Chemistry* **1990**, 28, (13), 3787-3793
16. Hermans, S.; Bernstein, R.; Volodin, A.; Vankelecom, I. F. J. *Reactive and Functional Polymers* **2014**, 86, 199-208
17. Pera-Titus, M. *Chemical Reviews* **2014**, 114, (2), 1413-1492
18. Luiten-Olieman, M. W. J.; Raaijmakers, M. J. T.; Winnubst, L.; Bor, T. C.; Wessling, M.; Nijmeijer, A.; Benes, N. E. *Journal of Membrane Science* **2012**, 407-408, 155-163
19. Luiten-Olieman, M. W. J.; Raaijmakers, M. J. T.; Winnubst, L.; Wessling, M.; Nijmeijer, A.; Benes, N. E. *Scripta Materialia* **2011**, 65, (1), 25-28
20. Kailani, M. H.; Sung, C. S. P. *Macromolecules* **1998**, 31, (17), 5779-5784

Dankwoord

Mijn proefschrift is mede tot stand gekomen door de productieve en prettige samenwerking met collega's van de vakgroep anorganische membranen en andere vakgenoten uit de hele wereld. In my personal view, the group of experts that has been closely involved in my research have been a great contribution to the originality and quality of this thesis.

Ik heb grote waardering voor de inspanningen van mijn begeleider, prof. dr. ir. Niek Benes, die de basis heeft gelegd voor dit onderzoek. Niek, je hebt een prachtig team aan onderzoekers weten te verzamelen, en een unieke infrastructuur op het lab opgebouwd waarmee inzicht in de fundamentele aspecten van dunne (membraan)lagen kan worden verkregen. De positie die je nu inneemt op de Universiteit Twente, als hoofd van de Films in Fluids groep, komt je dan ook terecht toe. Je bezit een scherpte die het mogelijk maakte om het meeste uit mezelf te halen, en je schroomde niet om de verwachtingen voor mij en mijn onderzoek hoog te houden. Niek, your contributions are appreciatively acknowledged.

Mijn promotietraject binnen IM en het CARENA project is mede mogelijk gemaakt door prof. dr. ir. Arian Nijmeijer. Arian, je sterke management en positieve inslag hebben er altijd voor gezorgd dat er een goede, constructieve sfeer was binnen de groep. Het is mooi om te zien dat je altijd energie over had voor de groep (of juist ervan kreeg), naast je vele verantwoordelijkheden voor Shell op de meeste afgelegen locaties wereldwijd. Ik ken weinig mensen die zowel voet op een booreiland mogen zetten, en zich met enig gemak tussen de fundamentele wetenschappers begeven (als dat überhaupt al mogelijk is). Ik ben ervan overtuigd dat we elkaar in de toekomst nog met enige regelmaat zullen tegenkomen.

I have experienced much pleasure in working within the Inorganic Membranes group. My thanks go out to the staff, technical support and fellow researchers. Henny en Louis, ik heb altijd met interesse gevolgd wat jullie aan het onderzoek op het gebied van anorganische materialen bijdragen. Ondanks dat mijn onderzoek voor een groot deel op polymeerchemie is gebaseerd, heb ik toch vaak met jullie van gedachten kunnen wisselen. Mieke, met erg veel plezier heb ik onder jouw begeleiding mijn Master thesis op het gebied van stalen holle vezels afgerond. Het gemak waarmee je in het lab iets nieuws probeert en de energie die je toont om je praktische vaardigheden over te dragen zijn bemoedigend geweest voor een niet zo praktisch ingesteld persoon

als ikzelf. Frank en Cindy, niet alleen bedankt voor de experimentele ondersteuning, maar ook voor de Twente grapjes (die ik vaak niet meteen begreep als Brabander), futsal, de Engelse drop en nog meer details die het dagelijks onderzoek aangenaam maakten.

All PhD's share a great deal of experiences, including the daily peaks and setbacks, surges of creativity and brilliance, and the difficulties of managing a multi-year project at your own responsibility. I have had the pleasure to work with a very mixed group of PhD's, which has taught me many things about the differences in intrinsic motivation, how one approaches problems and what you need for an effective cooperation. Emiel, by far you have been the largest contribution in all these learnings. The number of discussions we had are maybe only surpassed by the confusion our names caused (or did we cause the confusion?). Als "de Iels" waren we een team, altijd bereid om iets verder uit te denken en te optimaliseren. Ik genoot altijd van de momenten dat je zei: "Michiel, jij bent toch zo slim hè?" Om me uit te dagen binnen enkele minuten een vraagstuk op te lossen waar je zelf al een paar uur mee bezig was. Ondanks de substantiële afstand tussen Deventer en Frankfurt en het gegeven dat je voor de concurrent werkt, houden we zeker contact!

Wojciech, you definitely created an additional dimension to my path towards promotion (if not more than just one – if only we had the means to measure those!). You brought a lot of fun into the science we did, and you taught me so many things about polymers, physics and ellipsometry. Even at the end of my PhD you kept the learning curve steep, due to the vast knowledge you have gathered during your own scientific journey.

Evelien, you were the person that challenged me the most in the last year: you have an eye for detail and you always dare to ask (more) critical questions. Your strong rationale exemplifies how good a researcher you are, and I am sure you will manage just fine in these four (short) years. Keep up the enthusiasm you always show when working on something new, because it works contagiously. Kristianne, thanks for the positive attitude you have. It has been a pleasure teaching you the inside-outs of ellipsometry and polymer physics. Soon you will have more knowledge than I, and I will be the questioning you.

Marcel, thanks for always having my back during difficult experimental work and your patience to see whether things would work out. Bas, you are always down-to-earth (is that a regional thing?!) and I enjoyed that. You are always

up for a good talk, topped with a good deal of humor and some sarcasm. Patrick, you always amazed me with the next unexpected thing you managed to do in the lab or out in the field. You always made office-life interesting and lively. Sushumna, I had a lot of fun working with you – and I am happy we can stay in touch over this long distance. Giri, Wei-Chen, Martin, Chung-Yul, Hammad, Ana, Rian, Cheryl – it has been interesting to work alongside you, and I took a great deal of learnings from the contact we had over the years. I have had the pleasure to supervise Bachelor and Master students during my PhD. Mitchel, Lynn and Wouter, many thanks for the useful insights you provided and the pleasant cooperation. I am proud of the work that you managed to do in the – too short – timespan of these assignments.

At the University of Twente I worked together with a number of researchers from other research groups. Harro, as fellow CARENA project PhD you were always first in line with figuring out the project procedures and the whether the targeted application of the membranes that we developed were in reach. Thanks for all the discussions and exchange of thoughts we had over the years. Yali, it was always a pleasure to work with you on interfacial polymerization related things, or just to have a fun conversation on the way to the coffee corner. Rob and Kitty, thanks for the time I could spend on the laboratories of your groups. Also thanks for your help in deciding whether and where I should do a PhD. All the other SFI and MST members, thanks for the enjoyable moments we shared.

My special thanks go to all the co-authors of the work that is presented in this thesis.. I have had the pleasure to work together with many researchers from the AVT-CVT and DWI of the RWTH Aachen in Germany. Thomas and Monika, thanks for your persistent effort in repeating experiments and discussing the results for the enzymatically active pepsin films. Martin and Burkhard, thanks for the help with the gas sorption equipment. Matthias, thanks for all the support in the discussion we had over the years, and the unlimited access you provided for working with your group and on your laboratories. Your enthusiasm and creativity have been an inspiration for me, and I appreciate all the scientific and personal feedback you have given me. Aditya, Martijn, Christian, Vinod, thanks for all the effort you placed in the fluorescent proteins layers. This was by far the area in which I was least comfortable at the start of the project, but you helped to overcome all the gaps in my knowledge

All others from Aachen (Lars, John, Kurt, Serafin, Sebastian, Theresa, Tobias, Tim, Hans, Stefanie, Florian and more!), thanks for all the times I could stay in Aachen for work at the RWTH and enjoy dinner or party with you. You always gave me a genuine feeling of being welcome. I enjoyed all the Winterschool experiences we shared over the years. I hope we will stay in touch somehow – as colleagues within the field of chemical engineering and as friends.

Although not included in my thesis, I had the opportunity to work with researchers from TU Delft (Theo, Zeljka, Wouter), Institut Européen des Membranes (Anne, Martin), Université de Savoie (David, Sylvie), CSIRO (Anita). I would like to acknowledge the positive collaboration between our groups. Further help and learnings came from discussions with numerous fellow PhDs, and many, many others. Thanks to all of you!

Mijn familie is altijd een grote bron van ondersteuning en fijne momenten geweest door de jaren heen. Papa en mama, bedankt voor al het vertrouwen dat jullie altijd hebben in mij. Mijn broers, Erik, Paul, Ruud, bedankt voor de goede band die we delen. Ik geniet van alle tijd die we samen kunnen doorbrengen, ook met Melanie, Sandra & Marleen en Hanneke.

Ik heb altijd veel steun ondervonden van mijn vrienden, die me altijd weer energie weten te geven met een leuke avond uit, een lang weekend rapujuhlat of gewoon een gezellig bezoek in Den Haag, Amsterdam, Deventer, Enschede of ergens anders in Nederland. In het bijzonder dank aan Inge, voor het ontwerp van de omslag van mijn proefschrift.

De meest belangrijke bijdrage aan mijn thesis is geleverd door Karin. Je bent de dierbaarste persoon in mijn leven. Alle energie die je me geeft is de grote drijvende kracht geweest achter mijn vasthoudendheid om mijn promotie tot een succes te maken. Je enthousiaste en slimme persoonlijkheid is een aanvulling op, en ook een voorbeeld voor mij. Het Michelangelo-effect gaat ook op voor doorzettingsvermogen, sociale vaardigheden en persoonlijke presentatie. Waar wij staan, is omdat we dat samen hebben bereikt – en dat belooft alleen maar goeds voor de toekomst!

Curriculum Vitae

Michiel Raaijmakers was born on 11 May 1987 in Geldrop, the Netherlands. In 2005, he obtained his vwo-diploma at the Strabrecht College in Geldrop. In the same year, he started his bachelor studies in Chemical Engineering at the University of Twente. During these years, he was active as board member for the Erasmus Student Network Twente, worked for the International Office of the University of Twente for the Erasmus programme and was active in the organization of the study tour of C.T.S.G. Alembic to Malaysia and Singapore. For his contributions to the Erasmus programme in the Netherlands, he was awarded the Erasmus student award in 2012. In 2008, he performed his bachelor thesis at the Universitat de Barcelona in Spain. After his bachelor studies he started with the master Chemical Engineering at the University of Twente, in the track Process Technology. In 2010, he performed a four-month professional internship at Vaperma Inc. in Quebec City, Canada. In 2011, he graduated cum laude from the University of Twente on a master thesis entitled: Development of stainless steel hollow fiber membranes with small radial dimensions. He was awarded the Unilever Research Price for his Master thesis.

Starting from November 2010, he has been working as a PhD candidate at the Inorganic Membranes group at the University of Twente, under the supervision of prof.dr.ir. Nieck E. Benes. He presented his research at multiple international conferences and workshops, including the International Membrane Science and Technology conference (IMSTEC, 2014) in Melbourne, Australia and Euromembrane (2015) in Aachen, Germany. In addition, he has co-organized a number of scientific meetings, including the Gordon Research Seminar (GRS, 2014) on Membranes, Materials and Processes.

List of publications

Per August 2015

Peer-reviewed international journals

-
- 2015 **Macromolecules.** Thermal imidization kinetics of ultrathin films of hybrid poly(POSS imide)s. DOI: 10.1021/acs.macromol.5b00473
- 2015 **Angewandte Chemie International Edition.** Enzymatically Active Ultrathin Pepsin Membranes. DOI: 10.1002/anie.201411263
- 2015 **Thermochimica Acta.** Temperature calibration procedure for thin film substrates for thermo-ellipsometric analysis using melting point standards. DOI: 10.1016/j.tca.2014.12.017
- 2014 **Chemistry of Materials.** Hybrid polyhedral oligomeric silsesquioxanes-imides with tailored intercege spacing for sieving of hot gases. DOI: 10.1021/cm500691e
- 2014 **Journal of the American Chemical Society.** Sieving of hot gases by hyper-cross-linked nanoscale-hybrid membranes. DOI: 10.1021/ja410047u
- 2013 **Patent.** Highly crosslinked hybrid polyimide-silsesquioxane membranes. WO 2015030594 A1
- 2012 **Journal of Materials Chemistry.** Ultra-thin hybrid polyhedral silsesquioxane-polyamide films with potentially unlimited 2D dimensions. DOI: 10.1039/C2JM31941A
- 2012 **Journal of Membrane Science.** Towards a generic method for inorganic porous hollow fibers preparation with shrinkage-controlled small radial dimensions, applied to Al₂O₃, Ni, SiC, stainless steel, and YSZ. DOI: 10.1016/j.memsci.2012.03.030
- 2011 **Scripta Materialia.** Porous stainless steel hollow fibers with shrinkage-controlled small radial dimensions. DOI: 10.1016/j.scriptamat.2011.03.023
- 2011 **Ozone: Science & Engineering.** Influence of high salinity on the degradation of humic acid by UV₂₅₄ and H₂O₂/UV₂₅₄. DOI: 10.1080/01919512.2012.649998
-

Selected oral presentations

-
- | | |
|------|--|
| 2015 | M.J.T. Raaijmakers, W. Ogieglo, M. Wessling, A. Nijmeijer, N.E. Benes, Hybrid inorganic-organic gas separation membranes, <i>Euromembrane 2015</i> , Aachen, Germany. |
| 2015 | M.J.T. Raaijmakers, Z. Maradzevic, W. Ogieglo E.J. Kappert, T. Dingemans, N.E. Benes. Thermal imidization of polyimides studied by in-situ thermal analyses. <i>Workshop Spectroscopic Ellipsometry 2015 (WSE 2015)</i> , Enschede, Netherlands. |
| 2013 | Nanostructured polyhedral oligomeric silsesquioxane hybrid membranes, <i>International Membrane Science and Technology Conference (IMSTEC)</i> , Melbourne, Australia. |
| 2012 | M.W.J. Luiten, M.J.T. Raaijmakers, A.J.A. Winnubst, T. Bor, M. Wessling, A. Nijmeijer, N.E. Benes, Inorganic porous hollow fiber membranes: generic method for small radial dimensions, <i>Euromembrane 2015</i> , Londen, United Kingdom. |
-